Copyright

by

William John Durand

2015

**The Dissertation Committee for William John Durand Certifies that this is the approved version of the following dissertation:**

# Design, Synthesis, and Engineering of Advanced Materials for Block Copolymer Lithography

**Committee:**

Carlton Grant Willson, Supervisor

Christopher J. Ellison, Co-Supervisor

Roger T. Bonnecaze

Thomas M. Truskett

Deji Akinwande

# Design, Synthesis, and Engineering of Advanced Materials for Block Copolymer Lithography

**by**

**William John Durand, B.S.ChE.**

## Dissertation

Presented to the Faculty of the Graduate School of

The University of Texas at Austin

in Partial Fulfillment

of the Requirements

for the Degree of

**Doctor of Philosophy**

**The University of Texas at Austin**

**May 2015**

# Dedication

This dissertation is dedicated to my incredible family and friends that have supported me during my graduate school career.

# Acknowledgements

First, I acknowledge the advisors who have made my graduate work possible: Professors Grant Willson and Chris Ellison. I am honored to have been a part of their groups, having interacted with the wonderful people within, and having worked on engaging and impactful research. I entered the world of research after fortuitously asking Dr. Willson how undergraduates could get involved with research the same day I scored the highest grade on one of his exams. I was soon introduced to several exciting projects within the group and quickly found a new passion. I worked with many Willson Group graduate students who were great mentors and friends, teaching me the skills in chemistry and engineering I use today: Jacob Adams, Jeff Strahan, Xinyu Gu, Michael Jacobsson, Brian Long, and Adam Berro.

After beginning my graduate career at Stanford University, I found that life behind the computer was not nearly as exciting as lab work within the Willson Group. I am eternally grateful that I was offered a position to return to The University of Texas at Austin, and I immediately jumped at the opportunity to once again develop next-generation materials. The research work presented in this dissertation would not be possible without collaborations with many incredible graduate students: Christopher Chen (my hoodmate), Logan Santos, Christopher Bates, Julie Cushen, Takehiro Seshimo, Michael Maher, Greg Blachut, Kazunori Mori, Yusuke Asano, Austin Lane, and Sunshine Zhao. All of these people share credit for the effort put forth in this work and have provided valuable insight, experience, and intelligent discussions. In addition, many undergraduates contributed to the block copolymer projects, but two talented individuals directly helped my efforts: Matthew Carlson and Summer Tein.

I especially thank Kathleen Sparks and Donna Martin for helping organize and manage the students within the Willson Group – our research would not nearly be where it is today without them. Also, our close collaborator Steve Sirard provided many valuable contributions to understanding and processing our materials. Finally, I acknowledge the Cockrell School of Engineering Fellowship for generous financial support.

**Design, Synthesis, and Engineering of Advanced Materials for Block Copolymer Lithography**

William John Durand, Ph.D.

The University of Texas at Austin, 2015

Supervisor: C. Grant Willson
Co-Supervisor: Christopher Ellison

Block copolymers (BCPs) are an attractive alternative for patterning applications used to produce next-generation microelectronic devices. Advancements require the development of high interaction parameter $\chi$ BCPs that enable patterning at the sub-10 nm length scale. Several organosilicon BCPs were designed to both enhance $\chi$ and impart an inherent etch selectivity that facilitates pattern transfer processes. Increasing the BCP silicon content both increases $\chi$ and bolsters the etch resistance, providing a pathway to designing new high-$\chi$ materials.

Unfortunately, the BCPs investigated are not amenable to thermal annealing because the organosilicon block preferentially segregates to an air/vacuum interface and drives orientation parallel to the surface. A series of spin-coatable, polarity-switching top coats (as well as other strategies) were developed to provide a "neutral" top interface and promote the perpendicular orientation of BCP domains. In addition, a methodology for evaluating the neutral condition, relying on thickness quantization and the corresponding wetting behavior (*i.e.* island/hole topography) of lamellae. The top coat strategy was demonstrated for several BCP systems, and perpendicular structures can successfully be etched on commercial tools and be transferred into underlying substrates.

The interaction parameter $\chi$ was evaluated using two methods to compare the performance of several BCPs: the order-disorder transition (ODT) of symmetric diblock copolymers, and the absolute scattering profile of a disordered BCP melt. Both methods, while severely limited for quantitative comparison, indicate trends towards higher $\chi$ with additional appended polar and organosilicon functional groups. Furthermore, the pattern fidelity is shown to be a function of the overall BCP segregation strength.

The free energy of confined lamella was modeled algebraically to produce response surface plots capable of identifying process conditions favorable for perpendicular orientation. Thickness independent perpendicular orientation is only favorable using two neutral interfaces. Incommensurate film thicknesses are the most favorable, with commensurability conditions dependent on the wetting behavior at each interface. The modeling was supplemented with an extensive body of thin film experimental work that qualitatively agrees well with the above conclusions.

# Table of Contents

List of Tables ........ xiii

List of Figures ........ xv

List of Reaction Schemes ........ xxvi

Chapter 1: Lithography for Microelectronics ........ 1

1.1 Development of Modern day Computing ........ 1

1.2 Photolithography ........ 3

1.3 Alternative Lithographic Strategies ........ 5

1.4 Block Copolymer Self-Assembly ........ 7

1.4.1 Thin Film Self-Assembly of Block Copolymers ........ 10

1.4.2 Design of High-$\chi$ Block Copolymers ........ 11

1.4.3 Effect of Surface Energy on Orientation ........ 13

1.4.4 Block Copolymer Lithography ........ 16

BCP Alignment ........ 17

Chapter 2: Orientation Control Using Top Coat Polymers ........ 20

2.1 Evaluation of Wetting Behavior ........ 21

2.1.1 Island/Hole Phenomena ........ 22

2.1.2 Bottom Interface Wetting ........ 25

2.1.3 Top Interface Wetting ........ 26

2.1.4 Neutral Interface Phenomena ........ 28

2.1.5 Conclusions and Implications ........ 34

2.2 Ring-Opening Top Coats ........ 34

2.2.1 1st Generation Ring-Opening Top Coats ........ 37

2.2.2 2nd Generation Ring-Opening Top Coats ........ 44

2.3 Chemical Vapor Deposited Top Coats ........ 48

2.4 Elimination Top Coats ........ 52

2.4.1 Poly(*p*-Phenylene Vinylene)s ........ 54

2.4.2 Hofmann Elimination Polymers ........ 58

2.5 Conclusions....64
2.6 Experimentals....65
Chemicals:....65
Block Copolymers....65
Instrumentation:....65
2.6.1 Generalized Bottom Interface Wetting Procedure....66
2.6.2 Generalized Top Interface Wetting Procedure....67
2.6.3 Generalized Cross-linkable Surface Treatment (XST) Synthesis67
2.6.4 Generalized Ring-Opening Top Coat Synthesis....69
2.6.5 Poly(*p*-Xylylene) TC....70
2.6.6 Poly(*p*-Phenylene Vinylene)s....71
PPV TC Synthesis....71
Thin Film Preparation....72
2.6.7 Hofmann Elimination Polymers....73
(1S,4S)-5-(2-bromoethyl)bicyclo[2.2.1]hept-2-ene, 2.1....73
Bromoalkyl Norbornane Homopolymer, 2.2....73
Quaternary Ammonium Bromide TC, 2.3....74
Quaternary Ammonium Hydroxide TC, 2.4....75
Chapter 3: Organosilicon Block Copolymers....76
3.1 Etch Performance....77
3.1.1 $O_2$ Plasma Etching....78
3.1.2 $N_2/H_2$ Plasma Etching....81
3.2 Poly(styrene-*block*-4-trimethylsilylstyrene)....85
3.3 Poly(trimethylsilylstyrene-*block*-4-methyl methacrylate)....91
3.4 Poly(4-methoxystyrene-*block*-4-trimethylsilylstyrene)....97
3.5 Poly(styrene-*block*-4-pentamethyldisilylstyrene)....102
3.5.1 Nitroxide-Mediated Polymerization....104
Maleimide End-Capping of PS-b-PDSS....109
3.5.2 Anionic Polymerization....112
3.6 Poly(4-methoxystyrene-*block*-4-pentamethyldisilylstyrene)....117

3.7 Conclusions ........................................................................................ 120
3.8 Experimentals ....................................................................................... 121
Chemicals: ............................................................................................ 121
Instrumentation: .................................................................................... 121
3.8.1 Thin Film Etch Experiments ............................................................. 122
$O_2$ Plasma Etching ............................................................................... 122
$N_2/H_2$ Plasma Etching ........................................................................... 123
3.8.2 Generalized Procedure for Anionic Synthesis .................................... 124
Monomer Purification ............................................................................ 124
Anionic Polymerization .......................................................................... 125
3.8.3 Nitroxide-Mediated Polymerization of PS-*b*-PDSS ............................ 125
Styrene Macroinitiator 3.2 ...................................................................... 125
NMP PS-b-PDSS ................................................................................... 126
Maleimide End-Capped PS-b-PDSS ........................................................ 126
3.8.4 Thin Film Processing of Organosilicon BCPs ..................................... 127
Chapter 4: Evaluation of the Interaction Parameter $\chi$ for Block Copolymers ..... 129
4.1 Order-Disorder Transition Method ........................................................ 131
4.2 Disordered-State Scattering Method ...................................................... 134
4.3 Challenges for Evaluating High-$\chi$ Block Copolymers ............................. 144
4.4 Effect of Segregation Strength ............................................................... 147
4.5 Conclusions & Outlook ......................................................................... 150
4.6 Experimentals ....................................................................................... 151
Materials .............................................................................................. 151
Instrumentation .................................................................................... 151
4.6.1 Disordered-State Scattering Experiments ............................................ 152
4.6.2 Polymer Density Measurements ......................................................... 153
Chapter 5: Block Copolymer Orientation Control ............................................ 155
5.1 Algebraic Model Development ............................................................... 156
5.2 Orientation Behavior – Single Interface Modification ............................... 160
Response Surface Analysis ...................................................................... 161

Thin Film Experimental Analysis ........................................163
5.3 Orientation Behavior – Dual Interface Modification ........................170
Response Surface Analysis ........................................170
Thin Film Experimental Analysis ........................................173
5.4 Conclusions ........................................177
5.5 Experimentals ........................................178
Materials ........................................178
Instrumentation ........................................178
5.5.1 Thin Film Preparation ........................................178
Appendix A: Modified Purification Glassware for Anionic Polymerization ......181
Appendix B: Algebraic Model for Block Copolymer Orientation Free Energy Calculations ........................................185
B.1 Free Energy Adapted Model ........................................185
B.2 Response Surface Plots ........................................188
References ........................................192

## List of Tables

Table 2.1: $T_g$'s of copolymers of maleic anhydride and several styrenic derivatives. The titles represent abbreviated chemical names of the styrenic component. ....44

Table 2.2: Composition summary for representative set of 2nd Generation TCs.[a].46

Table 3.1: Calculated Ohnishi parameters for the all-organic homopolymers. .....79

Table 3.2: Polymer characterization data. ....90

Table 3.3: Polymer characterization data. ....93

Table 3.4: Polymer characterization data. ....101

Table 3.5: NMP polymer characterization data. ....106

Table 3.6: Anionic polymer characterization data. ....115

Table 3.7: Polymer characterization data. ....119

Table 3.8: Characterization data of polymers used for $N_2/H_2$ etch experiments. 123

Table 3.9: Neutral cross-linked surface treatments (XSTs) for organosilicon BCPs and their respective characterization data. ....127

Table 3.10: Neutral top coat (TC) materials for organosilicon BCPs and their respective characterization data. ....128

Table 4.1: Summary of symmetric organosilicon BCPs evaluated for $\chi$-parameter and segregation strength study. ....130

Table 4.2: Estimation of $\chi$ at $T_{ODT}$ by mean-field theory ODT method. ....133

Table 4.3: Parameters used in Eqns. 4.3-4.13 to estimate $\chi$. ....136

Table 4.4: Mass attenuation coefficients of the elements comprising the polymers of this work under CuKα irradiation. ....138

Table 4.5: Calculated attenuation coefficients of the homopolymers comprising the BCPs in this work. ........................................................................138
Table 4.6: $\chi(T)$ coefficients measured by disorder-state scattering. ....................142
Table 4.7: Density of homopolymer melts according to Archimedes' principle.154
Table 5.1 Characterization data of XST polymers..............................................179
Table 5.2 Characterization data of TC polymers.................................................179

## List of Figures

Figure 1.1: Photograph of the first programmable digital computer (ENIAC). ......1

Figure 1.2: The integrated circuit, developed by Jack Kilby (Courtesy of Texas Instruments). ..........................................................................2

Figure 1.3: Simplified photolithographic process flow. The topographical features of a resist provide the template for patterning an underlying substrate. .4

Figure 1.4: (Top) A diblock copolymer comprised of two components, block A (red) and block B (blue). (Bottom) Accessible morphologies of a diblock copolymer, dependent on the volume fraction of the blocks.[16] ..........8

Figure 1.5: Theoretically-predicted phase diagram for an A-B diblock copolymer, dependent on the block volume fraction $f_A$, the interaction parameter $\chi$, and the overall degree of polymerization $N$.[16,18] ................................9

Figure 1.6: Effect of surface energy on a lamellar BCP. Preferential surfaces induce parallel orientation, while “neutral” surfaces provide perpendicular orientation, evident as fingerprint-like patterns. Note: the top interface is ignored in this representative example. ..........................................14

Figure 1.7: Qualitative depiction of surface energy between *A* and *B* components of a diblock copolymer. Surface preference increases as the surface energy deviates from the neutral region. ....................................................15

Figure 1.8: Process flow schematic for production of perpendicularly oriented BCPs by thermal annealing. .......................................................................16

Figure 1.9: Simplified flow for a chemo-epitaxy density multiplication process. The purple color represents a neutral region while the red is a preferential guiding stripe. .......................................................................19

Figure 2.1: Image of dense hole-like structures by optical profilometry. The depth of the depressions relative to the matrix is approximately 1 $L_0$. ...........22
Figure 2.2: Quantization of film thickness for parallel-oriented lamellae, forming symmetric or asymmetric wetting depending on the substrate wetting. Note: the red block is assumed to wet the air interface for both parallel conditions. A neutral interface (*i.e.* perpendicular) will not quantize.23
Figure 2.3: Island/hole thickness dependence for symmetric and asymmetric wetting. At these thicknesses, dark spots are islands and light spots are holes. Reprinted (adapted) with permission from Maher et al.[67] ................24
Figure 2.4: "Classic" island/hole test, yielding island topography for a symmetric-wetting substrate and hole topography for an asymmetric-wetting substrate. The dotted line indicates the initial film thickness of $1.25L_0$. Note: the red block is assumed to wet the free interface. .................26
Figure 2.5: "Confined" island/hole test, yielding islands for symmetric wetting and holes for asymmetric wetting of a $1.25L_0$ BCP film. The top coat conforms to the underlying topography. ..........................................27
Figure 2.6: First demonstration of an island/hole "switch" using PTMSS-*b*-PMMA by changing the composition of an underlying XST containing TMSS. Films are all at *ca.* $1.75L_0$. Scale bar is 20 μm.................................29
Figure 2.7: Cartoon of $0.5L_0$ island/hole behavior for lamellar-BCP with one neutral and one preferential interface. Reprinted with permission from Kim et al.[69] .........................................................................................30
Figure 2.8: Thickness dependence of a single neutral interface with commensurability conditions at $0.5nL_0$. Reprinted with permission from Maher et al.[67]31

Figure 2.9: AFM height images (a-d) and height profiles (e-h) for a confined wetting test of 17-18 nm $L_0$ PS-*b*-PTMSS using a PS surface treatment. Top labels identify the wetting behavior. Note: the AFM height images have opposite contrast as previously shown optical micrographs, so dark regions correspond to holes and light regions to islands. Reprinted (adapted) with permission from Maher et al.[67] ................................32

Figure 2.10: Confinement-induced perpendicular orientation for a BCP between two neutral interfaces, showing thickness independent orientation control. Reprinted with permission from Maher et al.[67] ...............................33

Figure 2.11: Polarity-switching concept that allows top coat to be cast from an orthogonal polar solvent but result in neutral surface energy between BCP components..........................................................................35

Figure. 2.12: (a) Ring-opening/closing reaction of maleic anhydride with aq. trimethylamine and heat, respectively. (b) Bulk IR spectra showing carboxylate region reversion upon ring-opening/closing. Reprinted with permission from Maher et al.[67] .......................................................36

Figure 2.13: Process flow for ring-opening polarity-switching top coats. ............36

Figure 2.14: Generalized 1st Generation top coat designs, comprised of maleic anhydride, norbornene derivatives, and either (a) an acrylate or (b) a styrenic derivative. ..........................................................................38

Figure 2.15:ABA triblock PS-*b*-PTMSS-*b*-PS used with 1st Generation TCs.......38

Figure 2.16: First demonstration of perpendicular orientation using a 1st Generation TC, thermally annealed 24 hrs. Reprinted with permission from C.M. Bates.[76] .........................................................................................39

Figure 2.17: Full-wafer perpendicular orientation achieved by an extended thermal anneal (120 hrs.), albeit with high defect density. Reprinted with permission from C.M. Bates.[76] ........................................................40

Figure 2.18: Fluorinated styrene TC enables good quality perpendicular assembly for PS-*b*-PTMSS-*b*-PS. (Inset) In the absence of a TC, only parallel structures are seen. From Bates et al. (adapted)[70] Reprinted with permission from AAAS. ..................................................................41

Figure 2.19: Diblock PLA-*b*-PTMSS high-$\chi$ polymer..........................................42

Figure 2.20: TC enables good quality perpendicular assembly for high-$\chi$ PLA-*b*-PTMSS. (Inset) In the absence of a TC, only parallel structures are seen. From Bates et al. (adapted)[70] Reprinted with permission from AAAS. ..........................................................................................43

Figure 2.21: (a) Generalized 2nd Generation TC strategy using alternating copolymers of maleic anhydride and styrenic derivatives. (b) Neutral TCs can be produced by varying the composition between relatively low/high surface energy styrenic components ................................................45

Figure 2.22: (a) Top down images of perpendicular assembly at $1.5L_0$ produced using 2nd Generation TCs for BCPs of both different pitch (indicated by subscript) and chemistry. (b) Cross-section image of PS-*b*-PTMSS-*b*-$PS_{30\ nm}$ showing through-film perpendicular assembly using TCs. Reprinted (adapted) with permission from Maher et al.[67] ................47

Figure 2.23: Process flow for CVD top coats. TC is inherently neutral and can be directly etched to transfer the underlying pattern. ............................49

Figure 2.24: Initial orientation results for CVD TC, poly(*p*-xylylene), showing evidence of perpendicular self-assembly for a lamellar BCP, but with a high degree of defectivity. ....................................................................50
Figure 2.25: Film expansion curve for poly(*p*-xylylene) film on silicon wafer, showing $T_g$ near 122 °C. ....................................................................52
Figure 2.26: The polarity-switching mechanism of ring-opening TCs (represented by the curved arrow) can only access limited surface energies due to maleic anhydride's inherently high polarity. In contrast, elimination polymers can theoretically access all surface energy ranges. ..........................53
Figure 2.27: Process flow for polarity-switching elimination TCs. The TC must be etched through to the underlying structures. ....................................54
Figure 2.28: TGA trace of anhydrous PPV pre-polymer ....................................56
Figure 2.29: (a) SEM image of microstructure found using PPV as a top coat material. (b) Optical micrograph of macro-scale topography seen after annealing PPV TC film stack. Note difference in scale bars. ..........................57
Figure 2.30: TGA experiment with TC polymer **2.4** showing three different two hour isotherm segments: (a) 75 ºC, (b) 110 ºC, and (c) 200 ºC. ..............60
Figure 2.31: Bulk IR spectra of quaternary ammonium salt polymer **2.4** (blue) and the same sample after annealing at 160 ºC (red)....................................61
Figure 2.32: (a) SEM image of representative sample annealed with Hofmann elimination TC and without TC (inset). (b) Optical micrograph of film cracking induced by volume shrinkage during the elimination process. ....................................................................................................62
Figure 2.33: Poly(4-*tert*-butylstyrene-*r*-methyl methacrylate-*r*-vinylbenzyl azide) XST polymer used for substrate surface energy modifications. .......68

Figure 3.1: Etch depth of homopolymer films subjected to an $O_2$-RIE.[36] ............79

Figure 3.2: (a) A bowed organosilicon BCP profile after an oxidizing etch. (b) A straight BCP profile obtained after a short oxidizing etch followed by a reducing $N_2/H_2$ etch to transfer the pattern. Images courtesy of Steve Sirard, Lam Research Corporation.[119] ............................................82

Figure 3.3: Isolated effects of $N_2/H_2$ plasma components on a PDSS homopolymer sample as characterized by the Si-C FTIR signal.[119] .......................83

Figure 3.4: FTIR spectra of Si-O-Si bond region for PDSS film before and after VUV exposure.[119] .........................................................................83

Figure 3.5: Comparison of etch profiles of homopolymer films subjected to plasma/VUV exposure as a function of silicon content.[119] ...............84

Figure 3.6: SEC refractive index traces of the PS-*b*-PTMSS BCPs synthesized for study and their respective homopolymer aliquots.[36] .........................88

Figure 3.7: MALDI spectra of PS homopolymer aliquots.[36] ...............................89

Figure 3.8: MALDI spectra of PS-*b*-PTMSS BCPs.[36] ..........................................89

Figure 3.9: SAXS profile of ordered PS-*b*-$PTMSS_{20\ nm}$.[36] ...................................91

Figure 3.10: SEC refractive index traces of the PTMSS-*b*-$PMMA_{31\ nm}$ BCP synthesized for study and the respective homopolymer aliquot. ......93

Figure 3.11: SAXS profile of ordered PTMSS-*b*-$PMMA_{31\ nm}$. ............................94

Figure 3.12: SEM images of PTMSS-*b*-$PMMA_{31\ nm}$ showing perforated-like structures when confined between a neutral XST and ring-opening TC (left) versus perpendicular assembly when confined between two neutral XSTs (substrate and floated film). ..................................................95

Figure 3.13: Top coat substituent effects (*i.e.* surface energy) on the orientation of PTMSS-*b*-$PMMA_{31\ nm}$. ...................................................................96

Figure 3.14: SEC refractive index traces of the PMOST-*b*-PTMSS BCPs synthesized for study and their respective homopolymer aliquots.[36] ..................99
Figure 3.15: MALDI spectra of PMOST homopolymer aliquots.[36] ......................99
Figure 3.16: MALDI spectra of PMOST-*b*-PTMSS BCPs.[36] .............................100
Figure 3.17: SAXS profile of ordered (top) PMOST-*b*-$PTMSS_{20\ nm}$ and (bottom) PMOST-*b*-$PTMSS_{14\ nm}$.[36] ..............................................................102
Figure 3.18: SAXS profiles of NMP PS-*b*-PDSS materials. ..............................106
Figure 3.19: Thin film thermal annealing test using NMP PS-*b*-PDSS. The control (left) shows no assembly, while annealing between two neutral interfaces (right) shows defective perpendicular structures...........107
Figure 3.20: SEC RI traces of bulk NMP PS-*b*-PDSS before annealing (blue), and after annealing in an air (red) and nitrogen environment (purple)..108
Figure 3.21: TGA profiles of *N*-phenylmaleimide and alkoxyamine end-capped BCPs. .........................................................................................111
Figure 3.22: SEC RI traces of *N*-phenylmaleimide end-capped PS-*b*-PDSS before (blue) and after (purple) annealing. ..............................................111
Figure 3.23: SEC refractive index traces of the PS-*b*-PDSS BCPs synthesized for study and their respective homopolymer aliquots.[36].......................113
Figure 3.24: MALDI spectra of PS homopolymer aliquots.[36] ............................114
Figure 3.25: MALDI spectra of PS-*b*-PDSS BCPs.[36]........................................114
Figure 3.26: SAXS profile of ordered (top) PS-*b*-$PDSS_{20\ nm}$ and (bottom) PS-*b*-$PDSS_{14\ nm}$.[36]........................................................................116
Figure 3.27: SEC refractive index traces of the PMOST-*b*-PDSS BCP synthesized for study and the respective homopolymer aliquot.[36]..........................118
Figure 3.28: MALDI spectra of PMOST homopolymer and PMOST-*b*-PDSS.[36]118

Figure 4.1: Dynamic mechanical spectroscopy plots of the storage modulus (G') taken upon a constant 5°C/min temperature ramp for three block copolymer samples with an accessible $T_{ODT}$.................................132

Figure 4.2: Calibration of the x-ray source using a MMSE fit of LDPE to a pre-calibrated intensity profile, producing a scaling factor *K*. .............137

Figure 4.3: (a) SAXS profiles of PS-*b*-$PMMA_{Dis}$ and corresponding model fit near the first order scattering maximum, collected at several temperatures. (b) Plot of $\chi$ estimated from the scattering profile vs. $T^{-1}$ and the corresponding best fit line............................................................139

Figure 4.4: (a) SAXS profiles of PS-*b*-$PTMSS_{Dis}$ and corresponding model fit near the first order scattering maximum, collected at several temperatures. (b) Plot of $\chi$ estimated from the scattering profile vs. $T^{-1}$ and the corresponding best fit line............................................................140

Figure 4.5: (a) SAXS profiles of PMOST-*b*-$PTMSS_{Dis}$ and corresponding model fit near the first order scattering maximum, collected at several temperatures. (b) Plot of $\chi$ estimated from the scattering profile vs. $T^{-1}$ and the corresponding best fit line. ...............................................140

Figure 4.6: (a) SAXS profiles of PS-*b*-$PDSS_{Dis}$ and corresponding model fit near the first order scattering maximum, collected at several temperatures. (b) Plot of $\chi$ estimated from the scattering profile vs. $T^{-1}$ and the corresponding best fit line............................................................141

Figure 4.7: (a) SAXS profiles of PMOST-*b*-$PDSS_{Dis}$ near the first order scattering maximum, collected at several temperatures. (b) Plot of $\chi$ estimated from the scattering profile vs. $T^{-1}$ and the corresponding best fit line. ....141

Figure 4.8: The $\chi$ of each disordered BCP measured by absolute scattering, plotted as a function of temperature. ............................................................142
Figure 4.9: Tornado plot for PS-*b*-PMMA (ranked from high to low) emphasizing the sensitivity of $\chi$ to various experimentally derived parameters........146
Figure 4.10: Top-down and angled SEM images of Si-BCPs after etching. As cast film thicknesses are *ca.* $1.75L_0$. Scale bars are all 100 nm and apply to each row of figures, respectively. ..................................................148
Figure 5.1: The three orientations studied in the free energy model herein and the corresponding commensurability conditions. ................................155
Figure 5.2: A representative set of free energy curves produced using the algebraic model for parallel (symmetric/asymmetric) and vertical orientations. The lowest free energy of the three curves is predicted to be the favored orientation. ........................................................................158
Figure 5.3: Free energy difference between horizontal and vertical orientations for a representative condition. Regions above the zero-axis (green) indicate perpendicular orientation, while those below (red) are parallel. ....159
Figure 5.4: Response surface plots and x-z plane cross-sections thereof for a neutral bottom interface ($\Delta\gamma_{Btm} = 0$)..........................................................162
Figure 5.5: The bottom (XST), organosilicon BCP, and top coat (TC) materials used in the experimental analysis and the process flow used to generate the investigated samples. ..................................................................164
Figure 5.6: Perpendicular orientation generally transitioned to parallel orientation through more complex mixed or perforated morphologies as a function of surface preference......................................................................165

Figure 5.7: Top-down and angled SEM images of several morphologies observed in thin-film. Samples (*ca.* $2L_0$) were etched from both the top and side.166
Figure 5.8: Representative subset of the experimental matrix for a neutral substrate, evaluated at several film thicknesses using TCs incrementally more preferential towards the organosilicon domain. Note: subtle differences in the contrast and pattern quality are a result of the batch-wise process used to prepare groups of samples. ................................................168
Figure 5.9: Thickness windows corresponding to self-assembly quality for the neutral substrate expanded dataset. ..........................................................169
Figure 5.10: Response surface plots and x-z plane cross-sections thereof for a slightly preferential bottom interface ($\Delta\gamma_{Btm}$ = -1). ......................................171
Figure 5.11: Response surface plots for a preferential bottom interface ($\Delta\gamma_{Btm}$ = -2). ..........................................................................................172
Figure 5.12: Response surface plots for a preferential bottom interface ($\Delta\gamma_{Btm}$ = -3). ..........................................................................................173
Figure 5.13: Representative subset of the experimental matrix for a substrate weakly preferential towards the organic domain, evaluated at several film thicknesses using a range of TCs. Note: subtle differences in the contrast and pattern quality are a result of the batch-wise process used to prepare groups of samples. ........................................................................175
Figure 5.14: Thickness windows corresponding to self-assembly quality for the weakly preferential substrate expanded dataset. .............................176
Figure A.1: Schematics of anionic distillation flask, equipped with pressure release valve and extended inlet tube to promote active vacuum-distillations.182

Figure A.2: Photographs of anionic distillation round-bottomed flasks. Stop-cocks are not shown. ....183

Figure A.3: Schematic of angled distillation head, drawn with water cooling jacket. Heads were produced with/without the cooling jacket for flame-dried and non-flame-dried applications, respectively. ....184

Figure A.4: Photograph of angled distillation head (shown with jacketed condenser). ....184

## List of Reaction Schemes

Scheme 2.1: Formation of poly(*p*-xylylene) (parylene) by heating of cyclic [2.2]paracylcophane precursor to form a resonance-stabilized reactive di-radical intermediate. ....48

Scheme 2.2: Generalized scheme for the polymerization of PPV TCs from α,α'-disubstituted *p*-xylylenes. The water-soluble polyelectrolyte precursor eliminates to form PPV upon application of heat. ......55

Scheme 2.3: Generalized Hofmann elimination reaction, converting a polar quaternary ammonium salt into a non-polar alkene. ....58

Scheme 2.4: Synthesis of norbornene-based Hofmann elimination TC. ....59

Scheme 2.5 Generalized synthetic scheme for 2nd Generation top coats. ....69

Scheme 2.6: Synthesis of bis-(sulfonium chloride) monomer. ....71

Scheme 2.7: Synthesis of PPV pre-polymer polyelectrolyte. ....71

Scheme 3.1: Synthesis of TMSS monomer. ....87

Scheme 3.2: Anionic synthesis of PS-*b*-PTMSS. ....87

Scheme 3.3: Anionic synthesis of PTMSS-*b*-PMMA. ....92

Scheme 3.4: Anionic synthesis of PMOST-*b*-PTMSS. ....98

Scheme 3.5: Synthesis of DSS monomer. ....103

Scheme 3.6: Nitroxide-mediated polymerization scheme of PS-*b*-PDSS. ....105

Scheme 3.7: End-cap reaction of alkoyamine-terminated PS-*b*-PDSS with *N*-phenylmaleimide. ....110

Scheme 3.8: Anionic synthesis of PS-*b*-PDSS. ....112

Scheme 3.9: Anionic synthesis of PMOST-*b*-PDSS. ....117

# Chapter 1: Lithography for Microelectronics

## 1.1 Development of Modern day Computing

Tools have been used to aid in numerical computations since the advent of the abacus thousands of year ago. Since then, computers have evolved from mechanical instruments to all-electronic digital devices. The first programmable electronic computer, the Electronic Numerical Integrator and Computer (ENIAC) (Fig. 1.1), was developed by the United States Army as a system for performing ballistic calculations. Although an incredible advancement for the time, this type of computer by today's standards would be extremely limited and cumbersome; the machine weighed over 30 tons, took up 1800 sq. ft. of space, and consumed 150 kW of power.[1] The ENIAC's transistors directing current consisted of vacuum tubes, which are relatively large, power-hungry, and delicate components not suitable for manufacturing on a commercial scale.

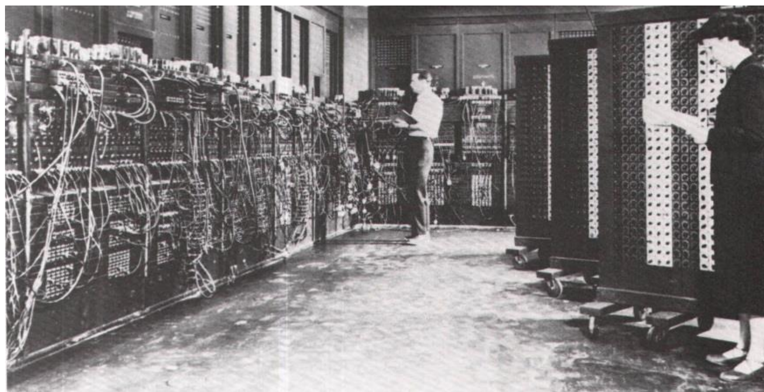

Figure 1.1: Photograph of the first programmable digital computer (ENIAC).

The transition to smaller electronic devices was dramatically advanced by the invention of the solid-state point contact transistor by William Shockley, John Bardeen, and Walter Brattain at Bell Labs in 1948. Their device could be made smaller, more

efficient, and scalable, making it relevant for industrial manufacturing. The solid-state transistor and other electronic components formed the basis of functioning circuits. Originally, these computer components were individually constructed and assembled, but it wasn't until Jack Kilby of Texas Instruments demonstrated in 1958 that the electronic circuit could be fabricated from a single semiconducting material as an "integrated circuit" (Fig. 1.2).

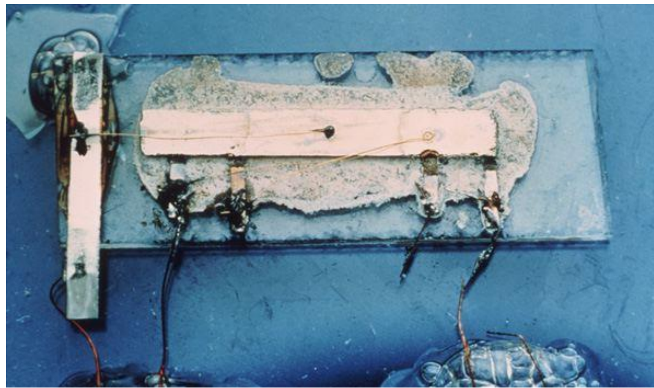

Figure 1.2: The integrated circuit, developed by Jack Kilby (Courtesy of Texas Instruments).

Robert Noyce and Gordon Moore of Fairchild Semiconductor capitalized on several practical shortcomings of Kilby's original integrated circuit (IC) design, inventing a planar device comprised of interconnecting layers of semiconducting and insulating materials. This creation led to the modern vision of an IC that is efficient, robust, and inexpensive to manufacture.

In the 1960's and 1970's ICs became nearly ubiquitous in modern day lifestyle, fueling the demand for continuous innovation. The cost of a chip could be decreased and the computing power increased by scaling the components smaller. This economic and performance-based impetus has driven the microelectronic industry towards increasing

the density of structures on a device. Gordon Moore, who with Noyce founded the multi-billion dollar semiconductor manufacturer Intel, famously observed in 1965 that the number of transistors on an IC doubled annually.[2] He foresaw this trend would continue barring no fundamental limits, and while his original estimate was later revised to doubling every two years, the industry has been effectively driven to maintain pace with "Moore's Law" ever since.

## 1.2 Photolithography

The interconnecting layers that make up integrated circuits are primarily defined by a process called photolithography. Advances to this process have been instrumental in maintaining progress with Moore's Law and accelerating the microelectronic industry towards faster and less-expensive devices. The limitations of patterning are therefore intimately tied with the future of semiconductor technology. The traditional photolithographic process used to fabricate devices is shown in Fig. 1.3. In this process, a photosensitive resist is applied above a layer that requires patterning. The resist is selectively exposed through a photomask, altering its solubility properties; either the exposed regions can be developed away (positive tone) or they become insoluble (negative tone). The topographical patterns of the resist can be transferred to the underlying substrate using an etch process, and the resist is finally stripped away to reveal the patterned layer.

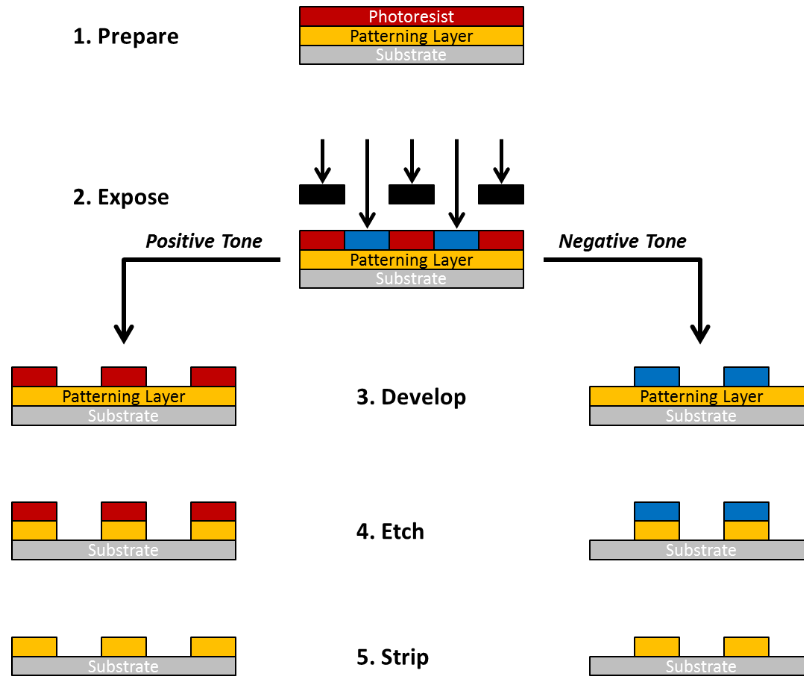


Figure 1.3: Simplified photolithographic process flow. The topographical features of a resist provide the template for patterning an underlying substrate.

A photoresist material itself is typically never a part of the actual microelectronic device, but it has several critical properties that enable its function: it provides topographical structures that *resist* an etch transfer step, and the materials are processable in a manner that can produce high-throughput, high-resolution patterns at low cost. Photolithography has continuously improved its performance by a variety of material, physical, and processing advancements, but its resolution is ultimately limited. The minimum resolution of optical lithography $R$ is described by the Rayleigh resolution criterion (Eqn. 1.1). In this equation, $k_1$ is a process-dependent scaling factor, $\lambda$ is the wavelength of the light source, and $NA$ is the numerical aperture of the lens system.

$$R = k_1 \frac{\lambda}{NA} \tag{1.1}$$

Several technological breakthroughs (*e.g.* immersion fluids,[3,4] off-axis illumination,[5] etc.[5,6]) have been used to reduce *R*, but historically, the most significant advancements have come by the introduction of smaller wavelength light sources. The advances have culminated in the development of current-generation deep UV ArF excimer lasers (193 nm) that are the backbone of today's fabrication facilities. Enormous monetary and scientific effort has been expended to adopt shorter wavelengths (157 nm deep UV, 13.5 nm EUV, x-ray, etc.), but all pathways have been met with considerable challenges.

EUV lithography stands as the most heavily supported platform to overtake 193 nm optical lithography, but it still suffers from several key drawbacks. The source power intensity has been one of the biggest limitations; a power output exceeding 100 W is a targeted requirement for sufficient throughput, but recent reports indicate the output is still too low.[7] The technological constraints, in addition to the enormous projected cost of individual tools (*ca.* $50-100M),[8] make alternative lithographic technologies highly attractive.

### 1.3 Alternative Lithographic Strategies

The physical and cost limitations of conventional photolithography have generated interest in alternative strategies that can reach the next-generation patterning targets. These techniques do not necessarily seek to supplant photolithography, but in some cases can be used to complement the existing methodology.

Single patterning photolithography using 193 nm immersion tools is limited to printing structures of *ca.* 36-40 nm.[4] This limit can effectively be overcome by printing many structures sequentially in a class of technologies called multiple patterning.[4]

Desired patterns can be decomposed into many sequential exposure, deposition, and etch steps. The most common procedure, self-aligned double patterning (SADP) (also SAQP, “Quad”) involves depositing conformal films atop a pre-patterned structure, then transferring the sidewall material into the underlying substrate. While these processes do not necessarily require new equipment or materials, they do consist of many additional steps. This dramatically increases the cost of the lithography and makes less complex alternatives more viable.

Electron beam lithography, which relies on electron-sensitive resist materials, is capable of sub-10 nm resolution,[9] but the serial nature of the process is prohibitive. The write time would be infeasible for production of highly dense arrays; for example, an e-beam pattern for the hard disk drive industry’s target of 1 Tbit/in$^2$ would require more than a month of continuous write time and exceed $1M in cost.[10] Parallel-write e-beam systems[11] have seen some academic interest, but have not shown competitive commercial results.

Step and flash imprint lithography (SFIL),[12] more commonly referred to today as nanoimprint lithography (NIL), can also provide sub-10 nm resolution.[13,14] This technology replicates physical templates into photocurable resists and is capable of printing hundreds of wafers per hour.[15] While this technology is promising for next-generation applications, some form of either conventional photolithography or e-beam lithography is required to produce the template. Once a template is manufactured, the pattern can be replicated many times over at minimal cost.

Block copolymer lithography, which is the primary focus of this dissertation and is introduced in the following sections, can complement the existing strategies to make them viable. This technology can efficiently access structures smaller than conventional

optical lithography and can enable high-resolution patterns suitable for producing NIL templates.

### 1.4 Block Copolymer Self-Assembly

Block copolymers (BCPs) are a special type of copolymer comprised of two or more distinct polymeric segments linked by covalent bonds. Typically, block copolymers are synthesized by subsequent addition of a monomeric component to the reactive chain end of a living homopolymer to form “blocks” or segments of each component. Like oil and water, most polymers macrophase separate, but because in a BCP the segments are joined by a covalent linkage, the different components *microphase* separate in some way to reduce the number of energetically unfavorable interactions. The microphase separation or “self-assembly” results in ordered, periodic structures on the nanometer length scale. Various morphologies can be accessed by tuning the volume fractions of the polymer blocks (Fig 1.4). The morphologies are a result of a balance between free energy costs of interaction between internal interfaces and conformational entropy loss as the macromolecules spatially organize.

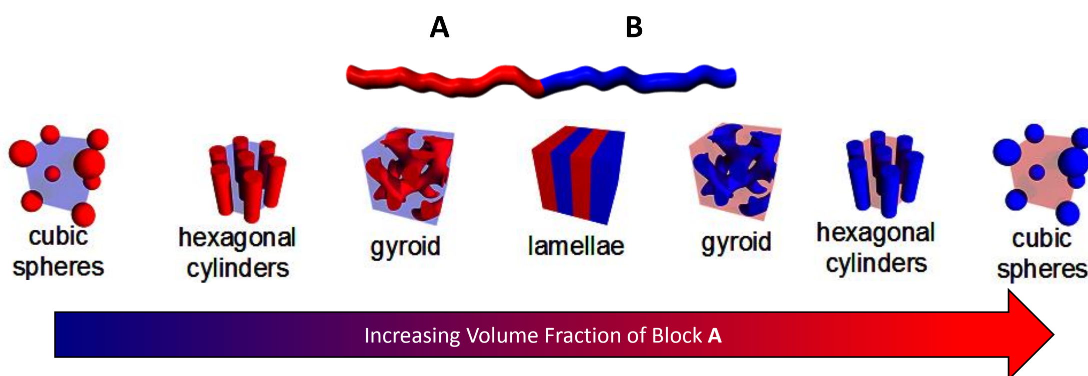


Figure 1.4: (Top) A diblock copolymer comprised of two components, block A (red) and block B (blue). (Bottom) Accessible morphologies of a diblock copolymer, dependent on the volume fraction of the blocks.[16]

The phase diagram for a diblock copolymer (Fig. 1.5) depicts the theoretically-predicted conditions suitable for producing several different BCP morphologies. These morphologies are dependent on the volume fraction $f_A$ and the BCP's segregation strength $\chi N$, where $\chi$ is the Flory-Huggins interaction parameter and $N$ is the overall degree of polymerization. The interaction parameter between two components, formally the energetic penalty of replacing one monomeric unit of a block with the second component, effectively represents component incompatibility.[17] As the segregation strength increases, the material crosses from the disordered state through an order-disorder transition (ODT) into a region of microphase separated domains. For a symmetric diblock copolymer ($f_A \approx 0.5$) to form ordered lamellar structures, $\chi N$ must be greater than 10.5.

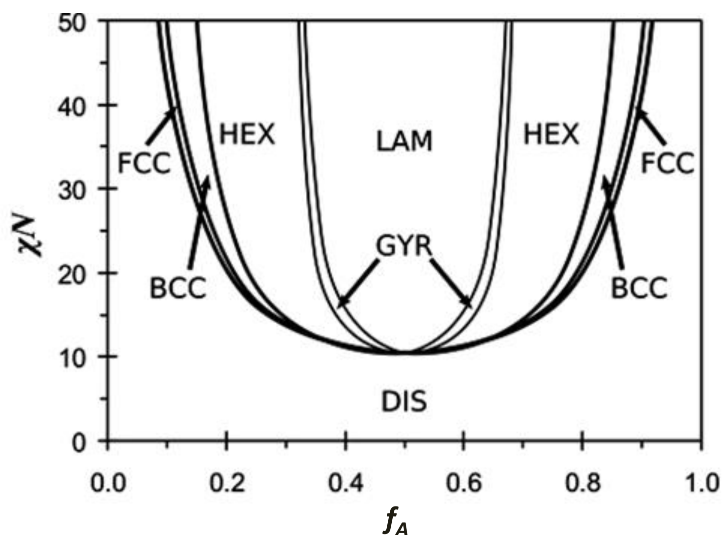


Figure 1.5: Theoretically-predicted phase diagram for an A-B diblock copolymer, dependent on the block volume fraction $f_A$, the interaction parameter $\chi$, and the overall degree of polymerization $N$.[16,18]

To form the phase-separated microstructures, the BCP must be annealed or processed to provide sufficient chain mobility for reorganization. Most commonly, this is accomplished by either heating the bulk material (thermal annealing) to temperatures greater than the glass-transition temperature ($T_g$) of each block or exposing the polymer to solvent vapors (solvent annealing) that plasticize one or more component. Upon cooling or removal of solvent, the domains are effectively frozen in a glassy (or crystalline) matrix.

The bulk equilibrium periodicity of the BCP domains $D$, often termed $L_0$ for lamellar morphology, is proportional to both $N$ and $\chi$. In the strong-segregation limit (SSL, $\chi N >> 10.5$) (Eqn. 1.2), $D$ is a much stronger function of $N$.[19] However, BCPs in the weak-segregation limit (WSL, $\chi N \approx 10.5$) (Eqn. 1.3) have a much weaker dependence on $N$.[20] The transition between the SSL to the WSL is not abrupt, and BCPs with segregation strength greater than ≈15 can be categorized as being in an "intermediate-

segregation regime" ($15 < \chi N < 60$).[21] The exponents of Eqn 1.2 and 1.3 have been the subject of both theoretical and experimental disagreement,[19,22] but in all regimes, the periodicity $D$ is a stronger function of $N$ than $\chi$. This provides a pathway to reduce $D$ by reducing the polymer molecular weight for fixed monomeric components (*i.e.* constant $\chi$).

$$\text{(SSL)} \quad D \propto N^{2/3}\chi^{1/6} \tag{1.2}$$

$$\text{(WSL)} \quad D \propto N^{1/2}\chi^{1/6} \tag{1.3}$$

The resolution limit of BCP structures has been dramatically reduced by the introduction of high-$\chi$ materials. To date, cylindrical domains have been reported as small as 3 nm using salt-complexed poly(styrene-*block*-ethylene oxide)[23] and 5 nm using oligosaccharide/organosilicon BCPs.[24] Several commercially available high-$\chi$ BCPs that self-assemble with sub-10 nm domains also exist. This includes: poly(styrene-*block*-2-vinylpyridine) (PS-*b*-P2VP),[25] poly(styrene-*block*-dimethylsiloxane) (PS-*b*-PDMS),[26] and poly(styrene-*block*-D,L-lactide) (PS-*b*-PLA).[27] Application of BCPs to lithographic patterning is discussed in the following section.

**1.4.1 Thin Film Self-Assembly of Block Copolymers**

Block copolymer self-assembly in thin films has drawn considerable attention, particularly within the semiconductor industry, because the nanoscale structures that are formed can be integrated with next-generation patterning processes. Due to the resolution limits and high-cost of traditional photolithography, a bottom-up self-assembled process can complement existing technology by serving as a cost-effective way to pattern regular, periodic device architectures commonly found in front-end-of-the-line (FEOL)

technology. BCPs have already been demonstrated for applications such as nanoimprint templates for storage media,[28] FinFET transistor architectures,[29] contact hole shrinkage,[30,31] and dielectric fabrication.[32] All applications leverage the nanoscale BCP domains as patterning templates for precise, periodic structures. Although nearly all morphologies have been demonstrated for patterning applications, the present work focuses primarily on lamellar morphology using symmetric A-B diblock (or ABA triblock) copolymers. Lamellae have unique advantages for lithographic applications over other morphologies: higher aspect ratio structures can be fabricated by simply changing film thickness, the wetting behavior can be probed easily (see Section 2.1), and advantageous rectangular geometries can be developed for bit-patterned media.[28] The behavior of BCP lamellae in thin films has been studied in great detail by both theoretical and experimental means.

Self-assembly in thin films presents complexities not evident in bulk phase behavior. Surface-block interactions, resulting in preferential wetting at the film interfaces, can induce morphological and orientation changes in the BCP (the effect of surface energy is discussed in further detail in Section 1.4.3). In addition, when films are confined between two hard surfaces, frustration cause by a mismatch between the bulk periodicity $L_0$ and the BCP thickness $t$ forces the copolymers to either change their period or adopt different morphologies/orientations. The theoretical and experimentally observed effects of interfacial interactions and confinement are discussed in Chapter 5.

### 1.4.2 Design of High-$\chi$ Block Copolymers

Poly(styrene-*block*-methyl methacrylate) (PS-*b*-PMMA) is the most thoroughly studied BCP for lithography in part because it is readily available, it has been well-studied, and under certain conditions, the phase separated domains spontaneously orient

perpendicular to the substrate when thermally annealed. However, the interaction parameter $\chi$ of PS-*b*-PMMA is relatively low, limiting the resolution of its domains to *ca.* 10-12 nm and restricting its utility for next-generation lithography.[33,34] Higher-$\chi$ materials[23,24,35-37] have been developed to overcome these limitations and enhance the material properties desirable for patterning.

Several design criteria are currently used to guide the development of new BCP materials:

1. Monomeric components are chosen to yield a high $\chi$ (relative to PS-*b*-PMMA).
2. Polymer domains have a large etch selectivity (high-contrast).
3. BCP microstructure orientation can be controlled in thin films.
4. Materials can be processed using methods and time scales amenable to industry practice.

Higher-$\chi$ materials are sought to reduce the minimum accessible feature size for BCPs, but also to increase the segregation strength (implications of segregation strength on pattern fidelity discussed in Section 4.4). Currently, there is no a priori method for accurately predicting $\chi$ between two polymer materials. Group-contribution solubility parameters[38] and homopolymer binary blend experiments[39] have often been used to estimate $\chi$ for a BCP, but have not always provided reliable predictions. For this reason, an empirical approach to increasing $\chi$ based on intuitive solubility properties of monomers has been used to guide the search towards new BCP combinations.

To function as a lithographic material, a BCP needs to not only self-assemble at length scales relevant to next-generation patterning nodes, but have inherent etch contrast. This etch contrast allows one of the block domains to be selectively removed

and the other serves as the resistant barrier needed to pattern underlying materials (semiconductors, conductors, dielectrics, etc.). Typical organic-organic materials do not have a large etch contrast, but incorporating a heteroatom into one block can increase selectivity.[40] The present strategy has been to develop organosilicon BCPs, as silicon is well known to form an etch-resistant silicon dioxide etch barrier upon exposure to an oxygen-rich plasma.[12,36]

Effective domain orientation control requires materials and/or solvents that minimize interfacial interactions. This necessitates films or atmospheric conditions with tunable surface energy properties (discussed in the subsequent sections).

The BCP should also be compatible with existing semiconductor manufacturing techniques. The polymer should be metal-free to avoid device contamination, produce defect-free uniform films over large areas using spin coating, and be glassy at room temperature for structural stability. The lithographic patterning process is serial in nature, so no step in the BCP flow should be the rate-controlling step (*i.e.* the annealing, etching, and alignment steps should be ideally accomplished in 30-60 seconds).

### 1.4.3 Effect of Surface Energy on Orientation

Surface energy, formally defined as the excess energy generated by creating a surface, is one of the strongest driving forces for BCP domain orientation.[41] For BCP materials, this type of energy arises as a result of intermolecular interactions directly between the two blocks *and* with the blocks and their respective top and bottom interfaces. Strong surface interactions induce an orientation parallel to the interface to minimize the energetic penalty of contacting the unfavorable block. Fig. 1.6 illustrates the effect of surface energy on lamellae orientation in thin films.

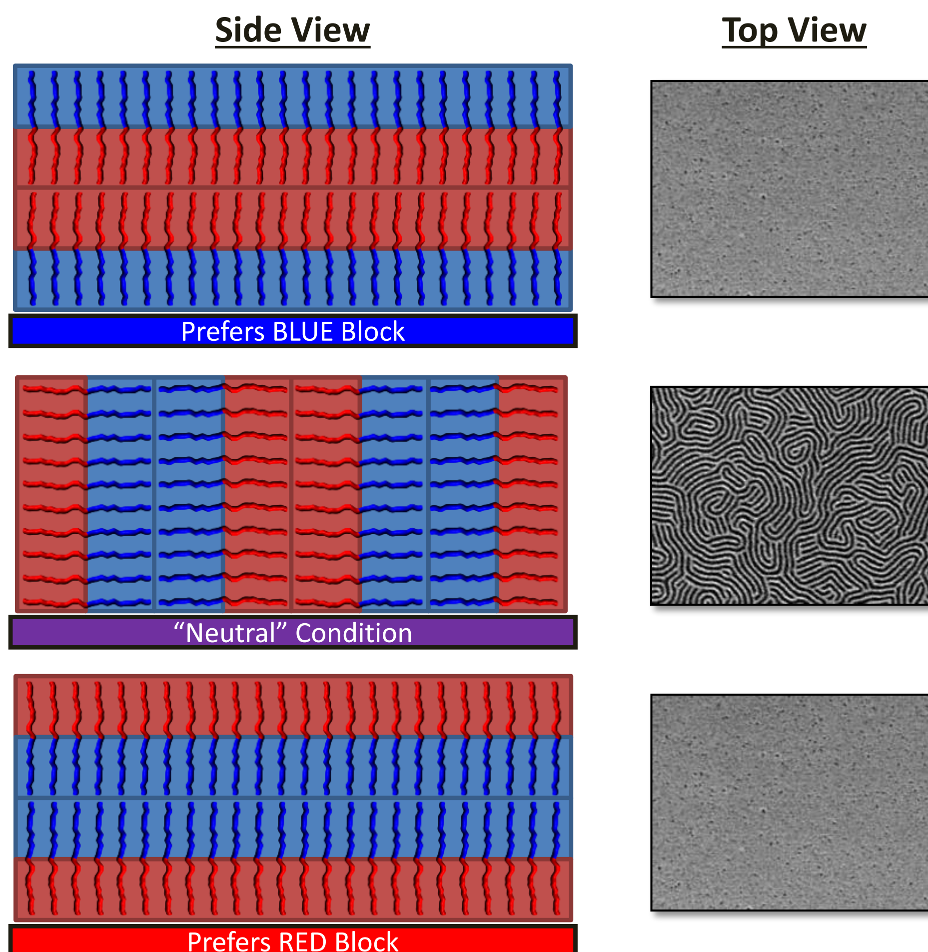


Figure 1.6: Effect of surface energy on a lamellar BCP. Preferential surfaces induce parallel orientation, while “neutral” surfaces provide perpendicular orientation, evident as fingerprint-like patterns. Note: the top interface is ignored in this representative example.

If a substrate is chosen such that the surface energy is minimized by interacting with one of the block components (*e.g.* the blue block, Fig. 1.6 Top), the BCP will segregate when annealed so that the domains are parallel to the substrate interface. Similarly, a substrate that minimizes surface energy by interacting with the *opposite* component (*e.g.* the red block, Fig. 1.6 Bottom) will induce parallel orientation, although with the *opposing* block wetting the substrate interface. For preferential substrates, the

parallel lamellae orientation produces no lithographically useful structures, as evidenced by top-down SEM images. A substrate that is equal in surface preference for each block component can be considered "neutral" (Fig. 1.6 Middle). A neutral substrate will not inherently *direct* the orientation of the BCP, so the lowest free energy orientation will be perpendicular to the substrate due to confinement effects.[41-43] Perpendicularly oriented lamellae are preferred over parallel for lithographic applications for obvious reasons, thus control over surface energy and the use of neutral interfaces is important.

A depiction of wetting behavior being "preferential" is somewhat vague, partly because experimentally quantifying surface energy differences and thus the strength of interactions is difficult. Although surface energy can be comprised of various intermolecular forces[44] (*i.e.* SFE is a multivariable function, typically described as polar or dispersive contributions), it can be useful to conceptualize the range of surface energies on a linear scale (Fig. 1.7).

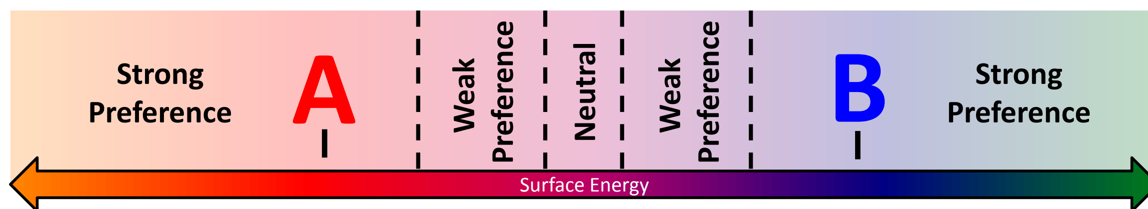


Figure 1.7: Qualitative depiction of surface energy between *A* and *B* components of a diblock copolymer. Surface preference increases as the surface energy deviates from the neutral region.

If components *A* and *B* lie on different positions of the arbitrary surface energy scale, a neutral surface energy can be envisioned intermediate of the two components. The farther the surface energy extends beyond the neutral region, the more preferential it is for a surface. A weakly preferential surface can be described by interactions that are

close to the neutral region, but far enough away to induce self-assembly that prefers one component. Strongly preferential surfaces are much farther from the neutral condition and will always induce orientations or morphology that results in wetting of that interface. The implications of strong and weak preference on island/hole phenomena and self-assembly are described in their respective sections (Chapter 2).

### 1.4.4 Block Copolymer Lithography

Control over both the BCP orientation relative to the substrate and alignment in the plane of the film is required to produce patterns relevant to semiconductor manufacturing. Various strategies have been implemented to both orient and neutralize the interfaces of BCP thin films. Vertical orientation has been demonstrated by solvent annealing,[45] but due to the process complexities and a lack of available industrial quality equipment, thermal annealing has been the target strategy employed herein. This requires specialized materials and/or several process steps, such as grafted polymer brushes,[46] cross-linkable surface treatments (XSTs),[47,48] modified surface chemistry,[49,50] and other approaches[51,52] to produce neutral interfaces and direct the self-assembly. Details of the present thermal annealing strategy are provided below (Fig. 1.8).

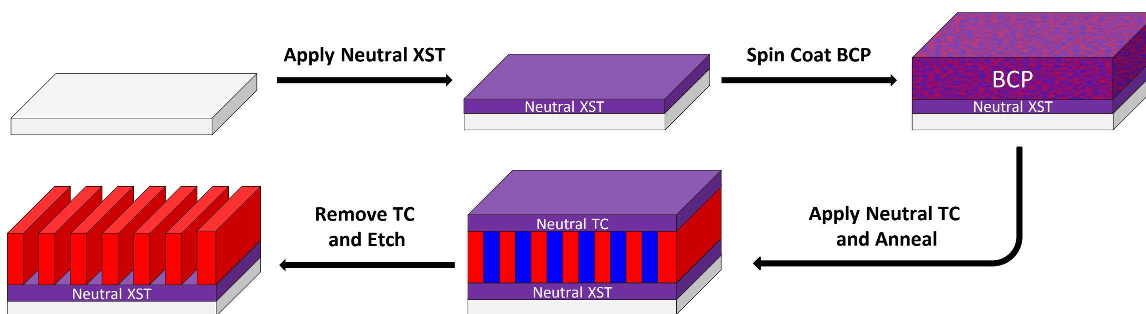


Figure 1.8: Process flow schematic for production of perpendicularly oriented BCPs by thermal annealing.

A substrate can be rendered neutral by coating with a cross-linkable surface treatment polymer (XST), which becomes insoluble upon a baking. The XST film is typically comprised of components similar to the BCP (usually a low surface energy component, *e.g.* MMA, and a relatively high surface energy component, *e.g.* 4-*t*-butylstyrene) such that the surface energy can be modified by tuning the composition of the polymer. The XST is cross-linked to prevent dissolution upon spin coating of the overlying BCP film. Previous discussions have concerned only the modification of the bottom interface of the BCP, but *both* interfaces affect the assembly in thin film. Therefore, after spin coating the BCP, an additional neutral material is applied to the top interface, which upon thermal annealing, induces the perpendicular orientation of the blocks. The top coat (TC) can be removed by dissolution or etching, and the oriented BCP pattern can then be transferred into the underlying substrate via reactive-ion etch (RIE).

Application of a neutral top coat material is a primary focus of this dissertation. A polymeric material must be deposited on the top surface of a BCP without damaging the film. Several strategies for accomplishing this have been tested. These include: ring-opening TCs (Section 2.2), chemical vapor deposited TCs (Section 2.3), and several elimination TCs (Section 2.4). Each method has advantages and disadvantages that will be discussed in their respective sections.

***BCP Alignment***

After orienting the BCP perpendicular to the substrate, the structures must be *aligned* in the plane of the film (termed directed self-assembly (DSA)) to produce patterns suitable to manufacture microelectronic devices. Two general strategies have been employed to align BCPs: chemo-[53] and grapho-epitaxy.[54,55] While neither is the

focus of the present work, understanding the approaches is useful to appreciate the scope of implementing BCP self-assembly for lithography.

Chemo-epitaxy functions by *chemically* guiding the assembly of the BCP. This implies control over the local nanostructures by providing a surface interaction to guide the self-assembly. As illustrated previously, surface energy driving forces can direct blocks to preferentially wet an interface. If a substrate (or top interface) is patterned on the length scale of the BCP period $L_0$, using a material that preferentially wets one component, the guiding pattern can direct the assembly by providing an energetic driving force aligning that phase along the guide pattern. Creating the guidelines typically requires surface chemistry modification, small molecular weight polymer brushes, or patterned photoresist with thicknesses $\ll L_0$.

Grapho-epitaxy guides self-assembly by *physically* confining the BCP between patterned structures. Surface topography on the order of $L_0$ is patterned using standard lithography techniques to develop guiding trenches or posts. Confinement effects create the energetic driving force for BCP alignment with respect the topography. Of course, the surface energy of the confining topography is also relevant to producing effective alignment. In practice, most alignment processes have both chemo- and grapho-epitaxy components.

Alignment pre-patterns are not necessarily advantageous if performed at nominally the same feature density as the BCP (although self-assembly has been shown to rectify poorly defined pre-patterns[10]). However, to reduce the burden of complex and/or time-consuming lithography steps, the BCP can be used to “multiply” the pitch of the pre-patterns (Fig. 1.9).[10,56,57]

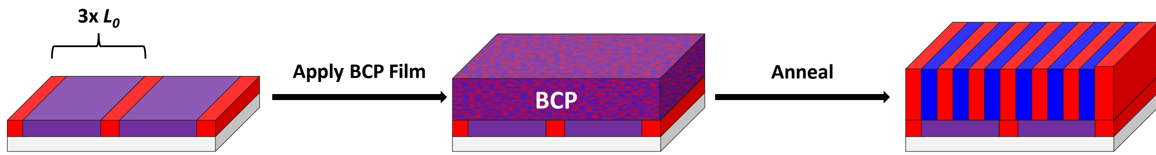


Figure 1.9: Simplified flow for a chemo-epitaxy density multiplication process. The purple color represents a neutral region while the red is a preferential guiding stripe.

Chemo- or grapho-epitaxy guide structures direct alignment of the assembly, while the interstitial region, if appropriately tuned in surface energy to be neutral with respect to both blocks, will be “filled in” with the periodic BCP domains. The pitch of the underlying pattern can therefore be multiplied, reducing the requirement of lithography steps in producing high-resolution, periodic patterns.

# Chapter 2: Orientation Control Using Top Coat Polymers

Effective orientation control of block copolymer structures is critical for patterning applications, particularly for next-generation high-$\chi$ materials. For PS-*b*-PMMA, an air/vacuum interface is fortuitously "neutral" at the anneal temperature. Therefore, thermal annealing requires only a neutral bottom layer to direct orientation perpendicular to the substrate. Unfortunately, high-$\chi$ materials almost always have one component that preferentially wets the air/vacuum interface due to the large surface energy difference between components (reflective of the same chemical dissimilarity that results in high-$\chi$). Therefore, a neutral material that can be applied to the top interface is required to implement high-$\chi$ BCPs for lithography. This chapter examines the methodology developed to evaluate the neutral condition required for orientation control and several top coat strategies for this process.

Top coat materials were designed to satisfy several criteria:

1. The deposition process is orthogonal (*i.e.* does not interact with the BCP)
2. The glass-transition temperature is relatively high ($T_{g\text{-}TC} >> T_{g\text{-}BCP}$)
3. The surface energy is tunable

An orthogonal deposition process, such as spin coating or vacuum deposition, is necessary to prevent disruption of the underlying BCP film. For solution deposited techniques, this requires solvents that are not miscible with the BCP components. A high $T_g$ top coat is necessary to give the BCP enough thermal energy for mobility ($T_{anneal} > T_{g\text{-}BCP}$) but prevent melt-mixing of the polymer layers ($T_{anneal} < T_{g\text{-}TC}$). Finally, the surface energy of the TC material must be tunable to allow facile control of conditions that induce vertical alignment of the BCP. This can be accomplished by synthetically controlling the TC polymer composition. Synthetic control often requires the use of

polymerization techniques and monomer selection that takes into account the reactivity ratios of components to preserve a pseudo-random monomer distribution (non-blocking) and predictable polymer composition. Several top coat strategies, as well as their respective advantages and disadvantages are discussed in the following sections (Section 2.2-4).

### 2.1 Evaluation of Wetting Behavior

A neutral top and bottom interface, created when the surface energy is equal between two components of a BCP, is necessary for orientation control in thin film self-assembly. Surface energy can be measured by well-known techniques such as contact angle goniometry,[58-60] but unfortunately difficulties with reproducibility[48,61,62] and liquid sorption[63,64] makes alternative approaches more attractive. A systematic method for evaluating BCP wetting behavior was therefore developed that leverages thickness quantization effects seen for lamellar BCPs. Without knowledge of wetting behavior or surface energy, the only appropriate method for verifying a neutral interface is by post-process imaging of the thin film structure. Not only is this procedure time consuming, as it requires coating, annealing, stripping, etching, and imaging, but it only provides post hoc knowledge of the complex variable space affecting the self-assembly. The following approach serves to initially guide the search for appropriate materials needed for orientation control. Unlike typical methodology used to evaluate surface energy, the island/hole phenomenon is easily observable by optical and/or atomic force microscopy. The structures are relatively large (*ca.* 1-10 μm) and the process does not require equipment more complicated than a spin coater and hotplate.

### 2.1.1 Island/Hole Phenomena

The equilibrium bulk periodicity of lamellae-forming BCPs is defined as $L_0$. If thin films of the BCP are produced such that the thickness is not commensurate with $L_0$ and the top interface allows unrestricted reorganization (unconfined), topographical structures termed "islands" and "holes" can be generated (Fig 2.1).[65,66]

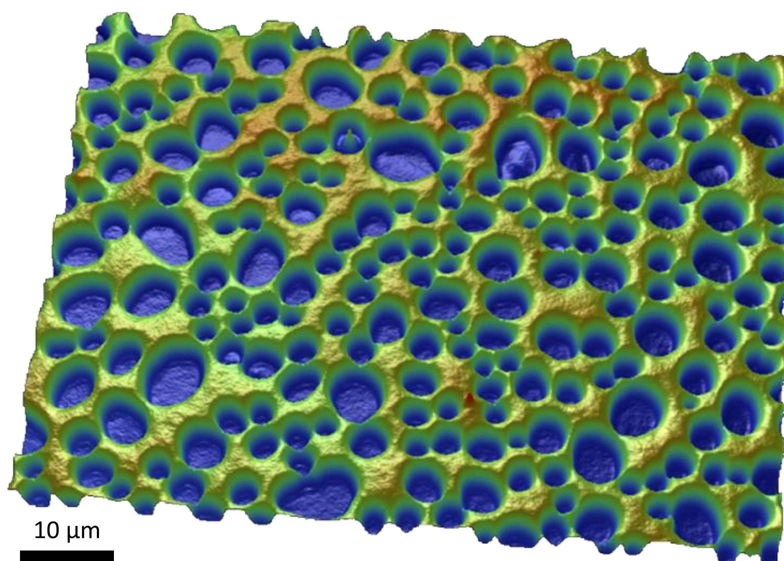


Figure 2.1: Image of dense hole-like structures by optical profilometry. The depth of the depressions relative to the matrix is approximately 1 $L_0$.

The formation of islands and holes is a result of the energetic penalty for confining or stretching films to an incommensurate thickness. Rather than assemble into an unfavorable configuration, the polymers develop characteristic $1L_0$ topography such that every layer maintains the bulk periodicity. Island/hole structures only form when one of the surfaces exhibits preferential wetting, thereby driving parallel orientation (Fig. 2.2).

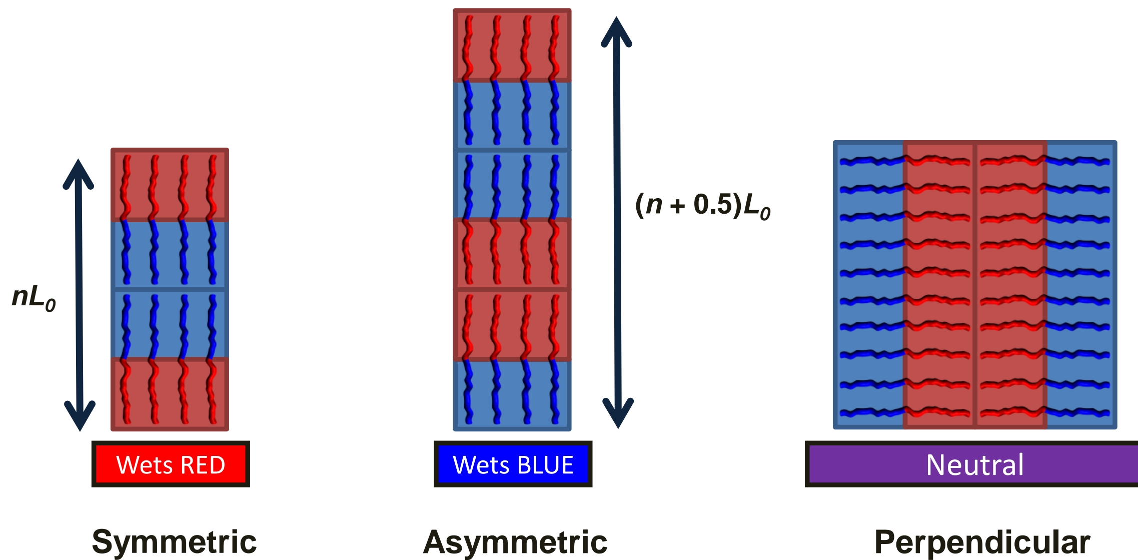


Figure 2.2: Quantization of film thickness for parallel-oriented lamellae, forming symmetric or asymmetric wetting depending on the substrate wetting. Note: the red block is assumed to wet the air interface for both parallel conditions. A neutral interface (*i.e.* perpendicular) will not quantize.

Thickness quantization is dependent on the wetting behavior at each interface. For a film that "symmetrically" wets each interface (*e.g.* red block prefers both top and bottom, Fig. 2.2, left), the BCP will quantize in integer $n$ multiples of $L_0$. Conversely, if the film "asymmetrically" wets each interface (*e.g.* red block prefers top and blue block prefers bottom, Fig. 2.2, middle), the BCP will quantize in multiples of $(n + 0.5)L_0$. Perpendicular structures formed on a neutral interface will not quantize nor form any topography (details of the neutral wetting condition are described in Section 2.1.4).

Whether island-like or hole-like structures form is dependent on the thickness $t$ of the sample. For symmetric wetting, island-like topography will form if $nL_0 < t < (n + 0.5)L_0$, and hole-like topography will form if $(n + 0.5)L_0 < t < nL_0$. Conversely, for asymmetric wetting, island-like topography will form if $(n + 0.5)L_0 < t < nL_0$, and hole-

like topography will form if $nL_0 < t < (n + 0.5)L_0$. An example of the thickness and wetting dependence of island/hole behavior is shown in Fig. 2.3.

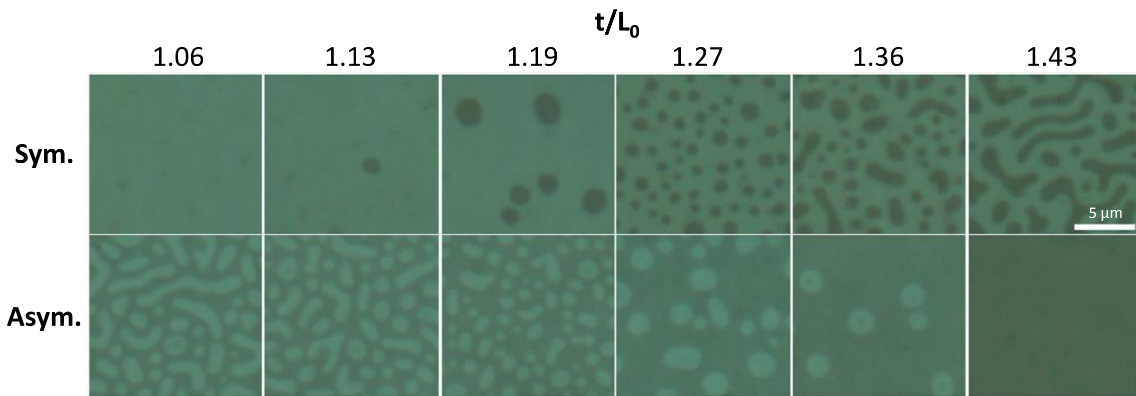


Figure 2.3: Island/hole thickness dependence for symmetric and asymmetric wetting. At these thicknesses, dark spots are islands and light spots are holes. Reprinted (adapted) with permission from Maher et al.[67]

The film thickness impacts the density of the observed island/hole topography. Close to the commensurate conditions ($nL_0$ for symmetric and $(n + 0.5)L_0$ for asymmetric), smooth films are formed with very little if any topography. As the thickness progresses away from the commensurate condition, sparse islands/holes can first be seen. The feature density increases the farther away the thickness is from the commensurate condition. For an incommensurate film, the structures are often so dense that they resemble spinodal-like, bicontinuous regions. Whether the topography observed is an island or hole depends on the configuration of the structures. If the topography is higher than the surrounding matrix, it is considered islands. If the topography depresses lower than the matrix, it is considered holes.

When probing the wetting behavior of a substrate, selection of the film thickness is clearly a critical issue. As is discussed in further depth in Chapter 5, self-assembly in

thin films is a function of both surface interactions and confinement effects. Furthermore, the impact of top and bottom interfacial interactions decay as the film thickness increases, thus it is best to choose relatively thin films (1-2$L_0$) to maximize the sensitivity towards surface energy effects. Films should be cast at incommensurate thicknesses to guarantee forming the islands/holes needed to interpret the wetting behavior.

### 2.1.2 Bottom Interface Wetting

The formation of islands or holes can be used to identify the wetting behavior of a substrate interface.[51,68] This so-called "classic" island/hole test requires simply coating a film of the BCP on top of the surface to be probed (Fig. 2.4). If the as-cast BCP film thickness is incommensurate for both symmetric *and* asymmetric wetting (*e.g.* 1.25$L_0$), either island or hole topography will form depending on the wetting behavior of the substrate (assuming one block preferentially wets the top). The free top interface allows reorganization of the polymer chains upon annealing at temperatures $T > T_{g\text{-BCP}}$ to develop the topography. At an initial film thickness of 1.25$L_0$, a symmetric-wetting substrate would produce islands, while the same thickness on an asymmetric-wetting substrate would produce holes. This dramatic difference in topography is immediately evident by optical or atomic force microscopy and provides a clear demonstration of the wetting preference of the substrate. The size of the topography in both cases is 1$L_0$, the periodicity of the block as seen by atomic force micrograph height profiles (Fig 2.4). Optical micrographs typically provide a clear indication of the presence of islands/holes; topography on the order of 1-100 nm (also the magnitude of BCP structures) will produce color changes in the film caused by interference effects. It should be carefully noted however that darker/lighter spots do not always indicate higher/lower topography, respectively. Atomic force microscopy or optical profilometry should be used to

supplement optical micrograph information to confirm the height profile of the island/hole structures.

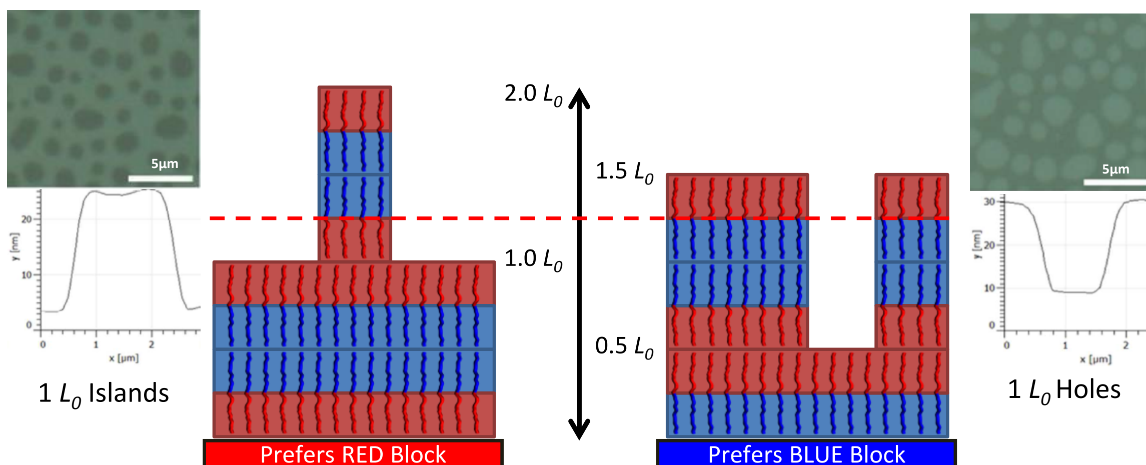


Figure 2.4: "Classic" island/hole test, yielding island topography for a symmetric-wetting substrate and hole topography for an asymmetric-wetting substrate. The dotted line indicates the initial film thickness of $1.25L_0$. Note: the red block is assumed to wet the free interface.

The substrate chemistry can be chosen such that one block preferentially wets the surface. The chemistry can then be modified until the opposing block is preferred, and a neutral material can then be easily designed by synthesizing a polymer with an appropriate ratio of the two preferential chemistries.

### 2.1.3 Top Interface Wetting

Bottom interface island/hole tests are effective at probing the wetting behavior for a variety of substrates: cross-linked polymer films, polymer brushes, metals, chemically-modified surfaces, etc. However, top coat materials have much more stringent process limitations. Most top coats, if tuned to be neutral, are soluble in the same solvents as those that dissolve at least one of the blocks. In addition, cross-linking top coats is non-

ideal because not only does it preclude post-anneal stripping, but the surface energy properties could be subtly modified post-reaction. An ideal solution requires testing the top coat *in situ* – as a thin film on the *top* interface of the BCP. For the above reasons, a unique method for evaluating the wetting behavior of top coat materials is required. The discovery of so-called "confined" islands/holes was critical in developing such a test.[67]

Intuitively, confining a BCP between two hard, glassy materials would preclude the formation of island/hole-like topography. As discussed previously, a *free* interface allows the polymer chains to reorganize upon annealing, assembling into topography that minimizes their free energy. However, it was discovered that for confined films *with at least one interface exhibiting strongly preferential wetting* (a description of preferential wetting is discussed in Section 1.4.3), island/hole structure were evident after annealing. This discovery suggests that island/hole topography can deform the overlying, glassy top coat and report on the wetting behavior at the top interface (Fig. 2.5).

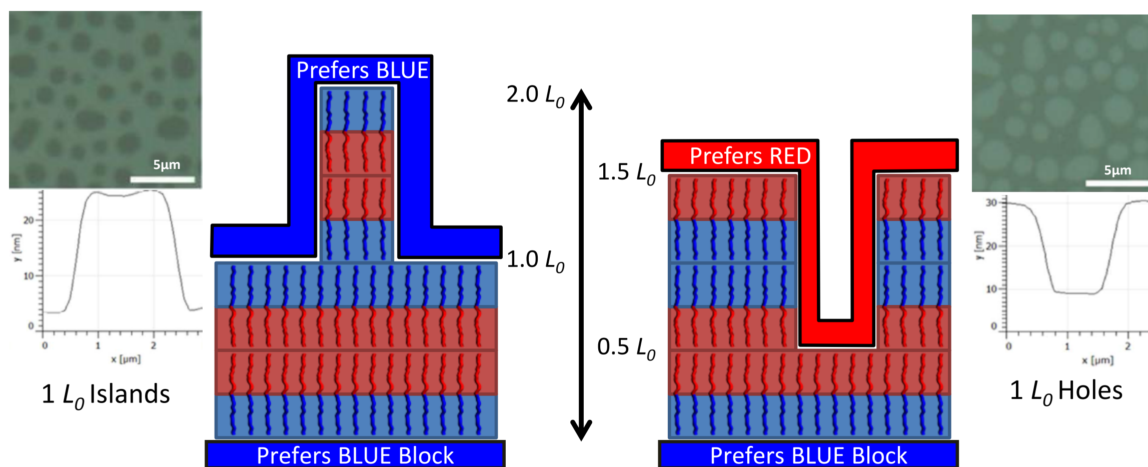


Figure 2.5: "Confined" island/hole test, yielding islands for symmetric wetting and holes for asymmetric wetting of a $1.25L_0$ BCP film. The top coat conforms to the underlying topography.

In the confined island/hole test, it is critical that the BCP film is applied on a substrate that is *strongly preferential* for one domain. This typically requires an XST or treated substrate comprised of the same or similar components as one of the blocks (see Fig. 1.7 for a qualitative picture of strongly preferential surface energy). The origin of this strong preference requirement for confined island/hole phenomena is still unknown, but it is presumed to reflect the high energetic frustration of unfavorable wetting against strongly preferential interfaces. This energetic driving force could potentially induce a plastic deformation of the overlying glassy top coat. In the above example (Fig. 2.5), the BCP is cast on a substrate that prefers to wet the blue component. The thickness of the BCP is incommensurate for both symmetric and asymmetric wetting ($1.25L_0$) such that either islands or holes will be observed, reflective of the wetting behavior at the top interface. The top coat to be probed can then be applied over the BCP film, and the entire film stack annealed at temperatures $T_{\text{g-BCP}} < T < T_{\text{g-TC}}$. If the top coat material prefers to wets the same component as the substrate (symmetric condition, Fig. 2.5, left), island-like structures will form. If the top coat asymmetrically wets (Fig. 2.5, right), hole-like structures form. The macro-scale structures can be observed (with or without the presence of the TC) by optical and atomic force microscopy and their data quickly yield information regarding BCP wetting behavior. Similar to a substrate island/hole experiment (Section 2.1.2), if the wetting behavior is switched by selecting two distinct chemistries, a neutral TC material can be found by synthesizing a copolymer of intermediate composition.

### 2.1.4 Neutral Interface Phenomena

The island/hole wetting test yields a binary result – either island or hole topography will form based on the wetting behavior of the interrogated interface. This

implies that at some surface energy intermediate between the two, a "switch" will occur. The first demonstration of such a switch was for a bottom interface wetting test using a silicon-containing BCP, poly(methyl methacrylate-*block*-4-trimethylsilylstyrene) (PMMA-*b*-PTMSS) (Fig. 2.6). The XST films, comprised of TMSS and MMA, were varied in surface energy by changing the ratio of the monomers (additional details of the experiment are provided in Section 3.3). Compositions high in TMSS showed hole topography at $1.75L_0$, indicating symmetric wetting (the organosilicon domain prefers the air interface). As the XST composition decreased to 0% (homopolymer of MMA), the topography switched to island topography, indicating asymmetric wetting. Qualitatively, the in-plane area of the topographical features decreased while their density increased, corroborating the trend in preference strength. As the preference between blocks became weaker, the structures became too small to resolve by optical microscopy and resembled spinodal bicontinuous-like regions. At the intermediate composition, 27% TMSS, the switch between holes to islands indicated a substrate with a neutral surface energy.

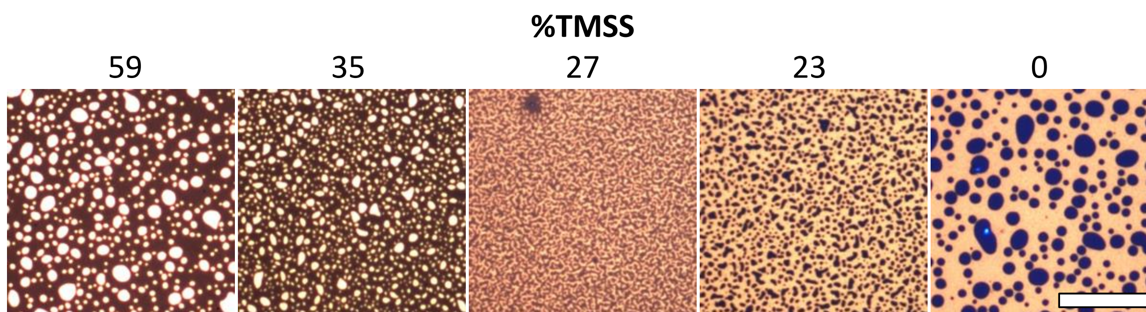


Figure 2.6: First demonstration of an island/hole "switch" using PTMSS-*b*-PMMA by changing the composition of an underlying XST containing TMSS. Films are all at *ca.* $1.75L_0$. Scale bar is 20 µm.

Upon careful inspection of the images found in Fig. 2.6, it may be noticed that the contrast of the image for the neutral substrate (27% TMSS) is approximately half that of

the more strongly preferential substrates. It was recently discovered that this insight is exactly true - layered BCP films, comprised of one neutral and one preferential interface, result in topography with $0.5L_0$ step heights.[69] The physical origin of such behavior is still unclear, but experimentally, verification of "half" island/hole topography has been documented. A cartoon representation of the layered BCP structure gives a perspective on the $0.5L_0$ topography (Fig. 2.7).

For a neutral free surface with a preferential substrate (Fig. 2.7, left), the parallel orientation is driven by the bottom interface wetting. The free surface has no preference, so both components are exposed at the top, resulting in step heights of $0.5L_0$. Similar behavior is observed for preferential free surfaces and a neutral substrate (Fig. 2.7, right); the top interface drives parallel orientation, but both components can wet the substrate interface. Both conditions provide unambiguous evidence of a neutral interface – the appearance of $0.5L_0$ topography.

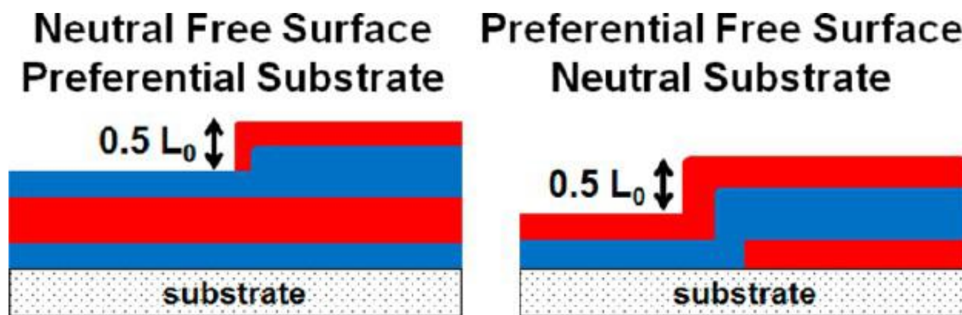


Figure 2.7: Cartoon of $0.5L_0$ island/hole behavior for lamellar-BCP with one neutral and one preferential interface. Reprinted with permission from Kim et al.[69]

Neutral interface $0.5L_0$ topography introduces a new commensurability condition; instead of either $nL_0$ or $(n + 0.5)L_0$ conditions for classic islands/holes, $0.5L_0$ topography will become commensurate at all $0.5nL_0$ conditions. An example of the thickness dependence for a single neutral interface is shown in Fig. 2.8 (compare to Fig. 2.3 for

classic island/hole thickness dependence). Similar to classic island/hole behavior, the density of $0.5L_0$ topography is dependent on BCP thickness. For the single neutral interface condition (*i.e.* the opposing interface is strongly preferential), $0.5nL_0$ thicknesses show no topography, while all other thicknesses show either $0.5L_0$ islands or $0.5L_0$ holes. A switch between $0.5L_0$ islands to $0.5L_0$ holes occurs at $(n \pm 0.25)L_0$.

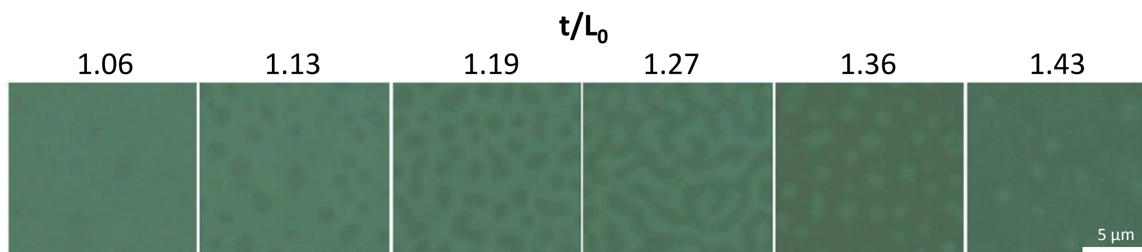


Figure 2.8: Thickness dependence of a single neutral interface with commensurability conditions at $0.5nL_0$. Reprinted with permission from Maher et al.[67]

The top interface wetting experiments (Section 2.1.3) use islands/holes in confined films to examine top coat wetting preference. Such experiments exhibit the same neutral interface behavior as free films; $0.5L_0$ topography develops as a result of a single neutral interface. Much like the classic islands/holes, the $0.5L_0$ topography deforms the overlying top coat. The origin of the deformation physics, however, is still under investigation. An example of confined $0.5L_0$ topography using PS-*b*-PTMSS is presented in Fig. 2.9.

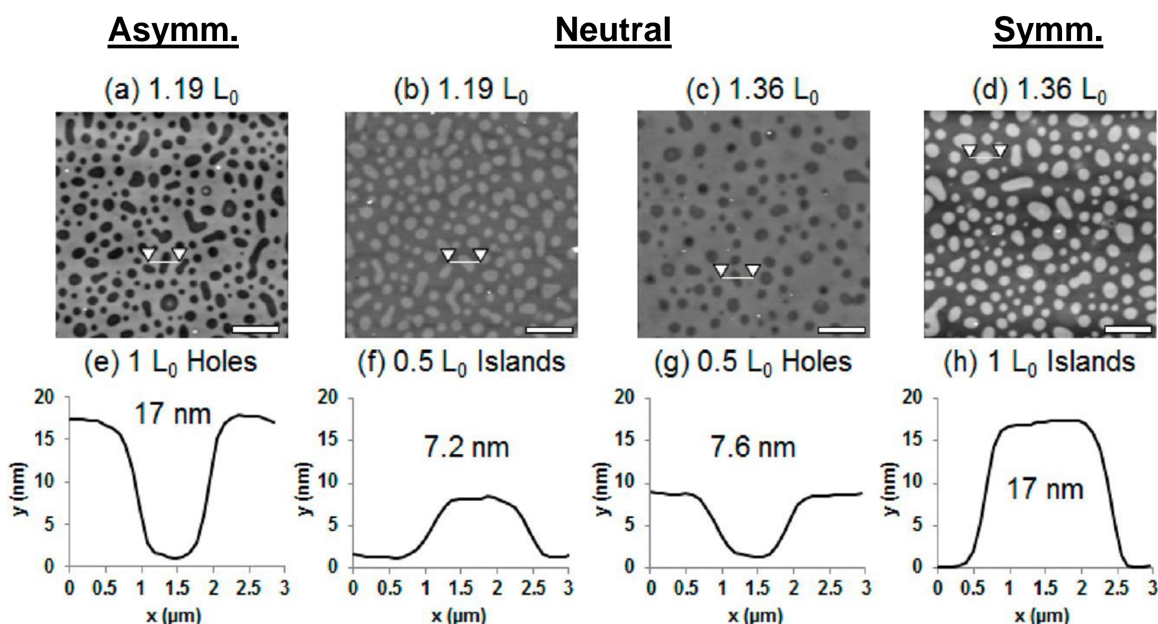


Figure 2.9: AFM height images (a-d) and height profiles (e-h) for a confined wetting test of 17-18 nm $L_0$ PS-*b*-PTMSS using a PS surface treatment. Top labels identify the wetting behavior. Note: the AFM height images have opposite contrast as previously shown optical micrographs, so dark regions correspond to holes and light regions to islands. Reprinted (adapted) with permission from Maher et al.[67]

Classic island/hole switching can be seen between Fig. 2.9 (a,e) and (d,h). At this particular BCP thicknesses, asymmetric wetting (a,e) shows holes and symmetric wetting (d,h) shows islands. The height profile of the topography in both cases is $1L_0$ (≈17-18 nm). When the TC surface energy is intermediate between the two previous conditions (*i.e.* neutral), $0.5L_0$ islands/holes are present (b,f) (c,g). The AFM profiles verify the height of the neutral island/hole structures to be approximately $0.5L_0$ (≈7-8 nm). Due to the additional commensurate conditions for $0.5L_0$ topography, a switch between $0.5L_0$ islands to $0.5L_0$ holes occurs at a thickness of $1.25L_0$. Indeed, the height images show the immediately evident contrast between $0.5L_0$ islands and $0.5L_0$ holes as the thickness is increased from $1.19L_0$ (b,f) to $1.36L_0$ (c,g), respectively.

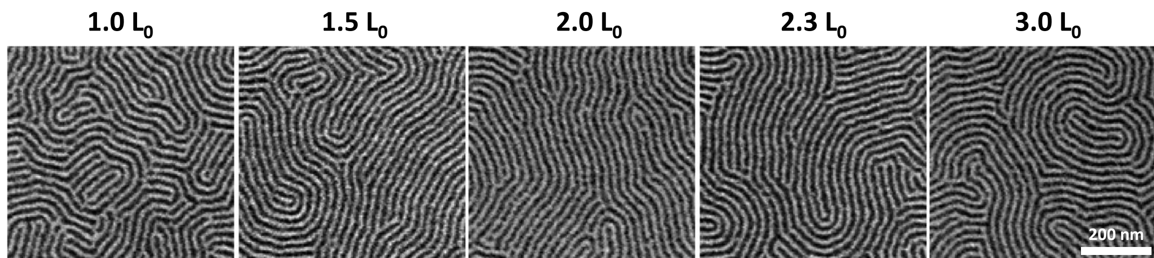


Figure 2.10: Confinement-induced perpendicular orientation for a BCP between two neutral interfaces, showing thickness independent orientation control. Reprinted with permission from Maher et al.[67]

Substrate and top interfacial energies can be modified to produce neutral materials and thereby provide control over the BCP orientation. Due to confinement effects, thin films between truly neutral surfaces orient perpendicular to the substrate. This confinement-induced orientation control is evident at *all* thicknesses if the surfaces are *exactly* neutral. This behavior is often termed thickness independence (Fig. 2.10). Theoretical descriptions of self-assembly corroborate these results, showing that thickness independence can be achieved when surfaces are exactly neutral (Chapter 5).

The use of both a neutral bottom and top interface to achieve thickness independence has several advantages. First, thicker films of perpendicular-orientation structures inherently produce higher aspect ratio structures. This is beneficial for pattern transfer steps, where the mask is slowly removed during the etching process. A high aspect ratio mask can directly translate into a high aspect ratio patterned feature. Additionally, thickness independence allows structures of *any* aspect ratio to be produced. While trivial sounding, lack of effective surface neutralization implies only very specific incommensurate thicknesses can produce perpendicular orientation. Surface neutralization therefore widens the orientation process window for self-assembled structures.

### 2.1.5 Conclusions and Implications

Island/hole topography is a well-studied and simple phenomenon for lamellar BCPs that provides useful information on the wetting behavior of polymer films. This behavior can be leveraged to evaluate the substrate and top surface interactions of BCPs to design and establish neutral materials. The experiment process flow is simple, and the results can be quickly and easily analyzed using simple tools like an optical microscope.

Half island/hole topography is believed to be the best indication of a neutral surface, and the phenomenon is evident when investigating both the top and bottom interface and when probing confined versus free films. When libraries of top and bottom polymers are synthesized, a neutral interface can be easily selected after verifying a classic island/hole switch and subsequent appearance of $0.5L_0$ topography for an intermediate surface energy material. Selecting neutral interfaces yields conditions suitable for vertical self-assembly, control of which is necessary to adopt BCPs for next-generation lithography. Confinement between two neutral interfaces induces perpendicular orientation that is independent of the BCP thickness.

## 2.2 Ring-Opening Top Coats

Spin coating is one of the most common processes used in semiconductor manufacturing to deposit uniform, defect-free polymer thin films over large areas. An ideal top coat solution would be a polymeric material that can be spin cast from a solvent over the underlying BCP to form a thin layer with a neutral surface energy. Unfortunately, materials that would intuitively be neutral towards the polymer blocks would also typically dissolve in the same casting solvent as the BCP, implying that neutral materials cannot be spin cast upon a BCP film. To resolve this paradox, top coats were designed that could be cast from solution in a state that is soluble in orthogonal BCP

solvents, but can revert or "switch polarity" to a state that is neutral upon heating (Fig. 2.11).[70]

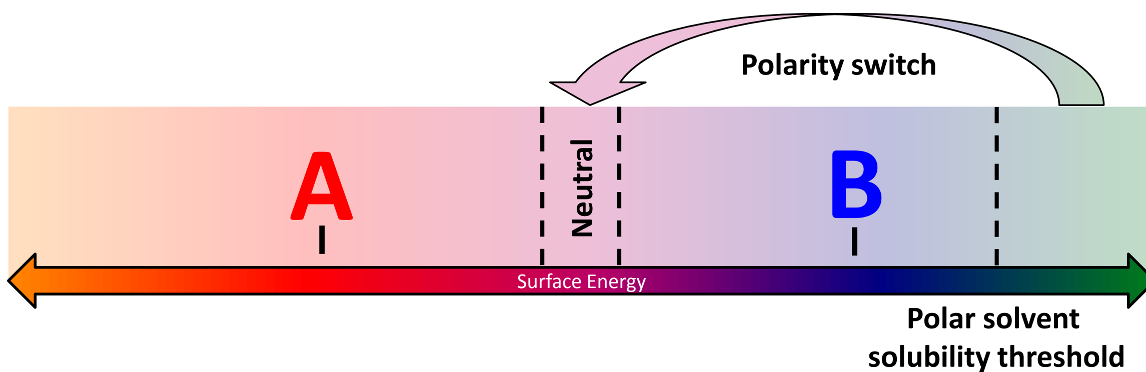


Figure 2.11: Polarity-switching concept that allows top coat to be cast from an orthogonal polar solvent but result in neutral surface energy between BCP components.

One of the strategies used to achieve the polarity-switching effect relies on the ring-opening reaction of maleic anhydride (Fig. 2.12). Maleic anhydride, when immersed in a basic solvent, such as aqueous trimethylamine, ring-opens to a form a charged, highly-polar dicarboxylate intermediate. This dicarboxylate salt can be isolated and has solubility properties typical of salt complexes; polar solvents such as water, methanol, isopropanol, etc. can be used to spin coat such materials without interacting with the relatively non-polar BCP (Fig. 2.13). When heated, the polar salt ring-closes to revert to its original, less-polar form, maleic anhydride, releasing trimethylamine gas and water. An additional advantage of a ring-opening polymer comprising maleic anhydride is the ability to remove the polymer film post deposition. The post-annealed ring-closed film can be easily re-dissolved in aqueous base to yield the annealed BCP film intact. This eliminates the need for post-process etch steps to break through the top coat layer.

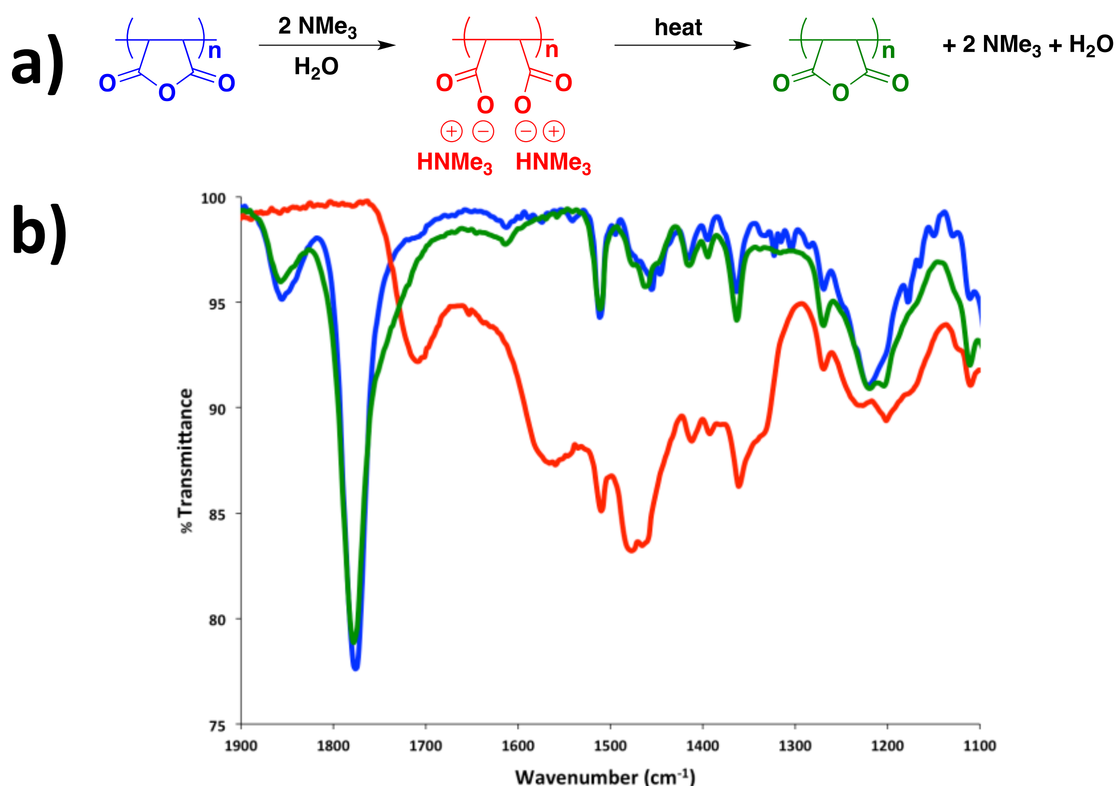


Figure. 2.12: (a) Ring-opening/closing reaction of maleic anhydride with aq. trimethylamine and heat, respectively. (b) Bulk IR spectra showing carboxylate region reversion upon ring-opening/closing. Reprinted with permission from Maher et al.[67]

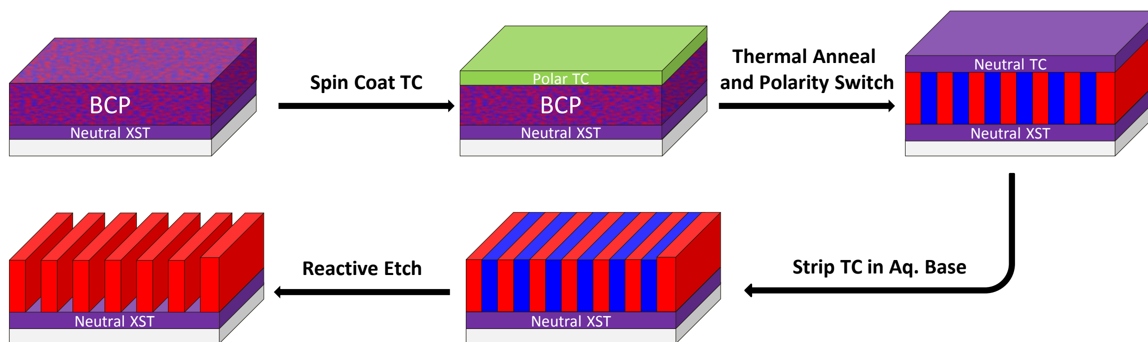


Figure 2.13: Process flow for ring-opening polarity-switching top coats.

It has been well-documented that maleic anhydride, due to its unique electronic character, forms alternating copolymers with a variety of monomers.[71,72] These

alternating copolymers typically have $T_g$'s greater than 150 °C,[71,73] a necessary requirement to prevent intermixing or dewetting of the top coat film.[74] The substituents on the comonomers provide a handle for modulating the surface energy of the top coat polymer. Generally, relatively low surface energy comonomers are targeted because of maleic anhydride's somewhat polar character. Surface energy can be reduced by decreasing the polarizability of the chemical bonds[75] (*e.g.* by introducing weakly polarizable fluorinated hydrocarbons) or by introducing large, lipophilic substituents (*e.g.* sterically bulky *tert*-butyl groups). The polymerization feed ratios of comonomers can be controlled to produce a top coat material that is neutral to various BCPs.

Two general strategies were taken to produce ring-opening TC materials: alternating copolymers comprised primarily of norbornene derivatives (1st Generation), and alternating copolymers comprised solely of styrenic derivatives (2nd Generation). Several representative examples of the top coat strategies are discussed in the following sections as well as relevant advantages/disadvantages. Additional chemistries investigated and full experimental details can be found elsewhere.[70,76]

### 2.2.1 1st Generation Ring-Opening Top Coats

Norbornene derivatives were chosen as the comonomers for the 1st Generation TC's because they are known to form high $T_g$ copolymers with maleic anhydride,[71] and a variety of fluorinated and chemically modified norbornenes have been developed for previous applications as photoresist materials. Top coats were typically designed as terpolymers of maleic anhydride, a norbornene derivative, and an acrylate or styrenic component (Fig. 2.14). The latter component was generally useful as an additional handle for surface energy modification. Many commercially available acrylate or styrenic

monomers exist, making development of diverse libraries of top coat polymers relatively simple.

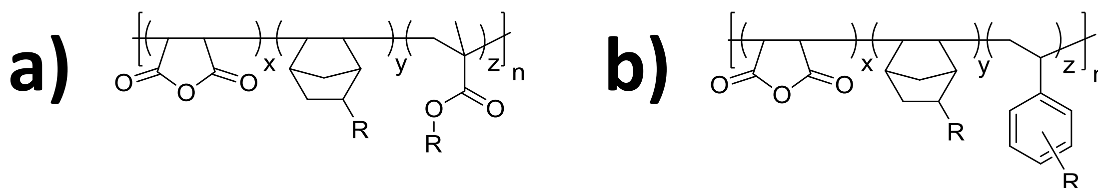


Figure 2.14: Generalized 1st Generation top coat designs, comprised of maleic anhydride, norbornene derivatives, and either (a) an acrylate or (b) a styrenic derivative.

A lamellae-forming ABA triblock, poly(styrene-*block*-4-trimethylsilylstyrene-*block*-styrene) (PS-*b*-PTMSS-*b*-PS) (Fig. 2.15),[76,77] was used as the representative test vehicle for all top coat orientation experiments. This is particularly because organosilicon BCPs are notorious for forming a silicon-domain wetting layer at the top interface when thermally annealed.[78] Although PS-*b*-PTMSS-*b*-PS does not have a significantly higher $\chi$ than PS-*b*-PMMA (see Chapter 4), it can demonstrate the efficacy of the top coat process prior to development of higher-$\chi$ organosilicon polymers. In addition, perpendicularly-oriented triblock polymers have been predicted to be slightly more energetically stable relative to diblock copolymers of the same composition.[79-81] Thus, a silicon-containing triblock polymer was chosen for initial top coat studies.

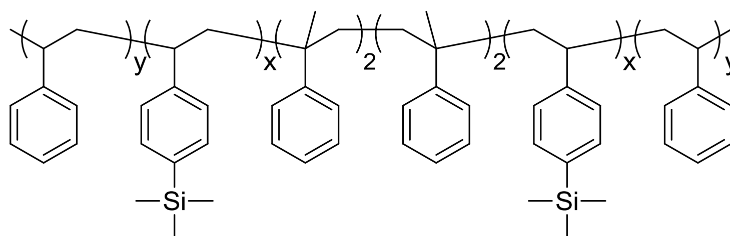


Figure 2.15:ABA triblock PS-*b*-PTMSS-*b*-PS used with 1st Generation TCs.

Initial attempts at orientation control using top coats were largely empirical. Methods for evaluating surface energy using contact angle goniometry were unsuccessful, and island/hole techniques for understanding wetting behavior (see Section 2.1) had not yet been developed. Therefore, an Edisonian approach was employed, relying on successful choice of BCP film thickness, deposition conditions, anneal temperature/time, etch conditions, and imaging to verify evidence of successful perpendicular orientation. These procedures were tedious and inefficient, but initial demonstration of orientation control was achieved.

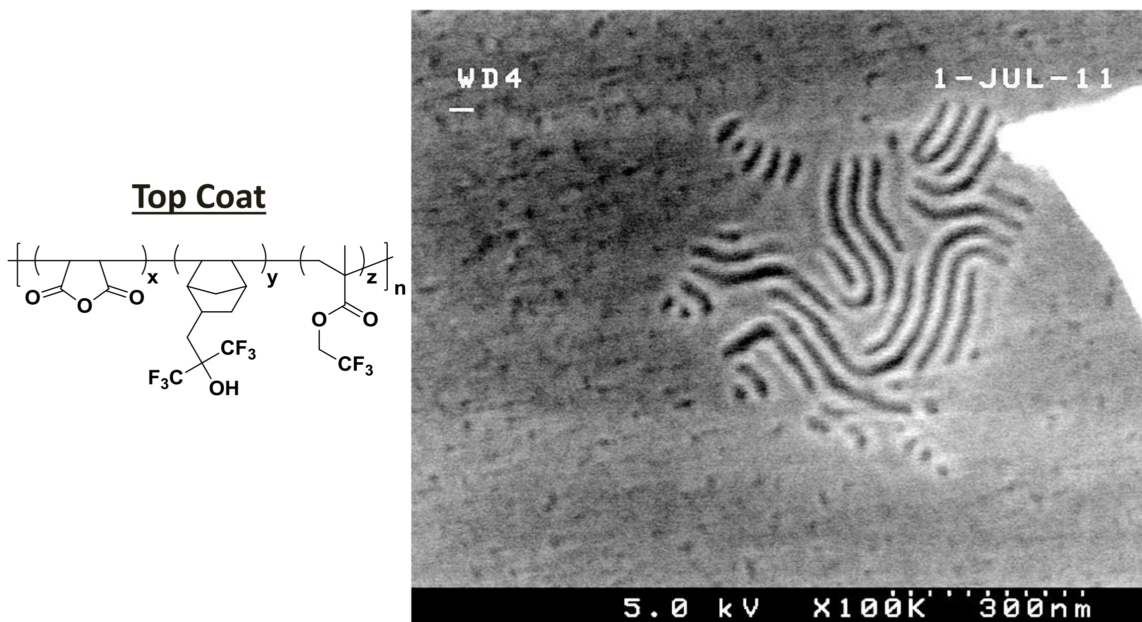


Figure 2.16: First demonstration of perpendicular orientation using a 1st Generation TC, thermally annealed 24 hrs. Reprinted with permission from C.M. Bates.[76]

The first demonstration of perpendicular orientation using a spin-on TC was achieved using the fluorinated ring-opening polymer containing an acrylate derivative shown in Fig 2.16, after thermally annealing for 24 hours. A small *ca.* 500 nm diameter patch was fortuitously discovered near a particle showing perpendicular orientation,

while the rest of the wafer was relatively featureless. Such behavior was encouraging however, given that the discovery implied certain process conditions could yield perpendicular structures. The origin of the particle-induced assembly is likely a result of confinement effects; particles commonly cause local thickness variability, which could unintentionally access favorable conditions for perpendicular orientation. Thus, sampling near particles was an effective method for testing multiple thickness conditions for the same as-cast film. A sample identical to that in Fig. 2.16 was annealed for an additional 100 hours to see if kinetic factors affected full-wafer perpendicular orientation (Fig. 2.17). The results showed that anneal time improved the lateral size of the oriented domains, but defects and patchy behavior were still evident. It is presumed that surface energy mismatching was the most likely cause of poor self-assembly.

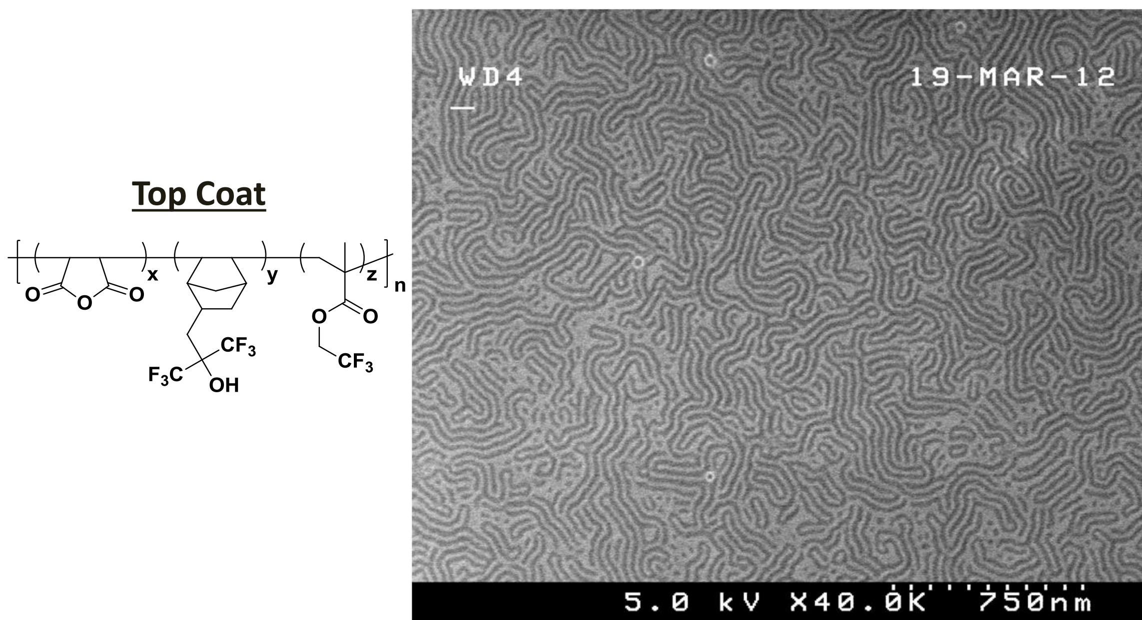


Figure 2.17: Full-wafer perpendicular orientation achieved by an extended thermal anneal (120 hrs.), albeit with high defect density. Reprinted with permission from C.M. Bates.[76]

The initial successes provided a starting point for future experimentation; top coats could be designed with higher/lower surface energy by compositional modification, and the orientation results would provide feedback on neutrality. Samples producing better self-assembly were presumed to be close to the neutral condition, while poorer self-assembly was farther away. The feedback by this Edisonian approach was used as the rationale for new top coat material design.

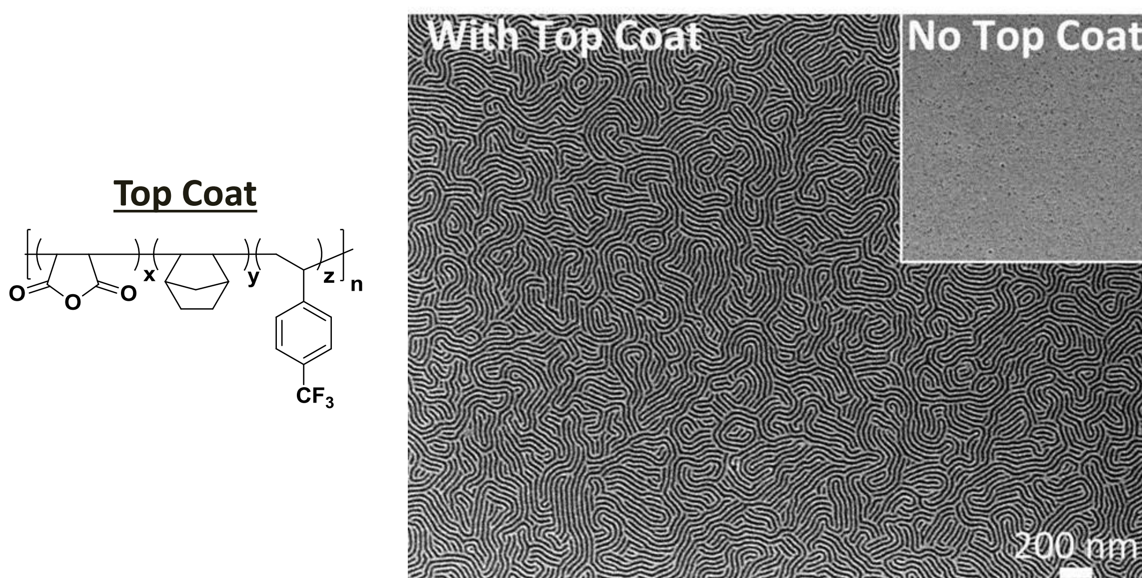


Figure 2.18: Fluorinated styrene TC enables good quality perpendicular assembly for PS-*b*-PTMSS-*b*-PS. (Inset) In the absence of a TC, only parallel structures are seen. From Bates et al. (adapted)[70] Reprinted with permission from AAAS.

Full-wafer defect-free assembly was eventually achieved for PS-*b*-PTMSS-*b*-PS after development of a 4-trifluoromethylstyrene top coat (Fig. 2.18). This top coat showed well-assembled structures after short (1 min) anneal times, suggesting that the surface energy was close to a neutral condition. The same sample, in the absence of a top coat, showed only parallel orientation (Fig. 2.18, inset). Unfortunately, the full-wafer perpendicular assembly was limited to very small thickness windows (*ca.* 1.35-1.40$L_0$).

This behavior was originally attributed to top coat design, but it was later discovered that a unique combination of top *and* bottom surface energy conditions can lead to perpendicular orientation *even in the presence of non-neutral interfaces* (see Section 5.3). Therefore, it is unlikely that the top coat system was truly neutral for PS-*b*-PTMSS-*b*-PS.

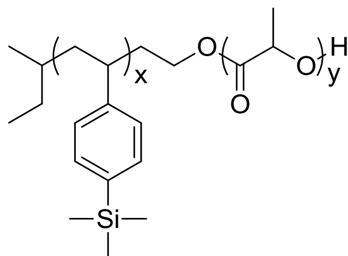


Figure 2.19: Diblock PLA-*b*-PTMSS high-$\chi$ polymer

The demonstration of full-wafer orientation control for PS-*b*-PTMSS-*b*-PS affirmed the potential of the top coat technology for high-$\chi$ systems. Poly(D,L-lactide-*block*-4-trimethylsilylstyrene) (PLA-*b*-PTMSS) (Fig. 2.19) was the first high-$\chi$ polymer used with the top coat process flow. This copolymer has lamellar domains as small as *ca.* 15 nm.[35] A fluorinated TC with an acrylate derivative (Fig. 2.20) was found to be approximately neutral for the BCP, showing full-wafer perpendicular orientation. PLA-*b*-PTMSS also demonstrated perpendicular orientation only in a very narrow thickness window. This behavior was ascribed to non-neutral interfaces that only favor perpendicular orientation at unique incommensurate thicknesses. Nevertheless, orientation control of PLA-*b*-PTMSS was the first demonstration for a sub-10 nm high-$\chi$ material.

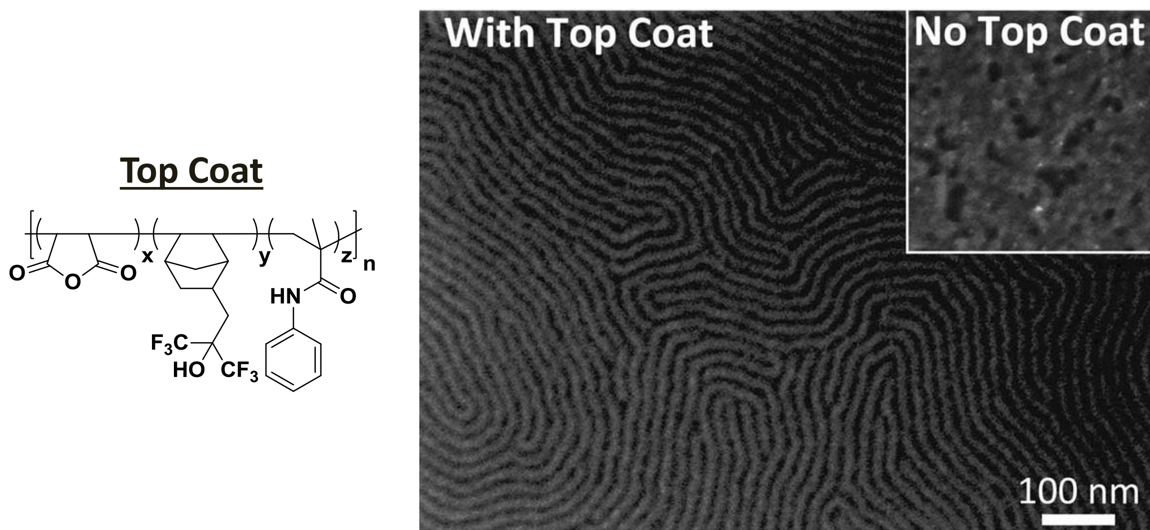


Figure 2.20: TC enables good quality perpendicular assembly for high-$\chi$ PLA-*b*-PTMSS. (Inset) In the absence of a TC, only parallel structures are seen. From Bates et al. (adapted)[70] Reprinted with permission from AAAS.

Several issues led to the development of a new generation of top coats not based on maleic anhydride-norbornene permutations. First, synthesis of substituted norbornene derivatives typically required multiple synthetic steps, often including low-yielding Diels-Alder reactions with various by-products. Also, the polymerization yields were often low (≈10-50%),[76] making scale-up of the processes prohibitive. Yields could occasionally be improved by increasing the acrylate or styrenic compositions, but this generally resulted in a depression of the top coat $T_g$. Most importantly, the compositions of the 1st Generation terpolymers were notoriously difficult to control. Multi-modal molecular weight distributions were typical and the terpolymers were not always necessarily alternating, potentially resulting in irreproducible blocky monomer sequences. Feed ratios were rarely indicative of the polymer composition, and low-conversion strategies were undesirable. It was soon discovered that alternating copolymers of maleic anhydride and styrenic derivatives bearing bulky substituents

produced well-controlled polymers with sufficiently high $T_g$'s (> 170 °C) (2nd Generation), thus top coat designs were shifted away from norbornene-based polymers.

### 2.2.2 2nd Generation Ring-Opening Top Coats

The limitations of the norbornene-based 1st Generation top coats led to the development of a new class of materials. It was discovered that styrenic derivatives, coupled with maleic anhydride, have sufficiently high $T_g$'s (Table 2.1) to function as TCs, significantly higher than literature reported values (*ca.* 170 °C) for alternating maleic anhydride/styrene copolymers.[73] In addition, maleic anhydride and styrene typically form alternating copolymers over a wide range of feed ratios, giving high-yielding, well-controlled polymers.[67,72,76] Thus, a top coat design based solely on maleic anhydride and styrenic derivatives was targeted to improve the reproducibility, yield, and simplicity over 1st Generation TCs.

Table 2.1: $T_g$'s of copolymers of maleic anhydride and several styrenic derivatives. The titles represent abbreviated chemical names of the styrenic component.

| **Styrenic** | $T_g$ (°C) |
|---|---|
| **Sty** | 197 |
| **4-$CF_3$-Sty** | 196 |
| **4-*t*BuSty** | 222 |
| **3,5-di-*t*BuSty** | 206 |

The 2nd Generation top coat motif relies on alternating copolymers of maleic anhydride and two styrenic derivatives (Fig. 2.21). With most feed compositions, the top coat polymer is close to *ca.* 50 mol% maleic anhydride, with the remainder styrenic. The styrene components can be chemically modified to produce various high and low surface energy derivatives (*e.g.* fluorinated or *tert*-butyl substituents), such that a wide range of

surface energies can be accessed. The ratio of the two styrenics can be tuned to produce a library of top coats with various surface energies, and a neutral material can be easily selected using previously discussed island/hole techniques (Section 2.1).

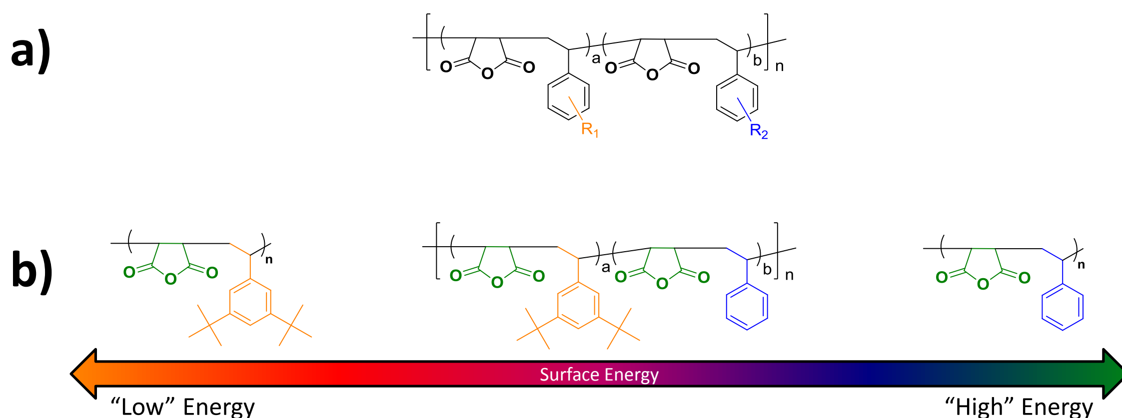


Figure 2.21: (a) Generalized 2nd Generation TC strategy using alternating copolymers of maleic anhydride and styrenic derivatives. (b) Neutral TCs can be produced by varying the composition between relatively low/high surface energy styrenic components

The 2nd Generation top coats are generally mono-modal and polymerize to high conversion. In addition, the polymer composition closely matches that of the feed composition (Table 2.2).[67] Although polymers synthesized to high conversion do not guarantee non-blocky behavior, the improved composition control over 1st Generation TCs enhances reproducibility. Literature evidence[82] also suggests that the surface energy of high-conversion random copolymers closely correlate with their composition, unlike binary blends of similar polymers. An internal control experiment also showed that polymers synthesized to various conversions produce similar wetting behavior by island/hole analysis. These results suggest that 2nd Generation TCs synthesized to high-

conversion are reproducible and the surface energy can be finely controlled by feed ratio modulation.

Table 2.2: Composition summary for representative set of 2nd Generation TCs.[a]

| **Feed Ratio (mol %)** | | | **Actual Ratio (mol %)[b]** | | |
|---|---|---|---|---|---|
| **MA** | **di-tBuS** | **S** | **MA** | **di-tBuS** | **S** |
| 50 | 5 | 45 | 52 | 6 | 42 |
| 50 | 10 | 40 | 52 | 12 | 36 |
| 50 | 26 | 24 | 51 | 25 | 24 |
| 50 | 50 | 0 | 51 | 49 | 0 |

[a] Abbreviations: maleic anhydride (MA), 3,5-di-tert-butylstyrene (di-tBuS), styrene (S).
[b] Calculated by combustion analysis.

Although a large variety of styrenic derivatives were investigated at TC platforms, copolymers comprised of maleic anhydride (MA), together with varying ratios of 3,5-di-tert-butylstyrene (di-tBuS) and styrene (S) were found to be suitable for a large variety of BCP systems. For this reason all TCs discussed herein will be referred by the nomenclature TC-XX, where XX represents the di-tBuS composition as determined by combustion analysis. Alternate top coat chemistries will be noted when applicable.

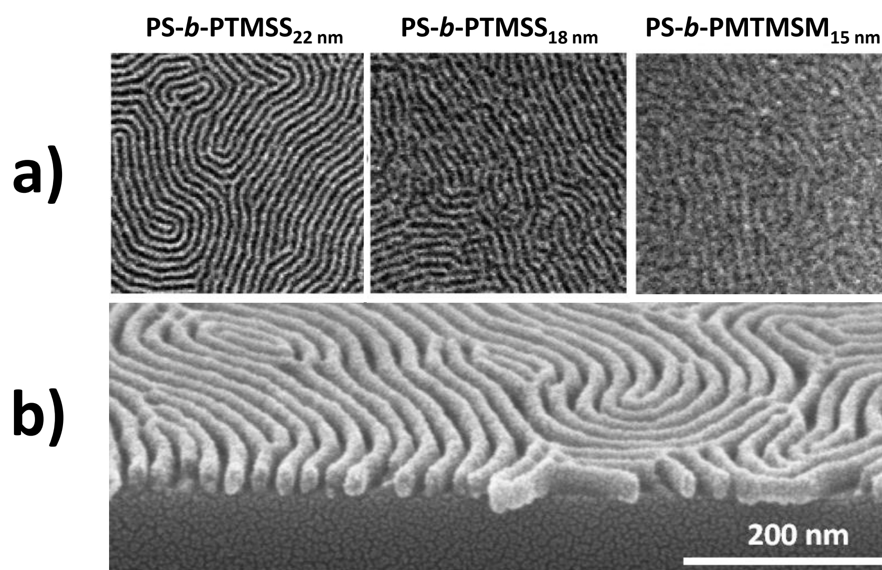


Figure 2.22: (a) Top down images of perpendicular assembly at $1.5L_0$ produced using 2nd Generation TCs for BCPs of both different pitch (indicated by subscript) and chemistry. (b) Cross-section image of PS-*b*-PTMSS-*b*-$PS_{30\ nm}$ showing through-film perpendicular assembly using TCs. Reprinted (adapted) with permission from Maher et al.[67]

The wetting characteristics of 2nd Generation TCs were evaluated using the island/hole methodology, and TC chemistries were found that are neutral for various BCP systems. For example, diblock copolymers PS-*b*-PTMSS and poly(styrene-*block*-methyl trimethylsilylmethacrylate) (PS-*b*-PMTMSM) have neutral 2nd Generation TCs, as determined by half-island hole topography. Both the top and bottom interfaces could be effectively neutralized, resulting in perpendicular assembly at any thickness (Fig. 2.22a). The cross-section image (Fig. 2.22b) indicates that the perpendicular self-assembly persists through the film when two neutral interfaces are used. These results demonstrate that 2nd Generation TCs can be evaluated, tuned, and applied using the same techniques discovered for 1st Generation TCs. The materials are effective not only for a variety of

BCP systems, but various periodicities as well, suggesting that the strategy is universal to nearly all BCPs.

## 2.3 Chemical Vapor Deposited Top Coats

Chemical vapor deposition (CVD) is a common process for semiconductor manufacturing in which volatile precursors are reacted and/or decomposed onto an exposed substrate to produce thin films of organic/inorganic material. A technique for chemical vapor depositing organic materials was pioneered by William F. Gorham at Union Carbide in the late 1940's, utilizing a cyclic "dimer" precursor [2.2]paracylcophane (Scheme 2.1, left).[83] When heated to high temperature, the structure decomposes into a resonance stabilized di-radical species, *p*-xylylene (Scheme 2.1, middle). This intermediate will quickly polymerize when physisorbed on a surface into a conformal film of the linear polymer poly(*p*-xylylene) (trade named "parylene") (Scheme 2.1, right). This process has found a large commercial use for depositing polymeric films on a wide variety of substrates for applications such as barrier layers for circuit boards and medical devices.

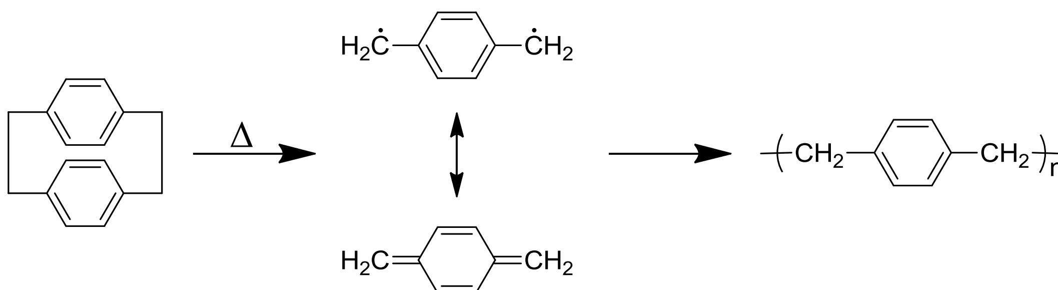


Scheme 2.1: Formation of poly(*p*-xylylene) (parylene) by heating of cyclic [2.2]paracylcophane precursor to form a resonance-stabilized reactive di-radical intermediate.

Poly(*p*-xylylenes) have many unique properties that made them an attractive initial candidate as a TC material. Unlike many reactive CVD processes, which require high temperatures or specific surface chemistries, poly(*p*-xylylenes) are deposited at low temperature ($T << T_{g\text{-BCP}}$) by a physical mechanism. This is necessary because high temperature process steps used in reactive CVD can unintentionally anneal the BCP prior to TC deposition. The vapor-phase deposition also requires no solvents, so unlike solution deposited materials (*e.g.* Section 2.2 and 2.4), it can theoretically be applied over the BCP as an inherently neutral material without requiring a polarity-switch. Poly(*p*-xylylene) typically does not have good solubility properties,[83] so it cannot be stripped post anneal; however, physisorbed materials produce highly conformal films, implying that the TC can be uniformly etched away using standard RIE plasmas to transfer the underlying pattern of an inherently etch-resistant BCP (Fig 2.23). The surface energy of the polymer can be tuned through direct functionalization of the [2.2]paracylcophane precursor,[84] and a neutral material can be accessed by vapor-phase copolymerization of selected monomers, as has been established in previous reports.[85,86] Alternative vapor deposition techniques have also been presented that could be adapted to the same end use.[87,88]

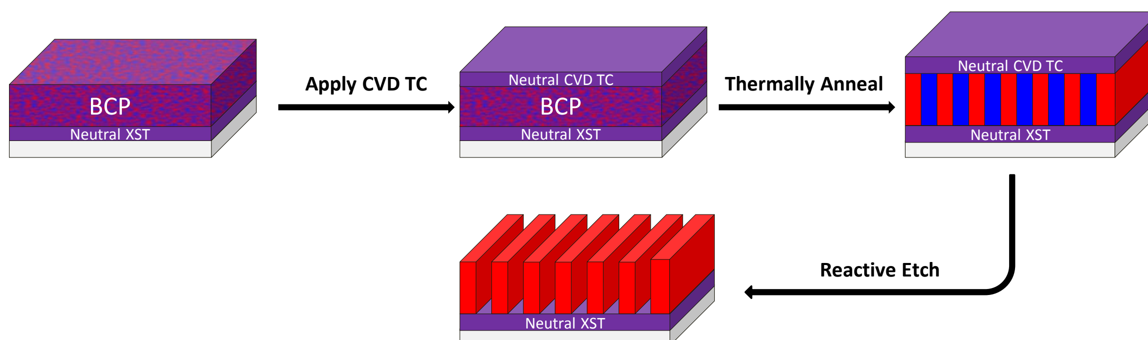


Figure 2.23: Process flow for CVD top coats. TC is inherently neutral and can be directly etched to transfer the underlying pattern.

Two organosilicon BCPs (known to orient parallel to the substrate due to top surface energy effects) were used as test vehicles to demonstrate the applicability of the CVD TC process. Due to the large variable space for the process (bottom surface treatment, thickness, top surface coating, annealing temperature, and annealing time), some of the conditions were held constant to isolate the effects of others. For example, XSTs were not optimized for neutrality (a wetting test methodology had not yet been developed), so the choice of materials was essentially arbitrary. Nevertheless, a matrix of various XSTs and thicknesses were chosen to probe the CVD TC orientation behavior as a function of bottom surface energy and commensurability conditions. Samples were individually prepared and bonded to a single large wafer, which was coated uniformly with poly(*p*-xylylene) by a third party, Specialty Coating Systems. After annealing and etching through the TC, the orientation behavior gave feedback on the neutrality conditions.

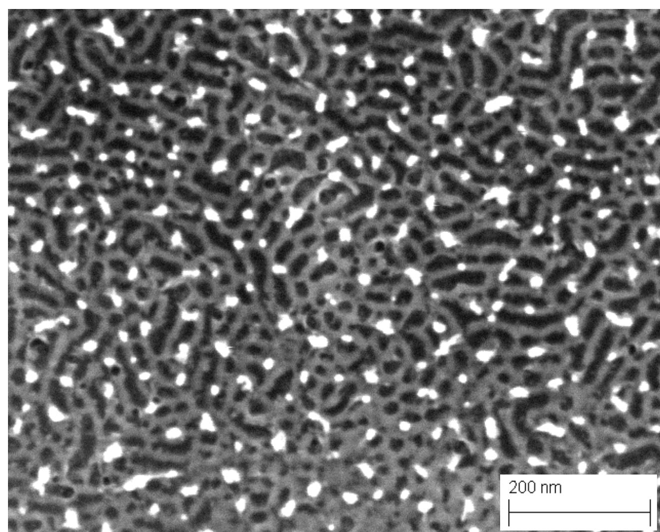


Figure 2.24: Initial orientation results for CVD TC, poly(*p*-xylylene), showing evidence of perpendicular self-assembly for a lamellar BCP, but with a high degree of defectivity.

Several samples using the poly(*p*-xylylene) TC show of perpendicular self-assembly, but contain significant levels of defects, suggesting the assembly process with poly(*p*-xylylene) is not perfectly compatible with the BCP system. For example, a lamellar BCP, PS-*b*-PMTMSM (Fig. 2.24), was etched using an oxygen-based plasma to show prototypical fingerprint-like nanostructures on the order of the BCP length scale (≈ 25-30 nm), but with small protrusions from the domains. The white/grey structures in the image correspond to remaining oxidized silicon residue, evidence that the protrusions are comprised of the silicon-domain of the BCP. These results suggest that the TC is inter-diffusing into the BCP layer, causing disruption of the underlying morphology. It is likely that the melt-mixed TC induced a morphological change, producing cylindrical-like topography on top of the underlying vertical lamellae. Similar results have been observed for multilayer films of lamella/cylinder morphologies.[89] The inter-diffusion of the TC is corroborated by a volume expansion experiment of a poly(*p*-xylylene) film on a silicon wafer (Fig. 2.25). In this experiment, the non-linearity of the thickness profile indicates a melt transition of the poly(*p*-xylylene). This is due to a change in the thermal expansion from a glassy to melted state, suggesting a $T_g$ exists near 120 °C.

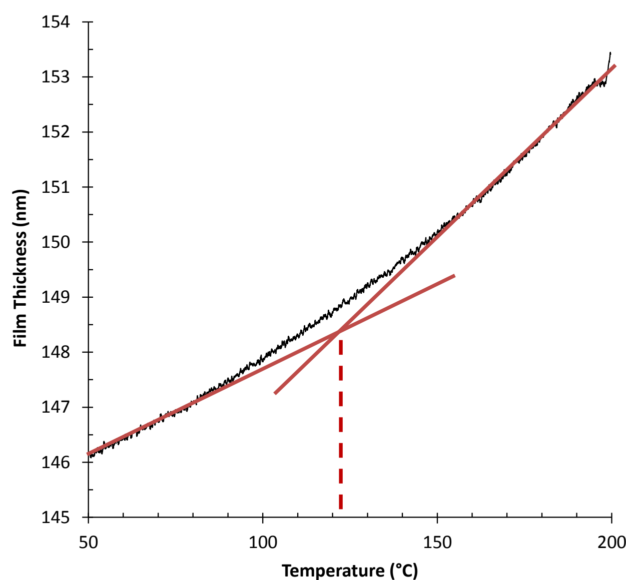


Figure 2.25: Film expansion curve for poly(*p*-xylylene) film on silicon wafer, showing $T_g$ near 122 °C.

Parylene possesses a high melting temperature (400 °C)[83] (*i.e.* crystallization temperature) and is insoluble in nearly all organic solvents, leading to the presumption it would produce a high-$T_g$ TC material suitable for orientation control. Unfortunately, the data depicted in Fig. 2.25 shows that the $T_g$ is not similarly high. However, evidence of fingerprint structures is encouraging; perpendicular lamellae suggest poly(*p*-xylylene) analogues can act to neutralize the top interface. Future work could attempt to alleviate the low $T_g$ issue, for example, by incorporating cross-linkable moieties in the polymer backbone to prevent polymer diffusion upon annealing.

## 2.4 Elimination Top Coats

Both ring-opening and CVD-based top coats have limitations making alternative TC designs desirable. For example, ring-opening TCs require at least some majority fraction of the polymer to be comprised of maleic anhydride to impart the solubility-

switching characteristics necessary for solution processing. The polarity-switching mechanism of maleic anhydride allows the TC to revert its surface energy to a state that is potentially neutral to the BCP, but unfortunately, the relatively high polarity of maleic anhydride's ring-closed form limits the range of accessible surface energies (Fig. 2.26). Efforts to reduce the maleic anhydride content have successfully lowered the overall TC surface energy, but it can only be reduced to the extent that the polymer is still soluble in polar solvents.[67,76] CVD top coats can overcome these issues by directly depositing neutral materials, but require expensive and complicated vacuum deposition equipment that is not now available to the microelectronic manufacurers. Thus, an alternative solution would be a spin-coatable TC that can undergo a polarity-switch, but *eliminates* the polar functionality that imparts its solubility. This provides a greater range of accessible surface energies but still utilizes processes amenable to manufacturing.

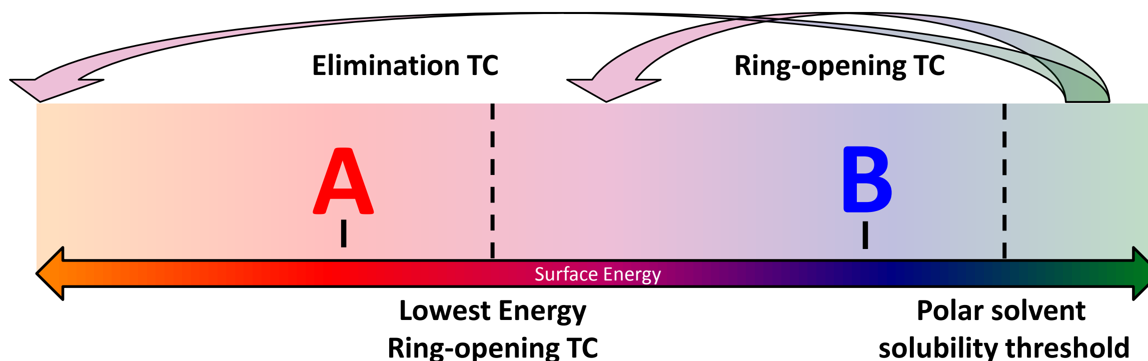


Figure 2.26: The polarity-switching mechanism of ring-opening TCs (represented by the curved arrow) can only access limited surface energies due to maleic anhydride's inherently high polarity. In contrast, elimination polymers can theoretically access all surface energy ranges.

Elimination TC schemes rely on chemistries that promote solubility in polar solvents, yet upon annealing, can polarity-switch to a lower-surface energy product. Unlike ring-opening TCs that can be re-dissolved post-anneal, the elimination pathway is

irreversible and produces an insoluble or low surface energy product that cannot be removed (*i.e.* without damaging the underlying BCP). Instead, the elimination TCs are comprised of organic materials that allow facile post-anneal etching to reveal the underlying BCP structures (Fig. 2.27). In this process, the top coat can be directly applied to the BCP top interface by spin coating from an orthogonal solvent, then baked to eliminate a component of the polymer and induce a polarity switch. The resulting neutral polymer can be etched completely through to the substrate, subsequently producing a relief image from the inherently etch-resistant domains, and the pattern can be transferred accordingly.

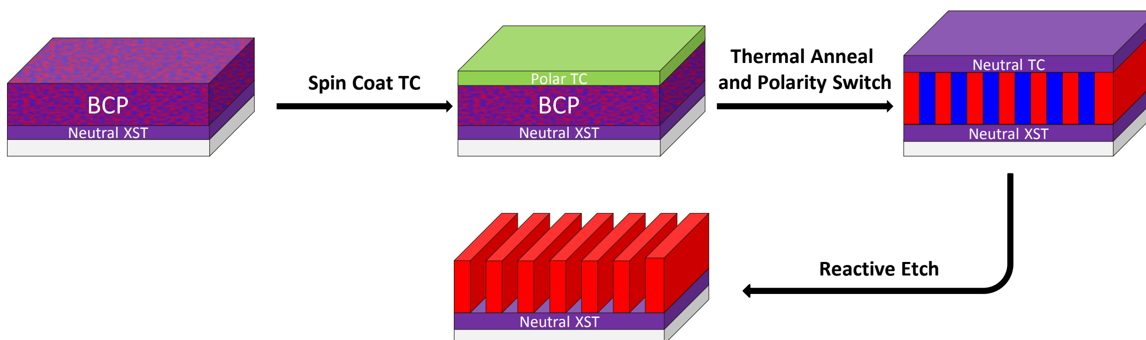


Figure 2.27: Process flow for polarity-switching elimination TCs. The TC must be etched through to the underlying structures.

Two overarching designs are discussed herein as elimination TCs: poly(*p*-phenylene vinylene)s (PPVs) and Hofmann elimination polymers. Each TC design and their respective results are discussed in the following sections.

### 2.4.1 Poly(*p*-Phenylene Vinylene)s

After discovering poly(*p*-xylylene)'s low-$T_g$ (Fig. 2.25), it was hypothesized that producing a similar polymer with a rigid backbone would increase the $T_g$ and yield a material suitable as a TC. Fortunately, a precedent exists for the preparation of poly(*p*-

phenylene vinylene) (PPV) derivatives from water-soluble precursors (Scheme 2.2).[90,91] In this scheme, sulphonium-salt precursors are polymerized in the presence of a strong base. The resulting water-soluble polyelectrolyte can be heated to eliminate residual sulphonium groups via a β-hydride elimination pathway, producing a rigid, conjugated PPV backbone.

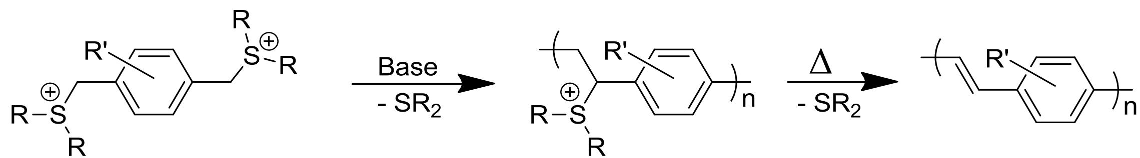


Scheme 2.2: Generalized scheme for the polymerization of PPV TCs from α,α'-disubstituted *p*-xylylenes. The water-soluble polyelectrolyte precursor eliminates to form PPV upon application of heat.

Polymers synthesized by this mechanism can conceptually function as top coats by being spin-coated from the water-soluble polyelectrolyte atop a BCP. After heating, the polyelectrolyte reverts to a lower surface energy PPV film by eliminating a volatile sulphonium group. The temperature of the reversion step is an important consideration, as it ideally should occur below the $T_g$ or decomposition temperature ($T_d$) of the BCP. The elimination kinetics can be tuned by modifying the leaving group and counter-ion of the polyelectrolyte.[91] The surface energy of the PPV TC can be tuned by copolymerizing various substituted PPVs. Once eliminated, a neutral material can induce perpendicular orientation and be subsequently etched to reveal the underlying patterns. The fully converted PPV film has a high $T_g$[92] and should preclude intermixing at moderate anneal temperatures ($T > T_{g\text{-BCP}}$).

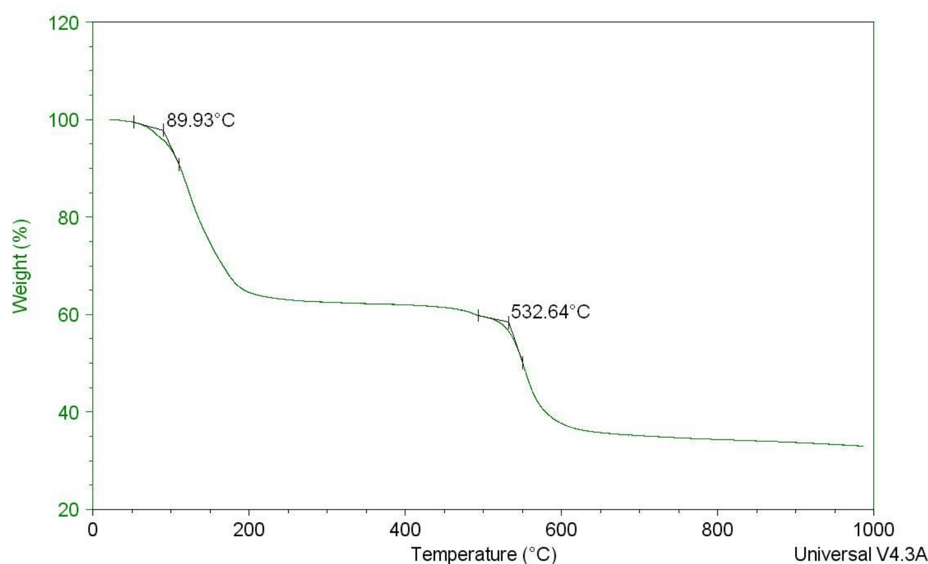


Figure 2.28: TGA trace of anhydrous PPV pre-polymer

PPV was tested as a TC candidate by synthesizing the polyelectrolyte with tetrahydrothiophene (THT) as the leaving group. Small molecule impurities and salts were separated from the reaction mixture by dialysis, and the resulting aqueous solution was directly spin cast to produce polymer films. Thermogravimetric analysis (TGA) of a vacuum-dried sample of the polyelectrolyte solution shows the elimination of THT to form PPV polymer (Fig. 2.28). Upon heating, significant mass loss is seen resulting from residual solvent and elimination of THT. Above *ca.* 100 °C, the elimination proceeds rapidly, producing PPV polymer that is stable until temperatures > 500 °C.

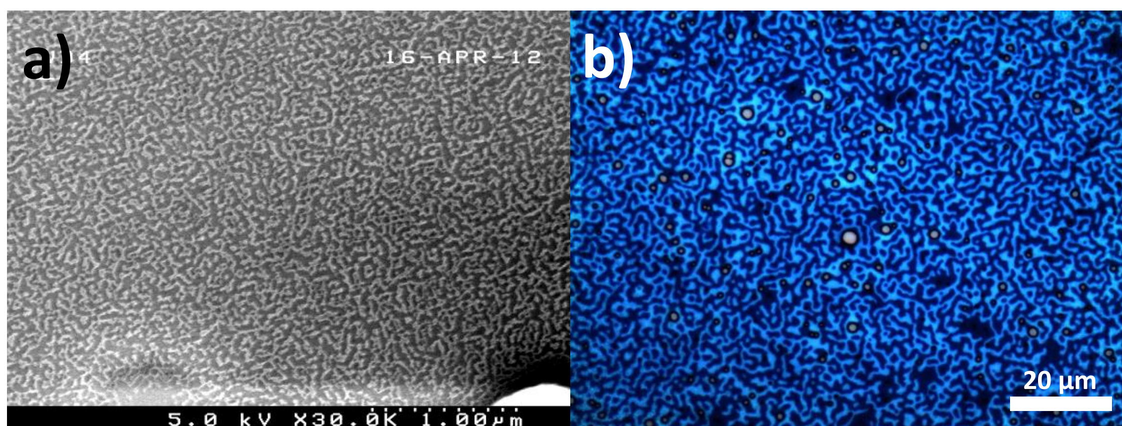


Figure 2.29: (a) SEM image of microstructure found using PPV as a top coat material. (b) Optical micrograph of macro-scale topography seen after annealing PPV TC film stack. Note difference in scale bars.

The water-soluble PPV pre-polymer was applied as a TC using PS-*b*-PTMSS as a test vehicle, and sampled at several annealing temperatures, substrate surface energies, and thicknesses. Under all observed conditions, evidence of nano-scale structures was observed (Fig. 2.29a), but the domains were not consistent with BCP morphologies. An optical micrograph (Fig. 2.29b) of the annealed film shows evidence of macroscopic reorganization. It is hypothesized that the volatile THT (BP: 119 °C), eliminated upon thermal annealing, could potentially disrupt the underlying BCP by plasticizing (*i.e.* solvent annealing) the film. Analogues of the PPV were synthesized with dimethyl sulfide (BP: 35 °C) as a leaving group, but such materials required elimination temperatures greater than 300 °C to fully convert the pre-polymer ($T > T_{\text{d-BCP}}$). An additional complicating issue arises from the elimination pathway; although PPV itself has a high $T_g$, the non-rigid pre-polymer presumably does not. The full conversion to PPV does not occur until after extended annealing at temperatures ($T > 200$ °C) well above the $T_g$ of the precursor.[90] It is possible that the macrostructure seen in Fig. 2.29b is a result of melt-mixing of the lower $T_g$ pre-polymer and BCP. Verification of the pre-

polymer properties is obfuscated by the material's inherent temperature sensitivity. Although the surface energy of the PPV might be suitable to control the BCP orientation, the process is incompatible with use as a TC.

### 2.4.2 Hofmann Elimination Polymers

The PPV TCs investigated in Section 2.4.1 suffered from several key limitations, thus a novel TC was designed leveraging the polarity-switching mechanism of the Hofmann elimination. This reaction, named after the German chemist August Wilhelm von Hofmann who discovered it in 1851, produces a relatively non-polar alkene upon elimination of a polar quaternary ammonium salt (Scheme 2.3).[93] The quaternary ammonium salt undergoes a β-hydride elimination upon heating to produce the alkene, releasing the volatile trialkylamine (*e.g.* trimethylamine, BP: 3 °C) as a by-product. Unlike the sulfides eliminated in PPV TCs, most amine by-products do not interact with the BCP and can easily be expelled as gases at moderate temperatures. Therefore, a polarity-switching TC polymer can be designed by incorporating the Hofmann elimination chemistry.

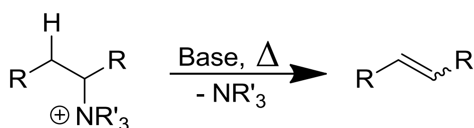


Scheme 2.3: Generalized Hofmann elimination reaction, converting a polar quaternary ammonium salt into a non-polar alkene.

In the PPV-based TC system, the rigid, high-$T_g$ polymer does not develop until *after* the elimination step. Consequently, a Hofmann elimination TC was designed to have an inherently high-$T_g$ polymer backbone. Addition polymers of norbornene were chosen because they are well known to produce high-$T_g$ polymers with controllable

molecular weight using nickel-based catalysts.[94,95] The quaternary ammonium functionality is conpatible with the highly sensitive nickel catalysts, but could be instilled using a post-polymer modification reaction. This framework was targeted to produce solution processable TC materials. The quaternary ammonium salt improves the polymer solubility in polar solvents, and when heated, the functional group reverts to the lower surface energy alkene. The alkene product can be removed after annealing by plasma etching. Finally, the surface energy of the top coat polymer can be tuned by copolymerizing various norbornene derivatives with high and low surface energy properties.

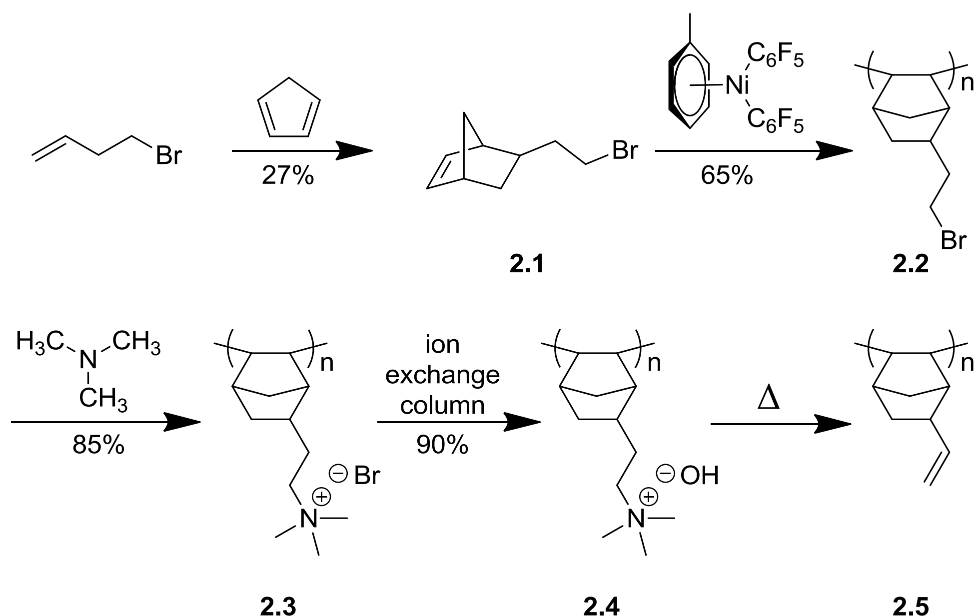


Scheme 2.4: Synthesis of norbornene-based Hofmann elimination TC.

A pathway was developed (Scheme 2.4) to produce addition polymerized norbornene derivatives with pendant quaternary ammonium functional groups, capable of undergoing a Hofmann-type elimination. The monomer **2.1** is synthesized from the Diels-

Alder adduct of cyclopentadiene and commercially available 4-bromobut-1-ene. The addition polymer **2.2** was generated using ($\eta^6$-toluene)Ni($C_6F_5$)$_2$ as a catalyst, and once obtained, was converted to the quaternary ammonium salt **2.3** through a post-polymer modification reaction using trimethylamine. A strongly basic anion exchange membrane was used to convert the halide salt to a hydroxide counterion **2.4**. When heated, the TC will undergo a Hofmann elimination to produce **2.5**.

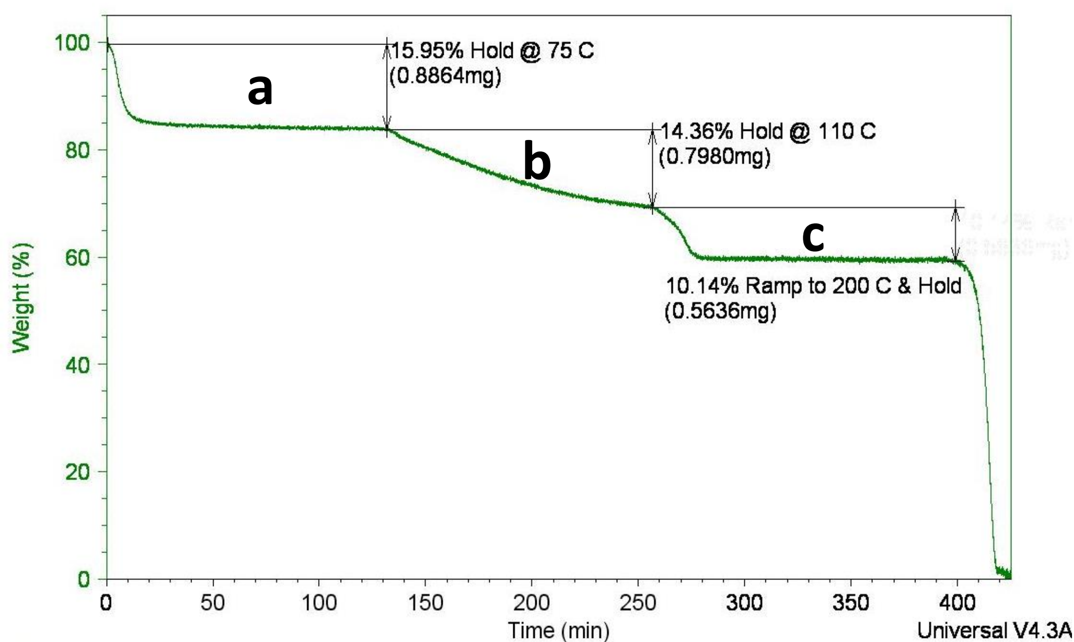


Figure 2.30: TGA experiment with TC polymer **2.4** showing three different two hour isotherm segments: (a) 75 ºC, (b) 110 ºC, and (c) 200 ºC.

An attempt was made to verify the elimination reaction for the TC polymer based on mass loss from the quaternary ammonium salt (197 amu) to the vinyl norbornane (110 amu). A sample of **2.4** was submitted for TGA using a custom temperature ramp profile. In this experiment, the polymer was initially ramped 10 °C/min and held at 75 °C for two hours to evaporate residual water absorbed by the highly hygroscopic polymer (Fig

2.30a). During this initial phase, the weight decreases 16% but quickly plateaus, suggesting that water is volatized after several minutes of mild heating but little elimination occurs. In the second phase (Fig. 2.30b), the sample is ramped again and held for two hours at 110 °C. Mass is continually lost during this phase, indicating that at elevated temperatures the elimination reaction takes place. For the third phase (Fig. 2.20c), the sample is heated to 200 °C and held for a final two hours before ramping at 10 ºC/min to 500 ºC. Within several minutes of heating, the mass loss plateaus again, indicating the elimination reaction is complete. The total mass loss (assuming all mass loss from the initial phase is water) is *ca.* 36%, close to the theoretical mass loss of 44%. The discrepancy between these numbers may reflect partially eliminated polymer or incomplete conversion of the alkyl halide. These results suggest that complete conversion to the elimination product **2.5** should occur after heating at elevated temperatures ($T >$ 150 °C) for several minutes.

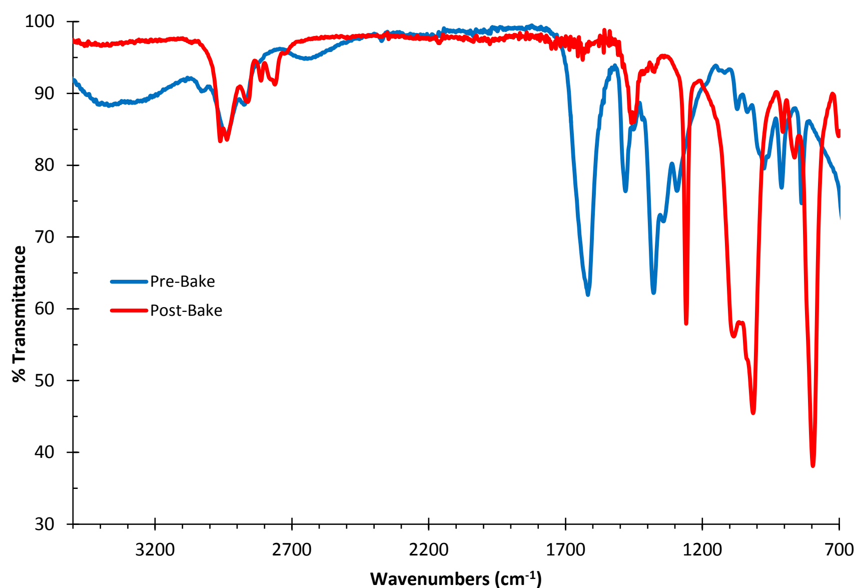


Figure 2.31: Bulk IR spectra of quaternary ammonium salt polymer **2.4** (blue) and the same sample after annealing at 160 ºC (red).

A bulk sample of **2.4** was annealed at 160 ºC for *ca.* 15 hours to document the polarity-switching behavior (Fig. 2.31). The quaternary ammonium salt (Fig. 2.31, blue) shows distinct broad alcohol bands at 3300 $cm^{-1}$, yet also evidence of alkene transitions (=C-H stretching, 3030 $cm^{-1}$; -C=C- stretching, 1620 $cm^{-1}$). This suggests the TC polymer is partially eliminated as synthesized and may be sensitive even at room temperature, implicating the material must be carefully processed. After baking (Fig. 2.31, red), the sample shows a dramatic shift. The alcohol and alkene transitions are virtually gone, while the remaining character is primarily alkane stretches, suggesting that upon annealing, the pendant vinyl substituents largely cross-link. This is corroborated by the solubility characteristics of the bulk polymer, which after heating is immiscible in all solvents.

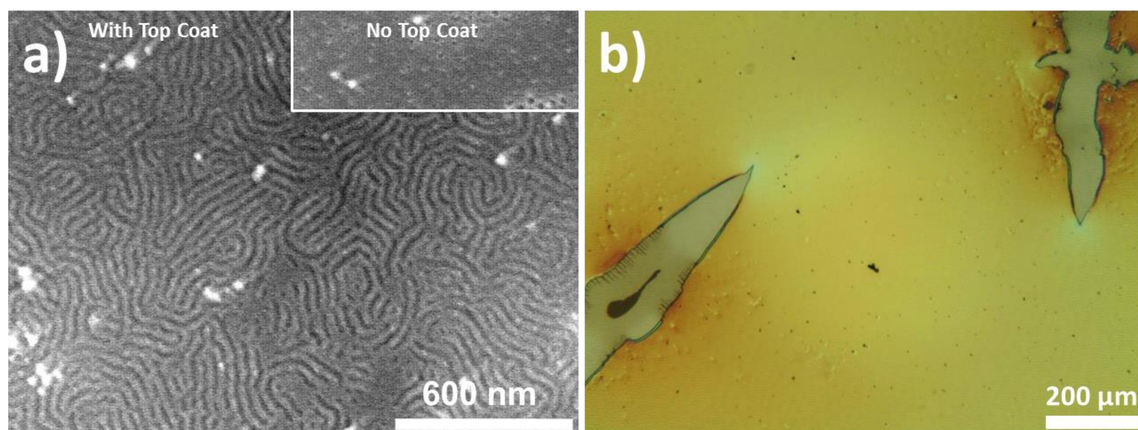


Figure 2.32: (a) SEM image of representative sample annealed with Hofmann elimination TC and without TC (inset). (b) Optical micrograph of film cracking induced by volume shrinkage during the elimination process.

The polarity-switching elimination polymer **2.4** was evaluated as a TC at several anneal conditions using PS-*b*-PTMSS and XST/thickness combinations found successful for the 1st Generation ring-opening TCs. A representative example of the results is shown

in Fig 2.32, after annealing and etching through the TC layer. For a sample annealed at 190 ºC in air for 30 minutes, several regions were discovered that show evidence of perpendicular self-assembly (Fig. 2.32a). This is distinctly contrasted by the control sample (inset) that showed only parallel orientation with minor defects for a sample with no TC. This establishes the proof of principle that the Hofmann elimination TC can modify the surface energy of the top interface and induce perpendicular orientation under certain conditions. Several defects are evident on the imaged sample, however; the small particulates appearing on top of the lamellar features are likely the result of residual inorganic salts or materials re-deposited during etch processing. The BCP self-assembly also shows defects, seen as regions of parallel wetting or dislocations between domains. Most of these issues are believed to be due to surface energy mismatching of the top (or bottom) interface (see Fig 5.7). Neither the TC or XST were evaluated for wetting behavior at the time of experimentation, thus it is likely that neither interface is truly neutral for the BCP. Further tuning of the surface energy through compositional variance and wetting preference evaluation by island/hole behavior could be used to develop neutral materials and optimize this process.

One issue that led to the discontinuation of progress with the Hofmann elimination TCs is seen in Fig. 2.32b. Shown is an optical micrograph of the BCP/TC film stack after annealing. Large cracks can be seen in the film, resulting in partial delaminated from the wafer. These defects may result from film stresses induced by volume contraction. Due to the significant mass loss during the elimination process (see Fig. 2.30), the film contracts in volume, typically *ca.* 40%. The stress induced by the film shrinkage is enough to cause large cracks and make processing of such TCs difficult.

## 2.5 Conclusions

Orientation control of BCPs in thin films requires not only careful consideration of confinement effects, but neutralization of surface energy at the top and bottom interfaces. To date, no simple method exists for quantifying the surface energy of polymeric materials, but the wetting behavior of lamellar BCPs can be easily probed by exploiting island/hole topography. This phenomenon provides direct and easily processed feedback on the wetting behavior based on surface energy and commensurability conditions of a film. Using this technique, it was shown that both the bottom interface and top coat materials can be studied, and a definitive evaluation of the neutral condition can be assigned based on the appearance of $0.5L_0$ topography.

Three distinct top coat designs were pursued for neutralizing the top interface of BCP thin films. Each technique exploits unique chemical or physical phenomena to deposit organic materials on BCPs without damaging the underlying film. Ring-opening top coats rely on the reversible opening/closing reaction of maleic anhydride to produce solution processable polymers that can switch polarity upon heating. Additionally, the TC films can be removed post-anneal by immersing in a basic solution, simplifying the etch processing. Ring-opening TCs have shown successful orientation control for a variety of BCP systems and are the focus of much of the discussion found in this text. Next, chemical vapor deposited TCs, in the form of poly(*p*-xylylene), can be deposited as thin films without solvent. This method can theoretically access greater ranges of surface energy, but must be directly etched after deposition. When poly(*p*-xylylene) was applied as a TC, evidence of perpendicular assembly was observed, but it was discovered melt-mixing occurred related to the TC's low $T_g$. Elimination TCs provide an opportunity for a wide range of surface energies as well, but are deposited from solution, relying on polarity-switching mechanisms that eliminate a polar functionality. This class of

materials also showed evidence of perpendicular self-assembly, proving their conceptual application, but were more difficult to process than ring-opening TCs.

## 2.6 EXPERIMENTALS

***Chemicals:***

All chemicals were purchased from Sigma Aldrich and used as received unless otherwise noted. Azoisobutyronitrile was recrystallized from methanol. THF (uninhibited) and diethyl ether were purchased from Fischer Scientific. CVD deposited poly(*p*-xylylene) was provided by Specialty Coating Systems. Nickel catalyst ($\eta^6$-toluene)Ni($C_6F_5$)$_2$ was provided as a generous gift by Promerus LLC.

***Block Copolymers***

Details of the design, synthesis and characterization of the majority of BCPs discussed herein can be found in Chapter 3. Synthetic details and characterization of the triblock PS-*b*-PTMSS-*b*-PS can be found in the dissertation of C.M. Bates.[76]

***Instrumentation:***

All films were coated on a Brewer Science CEE 100CB Spincoater. Annealing was performed on a Thermolyne 11515B hot plate. Ellipsometry measurements were taken with a J.A. Woolam Co., Inc. VB 400 VASE Ellipsometer. Reactive ion etching was performed on an Oxford Instruments PlasmaLab 80+ in inductively coupled plasma mode using the following settings unless otherwise noted: (RF power: 20 W, ICP power: 10 W, pressure: 50 mtorr, $O_2$ flow rate: 75 sccm, Ar flow rate: 75 sccm). A Zeiss Supra 40 VP and Hitachi S-4500 were used for all SEM images. SEC Data were collected with an Agilent 1100 Series isopump and autosampler with a Viscotek Model 302 TETRA detector platform using THF as an eluent at 23 ºC. Three I-series mixed bed high-MW

columns were calibrated relative to polystyrene standards. Small molecule IR data were recorded on a Nicolet Avatar 360 FT-IR. Polymeric IR were recorded on a Nicolet 380 FT-IR diamond ATR. Dynamic heating experiments were performed using an Instec mK 1000 temperature controller with a HCS 402 hot stage and a J.A. Woolam XLS-100 Ellipsometer. TGA/DSC data were collected on a TA Instruments Q500/Q100, respectively. $^{1}$H NMR spectra were recorded on a Varian Unity Plus 400 MHz instrument, with chemical shifts reported downfield in ppm from TMS using residual protonated solvent as an internal standard (CDCl3, $^{1}$H 7.29 ppm, $^{13}$C 77.0 ppm). AFM images are produced using an Asylum MFP 3D AFM. Combustion analysis was performed by Midwest Microlab, LLC.

### 2.6.1 Generalized Bottom Interface Wetting Procedure

The following generalized procedure is used for evaluating the wetting preference of a substrate interface using the "classic" island/hole methodology (see Section 2.1.2). The given representative example is for preparation and evaluation of a cross-linked polymer (XST) poly(4-*tert*-butylstyrene-*r*-methyl methacrylate-*r*-vinylbenzyl azide).

A 0.5-1 wt% solution of the XST polymer in toluene is filtered through a 0.22 μm disc filter into a clean vial. The polymer solution is dispensed onto a clean silicon wafer, and the wafer is then placed on a hotplate at 250 °C for 5 minutes, crosslinking the film. The wafer is quickly cooled on an aluminum block to room temperature (RT), then rinsed sequentially with 3x10 mL acetone and 3x10 mL isopropanol. The XST film is blown dry with a compressed air stream, and soft baked at 110 °C for 1 min to remove any residual solvent.

A filtered solution of the BCP (*e.g.* 0.5-1.5 wt% in MIBK) is spin coated onto the XST film at an incommensurate thickness (*e.g.* 1.25$L_0$) as verified by ellipsometry. Note:

the commensurability conditions can be verified by coating multiple sequential thicknesses and observing switches between island/hole topography which occur at commensurate conditions. The film stack is annealed in air at 180 °C for 10 min., then cooled immediately to RT by placing on an aluminum block. Island/hole topography is imaged using optical microscopy.

### 2.6.2 Generalized Top Interface Wetting Procedure

The following generalized procedure is used for evaluating the wetting preference of a top coat material using the top interface wetting methodology (see Section 2.1.3). The given representative example is for preparation and evaluation of a 2$^{nd}$ Generation TC, but is applicable to any of the top coat materials.

A preferential XST film (*e.g.* poly(styrene-*r*-vinylbenzyl azide) (XST-Sty)) is prepared according to a similar procedure as described in Section 2.6.1. A filtered solution of the BCP (*e.g.* 0.5-1.5 wt% in MIBK) is spin coated onto the XST film at an incommensurate thickness (*e.g.* $1.25L_0$) as verified by ellipsometry. The ring-opened TC polymer salt (see Section 2.6.4), 0.5-1 wt% in methanol, is cast onto the BCP film, and the film stack is annealed in air at 180 °C for 10 min. The wafer is then cooled immediately to RT by placing on an aluminum block. The top coat layer can be removed by immersing the film stack in a bath of 1:1 50% aq. Trimethylamine:methanol for 2 min., rinsing with water, and blowing the film dry with compressed air. Island/hole topography is imaged using optical microscopy.

### 2.6.3 Generalized Cross-linkable Surface Treatment (XST) Synthesis

The following is a representative procedure for the synthesis of a cross-linkable XST polymer used for substrate surface energy modification. Typical XSTs were random terpolymers comprised of 4-*tert*-butylstyrene, methyl methacrylate, and vinylbenzyl azide

Fig. 2.33. Additional details regarding the design, synthesis, and characterization of such polymers can be found elsewhere.[48,76]

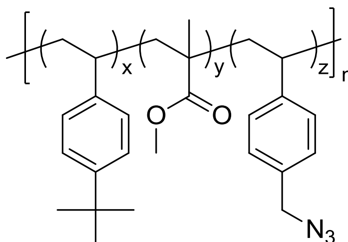


Figure 2.33: Poly(4-*tert*-butylstyrene-*r*-methyl methacrylate-*r*-vinylbenzyl azide) XST polymer used for substrate surface energy modifications.

Monomers were first purified by stirring over basic alumina (10 wt.% relative to monomer mass) until colorless and filtering through a glass-fretted filter, then subsequently a 0.2 µm filter disc into a clean vial. A 250 mL 3-neck round-bottom flask (RBF) equipped with rubber septa, reflux condenser, and magnetic stir bar was charged with 4-*tert*-butylstyrene (0.37 eq., 15.335 g, 95.7 mmol), methyl methacrylate (0.58 eq., 15 g, 150 mmol), 4-vinylbenzyl chloride (0.05 eq., 1.974 g, 12.9 mmol), azoisobutyronitrile (AIBN) (0.01 eq., 0.424 g, 2.586 mmol), and 100 mL of THF. The reaction mixture was degassed by bubbling a nitrogen stream through the reactor for 30 minutes. The reactor was immersed in an oil bath at 65 °C for 24 hrs., then quenched at 0 °C. The polymer solution was concentrated and precipitated in 500 mL methanol, then filtered and dried at 65 °C in vacuo to yield a white powder (21.2 g, 70 %).

The poly(4-*tert*-butylstyrene-*r*-methyl methacrylate-*r*-vinylbenzyl chloride) (5.0 g) was transferred to a 100 mL RBF with *ca.* 50 mL DMF. The solution was heated until complete dissolution of the polymer, and sodium azide (> 3 eq., 0.5g, 7.7 mmol) was added. A large excess of sodium azide is added to ensure complete conversion of the

chloride. The reaction slurry was stirred at 65 °C overnight, quenched at 0 °C, and then precipitated into 500 mL of a 5:95 water:methanol mixture. The polymer was filtered in a Buchner funnel, the filtrate washed 3x100 mL water and 3x100 mL methanol, then dried at 65 °C to yield a white powder (3 g, 60%).

### 2.6.4 Generalized Ring-Opening Top Coat Synthesis

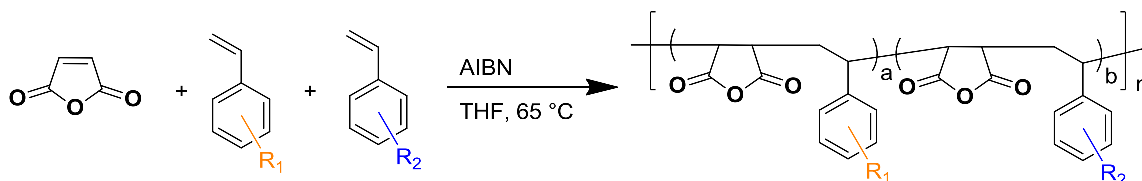


Scheme 2.5 Generalized synthetic scheme for 2nd Generation top coats.

The following synthetic procedure is representative of all 2nd Generation top coat materials. Typical top coats were terpolymers comprised of maleic anhydride and two styrenic derivatives (see Section 2.2). Additional details regarding the design, synthesis, and characterization of such polymers, including 1st Generation top coats, can be found elsewhere.[67,76] The following example describes the polymerization of poly(maleic anhydride-*alt*-4-*tert*-butylstyrene)

A 1 L 3-neck RBF equipped with rubber septa, reflux condenser, and magnetic stir bar was charged with maleic anhydride (1 eq, 30.6 g, 312 mmol), 4-*tert*-butylstyrene (1 eq., 50 g, 312 mmol), azoisobutyronitrile (AIBN) (0.01 eq., 1.025 g, 6.25 mmol), and 400 mL of THF. The reaction mixture was degassed by bubbling a nitrogen stream through the reactor for 30 minutes. The reactor was immersed in an oil bath at 65 °C to initiate the polymerization, heated for 24 hrs., then quenched at 0 °C. The polymer solution was concentrated in vacuo and precipitated in 2 L of a 3:1 hexanes:DCM mixture, then filtered and dried at 65 °C in vacuo to yield a white powder (66.3 g, 83 %). The TC is ring-opened by immersing 1 g of polymer in 7 g of 50 wt% aq. trimethylamine

and stirred until complete dissolution. The viscous solution is precipitated by addition of 50 mL THF while stirring vigorously. The THF and water are removed in vacuo to yield a semi-crystalline polymer salt.

### 2.6.5 Poly(*p*-Xylylene) TC

A matrix of various conditions were used to test suitable conditions for perpendicular self-assembly using a poly(*p*-xylylene) TC. Wafers of three XSTs (poly(styrene-*r*-vinylbenzyl azide) (XST-Sty), poly(4-methoxystyrene-*r*-vinylbenzyl azide) (XST-OMe), and poly(*tert*-butyldimethylsiloxystyrene-*r*-vinylbenzyl azide) (XST-TBDMSO)) were used as bottom surface treatments for the BCPs. Lamellar and cylindrical morphologies of PS-*b*-PTMSS and PS-*b*-PMTMSMA were used at 4 different thicknesses each (*ca.* 1, 2, 3, and >3$L_0$) for a total of 48 samples. Several clean silicon wafers were used as controls for single films of poly(*p*-xylylene). The BCPs were applied on top of cross-linked XSTs, and all samples were bonded to a large 10 inch silicon wafer using double-sided scotch tape. The wafer was sent to Specialty Coating Systems and received a uniform film of poly(*p*-xylylene) of *ca.* 150 nm. Film thicknesses were verified on the BCP and control samples using ellipsometry. Samples were etched on an Oxford Instruments Plasmalab 80+ operating in inductively coupled plasma mode using the following conditions: RF power: 80 W, ICP power: 100 W, pressure: 90 mtorr, $O_2$ flow rate: 5 sccm. Samples were etched approximately 30 seconds to break through the TC layer and target a depth of 10 nm into the BCP. Films were then imaged by SEM to study the resulting morphology and orientation.

The volume expansion experiment was performed by heating a film of poly(*p*-xylylene) on a silicon wafer using an INSTEC heating stage coupled with dynamic ellipsometric measurements using a J.A. Woolam XLS-100 Ellipsometer. The film was

slowly heated from 40 °C to 190 °C at 2 °C/min with thickness measured at regular intervals. The intersection of the curves assuming constant expansion coefficients for the melt and glassy phases was used to estimate the $T_g$ of the polymer.

### 2.6.6 Poly(*p*-Phenylene Vinylene)s

***PPV TC Synthesis***

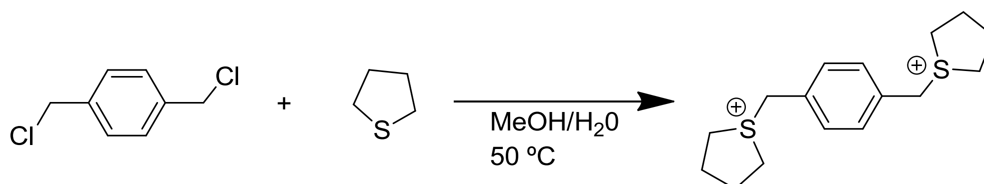


Scheme 2.6: Synthesis of bis-(sulfonium chloride) monomer.

PPV synthesis was adapted from literature-established procedures.[91] The starting material, α,α'-dichloro-*p*-xylylene (1 eq., 2.0 g, 9.8 mmol), was weighed into a 50 mL RBF with magnetic stirbar. A mixture of methanol and 4 v/v % water was added, and the reactor was charged with tetrahydrothiophene (>3 eq., 2.6 g, 29.5 mmol). The slurry was heated to 50 °C, and after *ca.* 30 minutes, the solution was homogenous and left to stir for 24 hrs. The reaction was concentrated in vacuo and precipitated into dried acetone. The product was filtered, washed 3x50 mL dry acetone, and dried on high vacuum to yield a white, crystalline solid (2.07 g, 52 %) (Note: solid extremely hygroscopic). Spectral data matched literature values.

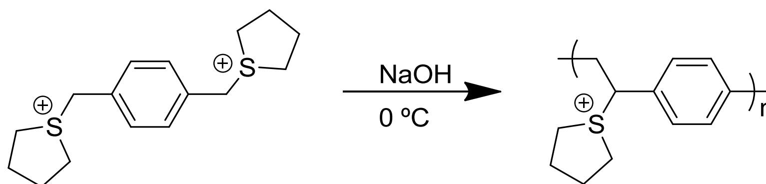


Scheme 2.7: Synthesis of PPV pre-polymer polyelectrolyte.

The monomer (1 eq., 1.5 g, 4.27 mmol) was dissolved in 12 mL methanol in a 50 mL RBF equipped with a rubber septum. The reactor was degassed by purging with dry nitrogen for 30 min., and the vessel was cooled to 0 °C. A 0.4 M solution of sodium hydroxide (10.7 mL) was added to the reaction mixture dropwise over 20 minutes to initiate the polymerization. After 2 hr., the polymerization was terminated by addition of 0.4 M HCl (2 mL). The contents of the reactor were transferred to a 12-14 kDa molecular weight cut-off (MWCO) Spectra/Por 2 dialysis membrane pouch and sequentially dialyzed against 3x2.5 L DI water for 24 hr, respectively. The dialyzed solution was concentrated en vacuo and immediately dissolved in methanol or water to prevent further elimination. The dried polymer's spectral data matched literature values.[96]

***Thin Film Preparation***

Wafers of XST-OMe were prepared according to aforementioned procedures. Films of PS-*b*-PTMSS were spin cast upon the XST layers at thickness *ca.* 1.3 L0 (which had shown success using ring-opening TC's) and baked at 110 °C to remove residual solvent. The PPV pre-polymer, dissolved in methanol, was directly spin cast atop the BCP film producing a slightly tacky film *ca.* 70 nm. The film stack was annealed at 200 °C in air for 10 min. to react the PPV TC, then subsequently annealed for 24 hrs. at 170 °C. The samples were etched for 140 s (RF power: 80 W, ICP power: 100 W, pressure: 90 mtorr, $O_2$ flow rate: 5 sccm) to break through the TC and etch into the BCP layer. Films were imaged by SEM and optical microscopy to study the resulting morphology and orientation behavior.

### 2.6.7 Hofmann Elimination Polymers

The majority of synthetic procedures for the small molecules and polymers of the Hofmann elimination TC were replicated or modified from literature references.[97-99] Characterization data, if not listed below, can also be found in these sources.

***(1S,4S)-5-(2-bromoethyl)bicyclo[2.2.1]hept-2-ene, 2.1***

A 250 mL steel Parr reactor vessel was equipped with a magnetic stirbar and charged with 4-bromobut-1-ene (1 eq., 150.5 g, 374 mmol), diclyclopentadiene (0.575 eq., 28.4 g, 215 mmol), 180 mL freshly dried toluene, and approximately 400 mg of hydroquinone inhibitor. A nitrogen stream was bubbled through the reactor using a steel needle for 30 min., then the lid was sealed and the reactor heated to 200 ºC in an oil bath. After 72 hrs., the reactor was slowly cooled to room temperature, and the contents transferred to a 250 mL RBF. The reaction mixture was concentrated in vacuo and the resulting oil was loaded onto a 1.5 inch silica gel plug. The plug was flushed with 2.5 L of hexanes, and the fractions were combined, concentrated, and distilled ( to yield **2.1** as a colorless oil (20.1 g, 27%, 3:1 mixture of isomers). BP = 35 ºC, 700 mtorr; $^{1}$H NMR (400 MHz; $CDCl_3$): (mixture of unresolved isomers) $^{13}$C NMR (101 MHz; $CDCl_3$): $\delta$ (ppm) = 137.55, 132.03, 49.50, 45.03, 42.44, 37.87, 37.39, 32.96, 31.68; HRMS (CI) M+H calc: 201.0279, found: 201.0273

***Bromoalkyl Norbornane Homopolymer, 2.2***

The bromoalkyl norbornene **2.1** (1 eq., 0.75 g, 3.7 mmol) was added to a 50 mL RBF equipped with a magnetic stirbar and rubber septum and the vessel was pump-purged three times with dry nitrogen. Ethyl acetate (EA) was prepared for the reaction by washing with $Na_2CO_3$ and brine, drying over $MgSO_4$, then distilling over $P_2O_5$ under inert gas. The dried EA was collected in a vessel containing molecular sieves, and was

bubbled with inert gas for 20 min. prior to use. A mixture of dry toluene and dry EA (17.5 mL, 5% v/v EA) was added to the reactor via syringe, and the contents were warmed to 40 ºC. The ($\eta^6$-toluene)Ni($C_6F_5$)$_2$ catalyst (0.015 eq., 27 mg, 0.056 mmol) was weighed in a 5 mL vial in a glove box, and capped with a rubber septa. The catalyst was dissolved in 1 mL dry EA, then quickly injected into the reactor to initiate the polymerization, forming a deep-orange colored solution. The reaction was quenched after 4 hrs. by injecting 0.3 mL of deionized water, leaving the reaction mixture a pale green color with some small black particulates. The polymer solution was filtered through a 0.22 µm disc filter, concentrated, re-dissolved in 10 mL THF, and precipitated in 125 mL methanol. The polymer was filtered, washed 3x10 mL methanol, and dried in vacuo to yield a white powder (0.491 g, 65%). The molecular weight was evaluated using a polystyrene standard ($M_n$ = 78 kDa, $M_w$ = 115 kDa, Đ = 1.47). $T_g$ = none, $T_d$ = 290 ºC. IR (cm$^{-1}$): 2934, 1449, 1259.

***Quaternary Ammonium Bromide TC, 2.3***

The bromoalkane homopolymer **2.2** (1 eq., 0.3 g, 1.5 mmol) was weighed into a 25 mL RBF equipped with a stirbar. The polymer was suspended in 10 mL of dimethylformamide, and a solution of 50 wt% aq. trimethylamine (5 eq., 0.44 g, 7.5 mmol) was added. The reactor was sealed with a rubber septum and stirred for 24. After 24 hrs., the polymer was fully in solution, but the mixture had a faint white hue. Approximately 2 mL of methanol was added to fully dissolve the reacted material, and the solution was stirred an additional 24 hrs. The reaction mixture was concentrated in vacuo, carefully avoiding heating, and then redissolved in 5 mL of methanol. The polymer solution was precipitated in 75 mL diethyl ether at 0 ºC, filtered, and dried to yield **2.3** as a white powder (0.33 g, 85%).

***Quaternary Ammonium Hydroxide TC, 2.4***

Amberlyst A-26 strongly basic ion exchange resin (10 mL) was prepared in a column by flushing through 2.5M NaOH until no precipitate was observed using a $AgNO_3/HNO_3$ test. The resin was then washed with deionized water until the pH was neutral, and the majority water of water was drained, while leaving the beads immersed. The water was slowly transitioned to methanol, with careful swishing to mitigate bead swelling. Once all water had been flushed from the system, the bromide salt **2.3** (0.35 g) was dissolved in 1 mL of methanol and added to the top of the column. The solution was drained through the column, continuously adding methanol on top of the column to maintain headspace. The methanol solution was collected until the pH returned to neutral, and the combined fractions were concentrated in vacuo and precipitated in diethyl ether at 0 ºC. The hydroxide polymer salt **2.4** was isolated and dried to yield a beige solid powder (0.24 g, 90%). IR ($cm^{-1}$): 3387, 3028, 2942, 1618, 1380.

# Chapter 3: Organosilicon Block Copolymers

The implementation of high-$\chi$ BCPs is necessary to extend the resolution limit and improve the pattern quality of self-assembled materials for lithography. However, the utility of block copolymers for patterning applications relies on their ability to transfer a BCP pattern into an underlying substrate. Etch selectivity between domains is required to generate high aspect ratio topography suitable for pattern transfer using traditional reactive-ion etch (RIE) processing. Organosilicon polymers and silicon additives have been extensively studied for microelectronic applications as resist films, in part because the materials form etch-resistant barriers during exposure to oxidizing plasmas.[6,100] Organosilicon BCPs are thus an attractive target because they have inherent characteristics ideal for patterning applications. Silicon[101,102] (and other heteroatoms[103,104]) can be selectively incorporated into BCP domains (*i.e.* non-covalent segregation) to impart etch selectivity, but covalent incorporation improves the simplicity of the process and reduces the need for additional processing steps. For example, organosilicon polymers such as poly(dimethylsiloxane) (PDMS),[105] poly(oligomeric silesquioxane) (POSS),[106] and poly(ferrocenyl dimethylsilane) (PFS)[107] have been synthesized in BCP architectures, but these materials have preclusive drawbacks for patterning. PDMS has a high silicon content (37.9 wt%), but also an extremely low $T_g$ (-127 ºC),[108] making structural integrity, pattern transfer, and defectivity a challenge. POSS polymers also have a high silicon content (≈ 30-40 wt%), but the unusually large hydrodynamic volume of the POSS cage skews the BCP phase diagram and makes synthesis challenging. PFS has produced high-$\chi$ materials, but its ability to crystallize is potentially disruptive for processing and metal incorporation is a concern for microelectronic devices. These challenges necessitate the development of novel high-$\chi$

organosilicon BCPs that have the capability to improve several performance characteristics ideal for patterning. These include: higher $\chi$ to enhance the minimum resolvable microphase-separated structures; directly patternable, inherently etch-resistance domains; and domain orientation control through the use of surface neutralization techniques discussed in Chapter 2.

The strategy employed herein relies primarily on styrenic derivatives as a framework for BCP components. Styrenic polymers have been well studied for controlled, anionic polymerization mechanisms[109,110] and produce relatively high-$T_g$ polymers suitable for mechanically robust nanostructures. The $\chi$ of the system can be modified by introducing high and low surface energy components, and the etch properties can be controlled by the polymer's silicon content. The synthesis, characterization, and processing of several organosilicon BCPs for lithographic applications are described in detail in the following sections. Subscripts appending the names of BCPs will refer to the nominal pitch of the ordered polymer (*e.g.* PS-*b*-PTMSS$_{XX\ nm}$). The $\chi$ estimations of the organosilicon BCPs as well as their relevant disordered-state scattering and rheological data are found in Chapter 4. In addition, Chapter 4 details the thin film processing and lithographic performance analysis for each material.

Many tables and figures of this chapter are reprinted with permission from Durand et al.[36] and are cited where appropriate.

## 3.1 Etch Performance

The organosilicon domain of the BCP confers a high etch selectivity relative to organic domains by the nature of the etch plasma chemistry. In principle, the etch reaction produces gaseous by-products for the organic domain (*e.g.* $CO_2$ and $H_2O$), which

can be pumped away. In contrast, the organosilicon domain is transformed into an inert refractory solid (*e.g.* $SiO_x$). The latent nanostructures of a BCP can thereby be transformed into topographical patterns by exposure to selective plasmas. The reactive-ion etch (RIE) process begins by generation of a plasma using a strong radio frequency electromagnetic field. The ionized gas molecules can be accelerated towards a planar electrode using a DC bias, and the ions chemically react with or physically sputter away the sample on the electrode. In addition to the ions, active radicals and high energy UV light are generated in the reaction chamber, which can also potentially interact with materials. The RIE process is complicated and has a large variable space, yet optimization of the step is critical for effective pattern development. Several etch process experiments were performed with the materials used for the present BCPs, both on academic and industrial RIE equipment, to test the efficacy of the plasma chemistry and importance of silicon content. None of the etch chemistry is fundamentally new, but the implications of the performance for BCP design is particularly valuable. Two different chemistries were investigated: an oxygen-rich plasma and a reducing $N_2/H_2$ plasma. These formulations, while chemically distinct, have only subtle performance differences. An investigation into their respective mechanisms has only recently been explored and is discussed in the following sections. Additional information on the development of etch formulas for organosilicon BCPs can be found in experimental studies by C.M. Bates.[76]

### 3.1.1 $O_2$ Plasma Etching

The relationship between etching characteristics and silicon content for organosilicon polymers has been well-studied for an oxygen reactive-ion etch ($O_2$-RIE).[40,111,112] A protective layer of $SiO_2$ forms, which has a high resistance against $O_2$-RIE, at the surface of films exposed to the plasma. The selectivity of the etch barrier

relative to organic domains increases to greater than 10:1 for formulations with silicon weight percent greater than 11%.[113] This is significantly better than all-organic BCPs such as PS-*b*-PMMA, which generally have low etch selectivity[114,115] (*ca.* 3:1, although recent reports have shown selectivity as high as 7:1 for more complex process conditions[116]). A relatively simple etch study was performed on the components investigated for BCPs herein to compare the performance of the materials as a function of their silicon content (Fig. 3.1).

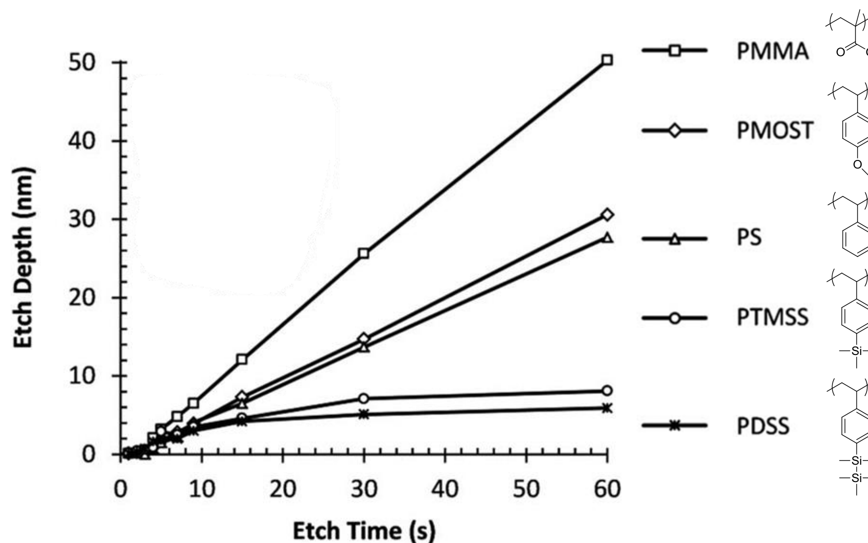


Figure 3.1: Etch depth of homopolymer films subjected to an $O_2$-RIE.[36]

Table 3.1: Calculated Ohnishi parameters for the all-organic homopolymers.

| Polymer | Ohnishi Parameter |
|---|---|
| PMMA | 5.0 |
| PMOST | 2.5 |
| PS | 2.0 |

Samples of the homopolymers were subjected to an $O_2$-RIE, and the post-etch thickness change was recorded. The all-organic samples (*e.g.* PMMA, PMOST, and PS)

show relatively constant etch rates (*i.e.* linear profiles) at all etch times. These polymers are continuously subject to both physical and chemical removal because no etch barrier is generated. Changes in the etch rates are qualitatively consistent with the calculated Ohnishi parameter[117] (Table 3.1), an empirically discovered factor that correlates the chemical structure and RIE rate. The oxygenated and aliphatic components (higher Ohnishi parameter) etch slightly faster than the aromatic counterparts (lower Ohnishi parameter). The difference in etch rates between organic components demonstrates the inferior etch rate selectivity seen between conventional polymers like PMMA and PS (≈1.8:1). In contrast, the etch selectivity dramatically increases (> 8:1) upon the introduction of silicon functional groups. PTMSS (16 wt.% silicon) and PDSS (24 wt.% silicon) both develop an etch barrier within several seconds and the etch rate subsequently slows to much less than 1 nm/s. The profiles are consistent with kinetic studies suggesting a transient period is necessary to fully develop the etch barrier.[40] After the barrier has formed, a steady-state period occurs, dependent on the sputtering rate of the RIE plasma. In the absence of sputtering, the steady-state period has a theoretical etch rate of zero (*i.e.* chemically inert). Although there is little difference between the steady-state sputter rates of PTMSS and PDSS, the transient period is shorter for PDSS, resulting in a smaller etch depth for extended process times. While the difference between the PTMSS and PDSS steady-state etch depth is relatively small (*ca.* 2 nm), the implications can be significant for smaller BCP domains (*i.e.* thinner etch barrier). For BCPs with dimensions below 10 nm, the details of the etch barrier formation become increasingly important, as loss of a few nanometers of material constitutes a significant portion of the total thickness of the organosilicon domain. Furthermore, pattern transfer into the substrate is limited by the thickness of the mask and its corresponding sputter rate.[118] For example, when using parallel-oriented cylinders for lithographic applications, the initial

film thickness is limited to ≈1 period in thickness. This increases the difficulty of producing high aspect ratio developed features because barrier formation requires a transient period and is subsequently sputtered away during pattern transfer. This emphasizes the need to utilize perpendicularly-oriented lamellae and cylinders for patterning, because thickness can be much greater than $1L_0$, thus producing high aspect ratio structures.

### 3.1.2 $N_2/H_2$ Plasma Etching

When perpendicularly-oriented organosilicon BCP samples were subjected to an oxidizing RIE ($CO_2$ gas) to transfer the latent pattern using commercial equipment, it was discovered that significant bowing occurred, likely due to the low pressures required for the process (Fig. 3.2a). A novel reducing chemistry comprised of nitrogen and hydrogen gas mixtures was discovered that operates at higher pressures, which could reduce sputtering effects and mitigate the bowing issues (Fig. 3.2b). A vertical profile was achieved by first applying the oxidizing RIE to presumably form an $SiO_2$ etch barrier, then switching to the $N_2/H_2$ recipe to anisotropically etch away the organic domain. It was surmised that the oxidizing RIE was required to form an etch barrier, but subsequent experiments showed that a similar relief image could be fabricated by using *only* a $N_2/H_2$ etch.

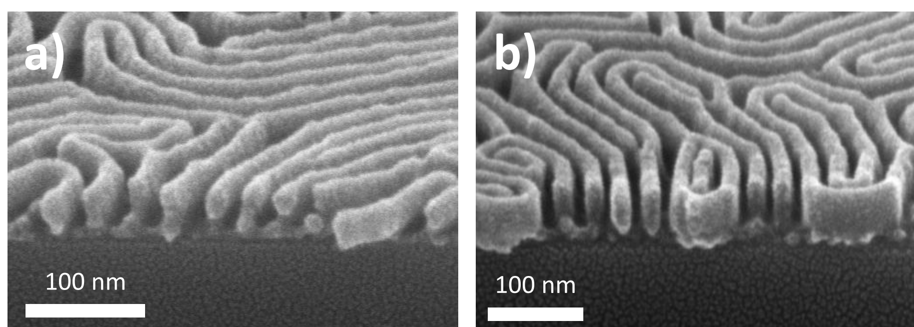


Figure 3.2: (a) A bowed organosilicon BCP profile after an oxidizing etch. (b) A straight BCP profile obtained after a short oxidizing etch followed by a reducing $N_2/H_2$ etch to transfer the pattern. Images courtesy of Steve Sirard, Lam Research Corporation.[119]

Lyman-Werner photons,[120] which are high energy ultraviolet (VUV) energy transitions of molecular hydrogen, were hypothesized to be responsible for some of the etch characteristics. Hydrocarbon polymers are known to absorb VUV irradiation and either transfer the photoexcitation energy thermally via fluorescence or by cross-linking.[121] Organosilicon materials can also absorb VUV irradiation, but have been shown to photolyze.[122,123] Therefore, studies were performed in collaboration with the Graves Research Group at Cal Berkeley and Lam Research Corporation to understand how a $N_2/H_2$ RIE can form an etch barrier layer for an organosilicon BCP. Several organosilicon homopolymers (PTMSS and PDSS) and random copolymers (PS-*r*-PDSS) were synthesized to test the etch characteristics as a function of silicon content. Films of the polymers were subjected to a $N_2/H_2$ plasma and the effects of UV/VUV light, directed ions, and radicals were individually characterized using transparent windows and custom wafer configurations (Fig. 3.3).

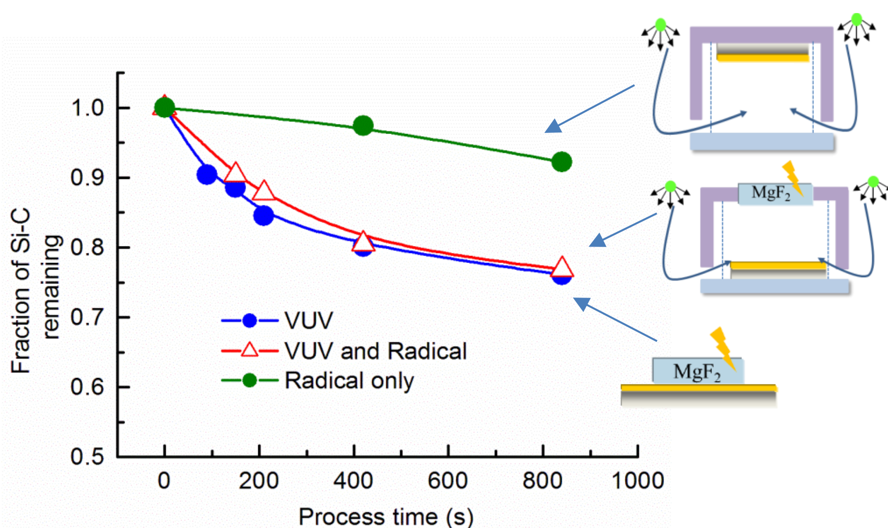


Figure 3.3: Isolated effects of $N_2/H_2$ plasma components on a PDSS homopolymer sample as characterized by the Si-C FTIR signal.[119]

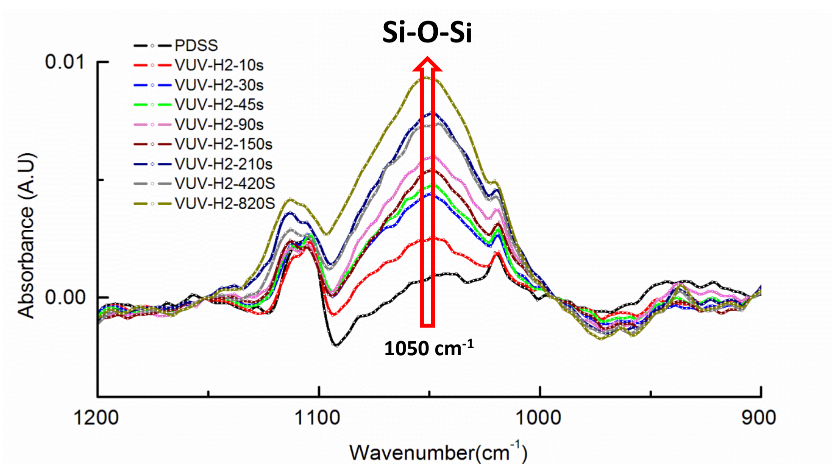


Figure 3.4: FTIR spectra of Si-O-Si bond region for PDSS film before and after VUV exposure.[119]

Radicals were isolated from the plasma by mounting a PDSS sample film upside-down, allowing diffusion of reactive species through a wire structure. Almost no change in the Si-C FTIR transition is seen when exposed to radicals only. If the sample is instead exposed through a $MgF_2$ window, which allows VUV photons to pass through but not

radicals, the Si-C signal immediately decays over time. Similarly, addition of background radicals to a sample exposed through a window (both VUV and radicals) shows nearly identical results. These data show that the pendant Si-C bonds are being photolyzed by the VUV exposure, but are relatively inert to the radical components. The Si-C or Si-Si bond scission can potentially result in cross-linked substances or produce gaseous by-products,[124,125] thereby producing an insoluble inorganic network that could act as an etch barrier. Strangely, the post-$N_2/H_2$ RIE films show evidence of Si-O-Si character by FTIR (Fig. 3.4). Films exposed to VUV irradiation for longer process times see an increase of the Si-O-Si signal at 1050 $cm^{-1}$.The formation of these bonds corresponds to oxidation of the organosilicon material, but no oxygen is present in the etch formula. Therefore, it is believed that the dangling silicon bonds induced by VUV photolysis lead to $SiO_x$ formation either by trace oxygen in the etch chamber or atmospheric exposure after the process, although the exact origin of the oxygen source is still unclear.

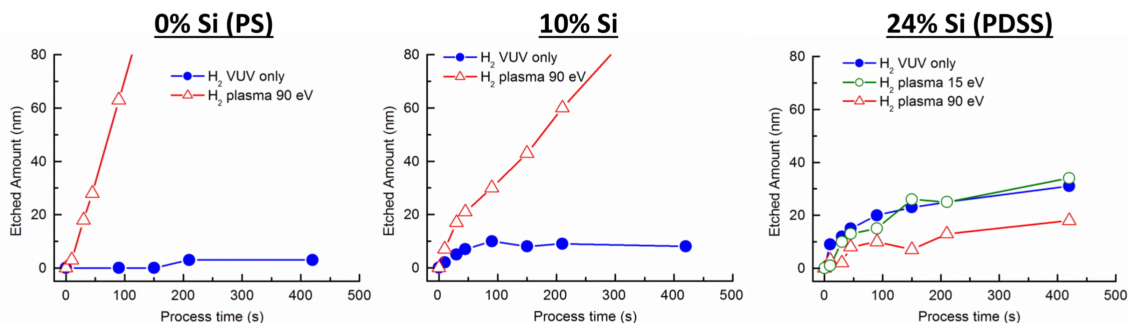


Figure 3.5: Comparison of etch profiles of homopolymer films subjected to plasma/VUV exposure as a function of silicon content.[119]

The homopolymer's response to VUV irradiation and plasma is highly dependent on the silicon content (Fig. 3.5). For 0 wt.% silicon (PS), VUV irradiation causes almost no thickness loss. Accordingly, only cross-linking reactions are likely to occur for the

fully organic material. In contrast, an identical sample exposed to a hydrogen RIE with a 90 eV bias was readily removed, seen by a steep etch profile. For a sample with a higher silicon content, such as PS-*r*-PDSS (10 wt.% Si), the VUV exposure causes several nanometers to be etched away during a transient period, presumably due to volatile by-product outgassing of the silicon component. The plasma exposed sample has a reduced etch rate relative to PS, with two linear regimes indicative of a transient phase followed by sputtered removal of the etch mask. The highest silicon-content polymer, PDSS (24 wt.%), shows similar etch profiles for all process conditions. The VUV only exposure resulted in the highest film loss compared to the lower silicon-content polymers, demonstrating that the primary mechanism for film thickness reduction is removal of Si-C and Si-Si components. Interestingly, the plasma exposure condition at 90 eV had less etch barrier removed than the VUV only condition, indicating that the addition of ion and radical sources can induce cross-linking or other reactions that more quickly stabilize the etch barrier layer of high silicon-content materials. To further illustrate this effect, a lower bias was applied to the plasma (15 eV), and the etch profile more closely resembled the VUV curve. This counterintuitive result indicates that higher plasma biases may be more beneficial for the formation of $SiO_x$ etch masks by limiting the outgassing of photolysis products.

### 3.2 POLY(STYRENE-*BLOCK*-4-TRIMETHYLSILYLSTYRENE)

The organosilicon polymer used as the primary test vehicle for top coat and other thin films studies was poly(styrene-*block*-4-trimethylsilylstyrene) (PS-*b*-PTMSS). Although initial investigations focused on an ABA triblock architechture, (as it has been reported that triblocks are slightly more favorable to form perpendicularly oriented

structures[79,81] and better accommodate pre-pattern mismatch[126] compared to similar AB diblocks) it has more recently been shown that AB diblock polymers perform satisfactorily when appropriate neutral interfaces are chosen.[36,67] Diblock polymers can be less synthetically challenging to produce, as they can use commercially available initiators (*e.g.* *sec*-butyllithium (*sec*-BuLi)) as opposed to more complicated *in situ* prepared bis-functional initiators (*e.g.* potassium napthalenide/α-methylstyrene oligomer[127]). Two symmetric ($f_A$ = 0.5), PS-*b*-PTMSS AB diblock polymers were targeted: an ordered sample which exhibits an order-disorder transition (ODT), and a disordered sample to be used for $\chi$ estimation using the scattering method (see Section 4.2). An ODT sample effectively represents the resolution limit of a given BCP material, but can also be used to evaluate the material's $\chi$ parameter (see Section 4.1).

The diblock copolymers of PS-*b*-PTMSS were synthesized from styrene and 4-trimethylsilylstyrene using controlled anionic polymerization procedures (a detailed description of the custom glassware used for the purifications and polymerizations can be found in the dissertation of J.R. Strahan (note: the flasks and distillation equipment have been recently modified to incorporate additional safety precautions and enhancements for high-boiling monomers (see Appendix A)).[128]. TMSS monomer was prepared from a Grignard reaction with 4-chlorostyrene and trimethylsilylchloride (Scheme 3.1), and the monomers were purified by multiple distillations over di-*n*-butyllithium (*n*-BuLi). After purification, the air- and water-free monomers were considered ready for polymerization. Targeted polymer molecular weight was modulated by varying the monomer/initiator ratio when setting up the reaction. Initiator (*sec*-BuLi) was added to -78 ºC tetrahydrofuran (THF), and the polymerization was initiated by addition of purified styrene (Scheme 3.2), forming a bright orange solution. After complete polymerization, the second block was grown by addition of 4-trimethylsilylstyrene, producing a bright red

color. The living BCP chain end was quenched by the addition of degassed methanol, and the polymers were isolated by precipitation and analyzed.

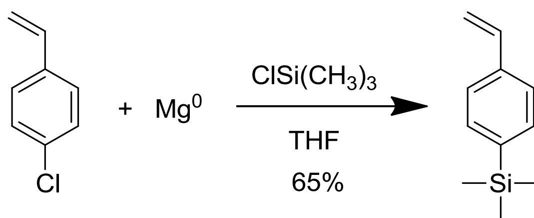


Scheme 3.1: Synthesis of TMSS monomer.

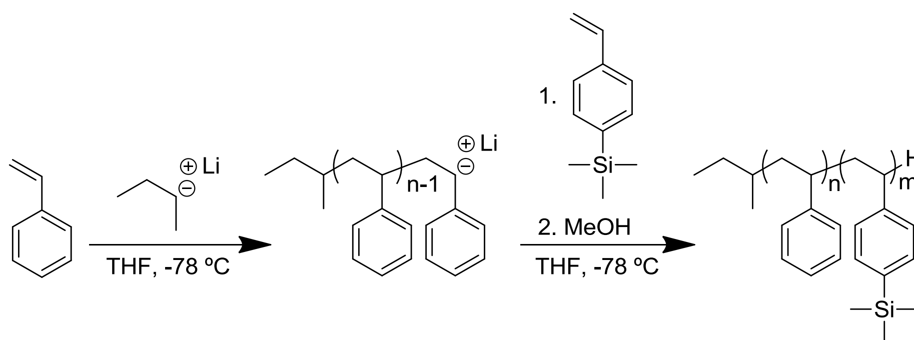


Scheme 3.2: Anionic synthesis of PS-*b*-PTMSS.

The PS-*b*-PTMSS polymers were synthesized at two molecular weights to target an ordered and disordered sample. The resulting polymers were characterized by size-exclusion chromatography (SEC) to show successful production of the BCP (Fig. 3.6). The PS aliquots (blue) shift from higher retention volumes (lower molecular weight) to lower retention volumes (higher molecular weight), indicating complete conversion to the BCP (red) upon addition of TMSS. All chromatograms show narrow, mono-modal distributions, signifying the polymerization was living and controlled with no side reactions.

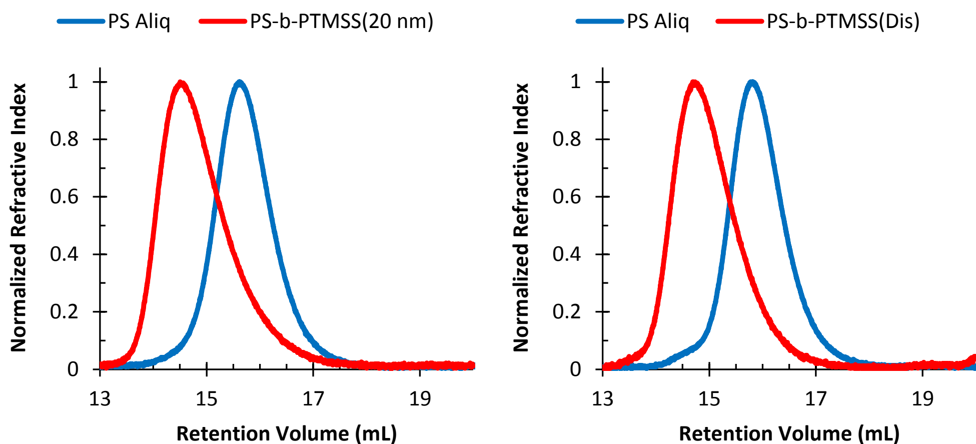


Figure 3.6: SEC refractive index traces of the PS-*b*-PTMSS BCPs synthesized for study and their respective homopolymer aliquots.[36]

The polymers were also characterized by matrix-assisted laser desorption/ionization (MALDI) to obtain accurate molecular weight information. The PS aliquots (Fig. 3.7) show monomodal distributions with a peak spacing of *ca.* 104-105 m/z, corresponding to the molar mass of the repeat unit, styrene (104.15 g/mol). The BCP MALDI spectra (Fig. 3.8) also show monomodal distributions, but with poorly defined molecular ion spacing. This feature is indicative of block copolymers, as the coupling between distributions of two unique monomer molecular weights will essentially produce a continuous spectrum of molecular ions.

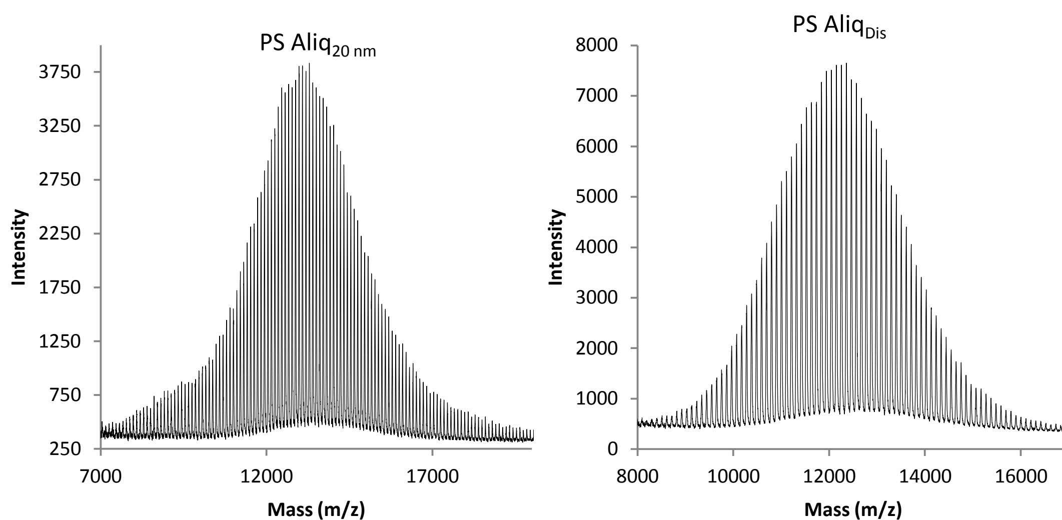


Figure 3.7: MALDI spectra of PS homopolymer aliquots.[36]

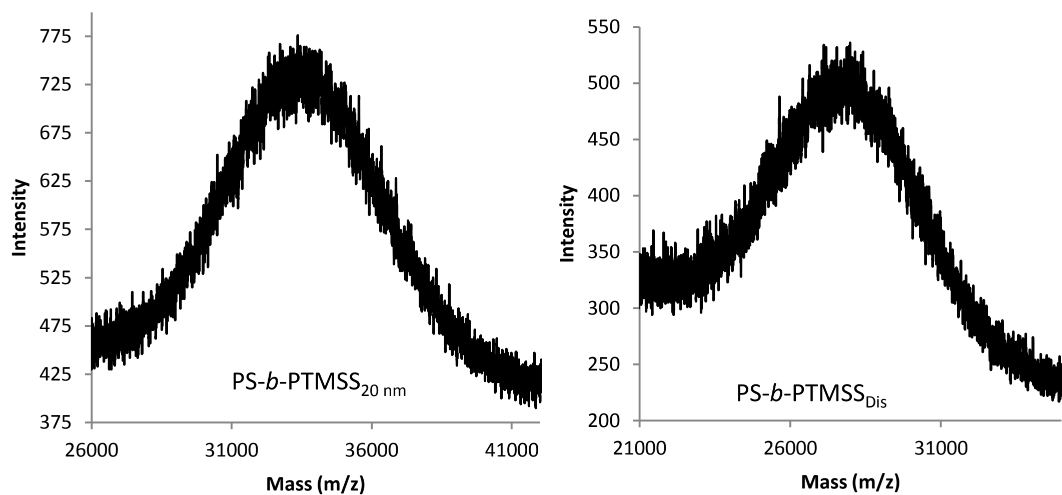


Figure 3.8: MALDI spectra of PS-*b*-PTMSS BCPs.[36]

A summary of the characterization data for the PS-*b*-PTMSS polymers is found in Table 3.2. The periodicity $L_0$ was verified using top-down SEM after annealing and etching a sample in thin film to give the best representation of the domain size for lithographic applications. The polymers both show a narrow dispersity and the volume

fractions are close to the targeted 50:50 ratio, suggesting that a lamellar morphology will form for the ordered sample. The $M_n$ of the BCP was not calculated from the MALDI spectrum in Fig. 3.8, but instead by the mol ratio determined by $^1$H-NMR and the $M_n$ of the first block. In a control experiment, it was independently estimated that the error in the molecular ion mass was approximately 5% based on sampling of PS homopolymer SEC standards. Therefore, to mitigate these errors, the $M_{n,A}$ of the lower molecular weight aliquot was used to evaluate the BCP. The decomposition temperature $T_d$, measured in a nitrogen atmosphere, is relatively high (*ca.* 370 ºC) and suggests the polymers will be stable during thermal annealing processes at elevated temperatures.

Table 3.2: Polymer characterization data.

| **Polymer** | $L_0$ [a] | $M_{n,A}$ [b] | $Đ_A$ [c] | $M_{n,BCP}$ [d] | $Đ_{BCP}$ [c] | $f_A$ [e] | $T_g$ [f] | $T_d$ [f] |
|---|---|---|---|---|---|---|---|---|
| PS-*b*-PTMSS$_{20\ nm}$ | 19.8 | 13.3 | 1.05 | 33.0 | 1.06 | 0.470 | 100/102 | 370 |
| PS-*b*-PTMSS$_{Dis}$ | (16.8) | 12.3 | 1.04 | 27.8 | 1.04 | 0.478 | 100/102 | 370 |

[a] Lamellae periodicity $L_0$ in nm, determined by top-down SEM. Values in parenthesis represent disordered samples calculated by SAXS at 200 ºC.
[b] $M_n$ in kDa of the first block, determined by MALDI.
[c] Dispersity index $Đ$, determined by SEC.
[d] $M_n$ in kDa of the BCP, determined by $M_{n,A}$ and $^1$H-NMR.
[e] Volume fraction $f_A$ of the first block, determined by $^1$H-NMR and the density of the respective homopolymers. Density was measured according to Archimedes' principle (see Chapter 4).
[f] $T_g$ and $T_d$ in ºC, measured by DSC/TGA.

A bulk sample of the ordered PS-*b*-PTMSS was prepared for small-angle x-ray scattering (SAXS) by melting the polymer powder at 180 ºC in air. The scattering profile shows a strong primary scattering peak corresponding to a periodicity of 18.9 nm, corroborating the $L_0$ measured by SEM (note: the SAXS periodicity has been observed to be consistently 1-2 nm lower than that determined by SEM). The higher order scattering peaks ($nq^*$) expected for lamellar morphology are extremely weak if evident at all, but

the thin film behavior (*i.e.* island/hole and top down SEM images) is consistent with lamellar structure and is corroborated by the calculated volume fraction.

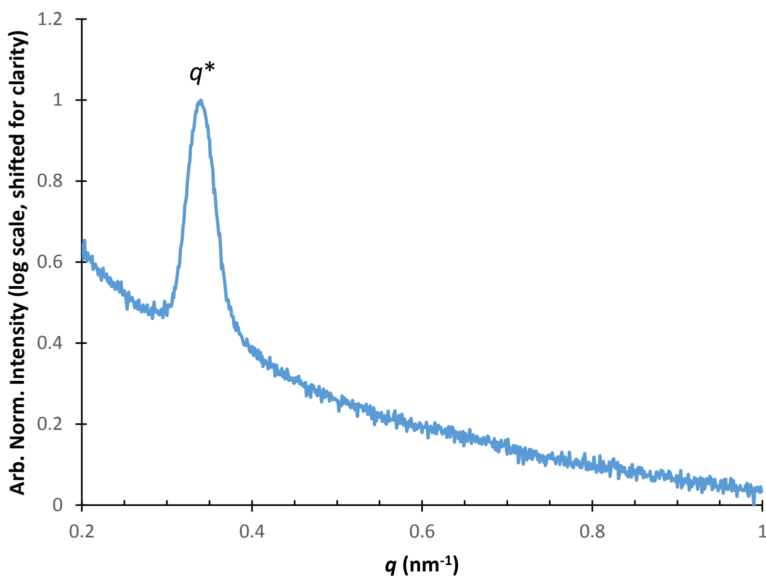


Figure 3.9: SAXS profile of ordered PS-*b*-PTMSS$_{20\ nm}$.[36]

The neutral top and bottom interface materials identified for the BCPs are documented in the experimental section. Analysis of the PS-*b*-PTMSS polymer behavior in thin films and characterization of the $\chi$ parameter is discussed in Chapter 4.

### 3.3 Poly(trimethylsilylstyrene-*block*-4-methyl methacrylate)

Substitution of the styrene block from PS-*b*-PTMSS to methyl methacrylate (MMA) was hypothesized to yield an ideal target for a novel organosilicon BCP. Block copolymers comprising MMA have been demonstrated to form high-$\chi$ materials with periodicities below 10 nm, albeit with unexplored etch selectivity.[37,129] Intuitively, because MMA is more hydrophilic relative to styrene (and TMSS), it was speculated that

polymerization with TMSS would produce a high-$\chi$ material with an etch resistant domain. In addition, the microelectronic industry has familiarity with methacrylates as electron-beam resists,[6] thus processing of such materials for patterning applications has been established.

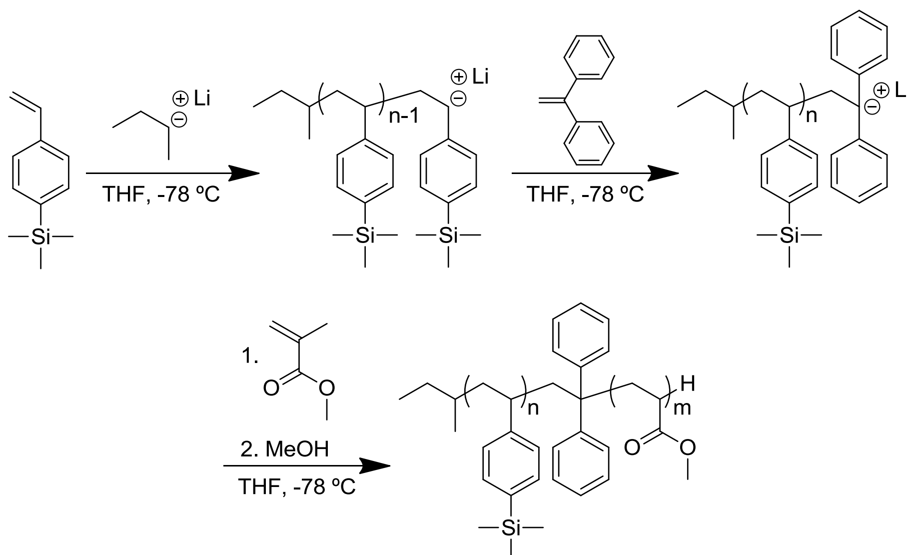


Scheme 3.3: Anionic synthesis of PTMSS-*b*-PMMA.

PTMSS-*b*-PMMA was synthesized anionically using several established procedures (Scheme 3.3).[76,130,131] TMSS, purified over *n*-BuLi, was initiated using *sec*-BuLi to grow the first block. Diphenylethylene (DPE) is then added to the living polymer as a transfer agent to reduce the basicity of the anion for initiation of the methacrylate. Only a single addition of DPE occurs due to its steric bulk. MMA, purified sequentially over calcium hydride and trioctylaluminum, was added to the end-capped PTMSS to grow the second block before being quenched with degassed methanol.

Table 3.3: Polymer characterization data.

| Polymer | $L_0$ [a] | $M_{n,A}$ [b] | $Đ_A$ [b] | $M_{n,BCP}$ [b] | $Đ_{BCP}$ [b] | $f_A$ [c] | $T_g$ [f] | $T_d$ [f] |
|---|---|---|---|---|---|---|---|---|
| PTMSS-*b*-PMMA$_{31\ nm}$ | 30.6 | 18.6 | 1.04 | 33.6 | 1.03 | 0.45 | 102/105 | 343 |

[a] Lamellae periodicity $L_0$ in nm, determined by SAXS.
[b] $M_n$ in kDa of the first block, determined by SEC relative to a PS standard, dn/dC = 0.138.
[c] Volume fraction $f_A$ of the first block, determined by ^{1}H-NMR and the density of the respective homopolymers. Density was measured according to Archimedes' principle (see Chapter 4).
[d] $T_g$ and $T_d$ in °C, measured by DSC/TGA.

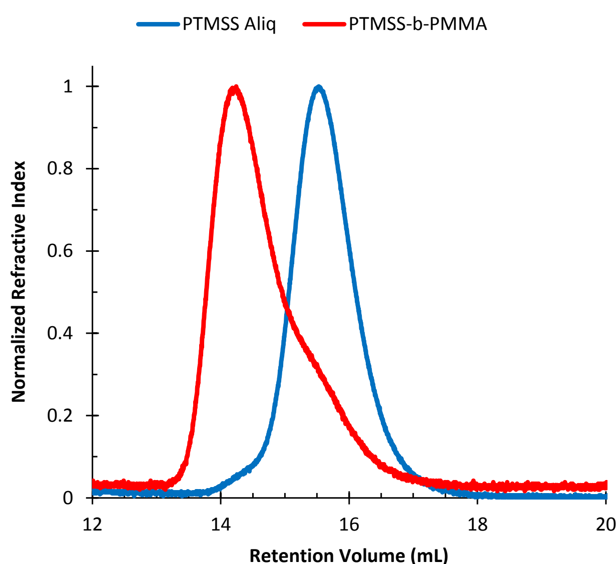


Figure 3.10: SEC refractive index traces of the PTMSS-*b*-PMMA$_{31\ nm}$ BCP synthesized for study and the respective homopolymer aliquot.

A sample of PTMSS-*b*-PMMA was characterized to assess the potential for thin film applications. The SEC refractive index trace of the PTMSS homopolymer shows a distinct shift in retention volume towards higher molecular weight after growth of the PMMA block, signifying the successful formation of the block copolymer (Fig. 3.10). A small shoulder evident on the BCP trace (red) matches the retention time of the PTMSS aliquot, indicating a small amount of homopolymer was likely terminated upon addition of the MMA monomer. Nevertheless, the BCP shows a low dispersity and controlled molecular weight distribution (Table 3.3), suggesting that anionic polymerization is

suitable for the production of PTMSS-*b*-PMMA materials. The volume fraction $f_A$ of the TMSS block was measured to be 0.45, indicating a near-symmetric ratio.

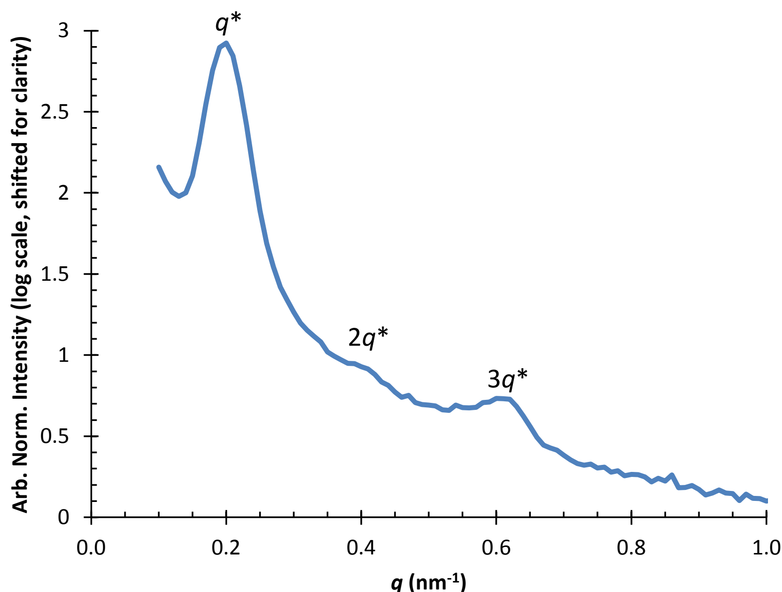


Figure 3.11: SAXS profile of ordered PTMSS-*b*-$PMMA_{31\ nm}$.

The SAXS profile of a bulk PTMSS-*b*-$PMMA_{31\ nm}$ sample shows higher order reflections consistent with a lamellar morphology. The $2q^*$ peak has a lower intensity relative to the $3q^*$, indicative of near-symmetric domains. The primary scattering $q^*$ peak is located at 0.205 $nm^{-1}$, corresponding to a lamellar periodicity of 30.6 nm.

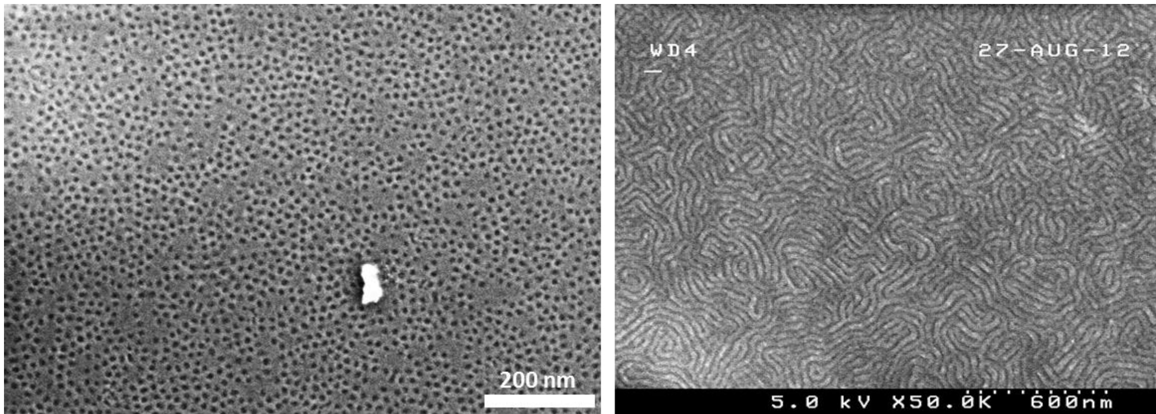


Figure 3.12: SEM images of PTMSS-*b*-PMMA$_{31\ nm}$ showing perforated-like structures when confined between a neutral XST and ring-opening TC (left) versus perpendicular assembly when confined between two neutral XSTs (substrate and floated film).

The PTMSS-*b*-PMMA$_{31\ nm}$ BCP was evaluated in thin films to assess the ability to control the domain orientation as a function of XST and TC surface energy. XSTs were assessed via the island/hole wetting methodology (see Section 2.1) to determine a composition that provided a neutral substrate interface. For PTMSS-*b*-PMMA, a neutral XST was produced by copolymerizing TMSS and MMA to yield a material comprising the same components of the BCP (Fig. 2.6). Although an organosilicon XST is not ideal for pattern transfer processes, the concept established the first proof-of-principle for production of a neutral interface for a high-$\chi$ material. However, even with the use of a neutral substrate interface, a screening of TCs yielded only perforated-like morphologies by thermal annealing (Fig. 3.12, left), colloquially referred to as "Durand Dots". At the time, the TCs (comprised of 4-trifluoromethylstyrene ($CF_3$-Sty)) resulting in perforated lamellae were the most hydrophobic (*i.e.* low surface energy) materials available. Therefore, it was assumed unlikely that any material could produce a neutral TC interface suitable for PTMSS-*b*-PMMA (as is discussed below, it was also discovered that TC materials could not be evaluated by confined island/hole methodology for PTMSS-*b*-

PMMA, therefore analysis of wetting preference was obscured). As a control experiment, the neutral XST material (comprised of TMSS and MMA), was floated onto the PTMSS-*b*-PMMA top interface to effectively confine the BCP between two verifiable neutral materials. After thermal annealing, the XST layer was removed using a fluorine-based RIE to expose the underlying BCP (Fig. 3.12, right). The film shows evidence of perpendicularly-oriented lamellae, suggesting that the appearance of perforated structures is indicative of poor top surface energy neutralization.

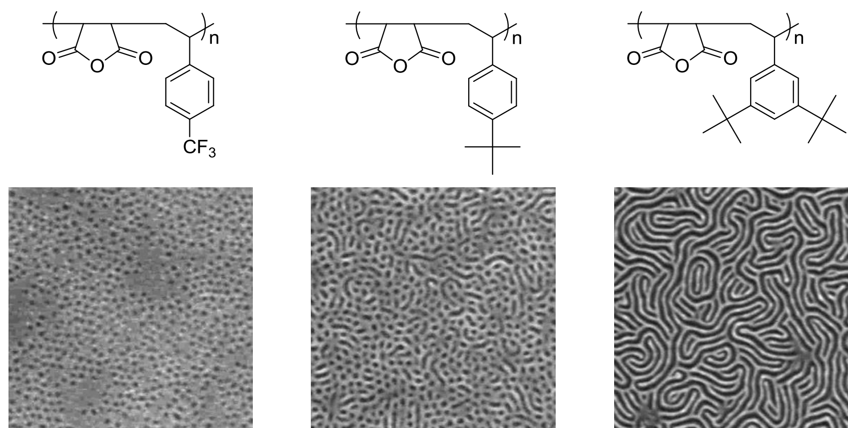


Figure 3.13: Top coat substituent effects (*i.e.* surface energy) on the orientation of PTMSS-*b*-PMMA$_{31\ nm}$.

Alternative top coat moieties were pursued to empirically evaluate the TC surface energy structure-property relationship and consequently the PTMSS-*b*-PMMA orientation behavior. Alternating copolymers of styrenic derivatives and maleic anhydride (2$^{nd}$ Gen. ring-opening TCs) were modified to enhance the hydrophobicity of the "conventional" $CF_3$-Sty materials. As shown in Fig. 3.13, the use of a hydrophobic, bulky *tert*-butyl moiety in the TC improves the thin film assembly of the PTMSS-*b*-PMMA. Although perforated "dots" are still evident, several low correlation length "worm-like" structures reminiscent of perpendicular lamellae are also observed. This

transition indicates that an alternative, more hydrophobic moiety is necessary to induce the perpendicular lamellar morphology. Appending an additional *tert*-butyl moiety to the TC, such as with 3,5-di-*tert*-butylstyrene (di-tBuS) (Fig. 3.13, right), improves the assembly further, resulting in nearly defect-free perpendicular lamellae.

The results shown in Fig. 3.13 confirm that a modified, low surface energy TC material is necessary to induce perpendicular orientation for PTMSS-*b*-PMMA. The di-tBuS TC series is the most hydrophobic TC polymer synthesized (inferred from non-MMA BCP wetting results), thus it is presumed that the alternating copolymer of maleic anhydride and di-tBuS is the closest material to a theoretically neutral interface that can currently be accessed. To complicate these matters, PTMSS-*b*-PMMA has not been demonstrated to show island/hole structures using the confined TC wetting test (see Section 2.1.3), thus neutrality cannot be probed directly. Due to the above considerations, PTMSS-*b*-PMMA was abandoned as a candidate for patternable, organosilicon high-$\chi$ materials. Further research is required to understand the physical properties that govern the formation of confined island/hole topography to enable a thorough evaluation of the process conditions suitable for PTMSS-*b*-PMMA orientation control.

### 3.4 POLY(4-METHOXYSTYRENE-*BLOCK*-4-TRIMETHYLSILYLSTYRENE)

The first organosilicon BCP investigated, PS-*b*-PTMSS, succeeded in improving the etch selectivity relative to the more conventional material PS-*b*-PMMA, but the minimum attainable feature size for both polymers (related to their respective $\chi$-values, Chapter 4) are approximately the same. It was hypothesized that appending polar moieties (*i.e.* methoxy, hydroxyl, halogen, etc.) to the relatively *more polar* block (PS) of PS-*b*-PTMSS would enhance the chemical dissimilarity between the components and

increase $\chi$. A commercially available monomer, 4-methoxystyrene (MOST), has been anionically polymerized by other researchers[109] and was therefore an ideal target to test the hypothesized structure-property relationship of $\chi$. Three symmetric diblock PMOST-*b*-PTMSS polymers were targeted for polymerization: an ordered 20 nm $L_0$ sample (comparable to the 20 nm $L_0$ PS-*b*-PTMSS), a sample possessing an ODT, and a disordered sample for scattering experiments.

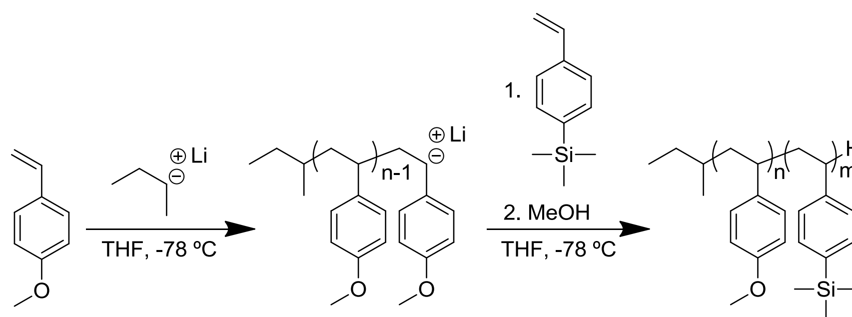


Scheme 3.4: Anionic synthesis of PMOST-*b*-PTMSS.

Commercially received MOST was purified over BuLi to produce a monomer suitable for anionic polymerization. The targeted polymer molecular weights were modulated by varying the monomer/initiator ratio when setting up the reaction, and the polymerization was initiated using *sec*-BuLi in THF at -78 ºC to produce a bright yellow solution (Scheme 3.4). A subsequent injection of TMSS grew the second block, and the reaction was quenched with degassed methanol to produce PMOST-*b*-PTMSS. The polymers were isolated via precipitation and then characterized to evaluate their properties.

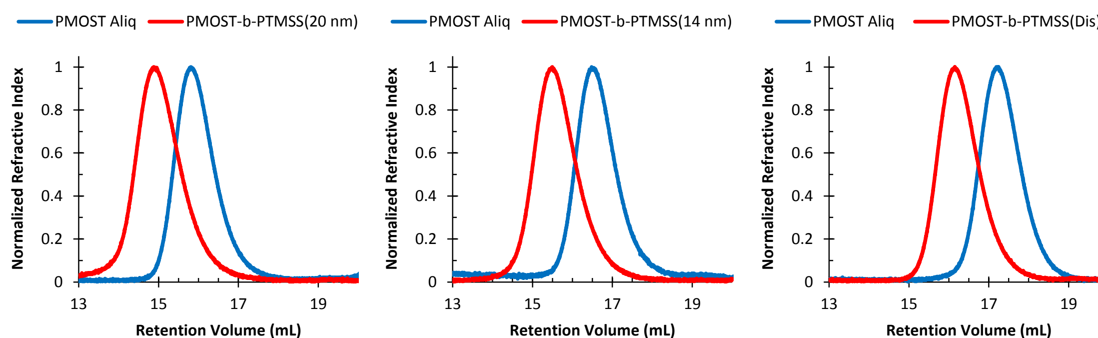


Figure 3.14: SEC refractive index traces of the PMOST-*b*-PTMSS BCPs synthesized for study and their respective homopolymer aliquots.[36]

Complete reaction of the living PMOST homopolymer was verified using SEC (Fig. 3.14). Each sample showed successful and full conversion to the BCP after addition of the second monomer, indicated by a complete shift to lower retention time. All polymers show mono-modal molecular weight distributions with narrow dispersity, and the traces show no evidence of coupled polymer as a result of side reactions.

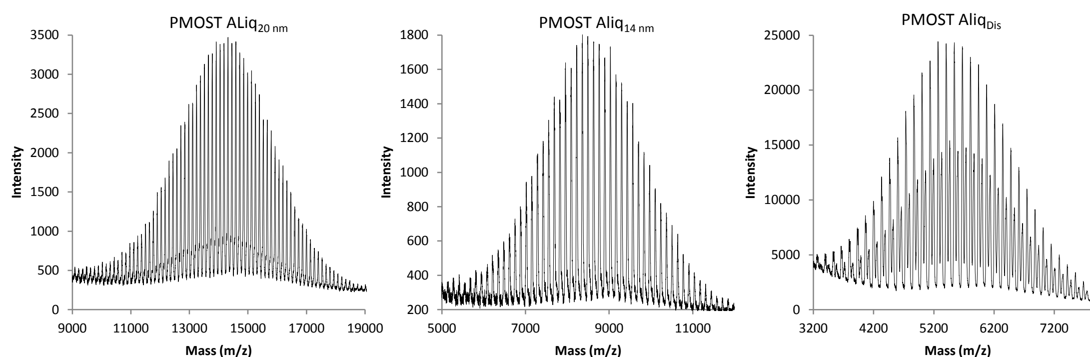


Figure 3.15: MALDI spectra of PMOST homopolymer aliquots.[36]

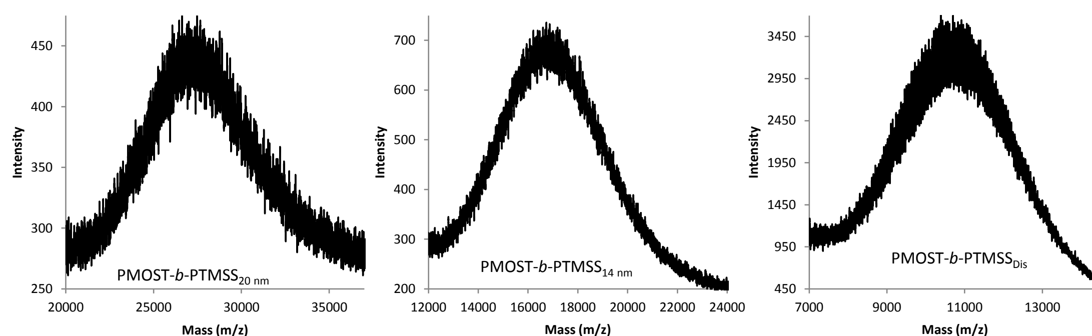


Figure 3.16: MALDI spectra of PMOST-*b*-PTMSS BCPs.[36]

The polymer molecular weights were additionally analyzed by MALDI. The aliquots (Fig. 3.15) all show uniform molecular weight distributions with peak spacings of approximately 133-134 m/z, corresponding to units of MOST (134.18 g/mol). The disordered aliquot (Fig 3.15, right) has a unique spectrum, appearing to have a convolution of two near-identical distributions of differing intensity, offset by 45-60 m/z. The observance of two spectra is likely due to trace impurities/salts in the polymer matrix that manifest themselves as unique counter-ions of the ionized polymer. The molecular weight calculated for this sample is not greatly affected by this error, thus the higher intensity signal was used. The BCP MALDI spectra (Fig. 3.16) all show non-resolved peak spacing typical of multi-component polymer architectures.

Table 3.4: Polymer characterization data.

| **Polymer** | $L_0$[a] | $M_{n,A}$[b] | $Đ_A$[c] | $M_{n,BCP}$[d] | $Đ_{BCP}$[c] | $f_A$[e] | $T_g$[f] | $T_d$[f] |
|---|---|---|---|---|---|---|---|---|
| PMOST-*b*-PTMSS$_{20\ nm}$ | 20.7 | 14.4 | 1.01 | 27.4 | 1.05 | 0.471 | 125/102 | 363 |
| PMOST-*b*-PTMSS$_{14\ nm}$ | 14.4 | 8.5 | 1.05 | 16.8 | 1.04 | 0.467 | 125/102 | 370 |
| PMOST-*b*-PTMSS$_{Dis}$ | (9.9) | 5.5 | 1.02 | 10.8 | 1.03 | 0.464 | 125/102 | 370 |

[a] Lamellae periodicity $L_0$ in nm, determined by top-down SEM. Values in parenthesis represent disordered samples calculated by SAXS at 200 ºC.
[b] $M_n$ in kDa of the first block, determined by MALDI.
[c] Dispersity index $Đ$, determined by SEC.
[d] $M_n$ in kDa of the BCP, determined by $M_{n,A}$ and $^1$H-NMR.
[e] Volume fraction $f_A$ of the first block, determined by $^1$H-NMR and the density of the respective homopolymers. Density was measured according to Archimedes' principle (see Chapter 4).
[f] $T_g$ and $T_d$ in ºC, measured by DSC/TGA.

The polymer characterization data is summarized in Table 3.4. The largest polymer, PMOST-*b*-PTMSS$_{20\ nm}$, has a domain size comparable to PS-*b*-PTMSS$_{20\ nm}$, allowing a comparison between polymers of differing segregation strength. The smallest ordered material has a domain size of 14.4 nm. This polymer also has an observable ODT (see Section 4.1), suggesting that *ca.* 14 nm is the minimum resolvable feature size for such a BCP. All polymers synthesized have low dispersities characteristic of their living polymerization mechanism, and the calculated volume fractions are close to their targeted 50:50 ratio. All polymers have a high $T_d$ (> 360 °C), indicating that the materials are stable for thermal annealing at elevated temperature.

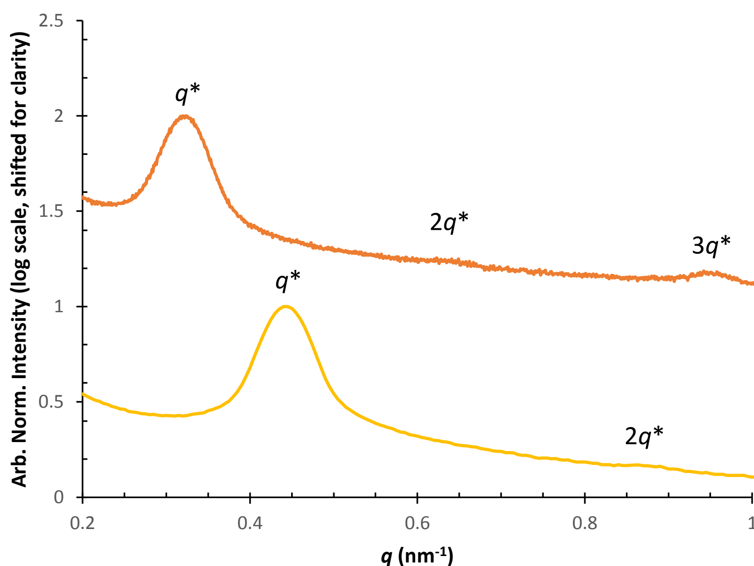


Figure 3.17: SAXS profile of ordered (top) PMOST-*b*-PTMSS$_{20\ nm}$ and (bottom) PMOST-*b*-PTMSS$_{14\ nm}$.[36]

The scattering data of the ordered polymers in bulk is presented in Fig. 3.17. Both polymers show higher order *nq** peaks indicative of lamellar morphology. The primary scattering peaks correspond to 20.1 nm (top) and 14.4 nm (bottom). Analysis of the disordered state scattering data for PMOST-*b*-PTMSS is presented in Section 4.2.

Additional information regarding identified neutral top and bottom coat materials is provided in the experimental section.

### 3.5 Poly(styrene-*block*-4-pentamethyldisilylstyrene)

PMOST-b-PTMSS was modified relative to PS-b-PTMSS by appending polar functional groups to enhance the chemical dissimilarity between components of the block. In a similar fashion, hydrophobic moieties appended to the lower surface energy component (PTMSS) were hypothesized to provide comparable improvements. Additional trimethylsilyl substituents could accomplish such an effect, in addition to

increasing the silicon content of the polymer. Published work has demonstrated that 4-pentamethyldisilylstyrene (DSS) can be polymerized by both controlled free-radical[132] and anionic polymerization[133] mechanisms and be copolymerized with various styrenic derivatives, thus this monomer was an attractive target to produce materials relevant for patterning applications. DSS copolymerized with styrene was therefore targeted as a material that could achieve higher etch contrast relative to PTMSS BCPs (see Section 3.1) and increase $\chi$.

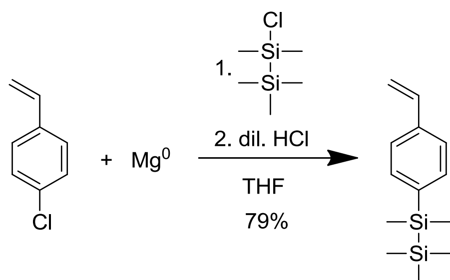


Scheme 3.5: Synthesis of DSS monomer.

DSS monomer was synthesized by a Grignard reaction with 4-chlorostyrene and pentamethyldisilylchloride (Scheme 3.5).[133] The crude monomer was fractionally distilled and could be further purified over *n*-BuLi for anionic polymerization. Purification over *n*-BuLi was particularly difficult, as the DSS monomer was more sensitive to autopolymerization relative to TMSS. For unknown reasons, it was observed that monomer freshly distilled over *n*-BuLi had small concentrations of high molecular weight homopolymer after storage in a glovebox freezer for less than 24 hours, confirmed by SEC traces. The homopolymer impurity was accompanied by a noticeable increase in the fluid viscosity while injecting the monomer into anionic reactors. To mitigate this effect, it is recommended to freshly distill and immediately inject the monomer into

anionic reactors prior to polymerization. Due to some of these preparation complications, both controlled free-radical and anionic polymerization mechanisms were pursued for BCP preparation, discussed in the following sections.

### 3.5.1 Nitroxide-Mediated Polymerization

Controlled free-radical polymerization of PS-*b*-PDSS was pursued to circumvent the purification difficulties of the DSS monomer. Free-radical polymerizations are generally less sensitive to trace impurities than anionic polymerizations, yet such techniques can still be used to produce "living" polymers with controlled molecular weight and narrow dispersity. One subclass of controlled free-radical polymerizations is nitroxide-mediated polymerization (NMP).[134,135] For NMP, a reversible radical scavenger significantly reduces the concentration of active chain ends, and the growing polymer is favored in a dormant state. This mechanism reduces the likelihood of permanent chain termination pathways and promotes the controlled growth of the polymer. NMP has not only been demonstrated to produce organosilicon BCPs, but PS-*b*-PDSS has been synthesized previously with controlled molecular weight and low dispersity.[132]

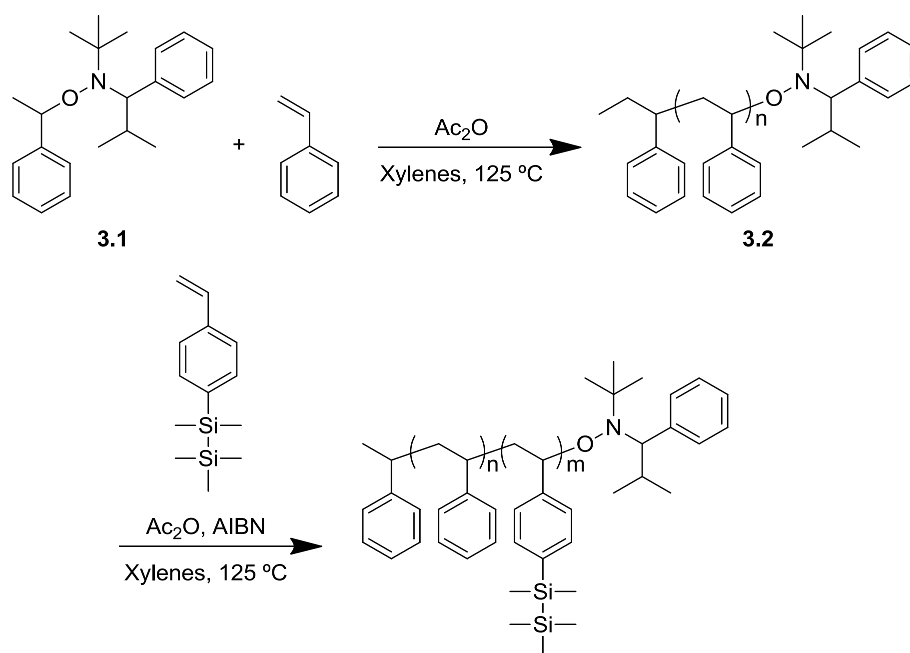


Scheme 3.6: Nitroxide-mediated polymerization scheme of PS-*b*-PDSS.

The reaction scheme for the production of PS-*b*-PDSS is shown in Scheme 3.6. The α-hydride nitroxide-mediated unimolecular initiator **3.1** was used to initiate the polymerization of styrene to grow the macroinitiator **3.2**. Since many organosilicon monomers are highly temperature sensitive, a rate-accelerating agent was introduced (acetic anhydride) to increase the polymerization conversion and shorten the reaction time. DSS monomer was sequentially grown from the macroinitiator **3.2** to produce PS-*b*-PDSS, end-capped with an alkoxyamine.

Table 3.5: NMP polymer characterization data.

| Polymer | $L_0$ (nm)[a] | Target $M_{n,A}$ (kDa) | Actual $M_{n,A}$ (kDa)[b] | $Đ_A$[b] | $M_{n,BCP}$ (kDa)[b] | $Đ_{BCP}$[b] | $f_A$[c] | Mass Yield (%) |
|---|---|---|---|---|---|---|---|---|
| PS-*b*-PDSS$_{23\ nm}$ | 22.7 | 15.0 | 14.9 | 1.03 | 24.3 | 1.15 | 0.515 | 94 |
| PS-*b*-PDSS$_{18\ nm}$ | 18.4 | 10.0 | 10.8 | 1.03 | 18.0 | 1.16 | 0.519 | 91 |
| PS-*b*-PDSS$_{Dis}$ | (16.9) | 7.5 | 8.4 | 1.03 | 14.3 | 1.16 | 0.506 | 95 |

[a] Determined by SAXS.
[b] Determined by SEC relative to a PS standard, dn/dC = 0.185.
[c] Volume fraction $f_A$ of the first block, determined by ^{1}H-NMR and the density of the respective homopolymers. Density was measured according to Archimedes' principle (see Chapter 4).

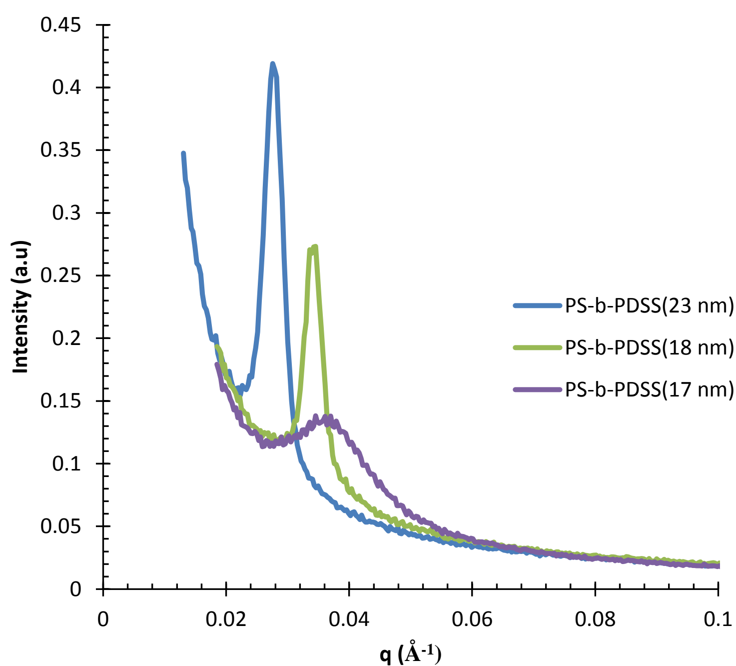


Figure 3.18: SAXS profiles of NMP PS-*b*-PDSS materials.

Several polymer molecular weights were targeted for synthesis by varying the styrene monomer/initiator ratio. The characterization data for the series of nitroxide-mediated PS-*b*-PDSS materials are presented in Table 3.5, with the polymer name ascribed with the nominal $L_0$ of the material. The actual molecular weights of the PS macroinitiators **3.2** match closely with the targeted molecular weights, and the

dispersities of the polymers are low, indicating the polymerization has controlled character. The NMP BCPs are successfully formed in high yield at near symmetric volume fractions, targeting lamellar morphologies. These results indicate that the organosilicon styrenic components are well-suited to form controlled lamellar BCPs with accurate control over the material properties. The polymers were characterized by SAXS to confirm the morphology and evaluate the BCP $L_0$ (Fig. 3.18). The SAXS profiles show a strong primary scattering peak for each BCP but no higher order signals. The scattering vector of the polymers increases inversely proportional to the BCP molecular weight, and the size of the periodicities decreases from *ca.* 23 to 17 nm. The smallest BCP, PS-*b*-PDSS$_{17\ \mathrm{nm}}$, has a broadened primary scattering peak, suggesting the material has transitioned to the disordered phase. This result is particularly unusual because the minimum periodicity discovered for an anionically synthesized PS-*b*-PDSS (see Section 3.5.2) is *ca.* 14 nm (note: the SAXS derived $L_0$ is typically 1-2 nm higher than that determined by top-down SEM, but the discrepancy is still large). The origin of this disagreement is unknown, but the degradation issues discussed in the following experiments may contribute to this effect.

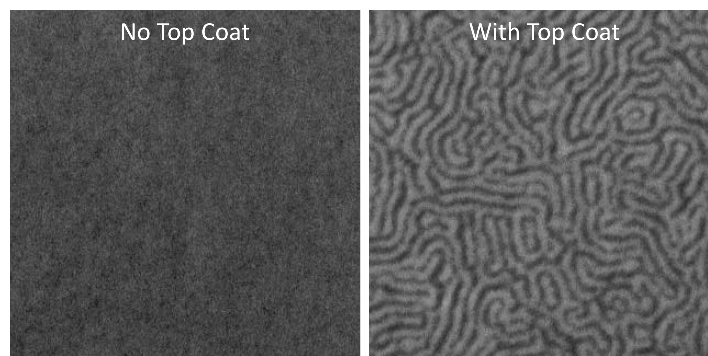


Figure 3.19: Thin film thermal annealing test using NMP PS-*b*-PDSS. The control (left) shows no assembly, while annealing between two neutral interfaces (right) shows defective perpendicular structures.

The orientation control of PS-*b*-PDSS$_{18\ nm}$ in thin films was evaluated by thermal annealing between two neutral interfaces. The control experiment with no top coat (Fig. 3.19, left) shows no evidence of perpendicular assembly, while the use a both a neutral bottom interface and a neutral top coat promotes perpendicular orientation (Fig. 3.19, right). The perpendicular structures observed in such experiments, while resembling the characteristic fingerprint-like patterns of BCPs annealed between uniform interfaces, have high concentrations of dislocation defects, seen as short segments of polymer domains. Additionally, the domain sizes appear irregular, with non-uniform periodicity. This unusual behavior prompted further study of the NMP PS-*b*-PDSS polymer to see if the alkoxyamine end-cap is sensitive to thermal annealing.

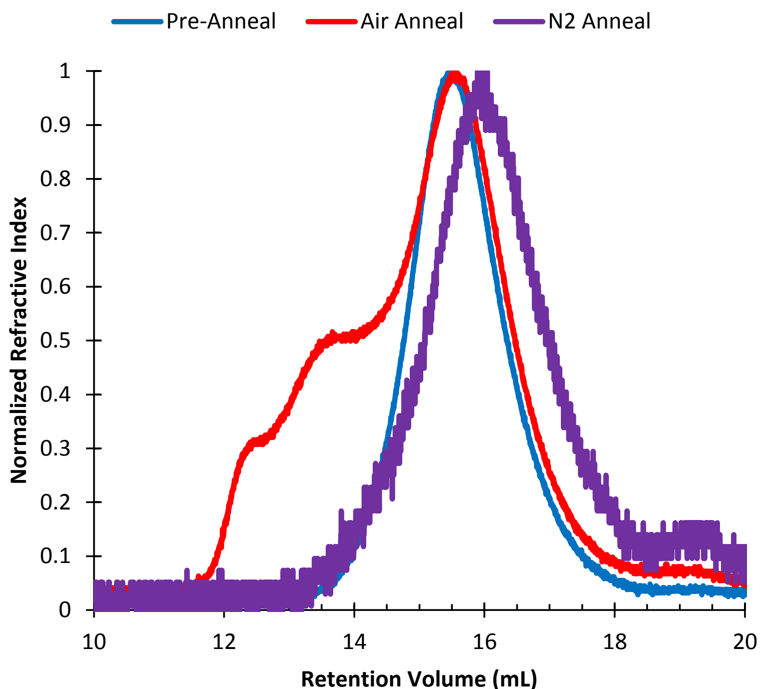


Figure 3.20: SEC RI traces of bulk NMP PS-*b*-PDSS before annealing (blue), and after annealing in an air (red) and nitrogen environment (purple).

Bulk samples of NMP PS-*b*-$PDSS_{18\ nm}$ were annealed to test the sensitivity of the polymer to elevated temperatures. Samples were annealed in a TGA chamber at 170 °C for 12 hours with a purge of either air or nitrogen gas. After annealing, the samples were dissolved in THF and submitted for SEC (Fig. 3.20) (note: at least some portion of insoluble material remained for both annealed samples, suggesting some degree of cross-linking occurred). The SEC refractive index traces show that the both samples exhibit evidence of thermal degradation. The sample annealed in air (red) has higher molecular weight distributions convoluted with some remaining material matching the non-annealed sample. This suggests that some portion of the material is coupled in the presence of oxygen, creating higher molecular weight by-products. The nitrogen-purged sample also shows evidence of degradation; the trace shifts toward lower molecular weight and has a higher dispersity. These results indicate that the alkoxyamine end-capped polymer is inherently unstable at elevated temperatures and is not suitable for thermal annealing processes.

***Maleimide End-Capping of PS-b-PDSS***

Harth et al. have shown that vinyl polymers prepared by NMP can react with maleic anhydride or maleimides to form a mono-adduct with greater thermal stability than the alkoxyamine end-capped polymer.[136] This strategy relies on the resistance of maleic anhydride and maleimides towards homopolymerization, thus an alkoyamine-terminated polymer can be heated in the presence of these reagents to append a single unit at the chain end (Scheme 3.7). PS-*b*-PDSS prepared by NMP was therefore reacted with *N*-phenylmaleimide to replace the polymer end-cap in an attempt to increase the thermal stability of the BCP.

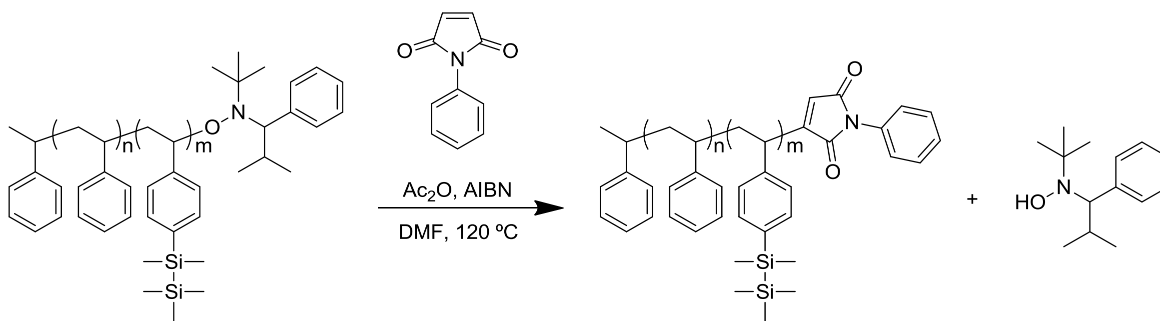


Scheme 3.7: End-cap reaction of alkoyamine-terminated PS-*b*-PDSS with *N*-phenylmaleimide.

A sample of *N*-phenylmaleimide-terminated PS-*b*-PDSS was submitted for TGA under a nitrogen purge to evaluate the thermal stability (Fig. 3.21). The alkoxyamine end-capped polymer has a $T_d$ close to 240 °C, while the *N*-phenylmaleimide end-capped polymer $T_d$ is approximately 290 °C. The thermal stability is significantly increased by removal of the labile alkoxyamine end-cap, but SEC results (Fig. 3.22) show that a similar sample heated to 170 °C for 12 hours under a nitrogen purge still exhibits degradation issues. After the anneal, the sample has a broadened molecular weight distribution with multi-modal character, similar to the alkoxyamine end-capped polymer (Fig. 3.22).

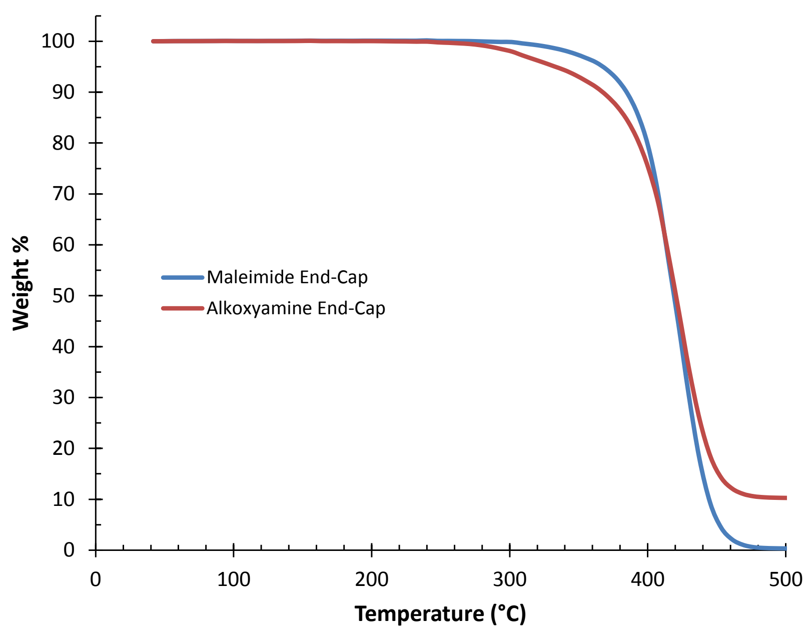


Figure 3.21: TGA profiles of *N*-phenylmaleimide and alkoxyamine end-capped BCPs.

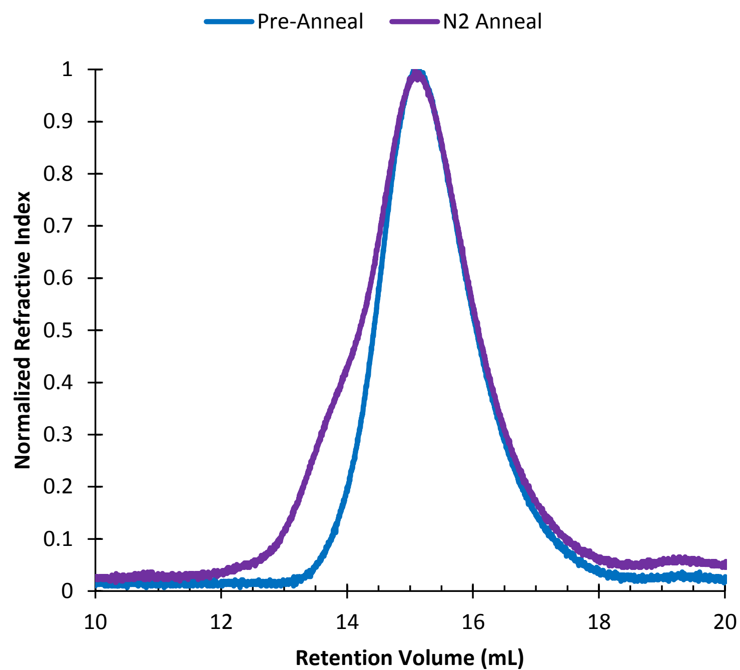


Figure 3.22: SEC RI traces of *N*-phenylmaleimide end-capped PS-*b*-PDSS before (blue) and after (purple) annealing.

The *N*-phenylmaleimide end-capped PS-*b*-PDSS thin film behavior was evaluated despite the indications of the aforementioned results, but no significant improvements were observed. It was therefore concluded that these particular NMP materials were unsuitable for thermal annealing and efforts were instead focused solely on anionically-derived polymers.

### 3.5.2 Anionic Polymerization

Three symmetric diblock PS-*b*-PDSS polymers were targeted for anionic polymerization: an ordered 20 nm $L_0$ sample (comparable to the 20 nm $L_0$ PS-*b*-PTMSS), a sample possessing an ODT, and a disordered sample for scattering experiments. The samples were targeted at varying molecular weights by changing the monomer/initiator ratio for each separate reaction.

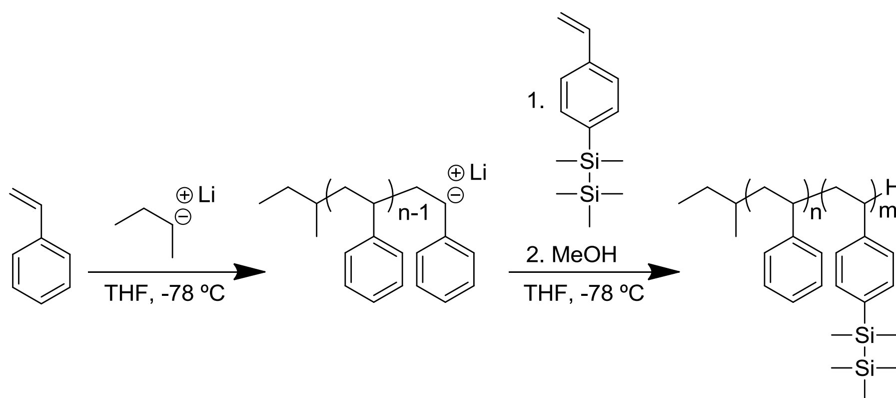


Scheme 3.8: Anionic synthesis of PS-*b*-PDSS.

The PS monomer was initiated with *sec*-BuLi in THF at -78 °C to grow the first polymer block (Scheme 3.8). DSS monomer, freshly distilled over *n*-BuLi, was added to living PS chain-end to grow the second block, producing a deep red colored solution. The PS-*b*-PDSS was quenched with degassed methanol and isolated to yield the polymers

used for study. As discussed earlier in Section 3.5, distillation of the DSS monomer was not trivial; DSS heated over aggressive reagents (*e.g.* *n*-BuLi) was highly susceptible to autopolymerization. It was therefore necessary to distill monomer using high-vacuum equipment (< 100 mtorr) to minimize distillation temperatures, and specialized glassware was fabricated to aid distillation yields (see Appendix A). Monomer could not be stored, even at reduced temperatures, and was therefore used immediately for reaction.

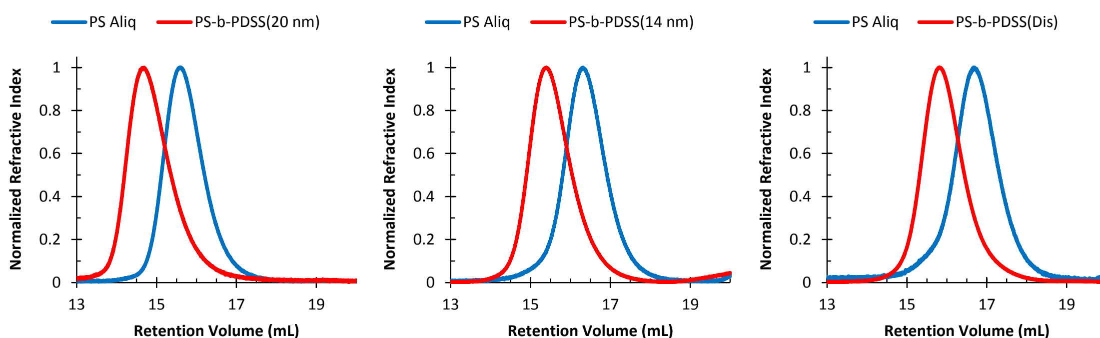


Figure 3.23: SEC refractive index traces of the PS-*b*-PDSS BCPs synthesized for study and their respective homopolymer aliquots.[36]

The SEC traces of the BCPs and their respective homopolymer aliquots are shown in Fig. 3.23. All polymers show mono-modal distributions and a distinct shift towards lower retention volume (higher molecular weight) after addition of the second monomer. None of the anionically synthesized polymers show evidence of coupled or terminated by-products.

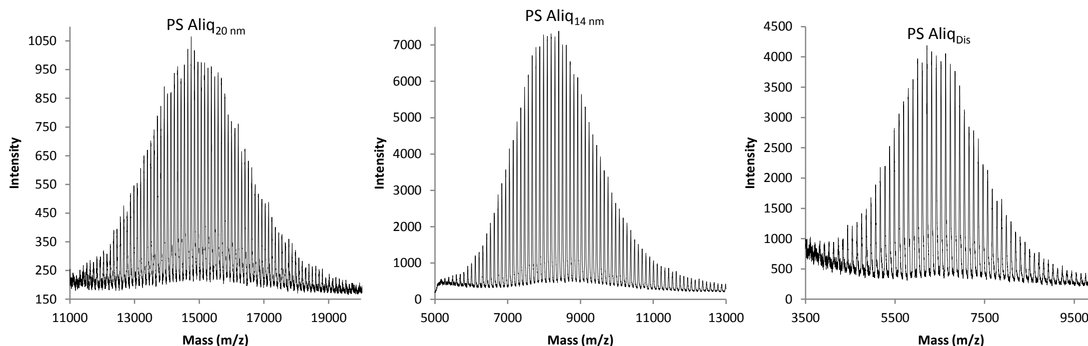


Figure 3.24: MALDI spectra of PS homopolymer aliquots.[36]

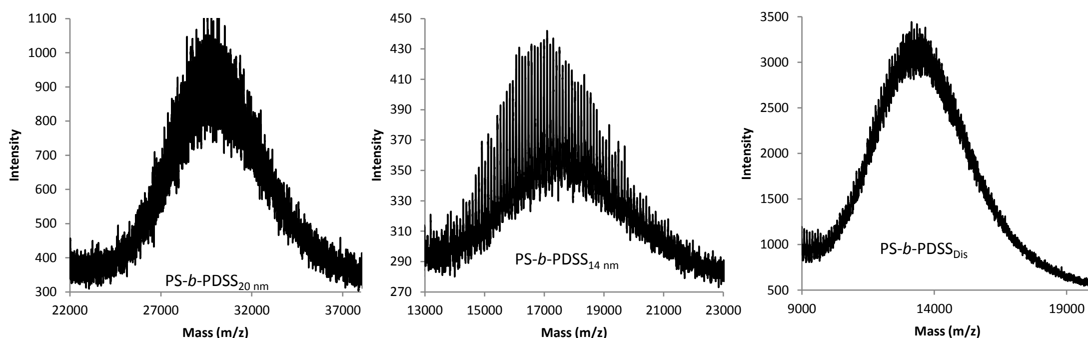


Figure 3.25: MALDI spectra of PS-*b*-PDSS BCPs.[36]

The molecular weight information of the PS homopolymer aliquots and BCPs were evaluated using MALDI (Fig. 3.24 and 3.25). All homopolymer aliquots show typical mono-modal distributions with peak spacings of 103-104 m/z, corresponding to styrene (104.15 g/mol). The BCP MALDI spectra for the PS-*b*-$PDSS_{20\ nm}$ and PS-*b*-$PDSS_{Dis}$ samples are typical of block polymers, showing non-resolved peak spacing. In contrast, PS-*b*-$PDSS_{14\ nm}$ (Fig. 3.25, middle) has a convolution of a homopolymer distribution with a more continuous BCP distribution of lower intensity. The resolved peaks for this sample have a spacing of 104 m/z, indicating that the contaminant is PS homopolymer. Although the intensity of the PS is comparable to the BCP signal, the SEC trace for the same sample (Fig. 3.23, middle) shows no evidence of a multi-modal trace

indicative of the contaminant. It is likely that the PS homopolymer is a trace contaminant of oxygen-coupled polymer, but its signal is amplified relative to the BCP (The MALDI signal intensity is not quantitative and is often dependent on many factors from sample preparation). This is corroborated by the fact that the $M_n$ of an oxygen coupled PS contaminant is calculated to be coincidentally within the same range of the BCP $M_n$.

Table 3.6: Anionic polymer characterization data.

| **Polymer** | $L_0$ [a] | $M_{n,A}$ [b] | $Đ_A$ [c] | $M_{n,BCP}$ [d] | $Đ_{BCP}$ [c] | $f_A$ [e] | $T_g$ [f] | $T_d$ [f] |
|---|---|---|---|---|---|---|---|---|
| PS-*b*-PDSS$_{20\ nm}$ | 20.7 | 15.0 | 1.01 | 29.7 | 1.02 | 0.499 | 100/95 | 378 |
| PS-*b*-PDSS$_{14\ nm}$ | 14.9 | 8.4 | 1.05 | 17.5 | 1.03 | 0.470 | 100/95 | 378 |
| PS-*b*-PDSS$_{Dis}$ | (12.0) | 6.5 | 1.04 | 13.1 | 1.04 | 0.468 | 100/95 | 370 |

[a] Lamellae periodicity $L_0$ in nm, determined by top-down SEM. Values in parenthesis represent disordered samples calculated by SAXS at 200 ºC.
[b] $M_n$ in kDa of the first block, determined by MALDI.
[c] Dispersity index $Đ$, determined by SEC.
[d] $M_n$ in kDa of the BCP, determined by $M_{n,A}$ and $^1$H-NMR.
[e] Volume fraction $f_A$ of the first block, determined by $^1$H-NMR and the density of the respective homopolymers. Density was measured according to Archimedes' principle (see Chapter 4).
[f] $T_g$ and $T_d$ in ºC, measured by DSC/TGA.

A summary of the polymer characterization data is presented in Table 3.6. The largest polymer, PS-*b*-PDSS$_{20\ nm}$, has a measured $L_0$ (20.7 nm) comparable to that of PS-*b*-PTMSS$_{20\ nm}$ and PMOST-*b*-PTMSS$_{20\ nm}$, enabling a comparison of their lithographic performance as a function of segregation strength (see Section 4.4). The smallest ordered polymer, PS-*b*-PDSS$_{14\ nm}$, has an ODT and effectively represents the resolution limit of this polymer system (see Section 4.1). All polymers synthesized anionically have low dispersity indexes and calculated volume fractions that closely match their targeted 50:50 ratio. The polymers were verified by TGA to have $T_d$'s (> 370 ºC) well above the anneal temperatures used in thin-film thermal annealing experiments (*ca.* 180-200 ºC).

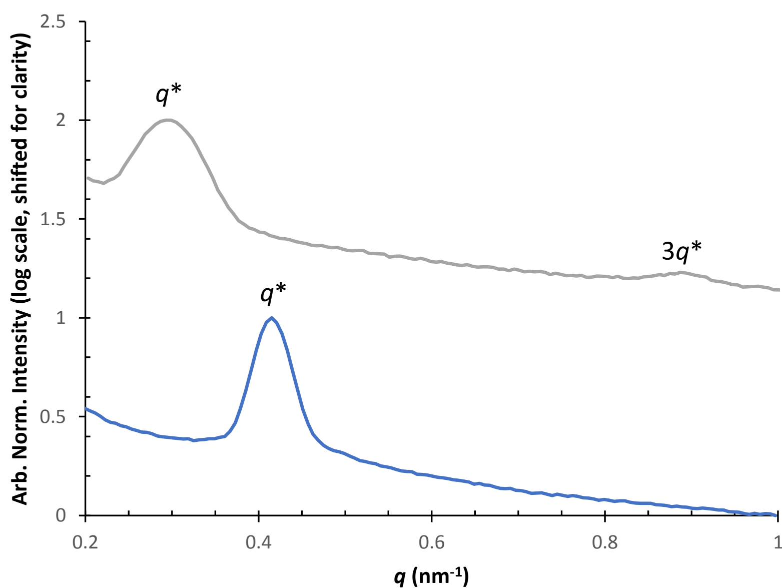


Figure 3.26: SAXS profile of ordered (top) PS-*b*-$PDSS_{20\ nm}$ and (bottom) PS-*b*-$PDSS_{14\ nm}$.[36]

The ordered polymers were analyzed by SAXS to verify the BCP morphology (Fig. 3.26). The largest polymer, PS-*b*-$PDSS_{20\ nm}$ (top), shows $nq^*$ scattering vectors indicative of the lamellar morphology. Extinction of the $2q^*$ peak is typical for BCPs with a 50:50 volume ratio, reflective of the calculated $f_A$ of 0.499. The primary scattering peak is located at 0.287 $nm^{-1}$ (21.9 nm), higher than the pitch calculated by top-down SEM (Table 3.6), although all BCP samples investigated appeared to have a SAXS bulk periodicity 1-2 nm higher than the top-down SEM derived result. The smaller ordered polymer, PS-*b*-$PDSS_{14\ nm}$ (bottom), has a primary scattering peak at 0.409 $nm^{-1}$, corresponding to a periodicity of 15.4 nm. No higher order peaks are visible, but thin-film behavior is consistent with lamellar morphology and the calculated PS volume fraction is close to symmetric (0.47).

### 3.6 POLY(4-METHOXYSTYRENE-*BLOCK*-4-PENTAMETHYLDISILYLSTYRENE)

The chemical modifications presented in Sections 3.4 and 3.5 were combined to evaluate the additive nature of the structure-property relationships. For this concept, both a hydrophilic functional group (-methoxy) was introduced to the organic component of PS-*b*-PTMSS, and a hydrophobic organosilicon functional group (-trimethylsilyl) was appended to the organosilicon domain to produce PMOST-*b*-PDSS. The combination of these modifications increases the chemical dissimilarity between the components, increasing $\chi$, while also imparting the improved etch selectivity of the DSS material (see Section 3.1). Only one sample of PMOST-*b*-PDSS was targeted: a disordered sample suitable for scattering experiments to evaluate $\chi$.

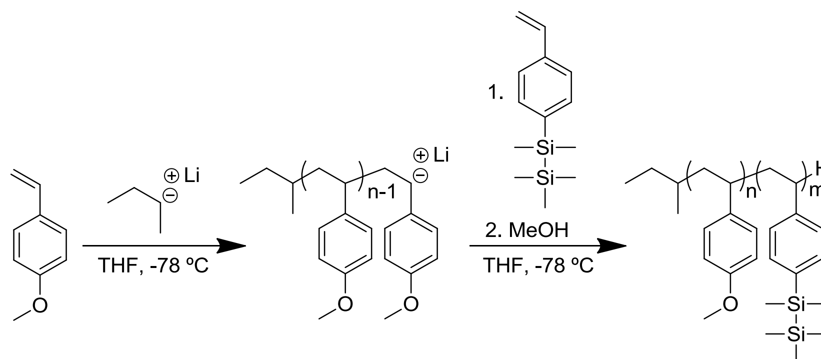


Scheme 3.9: Anionic synthesis of PMOST-*b*-PDSS.

PMOST-*b*-PDSS was synthesized anionically to yield the targeted polymer (Scheme 3.9). Similar to previously mentioned procedures, the MOST monomer was initiated via *sec*-BuLi in THF at -78 ºC. After the polymerization was complete, freshly distilled DSS monomer was added to the reaction to grow the second block. The BCP was terminated using degassed methanol, and the polymer is isolated for study.

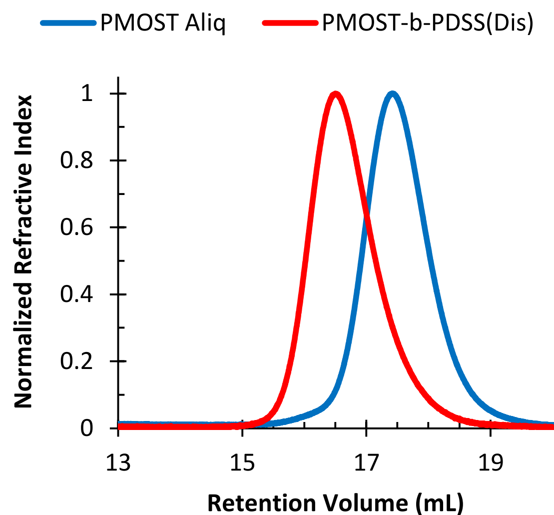


Figure 3.27: SEC refractive index traces of the PMOST-*b*-PDSS BCP synthesized for study and the respective homopolymer aliquot.[36]

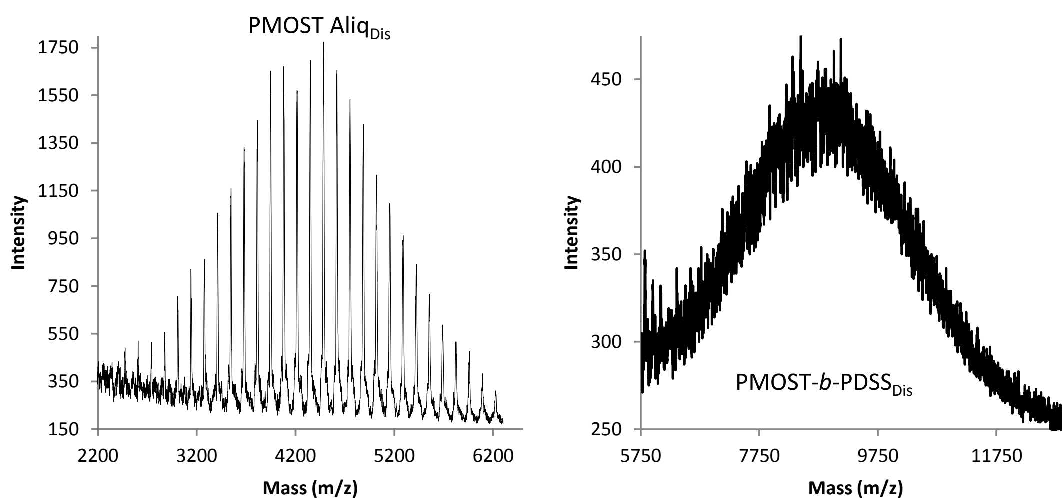


Figure 3.28: MALDI spectra of PMOST homopolymer and PMOST-*b*-PDSS.[36]

The growth of the BCP relative to the homopolymer was characterized by SEC (Fig. 3.27). Both the MOST aliquot and BCP show monomodal refractive index traces indicative of controlled polymerization with no evidence of side reaction. The

homopolymer trace shows a distinct shift to the BCP of higher molecular weight. These polymers were also analyzed by MALDI to yield accurate information on the molecular weight (Fig. 3.28). The aliquot (left) shows peak spacings of 133-134 m/z, corresponding to the molar mass of MOST (134.18 g/mol). The PMOST-*b*-PDSS sample (right) has the characteristic unresolved peak profile of a BCP, shifted to higher molecular weight.

Table 3.7: Polymer characterization data.

| **Polymer** | $L_0$ [a] | $M_{n,A}$ [b] | $Đ_A$ [c] | $M_{n,BCP}$ [d] | $Đ_{BCP}$ [c] | $f_A$ [e] | $T_g$ [f] | $T_d$ [f] |
|---|---|---|---|---|---|---|---|---|
| PMOST-*b*-PDSS$_{Dis}$ | (9.9) | 4.5 | 1.04 | 8.8 | 1.03 | 0.485 | 125/95 | 370 |

[a] Lamellae periodicity $L_0$ in nm, determined by top-down SEM. Values in parenthesis represent disordered samples calculated by SAXS at 200 ºC.
[b] $M_n$ in kDa of the first block, determined by MALDI.
[c] Dispersity index $Đ$, determined by SEC.
[d] $M_n$ in kDa of the BCP, determined by $M_{n,A}$ and $^1$H-NMR.
[e] Volume fraction $f_A$ of the first block, determined by $^1$H-NMR and the density of the respective homopolymers. Density was measured according to Archimedes' principle (see Chapter 4).
[f] $T_g$ and $T_d$ in ºC, measured by DSC/TGA.

The characterization data for the PMOST-*b*-PDSS polymer is summarized in Table 3.7. The disordered polymer has a domain spacing of 9.9 nm (determined by SAXS, see Section 4.2), indicating that the minimum resolvable periodicity for this material is above 10 nm. The material has a low dispersity reflective of the controlled polymerization, and the BCP successfully hit near the symmetric volume fraction target ($f_A$ = 0.485). The high decomposition temperature ($T_d$ = 370) suggests that the material is stable at elevated temperature required for high measurement experiments. Details of these studies are discussed in Chapter 4.

### 3.7 CONCLUSIONS

The $O_2$-RIE experiment demonstrates that the organosilicon polymers function as designed. The silicon functional groups impart an inherent etch selectivity that is necessary to transfer the latent BCP nanostructures. This etch selectivity is improved by increasing the silicon content of the organosilicon domain. This behavior was further studied using a $N_2/H_2$ RIE. In these experiments, it was found that VUV irradiation is the primary cause of $SiO_x$ etch barrier formation, and the thickness lost during the transient etch period can be traced to the removal of photolysis by-products. Initial results suggest that the transient period mask removal can potentially be mitigated by counterintuitively *increasing* the plasma bias. The high silicon-content polymers investigated are beneficial for minimizing etch-mask loss, and this characteristic will likely become more critical as the BCP pitch size is reduced and the mask loss becomes a larger proportion of the overall film thickness. These considerations further emphasize the need for high aspect ratio structures, as the taller features offset the inevitable film loss during etch processing. A BCP can therefore be designed based on intuition gleaned from homopolymer etch experiments. High silicon-content polymers can be combined with oxygenated or aliphatic polymers to produce high-$\chi$ and high etch contrast materials.

Several organosilicon BCPs were pursued for lithographic applications. The materials are primarily based on styrenic derivatives, which can be modified with various hydrophilic and hydrophobic moieties to alter the properties of the resulting BCPs. The various styrenic components were synthesized via anionic polymerizations to afford controlled and low dispersity polymers as evidenced by their characterization data. All BCPs were targeted for symmetric volume fractions ($f_A = 0.5$), and the BCPs result in lamellar morphologies by SAXS. The novel polymers are able to access domain sizes below 10 nm and are suitable for introduction as next-generation high-$\chi$ materials.

Neutral XST and TC materials were found for all organosilicon BCPs, enabling perpendicular orientation of the lamellae (*i.e.* high aspect ratio structures). The $\chi$ parameter estimations and lithographic performance are evaluated in Chapter 4.

### 3.8 EXPERIMENTALS

***Chemicals:***

All chemicals were purchased from Sigma Aldrich and used as received unless otherwise noted. Trimethylsilylchloride and pentamethyldislylchloride were purchased from Gelest, Inc. 4-chlorostyrene was purchased from Alpha Aesar. 4-methoxystyrene was purchased from Acros. 4-trimethylsilylstyrene (TMSS) was supplied as a generous gift from Nissan Chemical Company. 4-pentamethyldisilylstyrene (DSS) was synthesized according to the literature,[133] and the crude monomer was purified by vacuum distillation (BP 53-55 °C, 75 mtorr). Acetic anhydride and xylenes were distilled prior to use and stored in a refrigerator over molecular sieves. Azoisobutyronitrile (AIBN) was purchased from Sigma Aldrich and recrystallized from methanol before use. Uninhibited tetrahydrofuran (THF) was purchased from JT Baker and passed through a Pure Solv MD-2 solvent purification system containing two activated alumina columns. Ultra-high purity argon was purchased from Airgas.

***Instrumentation:***

All films were coated on a Brewer Science CEE 100CB Spincoater. Annealing was performed on a Thermolyne 11515B hot plate. Ellipsometry measurements were taken with a J.A. Woolam Co., Inc. VB 400 VASE Ellipsometer. Oxygen reactive ion etching was performed on an Oxford Instruments PlasmaLab 80+ in inductively coupled plasma mode using the following settings unless otherwise noted: (RF power: 20 W, ICP

power: 10 W, pressure: 50 mtorr, $O_2$ flow rate: 75 sccm, Ar flow rate: 75 sccm). A Zeiss Supra 40 VP and Hitachi S-4500 were used for all SEM images. SEC Data were collected with an Agilent 1100 Series isopump and autosampler with a Viscotek Model 302 TETRA detector platform using THF as an eluent at 23 ºC. Three I-series mixed bed high-MW columns were calibrated relative to polystyrene standards. Matrix assisted laser desorption/ionization (MALDI) data were collected on an AB SCIEX Voyager-DE PRO MALDI-TOF using *trans*-2-[3-(4-*tert*-butyl-phenyl)-2-methyl-2-propenylidene]malononitrile as a matrix with silver trifluoroacetate as a counterion. Small molecule IR data were recorded on a Nicolet Avatar 360 FT-IR. Polymeric IR were recorded on a Nicolet 380 FT-IR diamond ATR. TGA/DSC data were collected on a TA Instruments Q500/Q100, respectively. $^{1}$H NMR spectra were recorded on a Varian Unity Plus 400 MHz instrument, with chemical shifts reported downfield in ppm from TMS using residual protonated solvent as an internal standard (CDCl3, $^{1}$H 7.29 ppm, $^{13}$C 77.0 ppm). Combustion analysis was performed by Midwest Microlab, LLC. Small-angle x-ray scattering data was collected using a Molecular Metrology instrument equipped with a high brilliance rotating copper anode source ($K_{\alpha}$ radiation, $\lambda$ = 1.5418 Å) and a two-dimensional 120 mm gas filled multi-wire detector. Vertical focus was acquired with a single crystal germanium mirror, and horizontal focus and wavelength selection was made with an asymmetrically cut Si(111) monochromator. The beam was calibrated using silver behenate with its primary reflection peak set at 1.076 nm$^{-1}$.

### 3.8.1 Thin Film Etch Experiments

***$O_2$ Plasma Etching***

Uniform thin films of five homopolymers (PMMA, PMOST, PS, PTMSS, and PDSS) were spin cast upon bare silicon wafers at thicknesses *ca.* 50-100 nm. The wafers

were baked at 140 ºC (above the $T_g$ of all polymers) on a hotplate for 1 min. to remove residual solvent, and the initial film thicknesses were measured via ellipsometry. The samples were cut into smaller pieces (*ca.* 1 $cm^2$), and one piece from each homopolymer set was etched at a time. Etching was performed on an Oxford Plasmalab RIE tool (RF power: 20 W, ICP power: 10 W, pressure: 50 mtorr, $O_2$ flow rate: 75 sccm, Ar flow rate: 75 sccm) with the wafer chuck set at 20 ºC for various times. Post-etch film thicknesses were measured by ellipsometry.

### $N_2/H_2$ *Plasma Etching*

Table 3.8: Characterization data of polymers used for $N_2/H_2$ etch experiments.

| **Polymer** | $M_n$ **(kDa)**[a] | *Đ*[a] | **Si wt.%** |
|---|---|---|---|
| PS | 9.9 | 1.39 | 0.0 |
| PS-*r*-PDSS | 8.4 | 1.39 | 4.8 |
| PS-*r*-PDSS | 9.6 | 1.41 | 9.5 |
| PS-*r*-PDSS | 12.0 | 1.38 | 13.3 |
| PS-*r*-PDSS | 15.9 | 1.39 | 16.8 |
| PS-*r*-PDSS | 22.9 | 1.37 | 20.6 |
| PDSS | 31.9 | 1.40 | 24.0 |
| PTMSS | 30.2 | 1.43 | 15.9 |

[a] Determined by SEC relative to a PS standard, dn/dC = 0.185

Several homopolymers (PS, PTMSS, and PDSS) and copolymers (PS-*r*-PDSS) were produced for the $N_2/H_2$ etch experiments. All polymers were synthesized using standard free-radical polymerization techniques, and the characterization data are provided in Table 3.8. The polymers were spin cast on bare silicon wafers and baked at 150 ºC for 1 min., producing films with thicknesses *ca.* 300-350 nm according to ellipsometry.

Etching experiments were performed in an inductively coupled plasma (ICP) system, which has been detailed elsewhere.[137] The general recipe used was:

nitrogen/hydrogen gas (ratio 3:1), coil power 200 W, and a pressure of 10 mTorr. Under these conditions, the VUV and ion flux were $1.9\times10^{15}cm^{-2}s^{-1}$ and $6.0\times10^{15}cm^{-2}s^{-1}$, respectively. The bias was controlled using a 13.56 MHz RF power supply, and the temperature was controlled with a water bath. VUV photons were separated from the ion and radical sources using a $MgF_2$ window that selectively removes radiation below 115 nm. Radicals were separated from VUV photons using an inverted sample holder that allowed lateral diffusion of the radicals while block irradiation.

### 3.8.2 Generalized Procedure for Anionic Synthesis

A general synthetic procedure is described for the anionic polymerization of the styrenic derivatives. Additional details are provided in the text when appropriate, and a description of the custom glassware used can be found in the dissertation of J.R. Strahan (note: the flasks and distillation equipment have been recently modified to incorporate additional safety precautions and enhancements for high-boiling monomers (see Appendix A)).[128] Anionic polymerization with acrylates requires alternative purification procedures and the use of 1,1-diphenylethylene as a coupling agent, details of which can be found is the dissertation of C.M. Bates.[76]

#### ***Monomer Purification***

A 1.0 M di-*n*-butylmagnesium (*n*-BuLi) solution in heptane (*ca.* 1.5mL per 5 g monomer) was transferred to two 500 mL Schlenk round-bottomed flasks in a glovebox, and the solvent was removed in vacuo on a Schlenk line. The monomer was freeze-pump-thawed (three times) in a third 500 mL Schlenk round-bottom flask and subsequently distilled trap-to-trap through a flame-dried short path into the first *n*-BuLi flask cooled in liquid nitrogen. The monomer slurry was stirred for 1 hr. at room temperature, then distilled trap-to-trap into a flame-dried burette. Finally, the burette was

transferred into a glovebox where the monomer was dispensed using an oven-dried Gastight syringe.

***Anionic Polymerization***

A 5-port 500 mL glass reactor containing a magnetic stir bar was equipped with a thermocouple well, two glass plugs, a 500 mL Schlenk round-bottomed flask with purified THF, a pressure gauge, and manifold connected to the Schlenk line capped with a rubber septum. The reactor was flame-dried under high vacuum and purged with argon gas five times. Purified THF was dispensed into the reactor from its Schlenk flask, and the reactor vessel was cooled to -78 °C while maintaining a 3 psig overpressure of argon. A solution of *sec*-butyllithium (1.4 M in cyclohexane) was added to the reactor via syringe and the solution was stirred for 0.5 hr. The organic monomer was added drop-wise via syringe over 5 min. and stirred for 1 hr. An aliquot (5 mL) was taken via a purged syringe and injected into degassed methanol to evaluate the first block. The second block was prepared by adding the organosilicon monomer to the reaction mixture drop-wise via syringe over 5 min. The reaction was stirred for an additional hour and then terminated by the addition of 5 mL degassed methanol. The polymer solution was precipitate into methanol and the resultant white powder was dried in vacuo at elevated temperature.

### 3.8.3 Nitroxide-Mediated Polymerization of PS-*b*-PDSS

***Styrene Macroinitiator 3.2***

Styrene (72 eq., 5 g, 48 mmol) was purified over 10 wt. % basic alumina to remove inhibitor prior to use. The styrene, acetic anhydride (2 eq., 0.136 g, 1.33 mmol), 50 wt. % *p*-xylene, and the initiator **3.1** (1 eq., 0.217 g, 0.67 mmol) were combined in a 50 mL RBF equipped with a rubber septum and magnetic stirbar. The contents were

purged with nitrogen for 30 min. while stirring, and the reaction vessel was immersed in an oil bath at 125 °C. After several hours, the reaction mixture solidified and could no longer be stirred. The reaction was quenched after 15 hours by immersing in an ice bath, and the solid polymer was re-dissolved in THF. The solution was precipitated in methanol, and the precipitate was collected and dried under vacuum at room temperature, yielding **3.2** as a white solid in high yield (4.84 g, 97%).

***NMP PS-b-PDSS***

A 50 mL RBF with magnetic stirbar was charged with the styrene macroinitiator **3.2** (1 eq, 1.0 g, 0.119 mmol), DSS (35.9 eq., 1.0 g, 4.27 mmol), and 50 wt. % *p*-xylene. After complete dissolution, acetic anhydride (2 eq., 24 mg, 0.238 mmol) and AIBN (0.5 eq., 9.9 mg, 0.06 mmol) were added to the reactor, and the reagents were stirred an additional 20 min. The vessel was freeze-pump-thawed three times, backfilled with nitrogen, and warmed to room temperature. The polymerization was initiated by immersing the reaction vessel in a pre-heated oil bath at 125 ºC, and the reactions became significantly more viscous after *ca.* 2 hr of heating. After 15 hr., the reaction was quenched by cooling in a 0 ºC bath. The polymer was diluted in THF, precipitated in methanol, then collected and dried in vacuo to yield the BCP as a white powder in excellent yield (1.9 g, 95%).

***Maleimide End-Capped PS-b-PDSS***

A 50 mL RBF with magnetic stirbar was charged with the NMP PS-*b*-PDSS (1 eq, 0.50 g, 0.021 mmol) ($M_n$ estimated from SEC), *N*-phenylmaleimide (4 eq., 15 mg, 0.08 mmol), and 3 mL dimethylformamide. The reactor was purged with nitrogen gas for 30 min., and the vessel was immersed in a pre-heated oil bath at 120 ºC for 4 hr. The reaction mixed was cooled to room temperature and precipitated in methanol. The

precipitate was collected and dried in vacuo to yield the polymer as a white powder (0.475 g, 94%).

### 3.8.4 Thin Film Processing of Organosilicon BCPs

The organosilicon BCPs discussed herein were processed in thin films to produce perpendicular-aligned domains. Cross-linked substrate polymers (XSTs) and 2nd generation ring-opening top coats were synthesized to provide neutral bottom and top interfaces, respectively, evaluated by island/hole wetting behavior (see Section 2.1). Table 3.9 provides a summary of the XST materials found to be neutral for each BCP and their relevant characterization data. Each XST is comprised of 4-*t*-butylstyrene (tBuS), methyl methacrylate (MMA), and vinyl benzylchloride (VBzCl) (subsequently converted to the cross-linkable azide, see Section 1.4.3).

Table 3.9: Neutral cross-linked surface treatments (XSTs) for organosilicon BCPs and their respective characterization data.

| | **Feed (mol %)** | | | **Actual (mol %)**[a] | | | |
|---|---|---|---|---|---|---|---|
| **BCP** | **tBuS** | **MMA** | **VBzCl** | **tBuS** | **MMA** | **VBzCl** | **Đ**[b] |
| PS-*b*-PTMSS$_{20\ nm}$ | 58 | 38 | 4 | 54 | 42 | 5 | 1.587 |
| PMOST-*b*-PTMSS$_{20\ nm}$ | 37 | 58 | 5 | 37 | 57 | 6 | 1.537 |
| PMOST-*b*-PTMSS$_{14\ nm}$ | 35 | 61 | 4 | 40 | 56 | 4 | 1.497 |
| PS-*b*-PDSS$_{20\ nm}$ | 73 | 21 | 5 | 73 | 20 | 7 | 1.575 |
| PS-*b*-PDSS$_{14\ nm}$ | 81 | 14 | 5 | 77 | 17 | 6 | 1.502 |

[a]Determined by combustion analysis.
[b] Determined by SEC, relative to PS standard.

Table 3.10 provides a summary of the TC materials found neutral for each respective BCP and the corresponding characterization data. Each TC is a copolymer of maleic anhydride (MA) and a styrenic derivative (see Section 2.2.2). The 50:50

alternating copolymer shown in Table 3.10 is comprised of 4-*t*-butylstyrene (tBuS), while the terpolymers contain 3,5-di-tert-butylstyrene (di-tBuS) and styrene (S).

Table 3.10: Neutral top coat (TC) materials for organosilicon BCPs and their respective characterization data.

| BCP | Feed (mol %) | | | Actual (mol %)[a] | | | | | |
|---|---|---|---|---|---|---|---|---|---|
| | MA | tBuS or di-tBuS | S | MA | tBuS or di-tBuS | S | Đ[b] | $T_g$[c] | $T_d$[c] |
| PS-*b*-PTMSS$_{20\ nm}$ | 50 | 50 | - | 52 | 48 | - | 8.03 | 222 | 325 |
| PMOST-*b*-PTMSS$_{20\ nm}$ | 50 | 42 | 8 | 52 | 41 | 7 | 2.24 | 207 | 333 |
| PMOST-*b*-PTMSS$_{14\ nm}$ | 50 | 34 | 16 | 48 | 36 | 17 | 2.22 | 205 | 332 |
| PS-*b*-PDSS$_{20\ nm}$ | 50 | 50 | - | 52 | 48 | - | 8.03 | 222 | 325 |
| PS-*b*-PDSS$_{14\ nm}$ | 50 | 26 | 24 | 51 | 25 | 24 | 2.77 | 194 | 320 |

[a] Determined by combustion analysis.
[b] Determined by SEC, relative to PS standard.
[c] Determined by DSC/TGA.

# Chapter 4: Evaluation of the Interaction Parameter $\chi$ for Block Copolymers

Developing high-$\chi$ BCPs is necessary to extend the resolution limit of self-assembled materials and improve their pattern quality for lithographic applications. The designation of "high-$\chi$" is typically reserved for materials that access structures smaller than the most thoroughly studied BCP, PS-*b*-PMMA, which has minimum domain periodicities of 10-12 nm and hence has restricted utility for next-generation patterning targets.[33,34] Several high-$\chi$ materials have been published,[23,24,35,37,129] but very few if any of these materials have been amenable to industry manufacturing or been demonstrated to function as a resist. The present work focuses on four organosilicon BCPs (Si-BCPs) designed for high resolution patterning applications: PS-*b*-PTMSS, PMOST-*b*-PTMSS, PS-*b*-PDSS, and PMOST-*b*-PDSS (see Chapter 3). The values of $\chi$ were measured and compared using PS-*b*-PMMA as a reference material. In addition, the impact of $\chi$ on the lithographic performance of the materials was evaluated. The majority of the work in this chapter was reported by Durand et al.[36] and is reprinted with permission from John Wiley and Sons.

In the Flory-Huggins lattice treatment of polymer blends, the measure of component incompatibility $\chi$ is formally the exchange energy associated with inter-mixing the pure components.[17] This parameter also governs BCP phase separation, but unfortunately it is difficult to measure $\chi$ directly. Two indirect methods for estimating an *effective* BCP interaction parameter $\chi_{\text{eff}}$ (herein referred to as $\chi$ for simplicity) are generally accepted; the first is based on the order-disorder transition (ODT) predicted by mean-field theory[138-140] and the second on analysis of the absolute intensity scattering profile of a disordered melt.[139,141] These methods are rarely reported together, but both the ODT and absolute scattering methods were employed to estimate $\chi$ for the Si-BCPs

that are the subject of this work. The relevant trends provide a guide for the rational design of new Si-BCPs.

Table 4.1: Summary of symmetric organosilicon BCPs evaluated for $\chi$-parameter and segregation strength study.

| **Polymer** | **$L_0$[a]** | **$f_A$[b]** |
|---|---|---|
| PS-*b*-$PTMSS_{20\ nm}$ | 19.8 | 0.47 |
| PS-*b*-$PTMSS_{Dis}$ | (16.8) | 0.48 |
| PMOST-*b*-$PTMSS_{20\ nm}$ | 20.7 | 0.47 |
| PMOST-*b*-$PTMSS_{14\ nm}$ | 14.4 | 0.47 |
| PMOST-*b*-$PTMSS_{Dis}$ | (9.9) | 0.46 |
| PS-*b*-$PDSS_{20\ nm}$ | 20.7 | 0.50 |
| PS-*b*-$PDSS_{14\ nm}$ | 14.9 | 0.47 |
| PS-*b*-$PDSS_{Dis}$ | (16.7) | 0.47 |
| PMOST-*b*-$PDSS_{Dis}$ | (9.9) | 0.49 |
| PS-*b*-$PMMA_{Dis}$ | (16.5) | 0.53 |

[a] Lamellae periodicity $L_0$ in nm, determined by top-down SEM. Values in parenthesis represent disordered samples calculated by SAXS at 200 ºC.
[b] Volume fraction $f_A$ of the first block, determined by $^1$H-NMR and the density of the respective homopolymers. Density was measured according to Archimedes' principle (see experimental section).

A library of ordered and disordered Si-BCPs were synthesized anionically to produce symmetric ($f_A \approx 0.5$) diblock copolymers with a lamellar morphology (Table 4.1, with additional characterization data found in Chapter 3). These could be evaluated by the aforementioned methods to study the structure-property relationship of a family of Si-BCPs relevant for patterning applications. Insight into the relationship between chemical structure and $\chi$ can be found by comparing the BCPs with *constant* periodicity, but *dissimilar* components. The effect of segregation strength on self-assembly is extracted from comparison of BCPs with the *same* components, but *differing* periodicities (*i.e.* various degrees of polymerization, $N$). This latter category contains a set of materials in

the weak segregation regime ($\chi N \approx 10.5$) and a set in the intermediate segregation regime ($15 < \chi N < 60$).[41]

The effect of high-$\chi$ and segregation strength can be additionally evaluated by observing the self-assembly in thin films. Each polymer has a set of neutral bottom and top materials that induce perpendicular orientation in thin films. The oriented domains can be etched and imaged to produce topographical features reflective of the inherent BCP properties. This thin film behavior is indicative of the BCP etch mask after all processing steps, thus any defects or issues related to segregation strength become evident.

### 4.1 Order-Disorder Transition Method

The interaction parameter $\chi$ has shown a dependence on temperature that is approximately linear (Eqn. 4.1).[142] In this equation, $\alpha$ and $\beta$ represent the enthalpic and excess entropic contributions, respectively. Both the ODT and scattering methods used to estimate $\chi$ leverage this dependence by modulating the properties of the polymers as a function of temperature. This also presents several practical limitations for each method, which will be discussed accordingly.

$$\chi(T) = \frac{\alpha}{T} + \beta \tag{4.1}$$

Self-consistent field theory (SCFT) predicts that an ODT for symmetric diblock copolymers occurs when $\chi N_{\mathrm{ODT}} = 10.5$ (the subscript ODT represents the conditions that access this transition).[139] The ODT can be accessed by synthesizing a BCP with an appropriate $N$, then recording the physical properties (usually rheological or scattering) as

a function of temperature. Empirically, $\chi(T)$ can be obtained by fitting the ODT temperature ($T_{ODT}$) for multiple samples according to the relationship in Eqn. 4.2, and regressing the coefficients.[142]

$$\frac{10.5}{N_{ODT}} = \frac{\alpha}{T_{ODT}} + \beta \tag{4.2}$$

Three of the Si-BCPs (PS-*b*-PTMSS$_{20\ nm}$, PMOST-*b*-PTMSS$_{14\ nm}$, PS-*b*-PDSS$_{14\ nm}$) exhibit a distinct ODT, observed as a discontinuity in the dynamic elastic modulus during a temperature sweep in the linear viscoelastic regime (Fig. 4.1). The ODT is indicated by the onset of the storage modulus drop, and a $T_{ODT}$ is identified for each material.

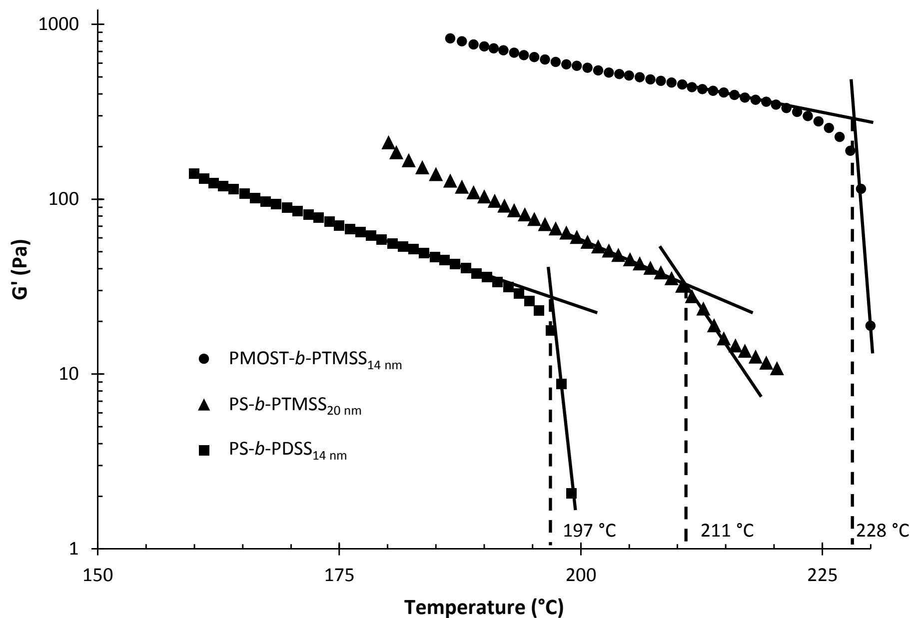


Figure 4.1: Dynamic mechanical spectroscopy plots of the storage modulus (G’) taken upon a constant 5°C/min temperature ramp for three block copolymer samples with an accessible $T_{ODT}$.

Table 4.2 lists $\chi$-values calculated by the ODT method, based on a reference volume of 118 Å$^3$. Reference volume normalization is necessary to account for the effects of segmental asymmetry, in which the dimensions of the repeat unit for each component may be different.[143] It should be noted that the choice of reference volume is completely arbitrary, but 118 Å$^3$ (the volume of a 4-carbon repeat unit) was chosen to conform to the conventions of most BCP and BCP-lithography literature.[37,118,144,145] It is necessary to either use an identical reference volume when making a comparison between BCPs on the basis of $\chi$, or to express $\chi$ in terms of an interaction energy density.[146] As will be discussed subsequently (see Section 4.3), comparisons of $\chi$'s magnitude is best used only for qualitative trends, as the theory that underscores the basis of a quantitative analysis is currently lacking.

Table 4.2: Estimation of $\chi$ at $T_{ODT}$ by mean-field theory ODT method.

| **Polymer** | $T_{ODT}$[a] | $N$[b] | $\chi$[c] |
|---|---|---|---|
| PS-*b*-PMMA[d] | 204 | 356 | 0.029 |
| PS-*b*-PTMSS$_{20\ nm}$ | 211 | 380 | 0.028 |
| PS-*b*-PDSS$_{14\ nm}$ | 197 | 238 | 0.044 |
| PMOST-*b*-PTMSS$_{14\ nm}$ | 228 | 227 | 0.046 |

[a] $T_{ODT}$ determined by rheology in ºC.
[b] Total degree of polymerization, based on a 118 Å$^3$ reference volume.
[c] A single value of $\chi$ is calculated based on the observed $T_{ODT}$.
[d] PS-*b*-PMMA data taken from Zhao et al.[33], with a $T_{ODT}$ determined by SAXS.

That magnitude of $\chi$ measured for PS-*b*-PTMSS$_{20\ nm}$ and PS-*b*-PMMA shows no statistical difference, corroborated by their similar lamellar periodicity (*ca.* 20 nm) at nearly identical $T_{ODT}$'s. Adding a methoxy or methylsilyl functional group, as in the case of PMOST or PDSS, respectively, increases the magnitude of $\chi$ relative to PS-*b*-PTMSS$_{20\ nm}$ by approximately 1.5 times. This increase is corroborated by the fact that both

PMOST-*b*-PTMSS$_{14\ nm}$ and PS-*b*-PDSS$_{14\ nm}$ remain ordered at periodicities *smaller* than the lower-$\chi$ BCPs. Furthermore, the fact that PMOST-*b*-PTMSS$_{14\ nm}$ and PS-*b*-PDSS$_{14\ nm}$ exhibit comparable $T_{ODT}$'s at nearly equivalent $N$ corroborates the similar estimated $\chi$-values.

With only one accessible ODT for each BCP, the functional form for $\chi(T)$ cannot be demonstrated, but because the measured $T_{ODT}$'s (see Table 4.2) are relatively close, a reasonable comparison can be made between the materials based on the magnitude of $\chi$ calculated in this fashion. For the systems investigated, $\chi(T)$ was instead measured via disordered-state small-angle x-ray scattering, as discussed in the following section. This choice was made because of certain practical limitations on the ODT method. First, the polymer sample must be in the melt state $T > T_g$, but must not degrade at elevated temperatures ($T < T_d$). As $\chi$ increases, the molecular weight window that accesses the region $T_g < T_{ODT} < T_d$ becomes increasingly difficult to target. That window is often less than several kDa, and for higher-$\chi$ materials, it becomes even smaller. Secondly, the investigation of novel monomer components, which must be produced by multi-step synthetic procedures, makes a less synthetically demanding technique more attractive.

### 4.2 Disordered-State Scattering Method

The absolute intensity scattering method for measuring $\chi$ does not require multiple polymer samples to produce the temperature dependent function $\chi(T)$, unlike the ODT method. A single, disordered BCP sample, which has a segregation strength strong enough to scatters x-rays due to density fluctuations in the bulk (*i.e.* $\chi N_{MF} < \chi N < \chi N_{ODT}$, MF = mean-field), is sufficient to calculate $\chi$-values at a range of temperatures.[147] Scattering profiles were measured for bulk samples of the disordered Si-BCPs mentioned

in Table 4.1 together with a disordered PS-*b*-PMMA reference sample. Bulk samples were prepared for SAXS by annealing in air for 30 minutes at 180 ºC, well above the $T_g$ of each block (PS = 100 ºC, PMOST = 125 ºC, PTMSS = 102 ºC, PDSS = 95 ºC)

The intensity and shape of the scattering peak is dependent on a variety of thermodynamic and physical properties of the polymers. The value of $\chi$ can be extracted from these scattering profiles by fitting to Leibler's mean-field theory predicted profile,[139] corrected for the effects of molecular weight dispersity and segmental volume asymmetry.[33,141,148] Since the majority of the parameters in the scattering model can be measured experimentally, $\chi$ can be determined using a minimum mean square error (MMSE) fit between the SAXS profile and the model. The derivations of the theory are not discussed here, but a summary of the equations used to determine the scattering profile of a disordered sample are found in Eqs. 4.3-4.13.

$$I(q) = K\left[\frac{S(q)}{W(q)} - 2\chi\right]^{-1} \tag{4.3}$$

$$S(q) = \langle S_{A,A}(q)\rangle + 2\langle S_{A,B}(q)\rangle + \langle S_{B,B}(q)\rangle \tag{4.4}$$

$$W(q) = \langle S_{A,A}(q)\rangle * 2\langle S_{A,B}(q)\rangle - \langle S_{B,B}(q)\rangle^2 \tag{4.5}$$

$$\langle S_{X,X}(q)\rangle = r_{c,n} f_{X,n}^2 g_{X,n}^{(1)}(q) \tag{4.6}$$

$$\langle S_{A,B}(q)\rangle = r_{c,n} f_A f_B g_{A,n}^{(1)}(q) g_{B,n}^{(1)}(q) \tag{4.7}$$

$$r_{c,n} = \left(v_A N_{A,n} + v_B N_{B,n}\right)/(v_A v_B)^{1/2} \tag{4.8}$$

$$g_{X,n}^{(1)}(q) = \frac{1}{x_{X,n}}\left\{1 - \left[x_{X,n}(Đ_X - 1) + 1\right]^{-(Đ_X - 1)^{-1}}\right\} \tag{4.9}$$

$$g_{X,n}^{(2)}(q) = \frac{2}{{x_{X,n}}^2}\left\{-1 + x_{X,n} + \left[x_{X,n}(Đ_X - 1) + 1\right]^{-(Đ_X - 1)^{-1}}\right\} \tag{4.10}$$

$$x_{X,n} = \left(N_{X,n} b_X^2/6\right)q^2 \tag{4.11}$$

$$Đ_A = N_{A,w}/N_{A,n} \tag{4.12}$$

$$Đ_B = \frac{Đ_{BCP} - 1 - (Đ_A - 1) * w_A^2}{(1 - w_A)^2} + 1 \tag{4.13}$$

The theoretical intensity profile $I(q)$ is dependent on a proportionality constant $K$, several correlation functions, and $\chi$. In the equations, $X$ represents either block $A$ (1$^{st}$ block) or $B$ (2$^{nd}$ block), $f_x$ is the volume fraction, and $v_x$ is the molar volume (determined from the molecular weight of each monomer and the respective polymer density). $N_{X,n}$ and $N_{X,w}$ are the number average and weight average degree of polymerization, respectively. $N_{X,n}$ was calculated for block $A$ using MALDI and the second block could be determined by $^1$H-NMR of the BCP. The segment length $b_X$ can be extracted from literature for certain materials, but was used as a fitted parameter for all materials herein. The dispersity $Đ$ for the second block $B$ was calculated using equation 4.13, based on $Đ$ characterized from SEC for $A$, the $Đ$ of the BCP, and the weight fraction of the $A$ block $w_A$. Both the experimentally derived and fitted parameters used to estimate $\chi$ by the disordered state scattering method are presented in Table 4.3.

Table 4.3: Parameters used in Eqns. 4.3-4.13 to estimate $\chi$.

| **Polymer** | $w_A$ | $f_A$ | $N_A$ | $N_B$ | $Đ_A$ | $Đ_B$ | $r_{c,n}$ | $b_A$ | $b_B$ |
|---|---|---|---|---|---|---|---|---|---|
| PS-*b*-PMMA$_{Dis}$ | 0.50 | 0.53 | 112 | 116 | 1.05 | 1.02 | 228 | 0.73 | 0.89 |
| PS-*b*-PTMSS$_{Dis}$ | 0.50 | 0.48 | 133 | 79 | 1.04 | 1.13 | 205 | 0.72 | 0.88 |
| PMOST-*b*-PTMSS$_{Dis}$ | 0.50 | 0.46 | 40 | 30 | 1.02 | 1.10 | 70 | 0.86 | 0.90 |
| PS-*b*-PDSS$_{Dis}$ | 0.50 | 0.47 | 63 | 28 | 1.04 | 1.13 | 84 | 0.75 | 1.16 |
| PMOST-*b*-PDSS$_{Dis}$ | 0.54 | 0.49 | 35 | 17 | 1.04 | 1.07 | 50 | 0.90 | 1.17 |

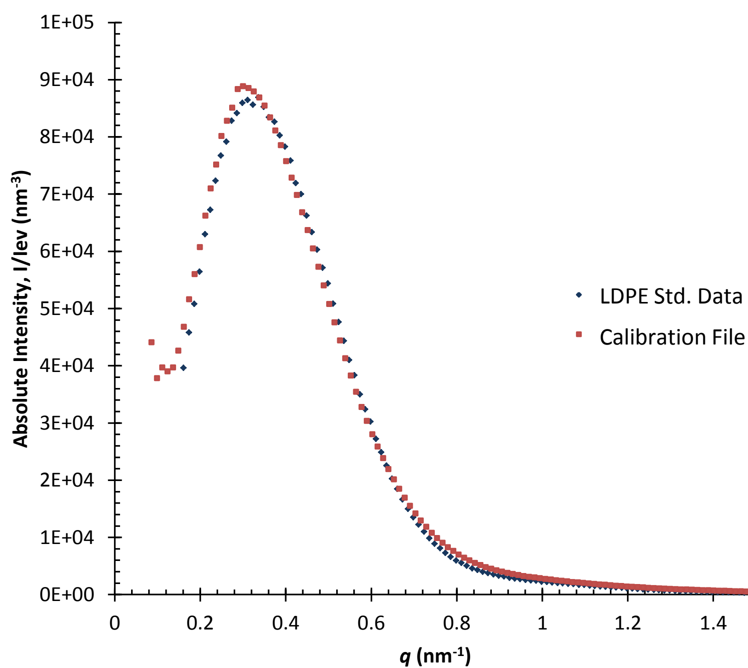


Figure 4.2: Calibration of the x-ray source using a MMSE fit of LDPE to a pre-calibrated intensity profile, producing a scaling factor *K*.

After the SAXS data of the BCPs were collected at various temperatures, the intensities were converted to an absolute scale. To do this, the lab x-ray source was calibrated against a sample with a known intensity. Typically, this calibration can be performed using a sample such as water exposed to synchrotron x-rays.[149] Although this exact calibration could not be performed, a low-density polyethylene (LDPE) standard, graciously donated by Prof. Rick Register of Princeton University, was used which had originally been calibrated against such an absolute standard. The intensity of the LDPE sample was scaled to match that of the absolute calibration file using a MMSE fit (Fig. 4.2). This scaling factor was then used to convert the intensity of all samples.

$$T = e^{-\mu t} \tag{4.14}$$

$$\mu_X = \rho_X \sum_j \left(\frac{\mu}{\rho}\right)_j w_j \tag{4.15}$$

Table 4.4: Mass attenuation coefficients of the elements comprising the polymers of this work under CuKα irradiation.

| **Element** | **$\mu/\rho$ ($cm^2/g$)** |
|---|---|
| C | 4.51 |
| H | 0.39 |
| O | 11.5 |
| Si | 63.7 |

Table 4.5: Calculated attenuation coefficients of the homopolymers comprising the BCPs in this work.

| **Polymer** | $w_C$ | $w_H$ | $w_O$ | $w_{Si}$ | **$\mu_X/\rho_X$ ($cm^2/g$)** |
|---|---|---|---|---|---|
| PS | 0.92 | 0.08 | - | - | 4.19 |
| PMMA | 0.60 | 0.08 | 0.32 | - | 6.41 |
| PMOST | 0.79 | 0.08 | 0.13 | - | 5.09 |
| PTMSS | 0.75 | 0.09 | - | 0.16 | 13.56 |
| PDSS | 0.67 | 0.09 | - | 0.24 | 18.30 |

After calibrating the source intensity, x-ray attenuation must be accounted for. The transmitted intensity was calculated from the transmission *T*, shown in Eqn. 4.14. The transmission depends on the attenuation coefficient $\mu$ (Eqn. 4.15) and the sample thickness *t*. The polymer attenuation coefficient $\mu$ was calculated from the mass attenuation coefficients $\mu/\rho$ of the elements *j*, their respective weight fractions $w_j$, and the density of the polymer $\rho_x$. The mass attenuation coefficients for the elements comprising the polymers in this study are found in Table 4.4.[150] The attenuation coefficients calculated for the homopolymer components of the BCPs are listed in Table 4.5.

$$I_{abs}(q) = K\left(\frac{I_{raw}(q)/T - I_B}{t}\right) \tag{4.16}$$

Finally, the scattered intensity was corrected for the background air concentration and Kapton tape used to contain the BCP samples. A blank sample was run containing no polymer, and the baseline was subtracted from all samples. The sample was converted to an absolute intensity scale according to Eqn. 4.16. In this equation, the absolute intensity $I_{abs}(q)$ is calculated using the scaling constant $K$, the sample transmission $T$, the background intensity $I_B$, and the sample thickness $t$. The absolute intensity profile, corrected for calibrated intensity, attenuation, and baseline, was then fitted to the theoretically predicted profile using a MMSE fit to evaluate $\chi$.

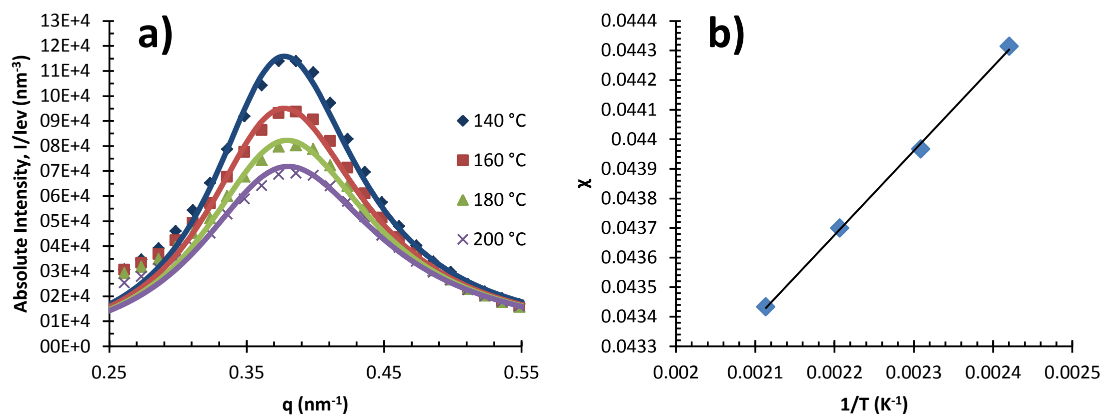


Figure 4.3: (a) SAXS profiles of PS-*b*-PMMA$_{Dis}$ and corresponding model fit near the first order scattering maximum, collected at several temperatures. (b) Plot of $\chi$ estimated from the scattering profile vs. $T^{-1}$ and the corresponding best fit line.

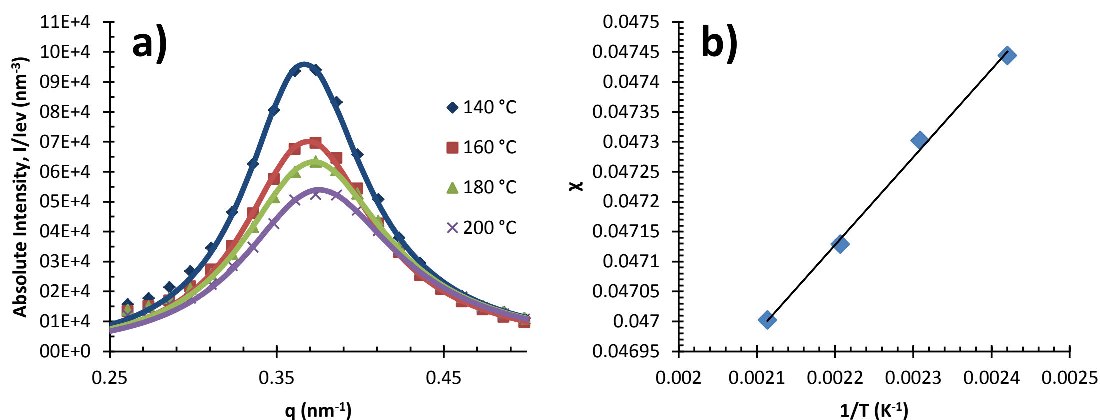


Figure 4.4: (a) SAXS profiles of PS-*b*-PTMSS$_{Dis}$ and corresponding model fit near the first order scattering maximum, collected at several temperatures. (b) Plot of $\chi$ estimated from the scattering profile vs. $T^{-1}$ and the corresponding best fit line.

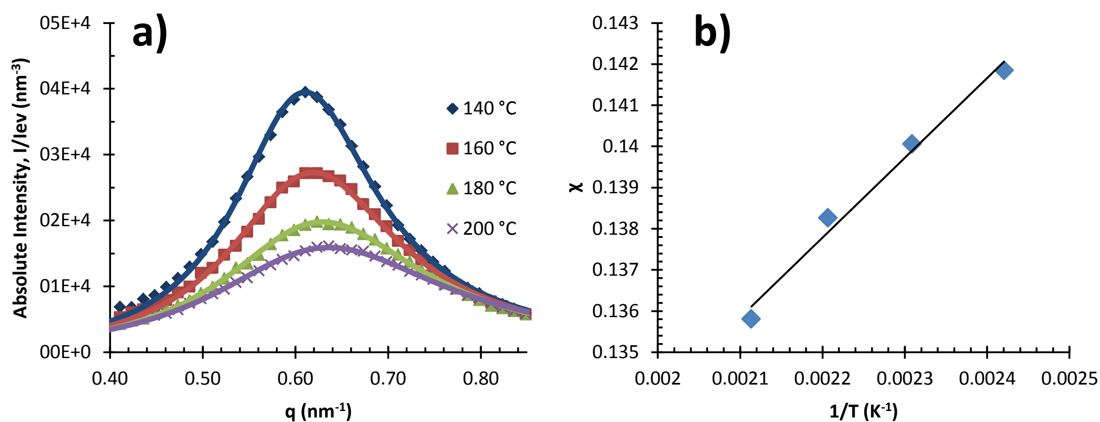


Figure 4.5: (a) SAXS profiles of PMOST-*b*-PTMSS$_{Dis}$ and corresponding model fit near the first order scattering maximum, collected at several temperatures. (b) Plot of $\chi$ estimated from the scattering profile vs. $T^{-1}$ and the corresponding best fit line.

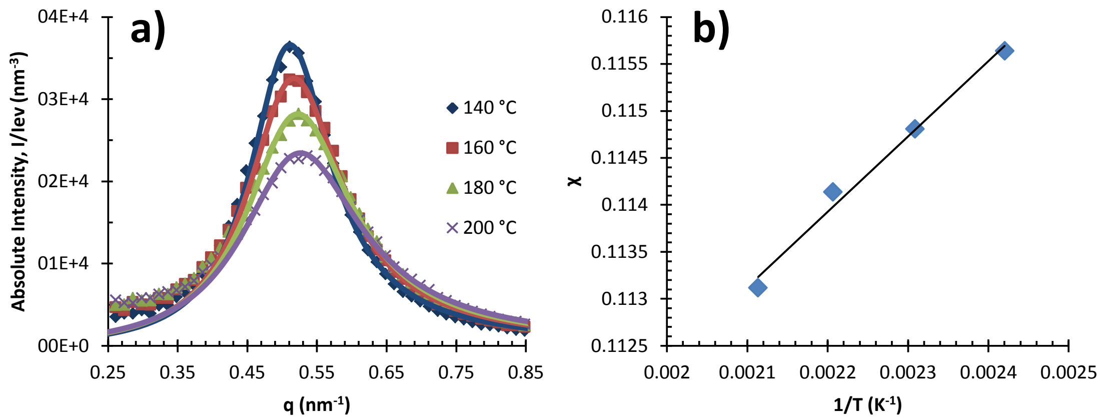


Figure 4.6: (a) SAXS profiles of PS-*b*-PDSS$_{Dis}$ and corresponding model fit near the first order scattering maximum, collected at several temperatures. (b) Plot of $\chi$ estimated from the scattering profile vs. $T^{-1}$ and the corresponding best fit line.

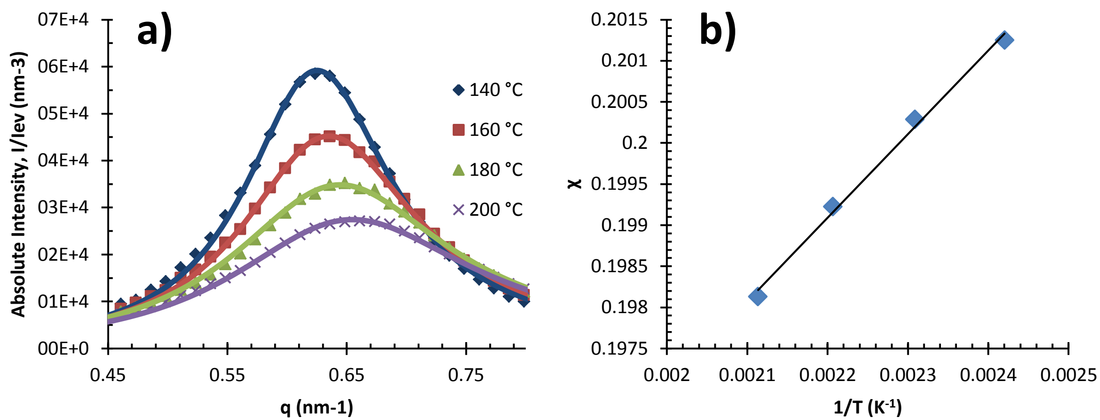


Figure 4.7: (a) SAXS profiles of PMOST-*b*-PDSS$_{Dis}$ near the first order scattering maximum, collected at several temperatures. (b) Plot of $\chi$ estimated from the scattering profile vs. $T^{-1}$ and the corresponding best fit line.

Figures 4.3-4.7a show the SAXS profiles of the scattering maximums for materials investigated herein. The absolute intensity of the scattered x-rays is plotted against the primary scattering vector $q$. SAXS profiles were collected over a range of

temperatures relevant to thermal annealing processing. As the temperature increases, the intensity of the scattering maximum decreases because $\chi$ is inversely proportional to $T$ and for these materials, the enthalpic contribution $\alpha$ is positive. For each sample and temperature, the model fit shows good agreement with the SAXS absolute intensity profile after a MMSE fit.

Table 4.6: $\chi(T)$ coefficients measured by disorder-state scattering.

| **Polymer** | $\alpha$ | $\beta$ |
|---|---|---|
| PS-*b*-PMMA$_{Dis}$ | 2.85 | 0.037 |
| PS-*b*-PTMSS$_{Dis}$ | 1.46 | 0.044 |
| PS-*b*-PDSS$_{Dis}$ | 8.02 | 0.096 |
| PMOST-*b*-PTMSS$_{Dis}$ | 19.38 | 0.095 |
| PMOST-b-PDSS$_{Dis}$ | 10.17 | 0.177 |

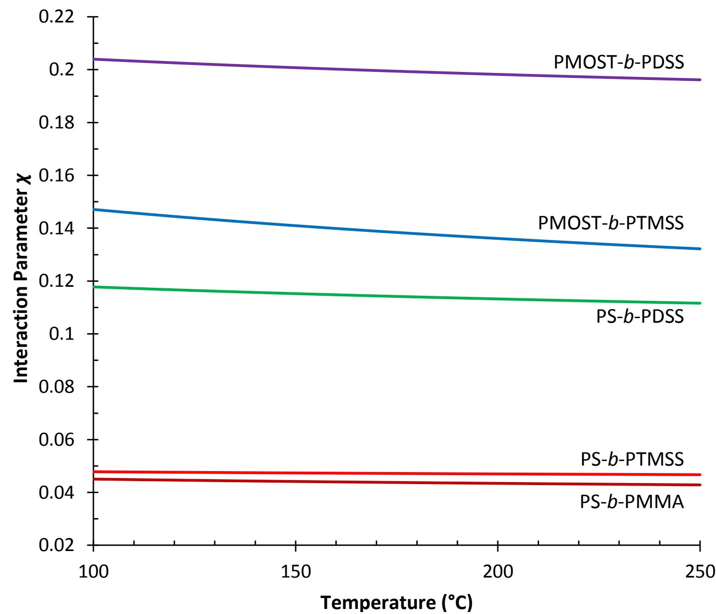


Figure 4.8: The $\chi$ of each disordered BCP measured by absolute scattering, plotted as a function of temperature.

The $\chi$-values estimated for each condition are plotted as a function of temperature in Figures 4.3-4.7b. The values are fitted with a linear least-squares regression to extract the coefficients $\alpha$ and $\beta$ of $\chi(T)$, presented for each BCP in Table 4.6. The magnitude of the coefficients represents the enthalpic and entropic contributions towards $\chi$ for each material. Fig. 4.8, which shows the temperature dependence of $\chi$ for all BCPs, also emphasizes these contributions based on the slope of the relationships and the relative magnitude of differences in $\chi$. None of the materials investigated have a strong temperature dependence in the range of interest, indicated by the shallow slope of the curves.

Within the PS-*b*-PTMSS styrene platform reported here, introducing a hydrophilic functional group such as methoxy increases the chemical distinction between the more hydrophobic domains, increasing $\chi$ by a factor of ≈3. Similarly, adding a more hydrophilic trimethylsilyl group to PTMSS, as with PDSS, also increases $\chi$ by a factor of ≈3. It is thus satisfying to see that changing *both* blocks simultaneously, such as with PMOST-*b*-PDSS, produces roughly additive gains in $\chi$ (*i.e.* an increase by a factor of ≈5). The ability to change $\chi$ in a rational way by appending these functional groups to the styrenic monomer suggests that similar trends could be predicted by appropriate addition of other moieties.

The qualitative results of the scattering study are consistent with those from the mean-field theory ODT method. The first set of materials, PS-*b*-PMMA and PS-*b*-PTMSS, have roughly equivalent $\chi$-parameters. The second set, PMOST-*b*-PTMSS and PS-*b*-PDSS, have a similar $\chi$-parameter, which is several times that of the first set. The qualitative trends from both methods support making reasonable distinctions between materials (*i.e.* the magnitude of PS-*b*-PDSS is consistently higher than PS-*b*-PMMA), however there is moderate disagreement between the quantitative values derived by the

two methods. For example, PS-*b*-PTMSS measured by scattering is approximately 70% higher than that predicted by the ODT method. Even the reference material, PS-*b*-PMMA, resulted in a measured $\chi$ that was 10-15% higher than recently reported values.[33] This specific error for PS-*b*-PMMA may be the result of $\chi$'s molecular weight dependence (*i.e.* using non-identical samples),[151] but a further discussion of the quantitative discrepancies is warranted, provided in Section 4.3. Nevertheless, this study implies that regardless of what method is used to make the measurements, quantitative comparisons of BCP systems should only be made with the inclusion of well-trusted reference materials.

### 4.3 Challenges for Evaluating High-x Block Copolymers

Analysis of the Si-BCP's $\chi$ by both the ODT and scattering methods demonstrates quantitative differences between the two theories. Maurer et al.[39] have presented a thorough experimental study of discrepancies that exist between $\chi$ measured using homopolymer blends, ODT experiments, and disordered-state scattering. Their evidence affirms that $\chi$ for BCPs may lie >20-40% above the value measured for homopolymer blends, which is assumed to be the most fundamental measure of the segment-segment interactions that control phase behavior. Both the magnitude and slope of $\chi(T)$ show significant differences when evaluated by the ODT and scattering methods. It is speculated that diblock polarization and chain stretching in the vicinity of the ODT contribute to most of these discrepancies. The study by Maurer et al. was focused on relatively low-$\chi$ materials (and hence relatively high $N$) compared with this work, so the even more dramatic discrepancies between methods investigated in this chapter are not surprising.

Most of the theories used to evaluate $\chi$ operate on the assumption of large $N$. for higher-$\chi$ systems and lower $N$, both an upwards shift of the phase boundary (see Fig. 1.5) and modification of the interfacial width are predicted.[22] Therefore, the MFT treatment of phase behavior may be non-ideal and the assumption of an ODT at $\chi N$ = 10.5 (used for Eqn. 4.4) may not be appropriate. Similar issues arise for scattering theory; thermal fluctuation effects can enhance the disordered-state peak intensity, artificially enhancing $\chi$ relative to homopolymer blend behavior.[147,152] These complications are presumed to be the dominant factors contributing to differences between the methods used to evaluate the Si-BCPs. Fortunately, the smaller accessible feature sizes for the higher-$\chi$ Si-BCPs (Table 4.1) corroborate trends in $\chi$-values for both the ODT and scattering methods.

Beyond the challenges of correctly describing the BCP theory, there are several practical limitations that make estimating $\chi(T)$ difficult. For the ODT method, multiple samples with an accessible $T_{\mathrm{ODT}}$ are required to produce the functional form of $\chi$. This synthetically rigorous process requires targeting a narrow molecular weight window, as discussed in Section 4.1. These limitations become even more strenuous as $\chi$ is increased. A higher $\chi$ requires lower molecular weights to produce samples with a $T_{\mathrm{ODT}}$, which can make processing more difficult as they resemble more oligomeric materials. In addition, for high-$\chi$ BCPs with a small $\alpha$ (*i.e.* weak temperature dependence, see Table 4.6), the targeted molecular weight window could be only a few repeat units, making synthesis of multiple materials prohibitive.

The scattering method also presented some practical challenges. The first reason is due to the fitting procedure, which requires minimization of errors as a function of multiple variables. This iterative process requires effectively choosing a starting condition that will yield a converged solution, a process that is not trivial when adjusting multiple parameters. Often, the estimated $\chi$ could change by several percentage points

simply by varying the initial guess. The best practice was found by seeding the initial guesses with experimentally derived data or intuitive results.

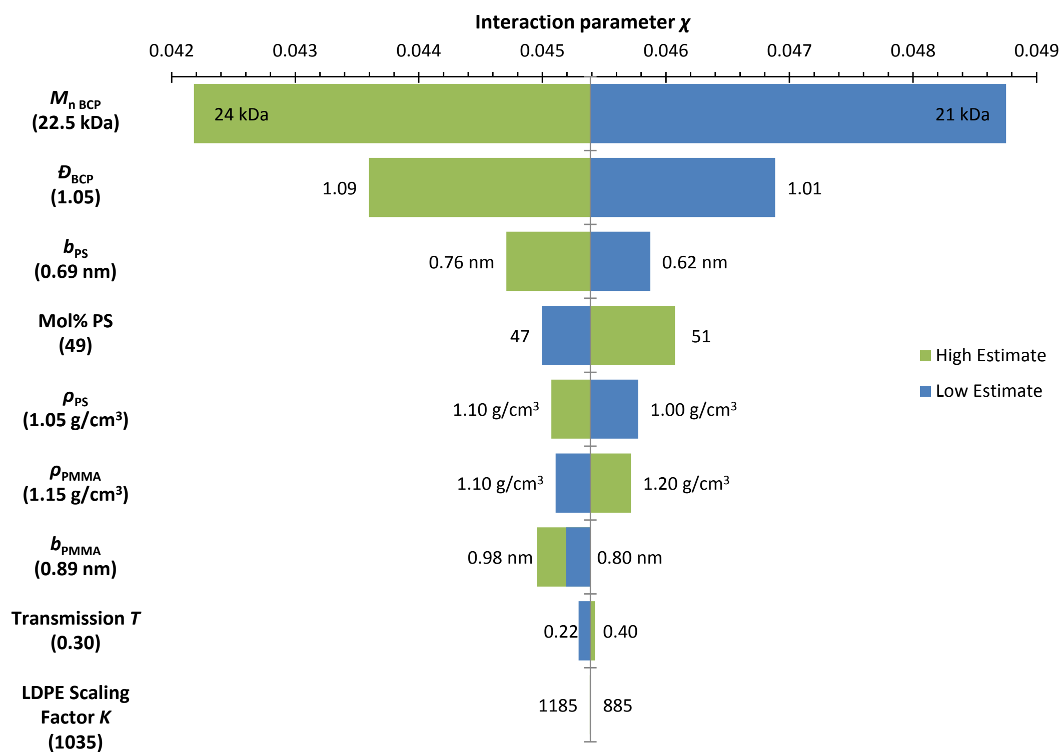


Figure 4.9: Tornado plot for PS-*b*-PMMA (ranked from high to low) emphasizing the sensitivity of $\chi$ to various experimentally derived parameters.

The second challenging limitation was the estimated $\chi$'s sensitivity to measurement errors. A tornado plot (Fig. 4.9) was produced for PS-*b*-PMMA to investigate the sensitivity of $\chi$ to multiple experimentally derived parameters of the scattering analysis. The base estimated $\chi$-value ($\approx$ 0.0454) is the center axis, calculated from the average value of each parameter. The investigated parameters (and their average value in parenthesis) are plotted on the vertical axis. The widths of the bars represent the magnitude of the deviation in $\chi$ for several low and high estimates of each parameter (values shown next to each bar). The sensitivity is ranked from high to low in the vertical

direction. The tornado plot shows that the estimated $\chi$ was most sensitive to the BCP molecular weight, producing errors greater than 7%. The second most significant parameter was the polymer dispersity $Đ$. Both these parameters have many experimental techniques to measure their values, thus it is recommended to use the most accurate techniques (*e.g.* MALDI) to ensure that the estimated $\chi$-values are reasonable. Some of the least sensitive parameters were the BCP transmission $T$ and LDPE standard scaling factor $K$. Both parameters are used to convert the SAXS intensity to an absolute scale, but seemingly do not have a strong impact on the calculated $\chi$.

The issues described above testify to the danger of evaluating lithographic materials using only $\chi$ as a metric of comparison. Not only is the theory not yet able to fully account for the quantitative disagreements between the measurement methods, but comparison between samples without a reliable reference material can be misleading. Perhaps reporting the minimum achievable feature size before disordering is a more relevant metric for lithographic applications, although factors such as etch contrast or segregations strength may limit practical performance.

## 4.4 Effect of Segregation Strength

The ordered Si-BCPs were annealed between two neutral interfaces to induce perpendicular orientation of the lamellar domains. The films were etched to expose the organosilicon domains, and the resulting structures are indicative of the pattern quality expected for each material. Not only is the fidelity dependent on the etch performance of each block, but the segregation strength affects the quality of the patterns. Figure 4.10 shows the etched images of the Si-BCPs from both a top-down and angled perspective.

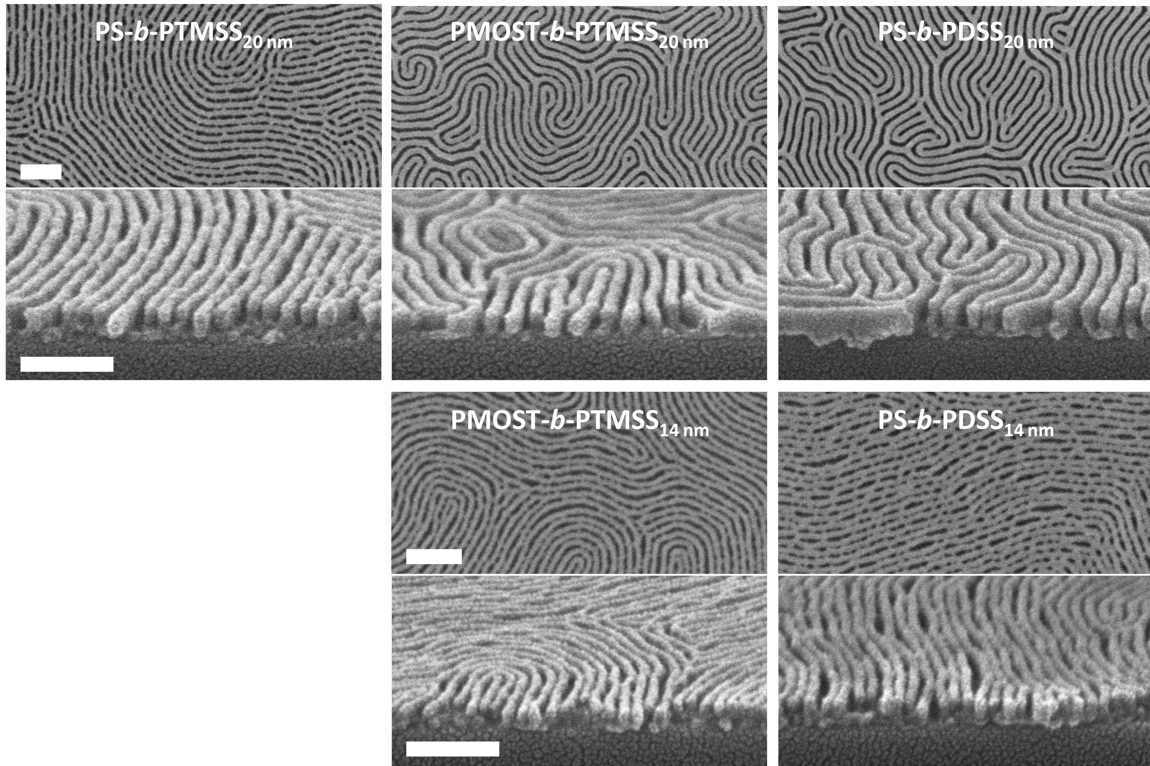


Figure 4.10: Top-down and angled SEM images of Si-BCPs after etching. As cast film thicknesses are *ca.* $1.75L_0$. Scale bars are all 100 nm and apply to each row of figures, respectively.

All the Si-BCPs show through-film perpendicular orientation with no observable dislocations or parallel features. This is significant because it not only demonstrates that the top coat process flow used to neutralize the interfaces is valid for a variety of Si-BCPs, but the materials can successfully function as a high aspect ratio etch masks for transferring the patterns into the underlying substrates.

The pattern fidelity of the processed films is directly related to the $\chi$ for each material and their corresponding segregation strength ($\chi N$).[138] The lower $\chi$ material, PS-*b*-PTMSS$_{20\ \mathrm{nm}}$ exhibits bridging between domains and line collapse that is not evident in the higher-$\chi$, intermediate-segregated PMOST-*b*-PTMSS$_{20\ \mathrm{nm}}$ or PS-*b*-PDSS$_{20\ \mathrm{nm}}$ of the same dimensions. The origin of this behavior is unclear, although it is potentially due to the

transition from a square-wave type composition profile in the more strongly segregated regime ($\chi N > 10.5$), versus a sinusoidal type composition profile in the weak segregation limit ($\chi N = 10.5$).[153] These phenomena may be observed in the weakly-segregated BCPs due to residual silicon oxide that remains between domains after etch processing. The effect of transitioning to weak segregation is further evidenced by PMOST-*b*-PTMSS$_{14\ nm}$ and PS-*b*-PDSS$_{14\ nm}$ (Fig. 4.10, bottom row). Both of these weak-segregated analogues of the 20 nm BCPs show bridging and line collapse, similar to that observed with PS-*b*-PTMSS$_{20\ nm}$. This demonstrates that weaker segregation strength impacts the pattern fidelity by introducing various defects into the assembly. High segregation strength materials are thus desirable because they produce well-defined domains suitable for patterning. Both the minimum resolvable periodicity (related to $\chi$) and the segregation strength ($\chi N$) are relevant concerns when designing BCPs for lithography.

It is also worth closely comparing the etch performance of the intermediate-segregated materials with a comparable $\chi$ and segregation strength (PMOST-*b*-PTMSS$_{20\ nm}$ or PS-*b*-PDSS$_{20\ nm}$). These materials have similar performance in terms of their minimum dimensions and estimated $\chi$, but their quality as an etch mask are slightly different. The BCP containing PTMSS has a silicon content of 16 wt. %, while the PDSS BCP contains 24 wt. %. The higher silicon content improves the etch contrast slightly (see Section 3.1), resulting in a post-RIE aspect ratio of 2.2:1 for the PTMSS material, versus 3:1 for PDSS. Thus, although the segregation properties of the polymers are similar, the lithographic performance may be disparate. This highlights the importance of etch contrast as a critical property for patterning BCPs, in addition to segregation strength and other factors.

### 4.5 Conclusions & Outlook

A series of lamellae-forming organosilicon BCPs, amenable to thermal annealing by polymeric top coats, were synthesized at a variety of molecular weights to study their properties. Using a material familiar to the authors as a baseline (PS-*b*-PTMSS), corresponding Si-BCPs with either a hydrophilic block (PMOST-*b*-PTMSS), or a hydrophobic block (PS-*b*-PDSS), or both "modifications" (PMOST-*b*-PDSS), were synthesized and evaluated for potential use as lithographic materials in self-assembly applications. The $\chi$ of the materials was estimated by two methods: the SCFT-predicted order-disorder transition and the absolute intensity scattering profile. Although there is some quantitative disagreement between the methods, the same qualitative behavior emerges from both approaches. As the polymers are modified to become more chemically distinct, the $\chi$ increases significantly. Further modifications produce additive improvements to the styrenic system, providing a design route to higher performing BCPs by appropriate choice of appended functional groups.

The quantitative discrepancies found when evaluating $\chi$ are likely a result of the theory used to describe self-assembly in the weak-segregation regime (*i.e.* accounting for thermal fluctuation effects, chain stretching, etc.). These issues make it difficult to compare materials evaluated by various experimental methods, complicated by the fact that the methods for measuring $\chi$ are often largely sensitive to experimental errors. Therefore, it is best to only consider the qualitative trends predicted by such techniques and perhaps instead focus on more physical metrics for comparison, such as minimum ordered resolution or lithographic performance.

The Si-BCPs were oriented in thin films to show perpendicular lamellae, and the films were etched to demonstrate their lithographic performance as a function of segregation strength. The weak-segregated materials show evidence of defects and poor

assembly not seen in the more strongly-segregated materials, thus segregation strength is a critical parameter to consider when evaluating BCPs for lithography. In addition, the materials can function differently depending on their silicon content; higher silicon-content produces greater etch contrast, thus performs better when fabricating high aspect ratio structures of BCPs.

### 4.6 EXPERIMENTALS

***Materials***

All organosilicon BCPs were synthesized anionically, as discussed in Chapter 3. Disordered PS-*b*-PMMA (nominally 10 kDa -*b*- 10kDa, $Đ$ = 1.05) was purchased from Polymer Source and used as received. The LDPE calibration sample was graciously provided by Prof. Rick Register of Princeton University

***Instrumentation***

Rheology data were collected on a TA Instruments AR-2000EX using a 25 mm parallel plate operating in strain controlled mode. Each sample was measured at strain = 2% and angular momentum ($\omega$) = 1 rad/s in the linear viscoelastic regime. Samples were ramped at 5 ºC/min under nitrogen flow until a discontinuity in the storage/loss modulus was observed.

Small-angle x-ray scattering data was collected using a Molecular Metrology instrument equipped with a high brilliance rotating copper anode source ($K_\alpha$ radiation, $\lambda$ = 1.5418 Å) and a two-dimensional 120 mm gas filled multi-wire detector. Vertical focus was acquired with a single crystal germanium mirror, and horizontal focus and wavelength selection was made with an asymmetrically cut Si(111) monochromator. The beam was calibrated using silver behenate with its primary reflection peak set at 1.076

$nm^{-1}$. Samples were heated using an Instec mK 1000 temperature controller with a HCS 402 hot stage.

All films were coated on a Brewer Science CEE 100CB Spincoater. Annealing was performed on a Thermolyne 11515B hot plate. Ellipsometry measurements were taken with a J.A. Woolam Co., Inc. VB 400 VASE Ellipsometer. Oxygen reactive ion etching was performed on a commercial 300 mm capacitively-coupled plasma reactor, Lam Research 2300® Flex™ E Series, which contained confined plasma technology and multi-source RF frequencies applied to the bottom electrode. Coupons (2000 $mm^2$) with assembled BCP patterns were thermally pasted (Type 120 Silicone, Wakefield Solutions) onto the center of 300 mm ArF resist carrier wafers for all etch tests. Top-down SEMs were collected using a Hitachi S-9380II CD-SEM operating at an accelerating voltage of 800 V and a working distance of 2.7-2.8 mm. A Zeiss Supra 55 SEM operating at 5 kV with the in-lens detector and a working distance of 2-4 mm was used to collected angled SEM data. Samples were sputtered with Au/Pd for 3 s prior to imaging. Additional details on thin film preparation of BCPs are found in Chapter 5.

### 4.6.1 Disordered-State Scattering Experiments

Disordered samples of each BCP were melted on a hot plate between Kapton tape, separated by a Viton o-ring. Polymer powder was continuously added within the space of the ring ($t \approx 2$ mm) until full with melted material. The BCP was then confined between the Kapton tape and annealed for an additional 30 minutes at 180 ºC.

A blank sample (two pieces of Kapton tape separated by a Viton o-ring, with a small perforation to vent air) was run at 35 ºC after pumping down for > 2 hrs. to the baseline pressure. Next, AgBe (5.838 nm) was run for *ca.* 3 min. to calibrate the detector. The LDPE standard was run at 35 ºC after pumping down the chamber for > 1hr. Finally,

the BCP was placed into the heat stage, pumped down for > 2 hr., and equilibrated at the first measured temperature (140 ºC) for 30 min. After finishing a sample run, the stage was set to the next temperature and equilibrated for an additional 15 min. Samples held at 35 ºC were done so to minimize any error due to fluctuations in room temperature. All samples unless otherwise specified were run for 30 minutes.

**4.6.2 Polymer Density Measurements**

The density of each homopolymer was measured according to Archimedes' principle, necessary for volume fraction and attenuation calculations. Homopolymer samples were synthesized by either anionic or free-radical polymerization and isolated as a powder. The powders were converted to small, melted polymer pellets by hot pressing the powder with a KBr pellet press. Dry powder was loaded into the press and packed loosely, and the metal sample holder was heated on a hot plate at 180 ºC, turning frequently (using metal tongs) to maintain a somewhat uniform heat distribution. While the sample holder was still hot (*i.e.* $T > T_g$), it was transferred and pressed using the KBr hand press. This process was repeated several times until a uniform, transparent glass was produced. A finished pellet was removed from the press after cooling (*i.e.* $T < T_g$) and was transferred to a piece of aluminum foil on the hotplate at 180 ºC. The pellet was annealed this last time to remove any residual stresses, and the pellet was cooled and collected for measurement. Pellets were ideally *ca.* 50 mg or more.

Table 4.7: Density of homopolymer melts according to Archimedes' principle.

| **Polymer** | **$\rho$ (g/cm$^3$)** |
|---|---|
| PS | 1.050 |
| PMMA | 1.180 |
| PTMSS | 0.963 |
| PDSS | 0.916 |
| PMOST | 1.128 |

Density measurements were performed on a Mettler Toledo XP105 mass balance using a standard Density Kit. Water was used as the immersion fluid, and the fluid temperature was recorded before every measurement. Density measurements were performed on five samples of each homopolymer, and the average of these measurements is shown in Table 4.5. Density values have a low standard deviation (< 1%) and samples of known materials (*e.g.* PS and PMMA) show excellent agreement with the literature.

# Chapter 5: Block Copolymer Orientation Control

Lamellar BCP orientation in thin films is primarily a function of two factors: the surface energy at the respective interfaces and the commensurability of the film thickness with the BCP's equilibrium bulk periodicity $L_0$.[34,41] For thin films annealed on a substrate with a free air/vacuum interface (*i.e.* unconfined), the BCP minimizes its free energy by forming layers commensurate with $L_0$. If thicknesses are incommensurate with the $L_0$, island/hole-like topography can form to alleviate entropic frustration (see Section 2.1). Films confined between hard walls cannot relax in such a fashion; the polymer chains must stretch or compress to occupy the space between the walls. This frustration can induce perpendicular orientation or create more complex morphologies.[43,154,155] Although the surface energy in the perpendicular orientation may not be minimized, the domain periodicity can relax to the bulk spacing $L_0$.

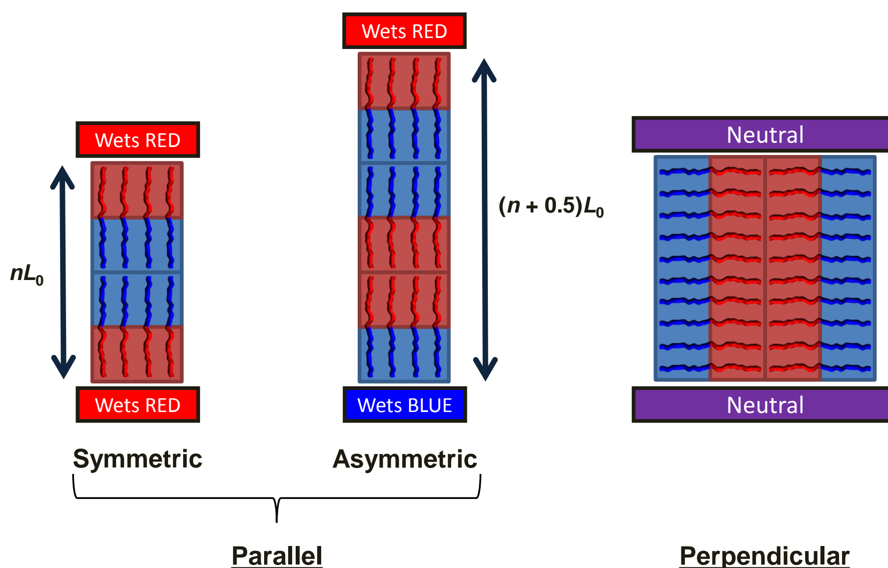


Figure 5.1: The three orientations studied in the free energy model herein and the corresponding commensurability conditions.

We utilized a free energy model to predict the process conditions most favorable for perpendicular orientation. For this model, three orientations are considered: parallel (symmetric and asymmetric) and perpendicular (Fig. 5.1). Parallel oriented films prefer to quantize into thicknesses that are commensurate with the bulk periodicity $L_0$. These commensurate conditions are dependent on the wetting behavior of the BCP. For example, if the BCP *symmetrically* wets each interface, it will prefer to quantize into integer multiples of $L_0$. If the BCP *asymmetrically* wets each interface, it will prefer to quantize into $(n + 0.5)$ multiples of $L_0$. Perpendicular orientation maintains the bulk periodicity and is not subject to such quantization effects.

The development of the free energy model and its extension to produce response surfaces capable of predicting orientation conditions are the subject of this chapter. The model is supplemented with an extensive body of experimental work that serves to support the qualitative conclusions and provide insight into the practical considerations that affect orientation. Finally, several applications of the model are provided as a future outlook.

## 5.1 Algebraic Model Development

For symmetric diblock copolymers in the strong segregation regime, theory has been developed to describe the free energy of self-assembly in terms of enthalpic $E_H$ and entropic $E_S$ contributions.[156,157] The driving force for microphase separation is a balance between the interfacial energy resulting from segregation ($E_H$) and the entropic penalty for organizing the chains from their disordered state conformations. The bulk free energy can be described by Eqn. 5.1 as a combination of these contributions, where $\zeta$ is the

number of polymer chains, $a$ is the statistical segment length, $\chi$ is the interaction parameter, $N$ is the number of polymer segments, and $L$ is the lamellar period.

$$\frac{F}{kT} = E_H + E_S = 2\zeta a\sqrt{\frac{\chi}{6}}\left(\frac{N}{L}\right) + \frac{3\zeta}{8a^2}\left(\frac{L}{N^{1/2}}\right)^2 \quad (5.1)$$

The derivative of the free energy with respect to $L$ gives the bulk equilibrium lamellar period $L_0$ (Eq. 5.2). This relation is consistent with experimental studies[158,159] showing that $L_0 \propto N^{2/3}$. The corresponding bulk equilibrium free energy can then be found as Eqn. 5.3.

$$L_0 = 2a\left(\frac{1}{3}\sqrt{\frac{\chi}{6}}\right)^{1/3} N^{2/3} \quad (5.2)$$

$$\frac{F_0}{kT} = \frac{3\zeta}{2}\left(\frac{\chi}{2}\right)^{1/3} N^{1/3} \quad (5.3)$$

These models were later extended to describe the behavior of BCPs confined between infinite, parallel plates as a function of surface interaction terms $\gamma$ and the plate spacing, or thickness $t$.[160,161] These equations were simplified herein to express the free energy normalized to the bulk equilibrium free energy $F_0$ for the three orientation conditions: parallel (horizontal) symmetric/asymmetric (Eqn. 5.4-5.5) and perpendicular (vertical) (Eqn. 5.6).

$$\frac{F_{H_SYM}}{F_0} = \frac{1}{3}\left[\left(\frac{t}{n}\right)^2 + \frac{2n}{t} + \frac{1}{t}\left(\frac{\gamma_{A_Top}+\gamma_{A_Btm}}{\gamma_{AB}}\right)\right] \quad (5.4)$$

$$\frac{F_{H_ASYM}}{F_0} = \frac{1}{3}\left[\left(\frac{t}{n+0.5}\right)^2 + \frac{2(n+0.5)}{t} + \frac{1}{t}\left(\frac{\gamma_{A_Top}+\gamma_{B_Btm}}{\gamma_{AB}}\right)\right] \quad (5.5)$$

$$\frac{F_V}{F_0} = \frac{1}{3}\left[3 + \frac{1}{2t}\left(\frac{\gamma_{A_Top}+\gamma_{B_Top}+\gamma_{A_Btm}+\gamma_{B_Btm}}{\gamma_{AB}}\right)\right] \quad (5.6)$$

This algebraic model considers the interactions $\gamma$ of the two components ($A$ and $B$ blocks) with the substrate and top interfaces (labeled Btm and Top, respectively). The system is defined such that $\gamma_A < \gamma_{B,}$ and $\gamma_{AB}$ represents the interaction between the two blocks.

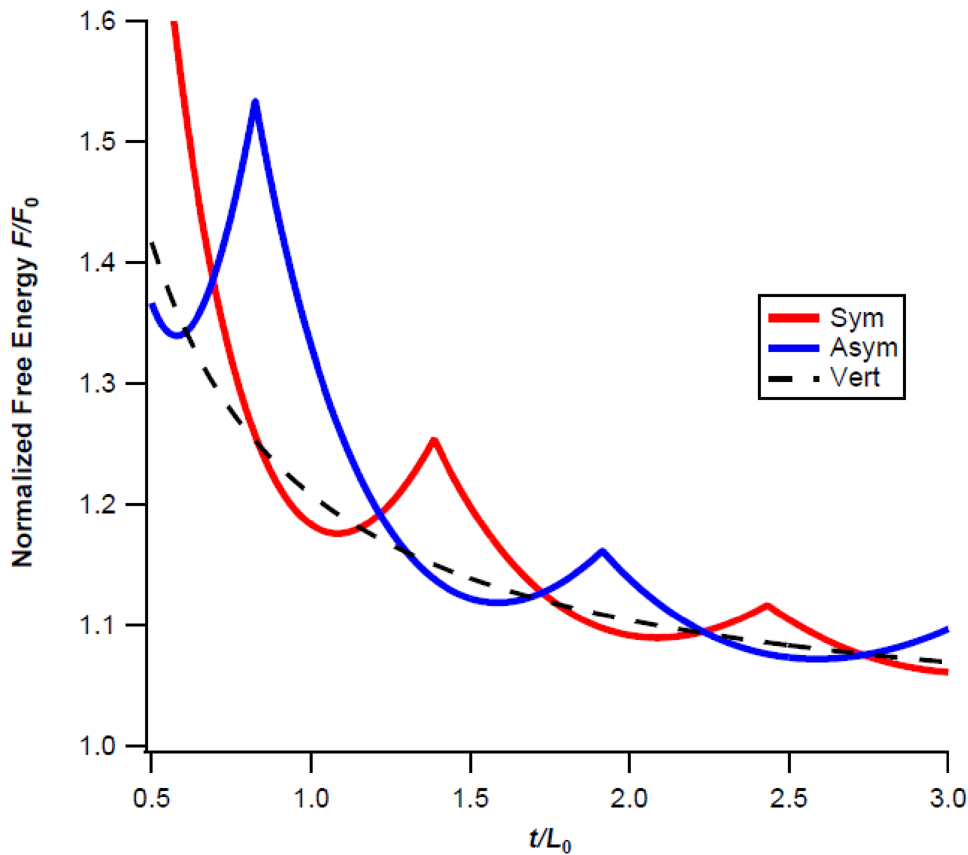


Figure 5.2: A representative set of free energy curves produced using the algebraic model for parallel (symmetric/asymmetric) and vertical orientations. The lowest free energy of the three curves is predicted to be the favored orientation.

When the free energy curves are plotted as a function of film thickness, the minimum free energy condition indicates the most favored orientation. Fig. 5.2 shows the free energy curves calculated for a representative condition ($\gamma_{A_Top} = 4$, $\gamma_{A_Btm} = 5$, $\gamma_{B_Top}$

= 5, $\gamma_{B_Btm}$ = 5, $\gamma_{AB}$ = 10). Each free energy curve for parallel orientation reflects the commensurate conditions for that configuration. For example, the parallel symmetric wetting curve (red) has local minima that exist near $nL_0$, while the asymmetric wetting curve (blue) has local minima near the $(n + 0.5)L_0$ conditions. As mentioned previously, the vertical orientation (dashed line) is not subject to these commensurability conditions.

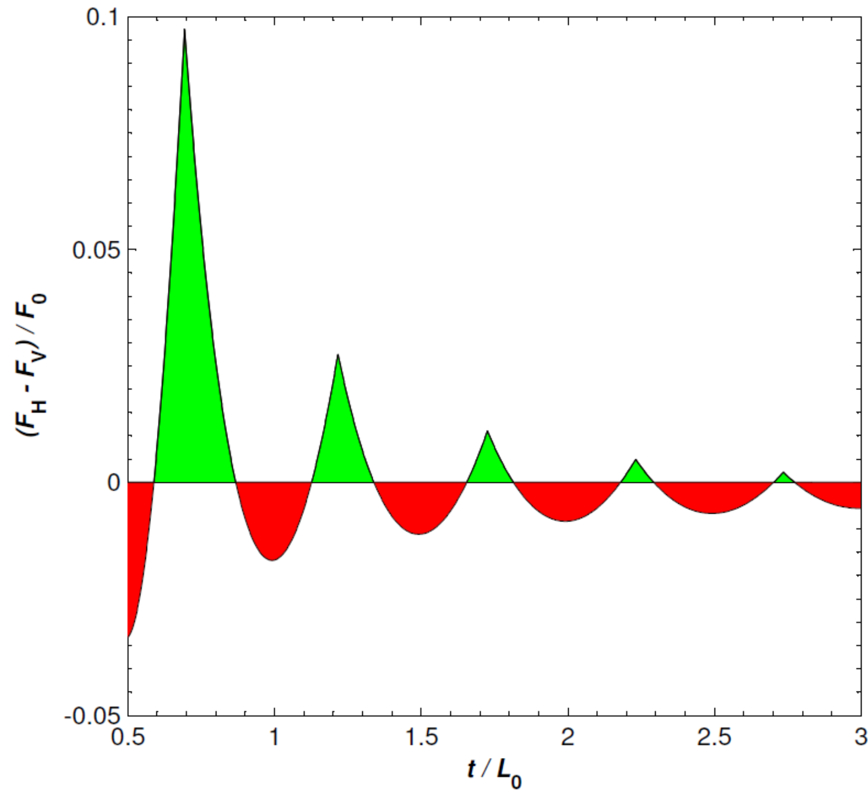


Figure 5.3: Free energy difference between horizontal and vertical orientations for a representative condition. Regions above the zero-axis (green) indicate perpendicular orientation, while those below (red) are parallel.

The model was further adapted to more easily depict the conditions favorable for perpendicular orientation. The free energy difference between the parallel and perpendicular conditions for the same representative set of parameters as above was

calculated to produce the graph shown in Fig. 5.3. In this figure, the regions above the zero-axis (green) represent favorable conditions (*i.e.* lowest free energy) for perpendicular orientation, whereas the regions below the zero-axis (red) are favorable for parallel orientation. The energetic driving force for a given orientation is indicated by the absolute magnitude of the calculated energy, and the width of each colored region is effectively the process window (*i.e.* thickness window) expected for each orientation.

Although this algebraic model is relatively simple, its qualitative behavior matches that of similar work performed by more complex SCFT[41,162] and Monte Carlo simulations[163]. The advantage of the algebraic model is its simplicity; calculations can be easily performed, thus many conditions can be modeled with few resources. As will be shown in the subsequent sections, multi-dimensional response surfaces can be generated to identify the conditions favorable for perpendicular orientation. These response surfaces describe the orientation behavior as a function of both the bottom and top interface preference to provide a rational guide for thin film processing.

## 5.2 Orientation Behavior – Single Interface Modification

Many different methods have been demonstrated that neutralize the bottom interface of BCP thin films (see Section 1.4.3), but only recently have methods for efficiently modulating the top interface been introduced (see Chapter 2). Thus, as an initial step, we consider a condition in which the bottom interface has no preference towards either component ($\gamma_{A_Btm} = \gamma_{B_Btm}$, *i.e.* neutral), and the top interface preference can be adjusted independently. The process conditions favorable for perpendicular orientation were then examined both by response surface analysis based on the algebraic model and by comprehensive thin film experiments.

***Response Surface Analysis***

Response surface plots for a neutral bottom interface are shown in Fig. 5.4. The free energy is shown as both a three-dimensional surface and as a color plot (essentially looking down the z-axis of the 3D surface). The surface plot emphasizes the magnitude of the changes in free energy while the color plot easily identifies the conditions favorable for a given orientation. The free energy is plotted as a function of the reduced film thickness $t/L_0$ and top surface preference. Surface preference is defined as the difference between $\gamma_A$ and $\gamma_B$. A positive surface preference implies attraction towards the block *A*, while a negative preference implies attraction towards block *B*. Therefore, by changing the magnitude and sign of the preference at each interface, various process conditions can be observed. It should be noted that only the magnitude of the *difference* between interaction strength impacts the qualitative behavior predicted by the model (*i.e.* the absolute values of $\gamma_A$ or $\gamma_B$ do not affect the qualitative results, only $\Delta\gamma \equiv \gamma_A - \gamma_B$).

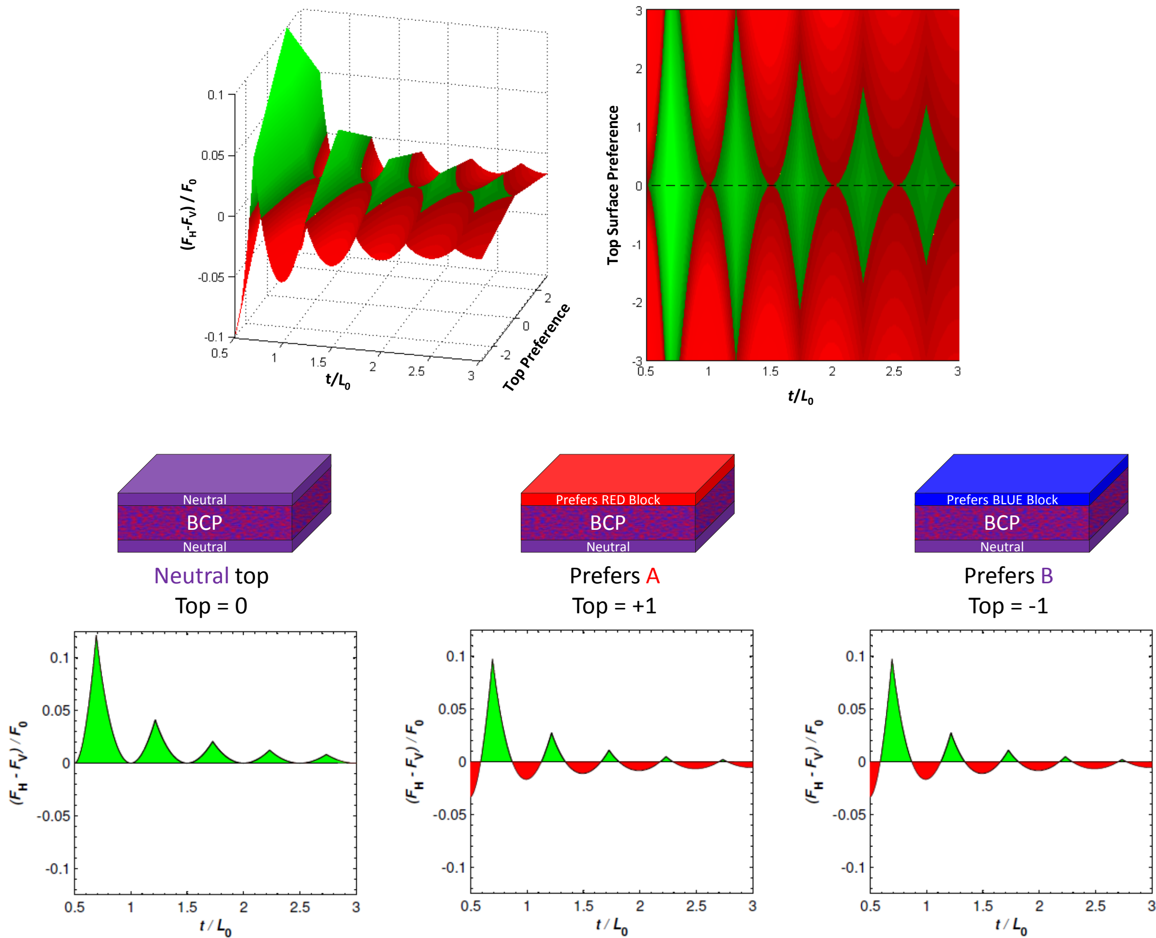


Figure 5.4: Response surface plots and x-z plane cross-sections thereof for a neutral bottom interface ($\Delta\gamma_{Btm} = 0$).

A cross-section of the response surface through the x-z plane represents a constant top coat preference, and enables free energy evaluation as a function of $t/L_0$. If the top surface preference is neutral (*i.e.* a cross-section through the zero-axis), the BCP film is confined between two neutral interfaces. Under this condition, perpendicular orientation is favored at all thicknesses. The thicknesses most favorable for perpendicular orientation are incommensurate for both $nL_0$ and $(n + 0.5)L_0$. Additionally, the driving force for the perpendicular orientation becomes weaker as the thickness is increased. As the top

becomes weakly preferential for one of the blocks (*e.g.* prefers block *A*, +1), only the incommensurate thicknesses remain favorable for perpendicular orientation. All commensurate thicknesses become favorable for parallel orientation because they allow the BCP to relax to its bulk periodicity $L_0$. Naturally, if the top is weakly preferential towards the opposite component (*e.g.* prefers block *B*, -1), the behavior is identical. These results indicate that in the presence of a single neutral interface, increasing the preference of the opposite interface simply reduces the thickness window for perpendicular orientation. These windows eventually only become favorable for thin, incommensurate thicknesses. Only the condition of two perfectly neutral interfaces is predicted to achieve thickness independent perpendicular orientation.

***Thin Film Experimental Analysis***

It was possible to directly test aspects of the response surface model because of the recent development of a large library of bottom[48,76] *and* top coat[67,70] materials that can provide independent control of the surface energy (*i.e.* preference) at each respective interface. Experimental thin film results were compared to the algebraic model to effectively calibrate the parameters of the model and corroborate the qualitative behavior to changes in the preference of the confining surfaces. The process flow and materials used in these experimental studies are outlined in Fig. 5.5. For all figures herein, the red block (block *A*) represents the organosilicon domain.

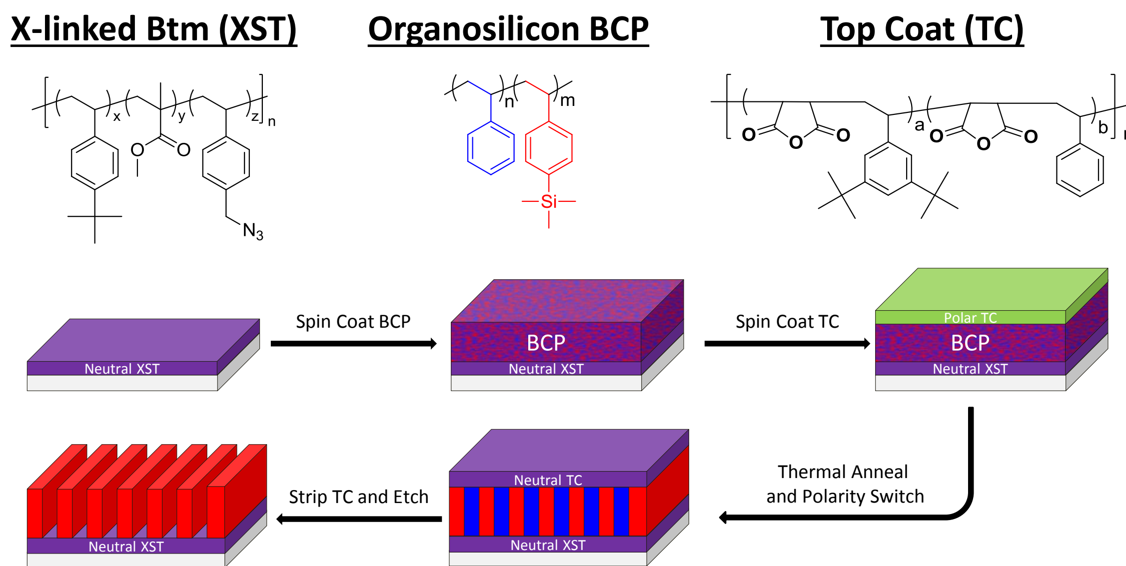


Figure 5.5: The bottom (XST), organosilicon BCP, and top coat (TC) materials used in the experimental analysis and the process flow used to generate the investigated samples.

For these experiments, the bottom substrate was a cross-linkable polymer (XST) comprised of 4-*tert*-butylstyrene, methyl methacrylate, and vinylbenzyl azide. The XST was cross-linked to prevent dissolution and the organosilicon BCP (PS-b-PTMSS) was spin coated on top at various thicknesses. A ring opening top coat (TC) (see Section 2.2.2) comprised of maleic anhydride, 3,5-di-*tert*-butylstyrene (di-tBuS), and styrene was spin coated over the BCP layer as a polymer salt (TCs are referred to herein as TC XX, where XX indicates the composition of di-tBuS in the polymer). The interface preference of both the top and the bottom could be adjusted by varying the ratio of their respective monomers. The film stack was heated to ring-close the TC and simultaneously anneal the BCP film. The annealed sample was stripped with aqueous base to remove the TC and the BCP was briefly etched to expose the organosilicon domains. The resulting topography, analyzed primarily by top-down SEM, was used to indicate the favored orientation for a given set of conditions.

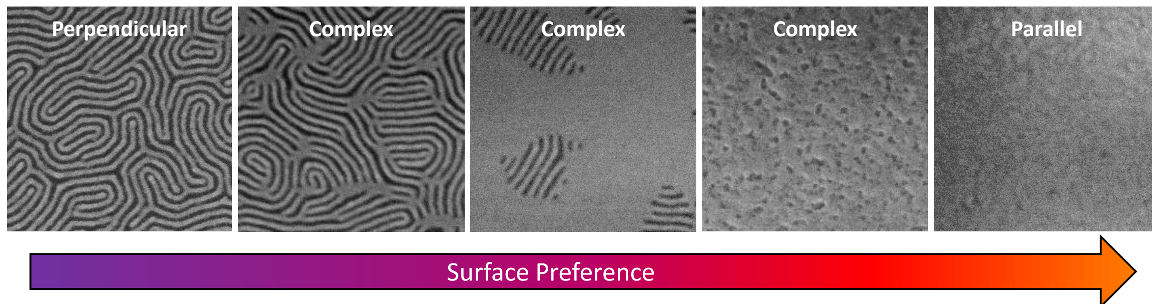


Figure 5.6: Perpendicular orientation generally transitioned to parallel orientation through more complex mixed or perforated morphologies as a function of surface preference.

Although only perpendicular and parallel orientations are predicted by the algebraic model, several more complex morphologies are observed experimentally. Figure 5.6 shows the general morphology trend in the present thin film experimental studies; perpendicular orientation transitions through several complex morphologies before completely orienting parallel as a function of surface preference strength. As the preference towards one domain increases, regions of *both* perpendicular and parallel orientation are seen. The density of the parallel regions generally increases for more strongly preferential surfaces. Other complex morphologies, such as perforated-like lamellae, are observed under highly frustrated conditions. Although the complex morphologies are not predicted to be thermodynamically stable,[41] control experiments show that they are kinetically stable enough to persist even at extended anneal times (> 72 hours). When the preference becomes strong enough towards one component, only parallel orientation persists.

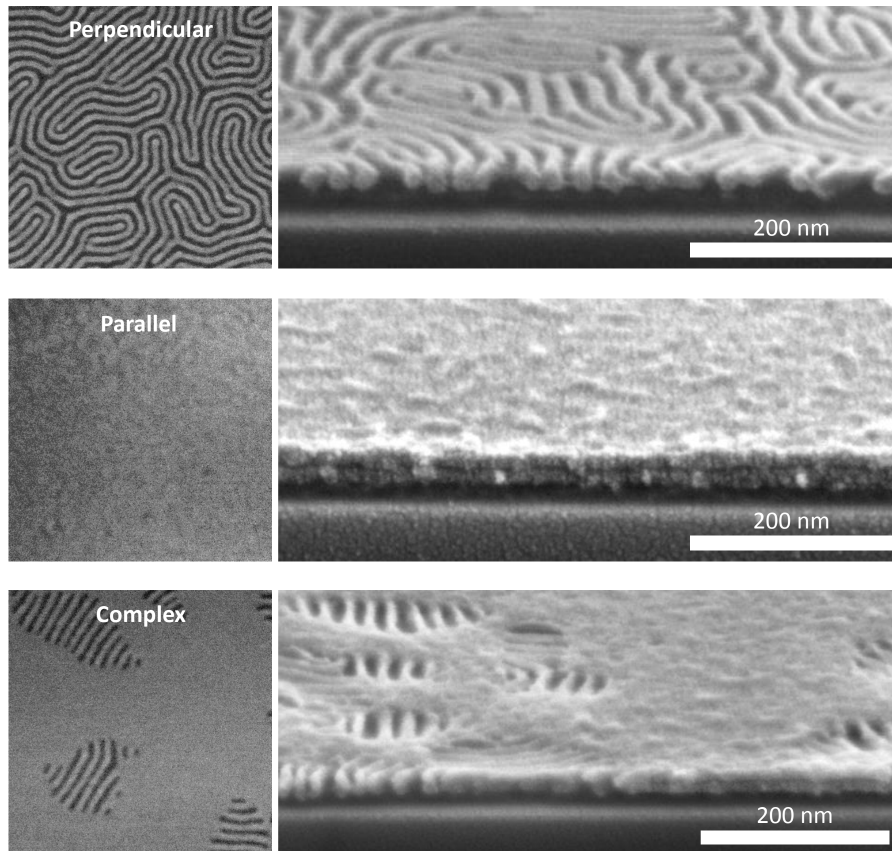


Figure 5.7: Top-down and angled SEM images of several morphologies observed in thin-film. Samples (*ca.* $2L_0$) were etched from both the top and side.

Several thin film samples were further analyzed by cross-section imaging to investigate the through-film behavior of the morphologies (Fig. 5.7). The samples (*ca.* $2L_0$ thickness) were briefly etched to expose the top-down topography, then cleaved and etched again on the side before imaging. The structures perpendicularly orientated persist through the film, confirming that the high aspect ratio features can be potentially transferred to an underlying layer for patterning applications. Several domains are tilted or distorted, but these effects are believed to be caused by sample preparation (*e.g.* feature collapse due to etch conditions). The parallel orientation was induced using a strongly preferential top surface. This condition shows two distinct layers corresponding

to the residual organosilicon domains. The complex morphology shows both perpendicular and parallel structures by top-down imaging. The angled profile shows regions where the perpendicular structures clearly persist through the film (left) together with areas where two distinct parallel layers exist (right). The transition between these orientations is remarkably abrupt; the parallel orientation appears to immediately transform into perpendicular structures, suggesting that both orientations persist through-film in the respective areas seen top-down. Thicker films (not shown here) have been shown to transition between perpendicular and parallel orientation through the film.[25,41,154,164]

A large experimental matrix was generated to demonstrate the effects of film thickness and surface preference on orientation behavior. XSTs and TCs were screened via island/hole methodology to identify neutral materials (as evidenced by $0.5L_0$ topography[67,69]). The BCP was coated at various thicknesses on a neutral XST and the wafer was diced into smaller, identical samples. These samples were coated with TCs that varied in di-tBuS composition from neutral (TC 20) to strongly preferential towards the organosilicon domain (TC 49). A subset of the experimental matrix is shown in Fig. 5.8. For the neutral TC (*i.e.* confinement between two neutral interfaces), perpendicular orientation was seen at all thicknesses. As the preference became stronger towards the organosilicon domain, the thickness window that favors perpendicular orientation decreased. For the most preferential material studied (TC 49), no thicknesses produced well-formed perpendicular lamellae.

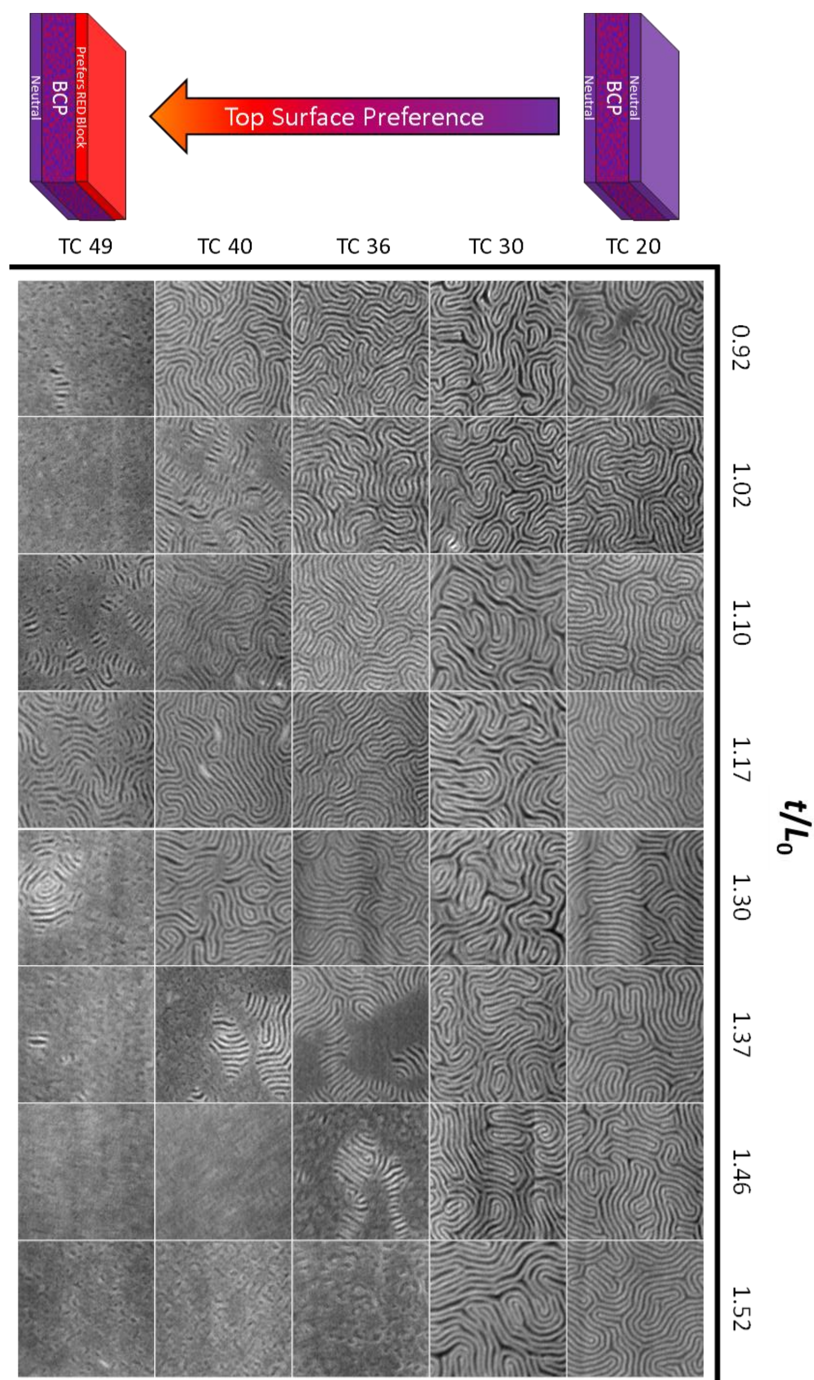


Figure 5.8: Representative subset of the experimental matrix for a neutral substrate, evaluated at several film thicknesses using TCs incrementally more preferential towards the organosilicon domain. Note: subtle differences in the contrast and pattern quality are a result of the batch-wise process used to prepare groups of samples.

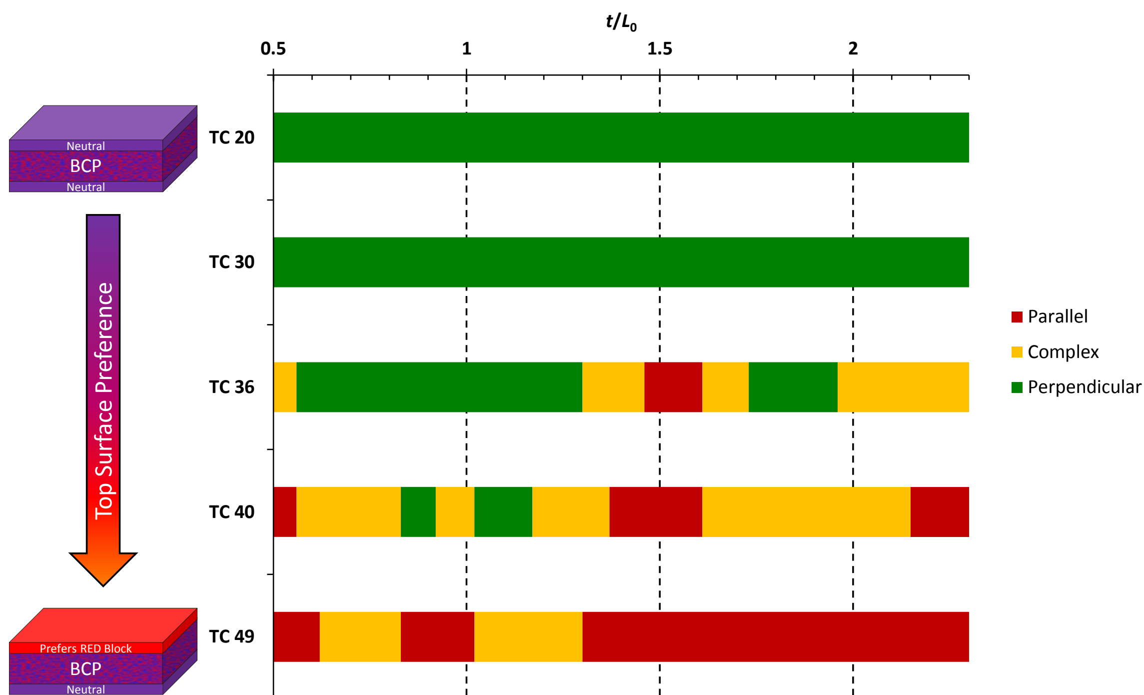


Figure 5.9: Thickness windows corresponding to self-assembly quality for the neutral substrate expanded dataset.

The large experimental dataset of the top-down SEM images was categorized by the quality of the self-assembly: good or perpendicular orientation (green), complex or mixed morphologies (yellow), and poor or parallel assembly (red). The thickness windows that correspond to each condition are plotted for the expanded dataset in Fig. 5.9. This figure again shows that perpendicular orientation is thickness independent for a neutral TC. Even the slightly off-neutral TC 30 shows perpendicular orientation for all conditions; however, as the preference increases, the windows for perpendicular assembly decrease in agreement with the algebraic model predictions. As the model also predicts, the perpendicular windows appear most favorable at the incommensurate conditions ($t \neq nL_0$, $(n+0.5)L_0$) and thinner thicknesses. As illustrated in Fig. 5.6, the perpendicular assembly typically transitions through more complex morphologies before

becoming fully parallel, suggesting that the regions predicted to have a weak energetic driving force by the algebraic model (*i.e.* close to the zero-axis) result in the more complex behavior.

## 5.3 Orientation Behavior – Dual Interface Modification

Section 5.2 explored modifying the top preference while using a neutral bottom interface, thereby producing a symmetric response surface plot. A more complex case considers top surface variation in the presence of a weakly preferential bottom interface (*i.e.* $\gamma_{A_Btm} \neq \gamma_{B_Btm}$); under such circumstances, the commensurability conditions associated with the wetting configuration (see Fig. 5.1) causes unique behavior. Although intuitively the best condition to favor perpendicular orientation would be the use of a neutral substrate, modification of both interfaces produces alternative favorable conditions.

### *Response Surface Analysis*

The response surface plots for a weakly preferential bottom interface (towards block $B$, $\Delta\gamma_{Btm}$ = -1) are shown in Fig. 5.10. Similar to the neutral bottom interface case (Fig. 5.4), the top surface preference is increased to favor either component (-3 to +3). For a neutral top interface (cross-section through the zero-axis), only the incommensurate thicknesses favor perpendicular orientation. This behavior is identical to the condition where the *top* interface is slightly preferential and the *bottom* interface is neutral (Fig. 5.4, bottom right). As the top preference becomes more negative (*i.e.* prefers the blue block $B$), the interfaces become symmetrically wetting. When the top preference equals -1, the cross section through this plane shows that the commensurate conditions ($nL_0$) now heavily favor parallel orientation, while the incommensurate conditions $(n + 0.5)L_0$ now

favor perpendicular orientation. The opposite is true if the top preference favors the red block *A* (+1); the $nL_0$ conditions now favor perpendicular while $(n + 0.5)L_0$ favors parallel. Therefore, the wetting behavior shifts the perpendicular window left or right depending on the commensurability, and is maximized when the interfaces are perfectly symmetric/asymmetric. For this particular case, symmetric wetting occurs when block *B* is preferred at both interfaces, but the same is obviously true if both interfaces favor block *A* instead. Another interesting observation is that the perpendicular windows are actually *wider* for the perfectly symmetric/asymmetric condition than when one interface is neutral (Fig. 5.10, bottom left).

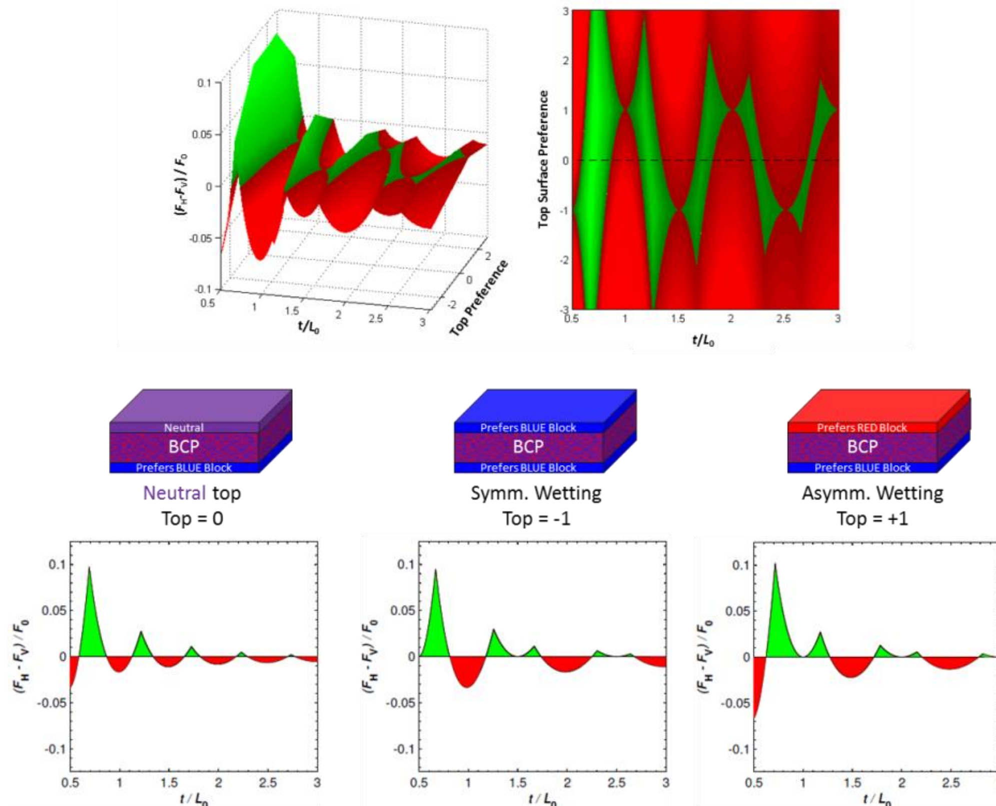


Figure 5.10: Response surface plots and x-z plane cross-sections thereof for a slightly preferential bottom interface ($\Delta\gamma_{\mathrm{Btm}} = -1$).

If strength of the bottom surface preference is increased, the response surfaces are correspondingly modified. For example, if the bottom preference is increased to $\Delta\gamma_{Btm}$ = -2 (Fig. 5.11) and $\Delta\gamma_{Btm}$ = -3 (Fig. 5.12), the windows favorable for perpendicular orientation continue to shrink, but the most favorable conditions are again either perfectly symmetric or asymmetric wetting. For $\Delta\gamma_{Btm}$ = -3 (Fig. 5.12), conditions exist where *only* the perfectly symmetric/asymmetric wetting favors perpendicular orientation – a neutral top would actually be *unfavorable* at those thicknesses.

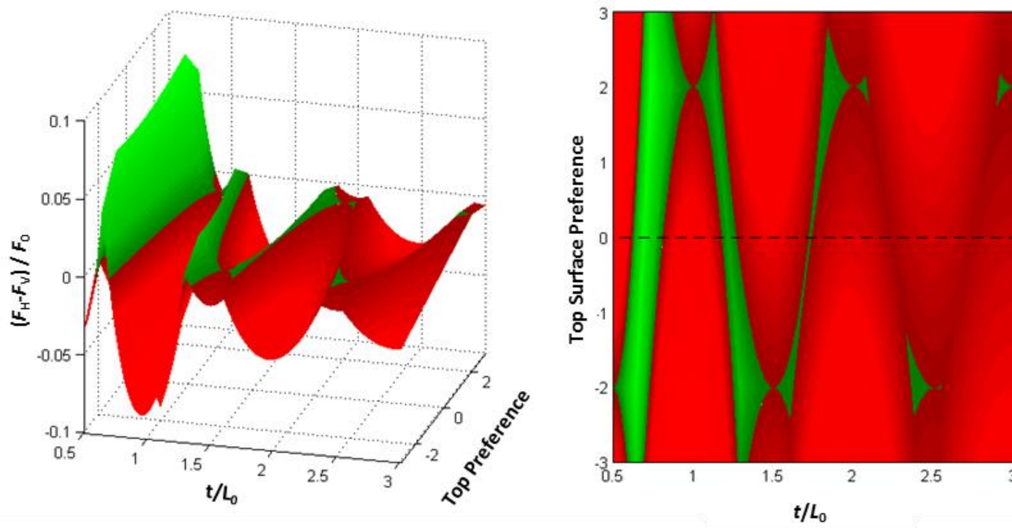


Figure 5.11: Response surface plots for a preferential bottom interface ($\Delta\gamma_{Btm}$ = -2).

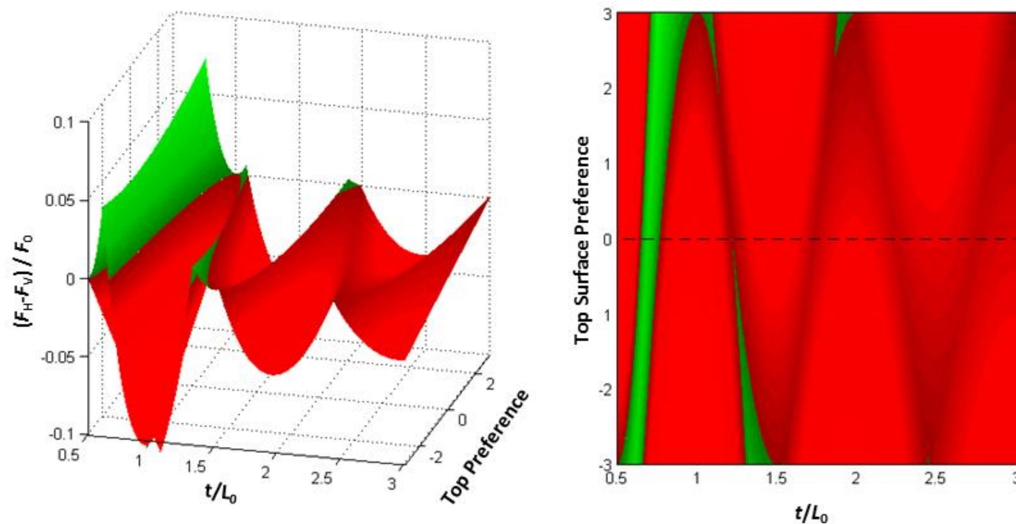


Figure 5.12: Response surface plots for a preferential bottom interface ($\Delta\gamma_{Btm}$ = -3).

The response surfaces indicate that independently modifying both interfaces can tune the perpendicular window towards certain thicknesses. Therefore, if certain applications require a certain orientation at a specific thickness, careful consideration of the wetting preference should be applied.

***Thin Film Experimental Analysis***

Dual interface modification was evaluated experimentally by spin coating the BCP at various thicknesses on an off-neutral XST (weakly preferential towards the organic domain). A series of TCs was applied to the top interface, spanning from neutral to preferential towards either component. A large experimental matrix was generated, and a subset of the data for this experiment is shown in Fig. 5.13.

As the TC di-tBuS composition increases (increasing preference towards the organosilicon domain), the system becomes asymmetrically wetting. The $(n + 0.5)L_0$ commensurate conditions for asymmetric wetting become favorable for parallel orientation. This parallel orientation window widens as the top surface preference

increases. In contrast, the incommensurate $nL_0$ conditions for asymmetric wetting are now more favorable for perpendicular orientation. Samples even with high di-tBuS composition show evidence of perpendicular assembly. The parallel/perpendicular windows thus shift towards the commensurate/incommensurate conditions, respectively. This shift is most strikingly evident when directly compared to the data for TC 12 (preferring the organic domain). For this TC/XST combination, the interfaces became symmetrically wetting, and the commensurate conditions are switched. The $nL_0$ conditions now favor parallel orientation, while the $(n + 0.5)L_0$ conditions favor perpendicular orientation.

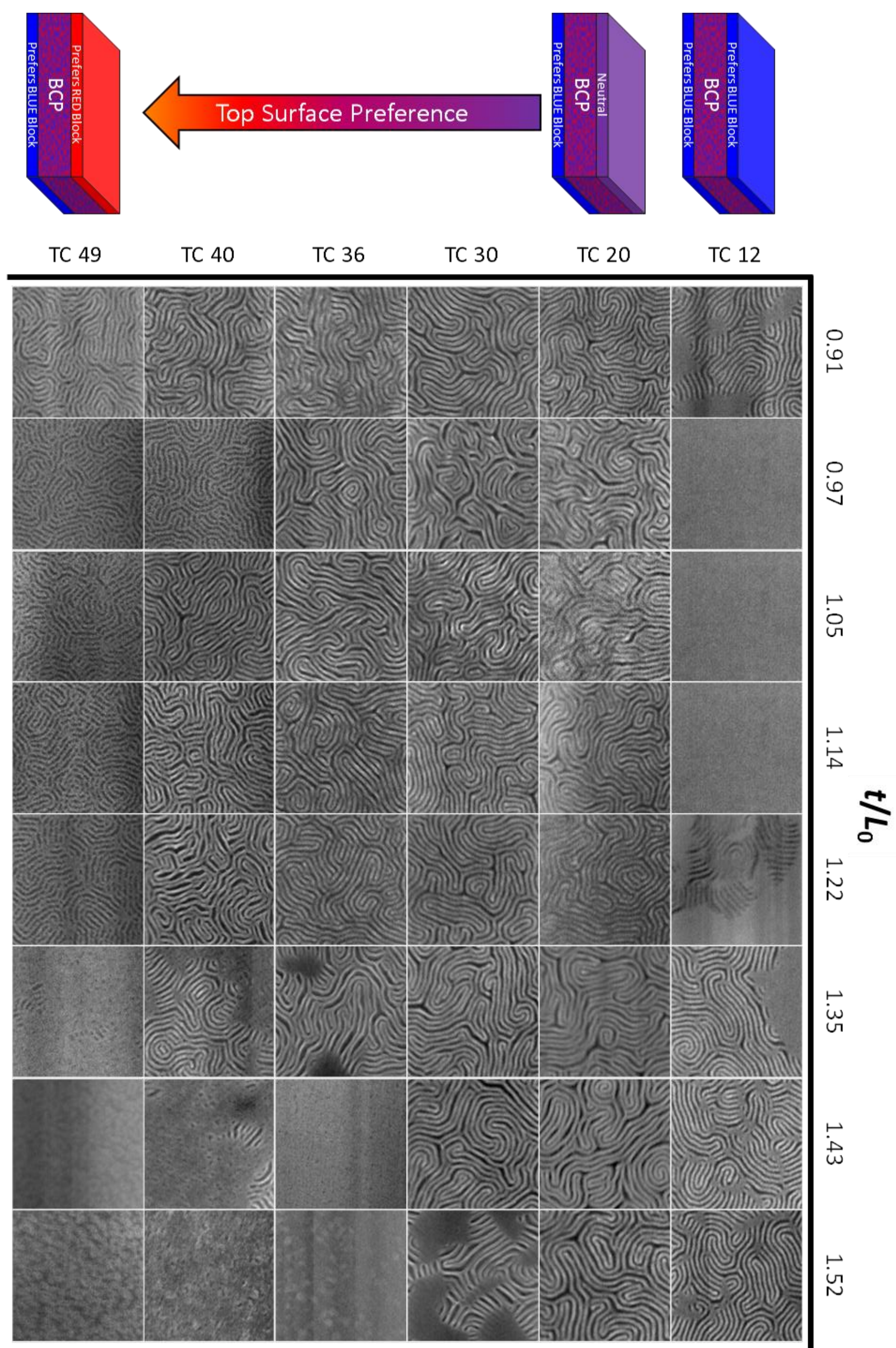


Figure 5.13: Representative subset of the experimental matrix for a substrate weakly preferential towards the organic domain, evaluated at several film thicknesses using a range of TCs. Note: subtle differences in the contrast and pattern quality are a result of the batch-wise process used to prepare groups of samples.

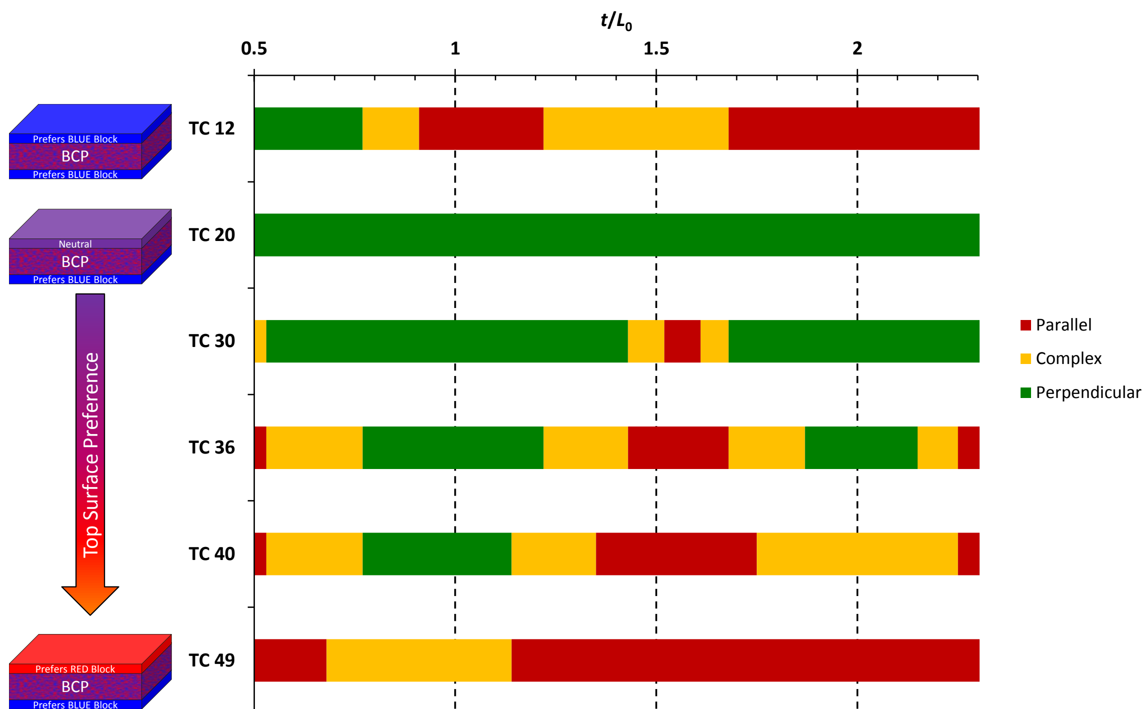


Figure 5.14: Thickness windows corresponding to self-assembly quality for the weakly preferential substrate expanded dataset.

The thickness windows that correspond to the expanded experimental dataset are shown in Fig. 5.14. Experimentally, the thin film behavior matches well with the qualitative predictions from the response surface plots. The incommensurate conditions favor perpendicular orientation and shift left or right dependent on the wetting behavior of the BCP. Several weakly preferential TCs have perpendicular windows that's are slightly wider than with the corresponding neutral substrate (Fig. 5.9). TCs that previously showed good assembly at all thicknesses (*e.g.* TC 30) now show poor assembly at the commensurate conditions. Furthermore, the perpendicular windows become smaller as thickness increases.

## 5.4 Conclusions

An algebraic model was adapted to describe the orientation behavior of lamellar BCP thin films as a function of interfacial interactions and film thickness. The thickness quantization effects for parallel-orientated lamellae induce windows of favorable perpendicular orientation that can be predicted by the model. Neutral interfaces favor thickness independent perpendicular orientation, but as the preference strength for single interface increases, the thickness windows diminish and are only favorable at incommensurate thicknesses ($t \neq nL_0$, $(n + 0.5)L_0$). Perpendicular orientation is also most favorable in the thinnest films. The qualitative predictions of the algebraic model match quite well with a thorough experimental study using various TC materials to modify interface preference.

Complex phenomena are observed when both interfaces are modified; depending on the commensurability of the wetting behavior, the thickness windows favoring perpendicular orientation shift. Incommensurate thicknesses ($nL_0$ for asymmetric wetting and $(n + 0.5)L_0$ for symmetric wetting) become most favorable for perpendicular orientation. Surprisingly, under certain conditions, these incommensurate thickness windows for weakly preferential interfaces are larger than an analogous case with a neutral interface. The dual interface modification behavior was also analyzed by a thorough thin film experimental study to show that the qualitative conclusions corroborate the algebraic model.

The results of this study show that BCP orientation behavior is multi-variable problem that should be carefully considered before evaluating certain process conditions. Evidence of thin film perpendicular assembly is occasionally used as justification for the assessment of a neutral interface, but these data clearly show that such behavior can occur under a variety of circumstances. A simple model can be used to guide intuition on

BCP orientation, and the ability to tune the perpendicular orientation windows may be potentially useful for certain applications. Further study would be valuable to assess how frustration-induced orientation may affect the quality of the assembled patterns or be applied to more complicated directed self-assembly processes.

## 5.5 EXPERIMENTALS

### *Materials*

PS-*b*-PTMSS (27 nm $L_0$, $f_{PS} = 0.49$) was anionically synthesized using procedures shown in Chapter 3. XSTs were synthesized as previously reported[48,76] and were comprised of 4-*tert*-butylstyrene, methyl methacrylate, and vinylbenzyl azide. TCs were all comprised of maleic anhydride, 3,5-di-*tert*-butylstyrene (di-tBuS), and styrene, and were synthesized as described in Chapter 2.

### *Instrumentation*

All films were coated on a Brewer Science CEE 100CB Spincoater. Annealing was performed on a Thermolyne 11515B hot plate. Ellipsometry measurements were taken with a J.A. Woolam Co., Inc. VB 400 VASE Ellipsometer. Oxygen reactive ion etching was performed on a Harrick plasma cleaner at a pressure of 350 mtorr. Top-down SEM imaging was performed on a Hitachi S-4500. Angled SEM imaging was performed using a Zeiss Supra 40 VP. Angled samples were sputtered with Au/Pd for 5 s prior to imaging.

### 5.5.1 Thin Film Preparation

Characterization data of the XST and TC materials used herein are provided in Table 5.1 and 5.2, respectively. The neutral conditions for the XST (XST 48) and TC (TC

20) were determined by evidence of half-island/hole topography, according to procedures described in Chapter 2.

Table 5.1 Characterization data of XST polymers.

| | Feed (mol %) | | | Actual (mol %)[a] | | | |
|---|---|---|---|---|---|---|---|
| **Polymer** | **tBuS** | **MMA** | **VBzCl** | **tBuS** | **MMA** | **VBzCl** | **Đ[b]** |
| XST-42 | 38 | 59 | 3 | 42 | 53 | 5 | 1.41 |
| XST-48 | 50 | 45 | 5 | 48 | 45 | 7 | 1.62 |

[a] Determined by combustion analysis.
[b] Determined by SEC.

Table 5.2 Characterization data of TC polymers.

| | Feed (mol %) | | | Actual (mol %)[a] | | | | | |
|---|---|---|---|---|---|---|---|---|---|
| **Polymer** | **MA** | **di-tBuS** | **S** | **MA** | **di-tBuS** | **S** | **Đ[b]** | **$T_g$[c]** | **$T_d$[c]** |
| TC-12 | 50 | 10 | 40 | 52 | 12 | 36 | 3.15 | 196 | 269 |
| TC-20 | 50 | 22 | 28 | 50 | 20 | 30 | 3.26 | 197 | 283 |
| TC-30 | 50 | 30 | 20 | 51 | 30 | 19 | 2.36 | 192 | 278 |
| TC-36 | 50 | 34 | 16 | 48 | 36 | 16 | 2.26 | 207 | 327 |
| TC-40 | 50 | 40 | 10 | 52 | 40 | 8 | 3.2 | 205 | 324 |
| TC-49 | 50 | 50 | - | 51 | 49 | - | 1.92 | 208 | 278 |

[a] Determined by combustion analysis.
[b] Determined by SEC.
[c] Determined by TGA/DSC

The substrate XST films were prepared by spin coating a 1 wt.% solution in toluene onto a bare silicon wafer. The films were annealed at 250 ºC for 5 min. to cross-link the polymer, and then washed with acetone/isopropanol to remove residual unbound material. The PS-*b*-PTMSS BCP was spin coated onto the XST layer and the thickness was measured by ellipsometry. The TC polymer salt was spin coated from a 1 wt.% methanol solution onto the BCP, and the film stack was annealed at 180 ºC for 10 min. The TC film was immediately removed by immersing the films in a bath of 1:1 methanol:aqueous trimethylamine (50 wt.%) for 1 min. The annealed BCP was etched

(times between 1.5-2 min., depending on film thickness) to provide sufficient topographical contrast to produce an SEM image.

Cross-sectioned samples were prepared in an identical fashion, except etching was performed sequentially. Films were uniformly etched for 1 min., cleaved, and then etched again for another 1 min. with the exposed edge. The cleaved edge was coated with Au/Pd for 5 s prior to imaging.

# Appendix A: Modified Purification Glassware for Anionic Polymerization

Glassware used in the purification of monomers for anionic polymerization was recently modified to incorporate additional safety precautions and enhancements for high-boiling monomers. All original glassware was purchased from ChemGlass, and the custom pieces were made by The University of Texas at Austin Chemistry Glass Shop. The round bottom flasks (Figs. A.1 and A.2) are designed with a pressure-release stopcock that ensures internal pressures never exceed the maximum rated pressure for the glassware. The pressure-release arm can also act as a secondary Schlenk line to connect to the manifold. The stopcock arms are configured to minimize the projected area allowing transfer of the glassware in/out of a glovebox small antechamber. The inlet tube of the 0.5” Schlenk line extends into the headspace of the flask, enabling active-vacuum distillation by flowing the monomer over the cooled outer region of the flask before passing out of the pressure-release arm.

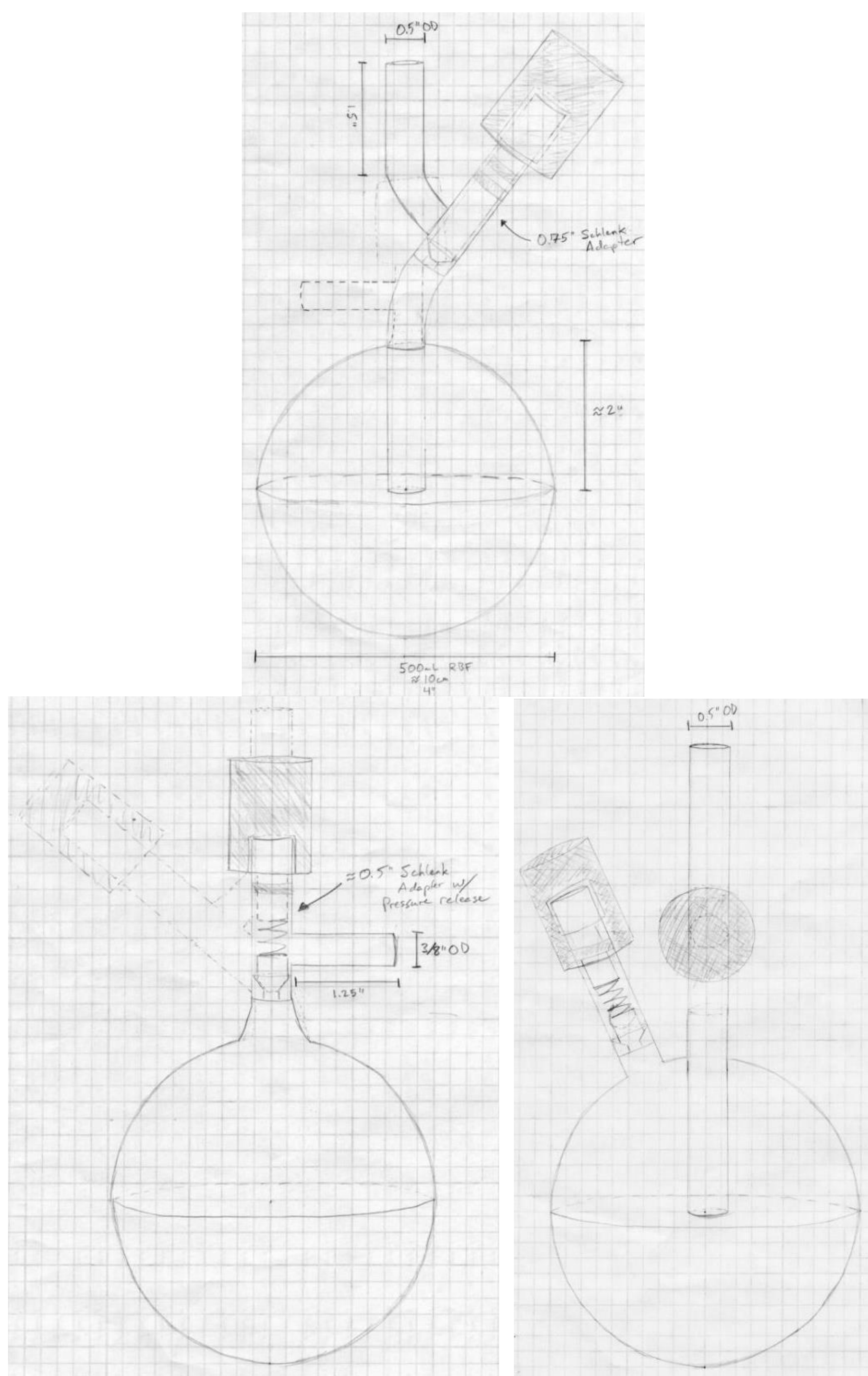


Figure A.1: Schematics of anionic distillation flask, equipped with pressure release valve and extended inlet tube to promote active vacuum-distillations.

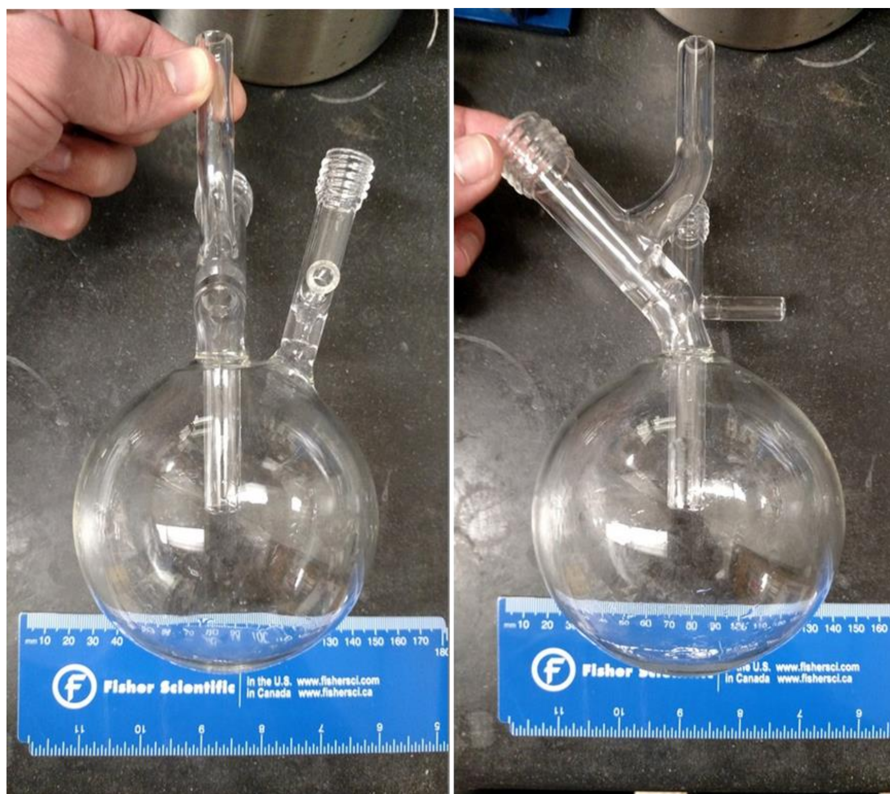


Figure A.2: Photographs of anionic distillation round-bottomed flasks. Stop-cocks are not shown.

A distillation head was modified to enhance the processing of high-boiling monomers (Figs. A.3 and A.4). The tubing is angled to allow condensed monomer to drip into the receiving flask, promoted by the force of gravity. The sans-jacketed distillation head can be cooled using removable plastic tubing with an active water flow, advantageous for conditions that require flame-drying. The jacketed distillation head was designed for early-stage distillation steps that do not require flame-dried glassware. This design incorporates a water cooling jacket over the angled distillation head with a barbed inlet/outlet to enable facile attachment of plastic tubing.

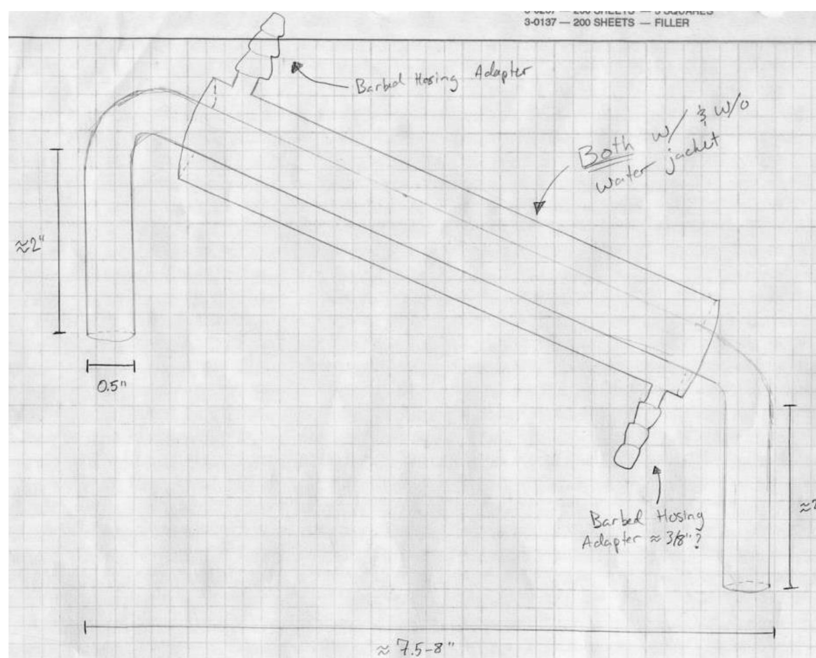


Figure A.3: Schematic of angled distillation head, drawn with water cooling jacket. Heads were produced with/without the cooling jacket for flame-dried and non-flame-dried applications, respectively.

Figure A.4: Photograph of angled distillation head (shown with jacketed condenser).

# Appendix B: Algebraic Model for Block Copolymer Orientation Free Energy Calculations

## B.1 Free Energy Adapted Model

The following MATLAB code was used to generate the free energy curves of lamellar BCPs for parallel-symmetric, parallel-asymmetric, and perpendicular orientations. The code generates the free energy curves as well as the adapted model emphasizing the conditions suitable for each orientation (*i.e.* the "cross-sections" of the 3D response surface plots).

```
%% Will Durand & Matt Carlson
%% 7/17/14

%% Variables =======================================================

clear all

Start=0.1;  %%Starting thickness (reduced)
f=3;  %% Ending thickness
points=1000;  %%Number of data points to calc for each curve

top_pref=1; %% positive if top prefers A (-5 to 5)
bot_pref=0; %% positive if bottom prefers A (-5 to 5)

%% Equations ===================================================

%% Interface 1 defined as top, 2 as btm
mod1=0;  %% Mod section specifies AS1 is always less than AS2, BS1
mod2=0;
if top_pref==0 | bot_pref==0
    mod1=max(abs(bot_pref),abs(top_pref));
elseif top_pref>0 && bot_pref>0
    mod1=max(abs(bot_pref),abs(top_pref));
    mod2=min(abs(bot_pref),abs(top_pref));
elseif top_pref<0 && bot_pref<0
    mod1=max(abs(bot_pref),abs(top_pref));
    mod2=min(abs(bot_pref),abs(top_pref));
elseif top_pref>0 && bot_pref<0
    mod1=max(abs(bot_pref),abs(top_pref));
    mod2=-min(abs(bot_pref),abs(top_pref));
elseif top_pref<0 && bot_pref>0
    mod1=max(abs(bot_pref),abs(top_pref));
    mod2=-min(abs(bot_pref),abs(top_pref));
```

```
end


gam_AS1=5-mod1; %% top interfacial tension b/w A&S1
gam_AS2=5-mod2; %% bottom interfacial tension b/w A&S2
gam_BS1=5; %% top interfacial tension b/w B&S1
gam_BS2=5; %% botom interfacial tension b/w B&S2
gam_AB=10; %% polymer interfacial tension b/w A&B

Gam1=gam_AS1/gam_AB; %% top ratio
Gam2=gam_AS2/gam_AB; %% bottom ratio
DGAM1=gam_BS1-gam_AS1; %%DELTA gamma term for top surface
DGAM2=gam_BS2-gam_AS2; %%DELTA gamma term for top surface
del1=(gam_BS1-gam_AS1)/gam_AB
del2=(gam_BS2-gam_AS2)/gam_AB

D=[Start:(1/points):f];  %% x-axis for VERTICAL SFE plot

%% Vertical Surface Free Energy / F0

Fv=1/3*(3+1./D.*((Gam1+del1/2)+(Gam2+del2/2)));

%% Symmetric Horizontal Surface Free Energy / F0

d=[Start:(1/points):f]; %% x-axis for HORIZONTAL SFE plots

for m=[1:f];
    lam_s=d/m;
    Fh_s(m,:)=1/3*(lam_s.^2+2./lam_s+1./(m*lam_s).*(Gam1+Gam2));
end

%% Anti-symmetric Horizontal Surface Free Energy / F0

for n=[0.5:1:f]
    lam_a=d/n;

Fh_a(n+0.5,:)=1/3*(lam_a.^2+2./lam_a+1./(n*lam_a).*(Gam1+Gam2+del2));
end

%%Results==================================================

[x,y]=size(Fh_a);

for i=[1:x]  %% Find the minimum of either the assym or sym case
    for j=[1:y]
        if Fh_a(i,j)<Fh_s(i,j)
            HMIN(i,j)=Fh_a(i,j);
        else
            HMIN(i,j)=Fh_s(i,j);
        end
```

```
    end
end

TMIN=min([min(HMIN);Fv]);  %%Curve representing minimum F/F0 for all
functions
OED=[min(HMIN)-Fv];   %%Overall energy driving force for a certain
orientation

for k=[1:y]  %% Split OED in positive and negative regions to plot
integrals
    if OED(1,k)<0
        OED_pos(1,k)=0;
        OED_neg(1,k)=OED(1,k);
    else
        OED_pos(1,k)=OED(1,k);
        OED_neg(1,k)=0;
    end
end

%% PLOTTING ==================================================

subplot(1,2,1); %%Plot of all curves together
plot(d,Fh_s,'r',d,Fh_a,'b',D,Fv,'--k',d,TMIN,'g')
legend('Sym','Asym','Vert')
axis([0.5 f 1 1.6])
xlabel('t / L_0','interpreter','tex')
ylabel('F / F_0')
title('Free Energy of All Morphologies')

subplot(1,2,2)  %%Shaded OED plot
H=area(d,[OED_pos;OED_neg]');
h1=get(H(1),'children');
h2=get(H(2),'children');
set(h1,'FaceColor',[0 1 0]);
set(h2,'FaceColor',[1 0 0]);
axis([0.5 f -.125 .125])
xlabel('t / L_0','interpreter','tex')
ylabel('(F_{H} - F_V) / F_0')
title('\DeltaFree Energy b/w Horizontal and Vertical')

%%Add super title %%Must have suplabel file in directory
[ax,h3]=suplabel(['Top \Delta\gamma = ',num2str(top_pref) ' ,Btm
\Delta\gamma = ',num2str(bot_pref)] ,'t');
set(h3,'FontSize',15)
```

## B.2 Response Surface Plots

The following MATLAB code was used to produce the 3D response surface plot and the corresponding color plot. The code varies the top surface preference as a function of thickness for a fixed bottom interface preference.

```
%% Will Durand & Matt Carlson
%% 10/08/14

%%Variables =====================================================

clear all

Start=0.5;  %%Starting thickness (reduced)
f=3;    %% Ending thickness
data=100;  %%Number of data points per each curve

del_start=-2;  %%Top coat preference start
del_end=2;    %%Top coat preference end

num=50;  %%Number of curves to generate
div=(del_end-del_start)/(num-1);  %%Divisions between del of curves

bot_pref=0.2;   %%Preference strength of btm interface

%% Equations =====================================================

for k=[1:num]

top_pref=del_start+(k-1)*div;
mod1=0;  %% Mod section specifies AS1 is always less than AS2, BS1
mod2=0;
if top_pref==0 | bot_pref==0
    mod1=max(abs(bot_pref),abs(top_pref));
elseif top_pref>0 && bot_pref>0
    mod1=max(abs(bot_pref),abs(top_pref));
    mod2=min(abs(bot_pref),abs(top_pref));
elseif top_pref<0 && bot_pref<0
    mod1=max(abs(bot_pref),abs(top_pref));
    mod2=min(abs(bot_pref),abs(top_pref));
elseif top_pref>0 && bot_pref<0
    mod1=max(abs(bot_pref),abs(top_pref));
    mod2=-min(abs(bot_pref),abs(top_pref));
elseif top_pref<0 && bot_pref>0
    mod1=max(abs(bot_pref),abs(top_pref));
    mod2=-min(abs(bot_pref),abs(top_pref));
end
```

```
gam_AS1=5-mod1; %% top interfacial tension b/w A&S1
gam_AS2=5-mod2; %% bottom interfacial tension b/w A&S2
gam_BS1=5; %% top interfacial tension b/w B&S1
gam_BS2=5; %% bottom interfacial tension b/w B&S2
gam_AB=10; %% polymer interfacial tension b/w A&B

Gam1=gam_AS1/gam_AB; %% top ratio
Gam2=gam_AS2/gam_AB; %% bottom ratio
DGAM1=gam_BS1-gam_AS1;  %%DELTA gamma term for top surface
DGAM2=gam_BS2-gam_AS2; %%DELTA gamma term for top surface
del1=(gam_BS1-gam_AS1)/gam_AB;
del2=(gam_BS2-gam_AS2)/gam_AB;

    D=[Start:(1/data):f];  %% Indep. var for VERTICAL SFE plot

    %% Vertical Surface Free Energy / F0

    Fv=1/3*(3+1./D.*((Gam1+del1/2)+(Gam2+del2/2)));

    %% Symmetric Horizontal Surface Free Energy / F0

    d=[Start:(1/data):f]; %% Indep. var for HORIZONTAL SFE plots

    for m=[1:f];
        lam_s=d/m;
        Fh_s(m,:)=1/3*(lam_s.^2+2./lam_s+1./(m*lam_s).*(Gam1+Gam2));
    end

    %% Anti-symmetric Horizontal Suraface Free Energy / F0

    for n=[0.5:1:f]
        lam_a=d/n;

Fh_a(n+0.5,:)=1/3*(lam_a.^2+2./lam_a+1./(n*lam_a).*(Gam1+Gam2+del2));
    end

%% Quantitative Results ========================================

    [x,y]=size(Fh_a);

    for i=[1:x]  %% Find the minimum of either the assym or sym case
        for j=[1:y]
            if Fh_a(i,j)<Fh_s(i,j)
                HMIN(i,j)=Fh_a(i,j);
            else
                HMIN(i,j)=Fh_s(i,j);
            end
        end
```

```
    end

    TMIN=min([min(HMIN);Fv]);  %%Curve representing minimum F/F0 for
all functions
    OED=[min(HMIN)-Fv];   %%Overall energy driving force for a certain
orientation

    OED_Curves(k,:)=OED;  %%combine the OED curves for different values
of Del1

    lgnd(k,:)={['\Delta\gamma_{Top}= ',num2str(del_start+div*(k-1))]};
%%Create string mat for legend

    for l=[1:y]  %% Split OED in positive and negative regions to plot
integrals
        if OED(1,l)<0
            OED_pos(1,l)=0;
            OED_neg(1,l)=OED(1,l);
        else
            OED_pos(1,l)=OED(1,l);
            OED_neg(1,l)=0;
        end
    end
end

%% MISCELLANEOUS ============================================

y_axis=[linspace(del_start, del_end, num)];

fprintf(['\nReduced Thickness Range: %.1f L0 to %.1f L0 \n' ...
    'Bottom Preferential Value: %.1f\n'...
    'Top Preferential Range: %.1f to %.1f \n'...
    'Number of Curves: %.0f \n' ...
    'Number of Data Points: %.0f
\n\n'],Start,f,bot_pref,del_start,del_end,num,data)

%% PLOTTING ==================================================

colormat=[linspace(1, 0, num)' linspace(0, 1, num)' zeros(num,1)];
%%Create color matrix for lines
set(gcf,'DefaultAxesColorOrder',colormat)
set(gcf, 'Colormap', colormat);

subplot(1,2,1);
surf(d,y_axis,OED_Curves); shading interp; grid ON; view(15, 20);
caxis([-.08 .08])
axis([Start f del_start del_end -0.1 0.1])
%xlabel('t/L_0','interpreter','tex')
%ylabel('Top Surface Preferential Interactions')
zlabel('(F_{H-min}-F_V)/F_0')
subplot(1,2,2)
```

```
hold on
pcolor(d,y_axis,OED_Curves); shading interp; box ON; caxis([-.08 .08]);
p2=plot(d,zeros(1,y)','--k');
xlabel('Reduced Film Thickness t/L_0','interpreter','tex')
ylabel('Top Surface Preferential Interactions')
axis([Start f del_start del_end])
hold off

%load('MyColormaps','mycmap')
%set(1,'Colormap',mycmap)

%xlswrite('C:\Documents and Settings\Will\Desktop\test.xls',[d'
OED_Curves' ])
```

# References


1. Weik, M. H. *Ballistic Research Laboratories Report No. 971: A Survey of Domestic Electronic Digital Computing Systems*, United States Department of Commerce Office of Technical Services, 1955.
2. Moore, G. E. *Electronics* **1965**, *38*.
3. French, R. H.; Tran, H. V. *Annual Review of Materials Research* **2009**, *39*, 93.
4. Vandeweyer, T.; Bekaert, J.; Ercken, M.; Gronheid, R.; Miller, A.; Truffert, V.; Verhaegen, S.; Versluijs, J.; Wiaux, V.; Wong, P.; Vandenberghe, G.; Maenhoudt, M. 2009; Vol. 7521, p 752102.
5. Mack, C. *Fundamental Principles of Optical Lithography: The Science of Microfabrication*; John Wiley & Sons: London, 2007.
6. Thompson, L. F.; Willson, C. G.; Bowden, M. J. *Introduction to Microlithography*; 2 ed.; American Chemical Society, 1994.
7. Yen, A. In *SPIE Lithography* 2015.
8. Clarke, P. Electronics360, 2014; Vol. 2015.
9. Yang, J. K. W.; Berggren, K. K.; 6 ed.; AVS: 2007; Vol. 25, p 2025.
10. Ruiz, R.; Kang, H.; Detcheverry Francois, A.; Dobisz, E.; Kercher Dan, S.; Albrecht Thomas, R.; de Pablo Juan, J.; Nealey Paul, F. *Science* **2008**, *321*, 936.
11. Chang, T. H. P.; Mankos, M.; Lee, K. Y.; Muray, L. P. *Microelectronic Engineering* **2001**, *57–58*, 117.
12. Colburn, M.; Grot, A.; Amistoso, M. N.; Choi, B. J.; Bailey, T. C.; Ekerdt, J. G.; Sreenivasan, S. V.; Hollenhorst, J.; Willson, C. G. *Proc. SPIE* **2000**, *3997*, 453.
13. Hua, F.; Sun, Y.; Gaur, A.; Meitl, M. A.; Bilhaut, L.; Rotkina, L.; Wang, J.; Geil, P.; Shim, M.; Rogers, J. A. *Nano Letters* **2004**, *4*, 2467.
14. Chou, S. Y.; Krauss, P. R. *Microelectronic Engineering* **1997**, *35*, 237.
15. Ye, Z.; Carden, S.; Hellebrekers, P.; LaBrake, D.; Resnick, D. J.; Melliar-Smith, M.; Sreenivasan, S. V. 2012; Vol. 8323, p 83230V.
16. Cochran, E. W.; Garcia-Cervera, C. J.; Fredrickson, G. H. *Macromolecules* **2006**, *39*, 2449.
17. Almdal, K.; Hillmyer, M. A.; Bates, F. S. *Macromolecules* **2002**, *35*, 7685.
18. Matsen, M. W. *J. Phys.: Condens. Matter* **2002**, *14*, R21.
19. Matsen, M. W.; Schick, M. *Macromolecules* **1994**, *27*, 187.
20. Bates, C. M.; Maher, M. J.; Janes, D. W.; Ellison, C. J.; Willson, C. G. *Macromolecules* **2013**, *47*, 2.

21. Matsen, M. W.; Bates, F. S. *The Journal of Chemical Physics* **1997**, *106*, 2436.

22. Matsen, M. W. *Macromolecules* **2012**, *45*, 8502.

23. Park, S.; Lee, D. H.; Xu, J.; Kim, B.; Hong, S. W.; Jeong, U.; Xu, T.; Russell, T. P. *Science* **2009**, *323*, 1030.

24. Cushen, J. D.; Otsuka, I.; Bates, C. M.; Halila, S.; Fort, S.; Rochas, C.; Easley, J. A.; Rausch, E. L.; Thio, A.; Borsali, R.; Willson, C. G.; Ellison, C. J. *ACS Nano* **2012**, *6*, 3424.

25. Yoshida, H.; Suh, H. S.; Ramirez-Herunandez, A.; Lee, J. I.; Aida, K.; Wan, L.; Ishida, Y.; Tada, Y.; Ruiz, R.; de Pablo, J.; Nealey, P. F. *Journal of Photopolymer Science and Technology* **2013**, *26*, 55.

26. Son, J. G.; Gotrik, K. W.; Ross, C. A. *ACS Macro Letters* **2012**, *1*, 1279.

27. Keen, I.; Yu, A.; Cheng, H.-H.; Jack, K. S.; Nicholson, T. M.; Whittaker, A. K.; Blakey, I. *Langmuir* **2012**, *28*, 15876.

28. Ruiz, R.; Dobisz, E.; Albrecht, T. R. *ACS Nano* **2010**, *5*, 79.

29. Tsai, H.; Pitera, J. W.; Miyazoe, H.; Bangsaruntip, S.; Engelmann, S. U.; Liu, C.-C.; Cheng, J. Y.; Bucchignano, J. J.; Klaus, D. P.; Joseph, E. A.; Sanders, D. P.; Colburn, M. E.; Guillorn, M. A. *ACS Nano* **2014**, *8*, 5227.

30. Wong *IEDM* **2009**.

31. Yi, H.; Bao, X.-Y.; Zhang, J.; Bencher, C.; Chang, L.-W.; Chen, X.; Tiberio, R.; Conway, J.; Dai, H.; Chen, Y.; Mitra, S.; Wong, H. S. P. *Advanced Materials* **2012**, *24*, 3107.

32. Ponoth, S.; Horak, D.; Nitta, S.; Colburn, M.; Breyta, G.; Huang, E.; Sucharitaves, J. T.; Landis, H.; Lisi, A.; Liu, X.; Vo, T.; Johnson, R.; Li, W.-k.; Purushothaman, S.; Cohen, S.; Hu, C.-K.; Kim, H.-C.; Clevenger, L.; Fuller, N.; Nogami, T.; Spooner, T.; Edelstein, D. In *214th ECS Meeting* 2008; Vol. MA2008-02, p 2074.

33. Zhao, Y.; Sivaniah, E.; Hashimoto, T. *Macromolecules* **2008**, *41*, 9948.

34. Anastasiadis, S. H.; Russell, T. P.; Satija, S. K.; Majkrzak, C. F. *Physical Review Letters* **1989**, *62*, 1852.

35. Cushen, J. D.; Bates, C. M.; Rausch, E. L.; Dean, L. M.; Zhou, S. X.; Willson, C. G.; Ellison, C. J. *Macromolecules* **2012**, *45*, 8722.

36. Durand, W. J.; Blachut, G.; Maher, M. J.; Sirard, S.; Tein, S.; Carlson, M. C.; Asano, Y.; Zhou, S. X.; Lane, A. P.; Bates, C. M.; Ellison, C. J.; Willson, C. G. *Journal of Polymer Science Part A: Polymer Chemistry* **2015**, *53*, 344.

37. Kennemur, J. G.; Hillmyer, M. A.; Bates, F. S. *Macromolecules* **2012**, *45*, 7228.

38. Fedors, R. F. *Polymer Engineering & Science* **1974**, *14*, 147.

39. Maurer, W. W.; Bates, F. S.; Lodge, T. P.; Almdal, K.; Mortensen, K.; Fredrickson, G. H. *The Journal of Chemical Physics* **1998**, *108*, 2989.

40. Watanabe, F.; Ohnishi, Y. *J. Vac. Sci. Technol. B* **1986**, *4*, 422.

41. Matsen, M. W. *The Journal of Chemical Physics* **1997**, *106*, 7781.

42. Koneripalli, N.; Singh, N.; Levicky, R.; Bates, F. S.; Gallagher, P. D.; Satija, S. K. *Macromolecules* **1995**, *28*, 2897.

43. Kellogg, G. J.; Walton, D. G.; Mayes, A. M.; Lambooy, P.; Russell, T. P.; Gallagher, P. D.; Satija, S. K. *Physical Review Letters* **1996**, *76*, 2503.

44. Israelachvili, J. N. *Intermolecular and Surface Forces*; Elsevier Science & Technology, 2011.

45. Sinturel, C.; Vayer, M.; Morris, M.; Hillmyer, M. A. *Macromolecules* **2013**, *46*, 5399.

46. Mansky, P.; Liu, Y.; Huang, E.; Russell, T. P.; Hawker, C. *Science* **1997**, *275*, 1458.

47. Ryu, D. Y.; Shin, K.; Drockenmuller, E.; Hawker, C. J.; Russell, T. P. *Science* **2005**, *308*, 236.

48. Bates, C. M.; Strahan, J. R.; Santos, L. J.; Mueller, B. K.; Bamgbade, B. O.; Lee, J. A.; Katzenstein, J. M.; Ellison, C. J.; Willson, C. G. *Langmuir* **2011**, *27*, 2000.

49. Suh, H. S.; Kang, H.; Nealey, P. F.; Char, K. *Macromolecules* **2010**.

50. Albert, J. N. L.; Epps, T. *Materials Today* **2010**, *13*, 24.

51. Peters, R. D.; Yang, X. M.; Kim, T. K.; Sohn, B. H.; Nealey, P. F. *Langmuir* **2000**, *16*, 4625.

52. Huang, E.; Russell, T. P.; Harrison, C.; Chaikin, P. M.; Register, R. A.; Hawker, C. J.; Mays, J. *Macromolecules* **1998**, *31*, 7641.

53. Peters, R. D.; Yang, X. M.; Wang, Q.; de Pablo, J. J.; Nealey, P. F. *J. Vac. Sci. Technol. B* **2000**, *18*, 3530.

54. Bita, I.; Yang, J. K. W.; Jung, Y. S.; Ross, C. A.; Thomas, E. L.; Berggren, K. K. *Science* **2008**, *321*, 939.

55. Segalman, R. A.; Yokoyama, H.; Kramer, E. J. *Adv. Mater.* **2001**, *13*, 1152.

56. Wan, L.; Yang, X. *Langmuir* **2009**, *25*, 12408.

57. Liu, C.-C.; Ramírez-Hernández, A.; Han, E.; Craig, G. S. W.; Tada, Y.; Yoshida, H.; Kang, H.; Ji, S.; Gopalan, P.; de Pablo, J. J.; Nealey, P. F. *Macromolecules* **2013**, *46*, 1415.

58. Yuan, Y.; Lee, T. R. In *Surface Science Techniques*; Bracco, G., Holst, B., Eds.; Springer Berlin Heidelberg: 2013; Vol. 51, p 3.

59. Korhonen, J. T.; Huhtamäki, T.; Ikkala, O.; Ras, R. H. A. *Langmuir* **2013**, *29*, 3858.

60. Kwok, D. Y.; Neumann, A. W. *Advances in Colloid and Interface Science* **1999**, *81*, 167.

61. Strobel, M.; Lyons, C. S. *Plasma Processes and Polymers* **2011**, *8*, 8.

62. Kwok, D. Y.; Lam, C. N. C.; Li, A.; Leung, A.; Wu, R.; Mok, E.; Neumann, A. W. *Colloids and Surfaces A: Physicochemical and Engineering Aspects* **1998**, *142*, 219.

63. Lam, C. N. C.; Wu, R.; Li, D.; Hair, M. L.; Neumann, A. W. *Advances in Colloid and Interface Science* **2002**, *96*, 169.

64. Sedev, R. V.; Petrov, J. G.; Neumann, A. W. *Journal of Colloid and Interface Science* **1996**, *180*, 36.

65. Russell, T. P.; Coulon, G.; Deline, V. R.; Miller, D. C. *Macromolecules* **1989**, *22*, 4600.

66. Coulon, G.; Russell, T. P.; Deline, V. R.; Green, P. F. *Macromolecules* **1989**, *22*, 2581.

67. Maher, M. J.; Bates, C. M.; Blachut, G.; Sirard, S.; Self, J. L.; Carlson, M. C.; Dean, L. M.; Cushen, J. D.; Durand, W. J.; Hayes, C. O.; Ellison, C. J.; Willson, C. G. *Chemistry of Materials* **2014**.

68. Mansky, P.; Russell, T. P.; Hawker, C. J.; Pitsikalis, M.; Mays, J. *Macromolecules* **1997**, *30*, 6810.

69. Kim, S.; Bates, C. M.; Thio, A.; Cushen, J. D.; Ellison, C. J.; Willson, C. G.; Bates, F. S. *ACS Nano* **2013**, *7*, 9905.

70. Bates, C. M.; Seshimo, T.; Maher, M. J.; Durand, W. J.; Cushen, J. D.; Dean, L. M.; Blachut, G.; Ellison, C. J.; Willson, C. G. *Science* **2012**, *338*, 775.

71. Houlihan, F. M.; Wallow, T. I.; Nalamasu, O.; Reichmanis, E. *Macromolecules* **1997**, *30*, 6517.

72. Cowie, J. M. G. *Alternating copolymers*, 1985.

73. Moore, E. R. *Industrial & Engineering Chemistry Product Research and Development* **1986**, *25*, 315.

74. Duda, J. L. In *Pure and Applied Chemistry* 1985; Vol. 57, p 1681.

75. Koberstein, J. T. *Journal of Polymer Science Part B: Polymer Physics* **2004**, *42*, 2942.

76. Bates, C. M. Dissertation, The University of Texas at Austin, 2013.

77. Seshimo, T.; Bates, C. M.; Dean, L. M.; Cushen, J. D.; Durand, W. J.; Maher, M. J.; Ellison, C. J.; Willson, C. G. *Journal of Photopolymer Science and Technology* **2012**, *25*, 125.

78. Ross, C. A.; Jung, Y. S.; Chuang, V. P.; Ilievski, F.; Yang, J. K. W.; Bita, I.; Thomas, E. L.; Smith, H. I.; Berggren, K. K.; Vancso, G. J.; Cheng, J. Y. *Journal of Vacuum Science & Technology, B* **2008**, *26*, 2489.

79. Matsen, M. W. *Macromolecules* **2010**, *43*, 1671.

80. Vu, T.; Mahadevapuram, N.; Perera, G. M.; Stein, G. E. *Macromolecules* **2011**, *44*, 6121.

81. Khanna, V.; Cochran, E. W.; Hexemer, A.; Stein, G. E.; Fredrickson, G. H.; Kramer, E. J.; Li, X.; Wang, J.; Hahn, S. F. *Macromolecules* **2006**, *39*, 9346.

82. Lin, J. W. P.; Dudek, L. P.; Majumdar, D. *Journal of Applied Polymer Science* **1987**, *33*, 657.

83. Gorham, W. *Journal of Polymer Science, A* **1966**, *4*, 3027.

84. Gleiter, R.; Hopf, H. *Modern cyclophane chemistry*; John Wiley & Sons, 2006.

85. Elkasabi, Y.; Chen, H. Y.; Lahann, J. *Advanced Materials* **2006**, *18*, 1521.

86. Elkasabi, Y.; Lahann, J. *Macromolecular Rapid Communications* **2009**, *30*, 57.

87. Tenhaeff, W. E.; Gleason, K. K. *Advanced Functional Materials* **2008**, *18*, 979.

88. Alf, M. E.; Asatekin, A.; Barr, M. C.; Baxamusa, S. H.; Chelawat, H.; Ozaydin-Ince, G.; Petruczok, C. D.; Sreenivasan, R.; Tenhaeff, W. E.; Trujillo, N. J.; Vaddiraju, S.; Xu, J.; Gleason, K. K. *Advanced Materials* **2010**, *22*, 1993.

89. Jung, H.; Hwang, D.; Kim, E.; Kim, B. J.; Lee, W. B.; Poelma, J. E.; Kim, J.; Hawker, C. J.; Huh, J.; Ryu du, Y.; Bang, J. *ACS Nano* **2011**, *5*, 6164.

90. Bradley, D. *Journal of physics D: Applied physics* **1987**, *20*, 1389.

91. Lenz, R. W.; Han, C.-C.; Stenger-Smith, J.; Karasz, F. E. *Journal of Polymer Science, Part A* **1988**, *26*, 3241.

92. Schäfer, O.; Greiner, A.; Pommerehne, J.; Guss, W.; Vestweber, H.; Tak, H. Y.; Bässler, H.; Schmidt, C.; Lüssem, G.; Schartel, B.; Stümpften, V.; Wendorff, J. H.; Spiegel, S.; Möller, C.; Spiess, H. W. *Synthetic Metals* **1996**, *82*, 1.

93. von Hofmann, A. W. *Justus Liebigs Annalen der Chemie* **1851**, *78*, 253.

94. Peruch, F.; Cramail, H.; Deffieux, A. *Macromolecular Chemistry and Physics* **1998**, *199*, 2221.

95. Haselwander, T. F. A.; Heitz, W.; Krügel, S. A.; Wendorff, J. H. *Macromolecular Chemistry and Physics* **1996**, *197*, 3435.

96. Burn, P. L.; Bradley, D. D. C.; Friend, R. H.; Halliday, D. A.; Holmes, A. B.; Jackson, R. W.; Kraft, A. *J. Chem. Soc. Perkin Trans. 1* **1992**, 3225.

97. Bell, A.; Elce, E.; Seto, K.; Promerus LLC, USA: 2011; Vol. WO2011072304A2.

98. Martínez-Arranz, S.; Albéniz, A. C.; Espinet, P. *Macromolecules* **2010**, *43*, 7482.

99. Clark, T. J.; Robertson, N. J.; Kostalik Iv, H. A.; Lobkovsky, E. B.; Mutolo, P. F.; Abruña, H. c. D.; Coates, G. W. *J. Am. Chem. Soc.* **2009**, *131*, 12888.

100. Larry F. Thompson, C. G. W., Seiichi Tagawa *Polymers for Microelectronics*; American Chemical Society, 1994.

101. Park, S.-M.; Park, O.-H.; Cheng, J. Y.; Rettner, C. T.; Kim, H.-C. *Nanotechnology* **2008**, *19*, 455304/1.

102. Peng, Q.; Tseng, Y.-C.; Darling, S. B.; Elam, J. W. *ACS Nano* **2011**, *5*, 4600.

103. Park, S.; Wang, J.-Y.; Kim, B.; Xu, J.; Russell, T. P. *ACS Nano* **2008**, *2*, 766.

104. Ruiz, R.; Wan, L.; Lille, J.; Patel, K. C.; Dobisz, E.; Johnston, D. E.; Kisslinger, K.; Black, C. T. *J. Vac. Sci. Technol. B* **2012**, *30*.

105. Jung, Y. S.; Ross, C. A. *Nano Letters* **2007**, *7*, 2046.

106. Hirai, T.; Leolukman, M.; Liu, C. C.; Han, E.; Kim, Y. J.; Ishida, Y.; Hayakawa, T.; Kakimoto, M.-a.; Nealey, P. F.; Gopalan, P. *Adv. Mater.* **2009**, *21*, 4334.

107. Kloninger, C.; Knecht, D.; Rehahn, M. *Polymer* **2004**, *45*, 8323.

108. Polymers, S. *Siloxane Polymers* **1993**.

109. Hirao, A.; Loykulnant, S.; Ishizone, T. *Prog. Polym. Sci.* **2002**, *27*, 1399.

110. Hirao, A.; Goseki, R.; Ishizone, T. *Macromolecules* **2014**.

111. Hartney, M. A.; Hess, D. W.; Soane, D. S. *J. Vac. Sci. Technol. B* **1989**, *7*, 1.

112. Gabor, A. H.; Lehner, E. A.; Mao, G.; Schneggenburger, L. A.; Ober, C. K. *Chemistry of Materials* **1994**, *6*, 927.

113. Colburn, M.; Grot, A.; Choi, B. J.; Amistoso, M.; Bailey, T.; Sreenivasan, S. V.; Ekerdt, J. G.; Grant Willson, C. *J. Vac. Sci. Technol. B* **2001**, *19*, 2162.

114. Farrell, R. A.; Petkov, N.; Shaw, M. T.; Djara, V.; Holmes, J. D.; Morris, M. A. *Macromolecules* **2010**, *43*, 8651.

115. Liu, C.-C.; Nealey, P. F.; Ting, Y.-H.; Wendt, A. E.; 6 ed.; AVS: 2007; Vol. 25, p 1963.

116. Rathsack, B.; Somervell, M.; Hooge, J.; Muramatsu, M.; Tanouchi, K.; Kitano, T.; Nishimura, E.; Yatsuda, K.; Nagahara, S.; Hiroyuki, I.; Akai, K.; Hayakawa, T. In *SPIE Advanced Lithography* 2012; Vol. 8323, p 83230B.

117. Gokan, H.; Esho, S.; Ohnishi, Y. *Journal of the Electrochemical Society* **1983**, *130*, 143.

118. Gu, X.; Gunkel, I.; Russell, T. P. *Philosophical Transactions of the Royal Society A: Mathematical, Physical and Engineering Sciences* **2013**, *371*.

119. Azarnouche, L.; Sirard, S.; Durand, W. J.; Gurer, E.; Hymes, D. B.; Willson, C. G.; Graves, D. B. In *36th DPS Conference* Yokohama, Japan, 2014.

120. Draine, B.; Bertoldi, F. *Astrophysical Journal* **1996**, *468*, 269.

121. Truica-Marasescu, F.-E.; Wertheimer, M. R. *Macromolecular Chemistry and Physics* **2005**, *206*, 744.

122. Saik, V. O.; Lipsky, S. *The Journal of Physical Chemistry A* **2001**, *105*, 10107.

123. Nate, K.; Ishikawa, M.; Ni, H.; Watanabe, H.; Saheki, Y. *Organometallics* **1987**, *6*, 1673.

124. Sakurai, H.; Abe, J.; Sakamoto, K. *Journal of Photochemistry and Photobiology A: Chemistry* **1992**, *65*, 111.

125. Ahmed, M.; Potzinger, P.; Wagner, H. G. *Journal of Photochemistry and Photobiology A: Chemistry* **1995**, *86*, 33.

126. Ji, S.; Nagpal, U.; Liu, G.; Delcambre, S. P.; Müller, M.; de Pablo, J. J.; Nealey, P. F. *ACS Nano* **2012**, *6*, 5440.

127. Hsieh, H. L.; Q., R. P. *Anionic Polymerization: Principles and Practical Applications*; Marcel Dekker Inc.: New York, 1996.

128. Strahan, J. R., The University of Texas at Austin, 2010.

129. Kennemur, J. G.; Yao, L.; Bates, F. S.; Hillmyer, M. A. *Macromolecules* **2014**, *47*, 1411.

130. Allen, R. D.; Long, T. E.; McGrath, J. E. *Polymer Bulletin* **1986**, *15*, 127.

131. Hadjichristidis, N.; Iatrou, H.; Pispas, S.; Pitsikalis, M. *Journal of Polymer Science Part A: Polymer Chemistry* **2000**, *38*, 3211.

132. Fukukawa, K.-i.; Zhu, L.; Gopalan, P.; Ueda, M.; Yang, S. *Macromolecules* **2004**, *38*, 263.

133. Hirao, A.; Ando, Y.; Ishizone, T.; Nakahama, S. *Macromolecules* **2003**, *36*, 5081.

134. Hawker, C. J.; Bosman, A. W.; Harth, E. *Chem. Rev.* **2001**, *101*, 3661.

135. Hawker, C. J.; Barclay, G. G.; Dao, J. *J. Am. Chem. Soc.* **1996**, *118*, 11467.

136. Harth, E.; Hawker, C. J.; Fan, W.; Waymouth, R. M. *Macromolecules* **2001**, *34*, 3856.

137. Lee, J.; Graves, D. *Journal of physics D: Applied physics* **2011**, *44*, 325203.

138. Kim, S.; Nealey, P. F.; Bates, F. S. *Nano Letters* **2013**, *14*, 148.

139. Leibler, L. *Macromolecules* **1980**, *13*, 1602.

140. Rosedale, J. H.; Bates, F. S. *Macromolecules* **1990**, *23*, 2329.

141. Sakamoto, N.; Hashimoto, T. *Macromolecules* **1995**, *28*, 6825.

142. Russell, T. P.; Hjelm, R. P.; Seeger, P. A. *Macromolecules* **1990**, *23*, 890.

143. Fetters, L. J.; Lohse, D. J.; Richter, D.; Witten, T. A.; Zirkel, A. *Macromolecules* **1994**, *27*, 4639.

144. Meuler, A. J.; Ellison, C. J.; Qin, J.; Evans, C. M.; Hillmyer, M. A.; Bates, F. S. *J. Chem. Phys.* **2009**, *130*, 234903/1.

145. Widin, J. M.; Kim, M.; Schmitt, A. K.; Han, E.; Gopalan, P.; Mahanthappa, M. K. *Macromolecules* **2013**, *46*, 4472.

146. Beckingham, B. S.; Register, R. A. *Macromolecules* **2013**, *46*, 3084.

147. Qin, J.; Morse, D. C. *Physical Review Letters* **2012**, *108*, 238301.

148. Sakurai, S.; Mori, K.; Okawara, A.; Kimishima, K.; Hashimoto, T. *Macromolecules* **1992**, *25*, 2679.

149. Kratky, O.; Pilz, I.; Schmitz, P. J. *Journal of Colloid and Interface Science* **1966**, *21*, 24.

150. Roe, R.-J.; Roe, R. *Methods of X-ray and neutron scattering in polymer science*; Oxford University Press New York, 2000; Vol. 554580219.

151. Dudowicz, J.; Freed, K. F. *Macromolecules* **1993**, *26*, 213.

152. Fredrickson, G. H.; Helfand, E. *The Journal of Chemical Physics* **1987**, *87*, 697.

153. Bates, F. S.; Fredrickson, G. H. *Annual Review of Physical Chemistry* **1990**, *41*, 525.

154. Koneripalli, N.; Levicky, R.; Bates, F. S.; Ankner, J.; Kaiser, H.; Satija, S. K. *Langmuir* **1996**, *12*, 6681.

155. Kikuchi, M.; Binder, K. *The Journal of Chemical Physics* **1994**, *101*, 3367.

156. Helfand, E.; Wasserman, Z. R. *Macromolecules* **1976**, *9*, 879.

157. Ohta, T.; Kawasaki, K. *Macromolecules* **1986**, *19*, 2621.

158. Hashimoto, T.; Shibayama, M.; Kawai, H. *Macromolecules* **1980**, *13*, 1237.

159. Hashimoto, T.; Fujimura, M.; Kawai, H. *Macromolecules* **1980**, *13*, 1660.

160. Turner, M. S. *Physical Review Letters* **1992**, *69*, 1788.

161. Walton, D. G.; Kellogg, G. J.; Mayes, A. M.; Lambooy, P.; Russell, T. P. *Macromolecules* **1994**, *27*, 6225.

162. Geisinger, T.; Müller, M.; Binder, K. *The Journal of Chemical Physics* **1999**, *111*, 5241.

163. Wang, Q.; Yan, Q.; Nealey, P. F.; de Pablo, J. J. *The Journal of Chemical Physics* **2000**, *112*, 450.

164. Ramírez-Hernández, A.; Suh, H. S.; Nealey, P. F.; de Pablo, J. J. *Macromolecules* **2014**, *47*, 3520.